# QUANTIFYING HIMALAYAN GLACIER CHANGE FROM THE 1960S TO EARLY 2000S, USING CORONA, GLIMS AND ASTER GEOSPATIAL DATA

Ryan WILSON

**Ph.D. Thesis** **2015**

# Quantifying Himalayan glacier change from the 1960s to early 2000s, using Corona, GLIMS and ASTER geospatial data

Submitted in candidature for the degree of
Doctor of Philosophy
to the University of Salford

by

**Ryan Wilson**

June 2015

**Acknowledgements**

Firstly, I would like to thank my fiancée Lauren whose support has been unwavering and faultless through all the many early mornings, late nights and intermittent periods of self-doubt she has had to endure. Academic ambitions aside, the sole driving force behind the completion of this thesis was the thought that it may one day help us both achieve all our hopes and aspirations. Furthermore, I would like to thank Lauren's mother Wendy, for providing me with a roof over my head back in the early days.

At the University of Salford there are a number of people who have played a central role in this PhD. My deepest gratitude goes first and foremost to Professor David Collins, who I would like to thank for giving me the opportunity to pursue a geographical passion that he himself ignited both in the lecture hall and in the waist-high snow of the Swiss Alps all those years ago. Professor Collins has also provided me with the financial means to be able to focus purely on my studies and the chance to gain vital experience as a Research Assistant. Additionally, I would like to thank Dr. Neil Entwistle for both his supervision and the many field-based based opportunities he has offered me; our Icelandic endeavours will never be forgotten.

I would also like to express my heartfelt gratitude to Dr. Richard Armitage who thanklessly made himself available as an ever present Remote Sensing & GIS mentor. His advice has been invaluable. Dr. Armitage is truly a credit to the University of Salford and I shall forever be indebted to his kindness.

Thanks to the University of Salford for allowing me the opportunity to be part of the Graduate Teaching Assistantship and the opportunity to research and teach in higher education. I would also like to acknowledge the financial support I received from the European Union Framework 7 (EU-FP7) High Noon Project. I must also thank the GLIMS project for giving me access to no-cost ASTER data, which represented a significant research component.

Finally, I would like to thank my parents Steven and Denise and my sister Janine, who have provided nothing but love and support and taught me from a young boy to aim high and work hard. I would also like to extend a big thank you to all my friends who have been there whenever needed. Vishal and Alberto, in particular, gave me the belief that that distant light would eventually be met.

Ryan Wilson

For Grandad Wilson

**Table of Contents**

**List of Figures**

**List of Tables**

**List of Abbreviations**

**ALOS:** Advanced Land Observing Satellite
**ASTER**: Advanced Spaceborne Thermal Emission and Reflection radiometer
**ASTER GDEM:** ASTER Global DEM

**ATM:** Automatic Terrain Extraction
**AVHRR:** Advanced Very High Resolution Radiometer
**DEM**: Digital Elevation Model
**DGPS:** Differential Global Positioning System
**DN:** Digital Number
**ELA:** Equilibrium Line Altitude
**EMR:** Electromagnetic Radiation

**ERDAS Imagine LPS:** ERDAS Imagine Lieca Photogrammetry Suite
**GCP**: Ground Control Point
**GIS**: Geographical Information System
**GLIMS**: Global Land Ice Measurements from Space project
**GSI:** Geological Survey of India
**HR:** High Resolution
**IPCC**: Intergovernmental Panel on Climate Change
**IR:** Infrared
**IRS:** Indian Remote Sensing Satellite
**Landsat ETM+:** Landsat Enhanced Thematic Mapper
**Landsat TM:** Landsat Thematic Mapper
**LIA:** Little Ice Age
**LIAM:** Little Ice Age Maximum
**LR:** Low Resolution
**METI:** Ministry of Economy, Trade and Industry
**MODIS:** Moderate Resolution Imaging radiometer
**NASA:** National Aeronautics and Space Administration
**NDSI:** Normalised Difference Snow Index
**NSIDC:** National Snow and Ice Data Centre
**SOI:** Survey of India

**SPOT:** System Pour l'Observatoire de la Terra
**SRTM**: Shuttle Radar Topography Mission
**SWIR:** Short Wave Infrared
**USGS:** United States Geological Survey

**TIR:** Thermal Infrared
**UTM:** Universal Transverse Mercator

**VHR:** Very High Resolution
**VNIR:** Visual Near Infrared
**WGMS:** World Glacier Monitoring Service
**WGS:** World Geodetic System

**Abstract**

Since reaching their LIAMs, Himalayan glaciers have generally undergone a period of retreat, evident from large moraines left at former ice limits. Currently, however, detailed assessments of Himalayan glacier fluctuations over the past century are limited and fail to compare spatially or temporally to records available in Central Europe, North America and Scandinavia. Consequently, the variability and magnitude of glacial change across the Himalayas, which is a key indicator of climatic change in this region, is yet to be fully understood.

Against a background of poor data availability, Corona imagery and historic GLIMS glacier outlines now offer an opportunity to assess glacier extent for regions of the Himalayas pre-1980. Corona imagery, acquired by a US space-borne reconnaissance mission operational from 1960 to 1970, represents a particularly unique dataset offering high resolution imagery (~1.8 m) with stereo-scopic capabilities. Utilising Corona imagery, there is an opportunity to produce detailed maps of Himalayan glacier extent and extract ice surface elevation estimations, in some instances, for the first time. Despite having been de-classified in 1995, the use of Corona data in the Himalayas has been neglected, mainly because of orthorectification challenges related to its unique geometric distortions. Hence, there remains a need to develop a low cost and easily replicable method of accurately orthorectifying Corona imagery enabling its use as a large-scale glacier mapping tool in the Himalayas. In response to this need, Corona images are orthorectified in this study through the use of: (1) a non-metric photogrammetry approach; and (2) horizontal and vertical reference data acquired from ortho-ASTER imagery and the freely available ASTER GDEM.

By comparing glacier measurements derived from Corona imagery, GLIMS data and more contemporary ASTER data, changes in glacier area, length and in some instances volume, between the 1960/70s and early 2000s, were quantified for glaciers selected within four study areas located in Uttarakhand, India and Central Nepal. Importantly, this cross-regional glacier change dataset both complements and enhances current Himalayan records. Most notably, results indicate that glaciers selected in the Bhagirathi and Pindar/Kali basins, Uttarakhand, reduced in area by a relatively small 7.97±0.29% and 7.54±0.26%, respectively. Contrastingly, glaciers selected in the more easterly located Seti and Trisula basins reduced in area by 29.78±0.2% and 50.55±0.08%, respectively. Comparisons of Corona DEM (derived from Corona stereo-pairs) and ASTER Global DEM elevations at the terminus regions of four glaciers revealed extensive surface lowering, ranging from 87±27 m to 142±27 m. For Corona processing, the methods applied were shown to orthorectify Corona images to an accuracy that allows comparable glacier outlines to be delineated, further demonstrating the mapping potential of this dataset. However, for Corona DEM extraction, the use of ASTER spatial control data was shown to be inadequate and the presence of large vertical errors in the DEMs generated hindered the measurement of glacier volume change. For this purpose, it is therefore recommended that the methods developed are tested with the use of very high resolution spatial control data.

## 1. Introduction

Glaciers are considered to be sensitive indicators of climatic variability in high mountain environments (Houghton *et al.*, 2001; Du *et al.*, 2004). Both national and international schemes aimed at monitoring fluctuations in glacier dimensions (area, length and volume) have therefore become vital prerequisites in order to better understand relationships between climatic variables and glaciers. Glaciers worldwide, in general, have undergone a prolonged period of areal shrinkage and thinning since reaching LIAMs (~1850), in response to rising air temperatures and reductions in levels of precipitation (Barry, 2006). Glacial mass loss has, in many areas, become more pronounced since the 1980s, prompting some to suggest that complete deglaciation of certain mountainous regions may take place in the coming decades (e.g. Zemp *et al.*, 2006; WGMS, 2008). Recent comments by the IPCC (2007), suggesting incorrectly that glaciers in the Himalayas would disappear by 2035, were particularly controversial and focused the attention of scientific communities on this important but scarcely studied region of the world.

As the most highly glaciated area outside the polar regions (Dyurgerov & Maier, 2005), glacier melt water from the Himalayan ranges is highly influential on regional hydrology and provides water resources to over 500 million downstream inhabitants (Mall *et al.*, 2006). Furthermore, Himalayan glaciers are estimated to contribute considerably to the ongoing rise in global sea levels under current warming conditions (Matsuo & Heki 2010). As a result, interest in the fluctuations of mountain glaciers in central Asia may be higher than anywhere else in the world.

Although proved erroneous and later discredited (see Cogley, 2010), the IPCC's '2035' claim followed several studies suggesting alarming rates of glacial wastage in the Himalayas (e.g. Dyurgerov & Meier (2005) and Fushimi (2000)). However the assumption, made by the IPCC's 2007 Working Group II report, that 'glaciers in the Himalaya are receding faster than in any other part of the world' (Parry *et al*. 2007)

was highly contentious. Recent glacier monitoring efforts have shown that some glaciers in the Himalayan region are now in stable or even advancing states (e.g. Raina, 2009; Hewitt, 2005), which without knowledge of individual glacier mass balance may contradict notions of an accelerated rate of ice mass reduction. Other studies have suggested that glacier areal reduction rates in certain areas of the Himalayas have reduced considerably over the past decade (e.g. Bolch *et al.*, 2010; Kumar *et al.*, 2008). Portraying a confused picture of glacial health, these observations have complicated attempts to understand glacier fluctuations across the Himalayan arc and have highlighted the need for further monitoring efforts.

Fluctuations in glacier dimensions are brought about by changes in mass balance, which are principally regulated by climatic variables. The climate of the Himalayan region varies significantly from east (dominated by summer monsoon precipitation) to west (dominated by winter precipitation). Reflecting this climatic gradient, glaciers in the Himalayas are believed to have summer-accumulation regimes in the eastern and central ranges and cold arid or Alpine regimes in the western ranges (Thayyen & Gergen, 2009). Consequently, glaciers across the Himalayan arc are likely to have responded in different ways to recent climatic events (Rees & Collins, 2006; Bishop *et al.*, 2007). In order to gain a representative understanding of glacier change in the Himalayas, glacier monitoring studies should therefore be well distributed across the mountain range.

Detailed assessments of glacier fluctuations in the Himalayas, since the end of the LIA, currently fail to compare spatially or temporally to datasets available in Europe, North America and Scandinavia (WGMS, 2008). Furthermore, the majority of Himalayan glacier mapping studies published neglect glacier volume change (a direct signal of mass balance change (Haeberli, 2004)), tending instead to focus on glacier length changes (e.g. Scherler *et al.*, 2011). These spatial and temporal gaps in the Himalayan glacier change record are a result of a limited availability of aerial survey data, field observations and accurate topographic maps (outside of Nepal) (Agarwal, 2001; Bhambri & Bolch, 2009).

With the introduction of advanced space-borne imagery and GIS techniques from the 1970s, the number of glaciers being continuously monitored worldwide has increased considerably. As a result, numerous international glacier inventories have been compiled, comparing historic (derived from pre-1970 aerial photography and topographic maps, for example) and modern satellite-based datasets (e.g. Kääb *et al.*, 2002), some of which are now included in the WGMS database. The development of automated mapping techniques has further aided glacier monitoring efforts, reducing image processing times (Racoviteanu *et al.*, 2008).

In the Himalayas, several studies have mapped spatio-temporal changes in glacial extent using satellite imagery, which has gradually improved knowledge of recent glacial fluctuations (e.g. Kulkarni *et al.*, 2007; Bolch *et al.,* 2008). Due to its ease of acquisition, near global coverage and adequate spatial resolutions, imagery from the Landsat satellite series has been particularly well utilised, allowing the areal extent of a number of Himalayan glaciers, from the 1980s onwards, to be manually delineated (e.g. Kulkarni, 1991). Efforts to automate glacier delineation in the Himalayas, however, have been hampered by the widespread presence of supragacial debris (Raup *et al.*, 2007). Supraglacial debris effectively masks glacier margins making it difficult to identify them from the surrounding terrain, this being one of the factors hindering large-scale glacier mapping efforts in the Himalayas (Bhambri & Bolch, 2009).

In addition to areal changes, a limited number of studies have also estimated temporal changes in volume for a small number of Himalayan glaciers using DEMs (e.g. Berthier *et al.*, 2007). DEMs can now be prepared from a number of sources, including stereoscopic space- and air-borne optical data and topographic maps. Importantly, comparisons of glacier DEMs acquired at differing points of time allow geodetic volume changes to be estimated which can be used to improve mass balance records in the Himalaya (e.g. Bolch *et al*., 2008). The ability to perform geodetic glacier measurements in the Himalayas has been aided by the free availability of global DEMs, such as the SRTM dataset, that provide useful elevation reference points (e.g. Paul and Haeberli, 2008).

The increased accessibility of satellite imagery and DEMs has greatly facilitated glacier monitoring efforts across the Himalayas. Unfortunately, however, both these geo-spatial datasets are temporally limited. Multispectral satellite imagery with pixel resolutions equal to or below 30 m, for example, is only available from 1982 (Landsat series), whilst space-borne DEM data only became available in 1999 (stereo ASTER imagery). Due to the unavailability of historic topographic maps and aerial survey data, the majority of glacier change assessments in the Himalayas are therefore restricted to the past four decades.

In 1995, imagery from the American intelligence Corona satellite missions was declassified and made available to the public for the first time. Collected between 1960 and 1972, Corona imagery covers large portions of the Himalayas, and provides an opportunity to map glacier dimensions pre-1980. Although exhibiting significant geometric distortions which have been shown to be difficult to rectify (e.g. Galiatsatos *et al*., 2008), against a background of low data availability in Himalayan region, Corona imagery is a valuable source of historic high resolution data, providing detail equal to that of 1:50,000 aerial photography (Slama *et al.*, 1980). Furthermore, the Corona sensor stereoscopic capabilities allow for detailed DEMs to be generated from image stereo pairs.

Despite its spatial coverage and low-cost ($30 per 17 x 232 km strip), Corona imagery and its stereoscopic capabilities have only recently begun to be explored as glacier mapping tools in the Himalayas (e.g. Bolch *et al*., 2008). The value of Corona data for such applications is determined by the accuracy of the orthorectification process (which removes both sensor- and terrain-related image orientation errors). The processing of Corona data in high mountainous terrain, however, presents challenges due to increased influence of terrain-induced errors. Despite these challenges, recent Himalayan mapping studies have successfully corrected Corona imagery and estimated glacier area and volume changes (Bolch *et al*., 2008; Bhambri *et al*., 2011; Bolch *et al*., 2010; Schmidt & Nusser, 2012)). However, these studies

are limited in their use of costly sources of ground control (i.e. very high resolution satellite imagery), custom-built processing software and cover relatively small areas.

Considering current limitations in the use of Corona imagery as a glacier mapping tool in the Himalayas, there is a need to test and formulate new processing methodologies that are easily replicable, low cost and allow the dataset to be sufficiently geometrically corrected. Such methodologies would improve the ability to perform large-scale multi-temporal analyses of glacier area, length and volume change in the Himalayas which would (1) enhance and complement other glacier mapping records which are limited; and, in doing so, (2) improve the understanding of glacier change across the Himalayas. Dating back to the 1960-70s, glacier measurements from the Nepalese Himalaya (derived from topographic maps) have recently become available via the GLIMS project. Supplementing 1960s Corona data, GLIMS data offers an additional opportunity for analyses of glacier area and length changes in the Nepalese Himalayas over the past 40-50 years.

Kargel *et al*. (2011) likened the Himalayas to a montage of glacier area, length and volume changes which are yet to be fully understood. Knowledge of past glacier fluctuations across the Himalayas, attained through assessment of 1960s Corona imagery and GLIMS glacier outlines, may therefore help to reduce this uncertainty and aid the future reporting of climate/glacier interactions.

### 1.1. Aims & Hypothesis

This investigation attempts to compare a number of geospatial datasets, available for the Himalayas, in order to map glacier change. Central to the success of this glacier mapping exercise is the use of Corona imagery, the processing of which will require the identification, development and modification of new GIS-based methodologies. The aims of this investigation are therefore divided accordingly into methodological aims and glaciological aims.

The principle methodological aims are to:

- Develop an easily replicable and low cost method for orthorectifying 1960s Corona imagery.

- Extract detailed DEMs of the high mountainous Himalayas from Corona stereo-pairs.

The principle glaciological aims are to:

- Quantify glacier area, length and volume changes across portions of the Himalayan arc from the 1960s-2000s, through the use of Corona, GLIMS and ASTER data, with a view to improving the understanding of glacier variability in the region.

- Use the resulting Himalaya glacier change data together with the ASTER GDEM to analyse differences in glacier hypsometry, elevation, and size. Such data is currently limited in the Himalayas.

With the aim of characterizing glacier area change and its distribution with elevation, the results of this investigation will provide useful inputs for hydrological models developed to forecast changing runoff from Himalayan glaciers, such as those used by the High Noon Project (http://www.eu-highnoon.org/), in which the author was employed between 2010 and 2011.

**1.2. Study Area**

The study area for this investigation included four sites spread along the main Himalayan arc from central Nepal to Uttarakhand, India (Figures 1.1-1.4). From east to west the sites include Langtang (LT), Setibeni (SB), Nanda Devi (ND) and Gangotri-Chaukhamba (GC). Study site selection was determined through balancing the aim of examining glacier changes in various Himalayan basins (taking into account the different climate regimes from east to west) with the spatial availability of good quality Corona and ASTER satellite imagery (discussed in Chapter 5), and GLIMS glacier outlines.

### 1.2.1. Langtang

Straddling the border of Tibet and central Nepal, the LT site includes almost all of the glaciated area contained within the Trisula River basin in the Langtang Himal (Figure 1.1). Draining into the Narayani River system, the Trisula River basin ranges in elevation from 569-7358 m.a.s.l (above a gauging site), covers an area of 4640 km$^2$, and is roughly 8.8% glaciated (above 569m.a.s.l). The glaciated area sampled within this basin equates to around 18% of the total glacierised area in the Narayani River system. The majority of these glaciers are included in the LT site. Situated in the eastern corner of the Trisula basin, the largest and most studied glacier (e.g. Kappenberger *et al.*, 1993; Tangborn & Rana, 2000) in the LT site is the Langtang glacier covering an area of 41 km$^2$ and measuring 18 km in length. Originating from a cirque below the Langtang Ri peak (7205 m.a.s.l) the Langtang glacier is located at the head of Langtang valley. As with other areas in the Himalayas, a significant

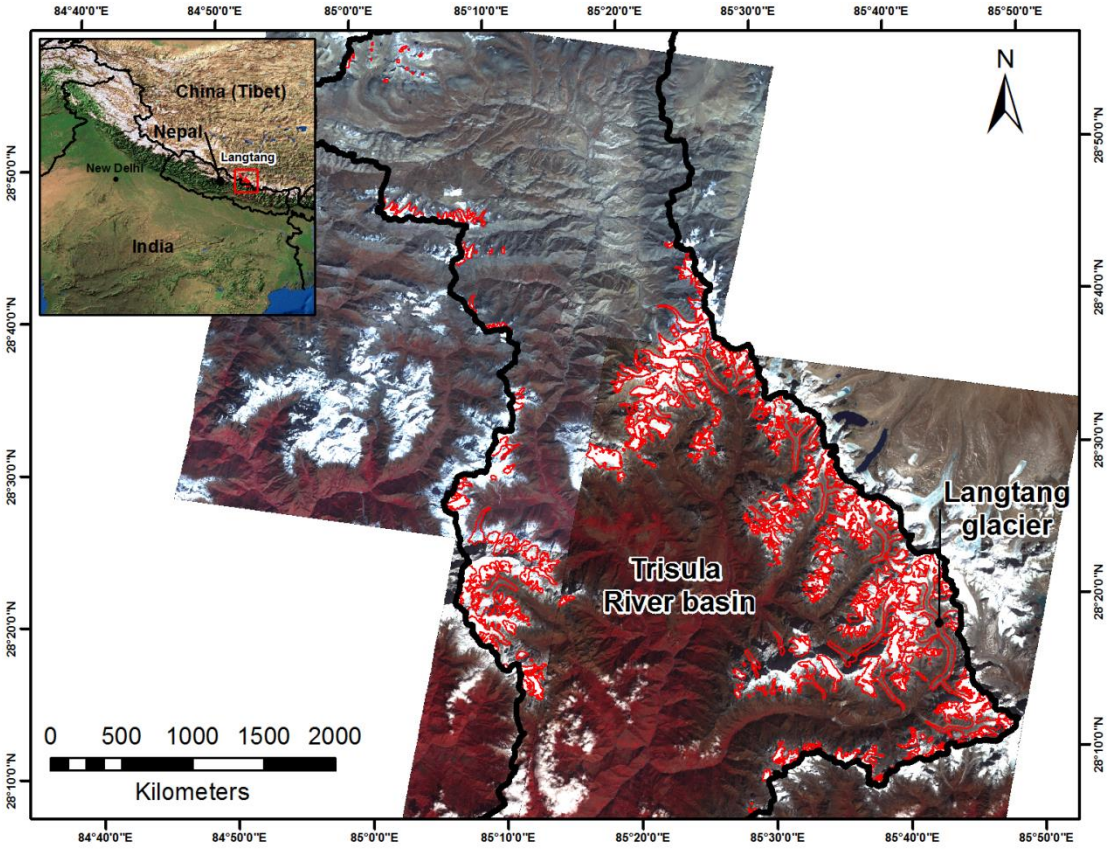


**Figure 1.1: Glaciers selected for the Langtang study site (outlined in red). Background: Terra ASTER satellite imagery.**

portion of the glaciated area in the LT site is covered with debris, especially in glacier ablation zones. The climate of the LT site is influenced by the summer monsoon and it experiences an extended monsoon season from late May to September, when 80% of its annual precipitation falls (DHM, 1997).

### 1.2.2. Setibeni

The SB site is located in the Himalayas of western Nepal and includes almost all the glaciated area of the Seti River basin (Figure 1.2). With a maximum elevation of around 8147 m.a.s.l (above a gauging site), the Seti River basin drains from the western portions of the Narayani River system (around 175 km west of the LT site). Overall, the Seti River basin includes around 400 glaciers and is roughly 6.7% glaciated (above 483 m.a.s.l). The majority of these glaciers are included in the SB site and represent around 23% of the total ice area in the Narayani catchment.

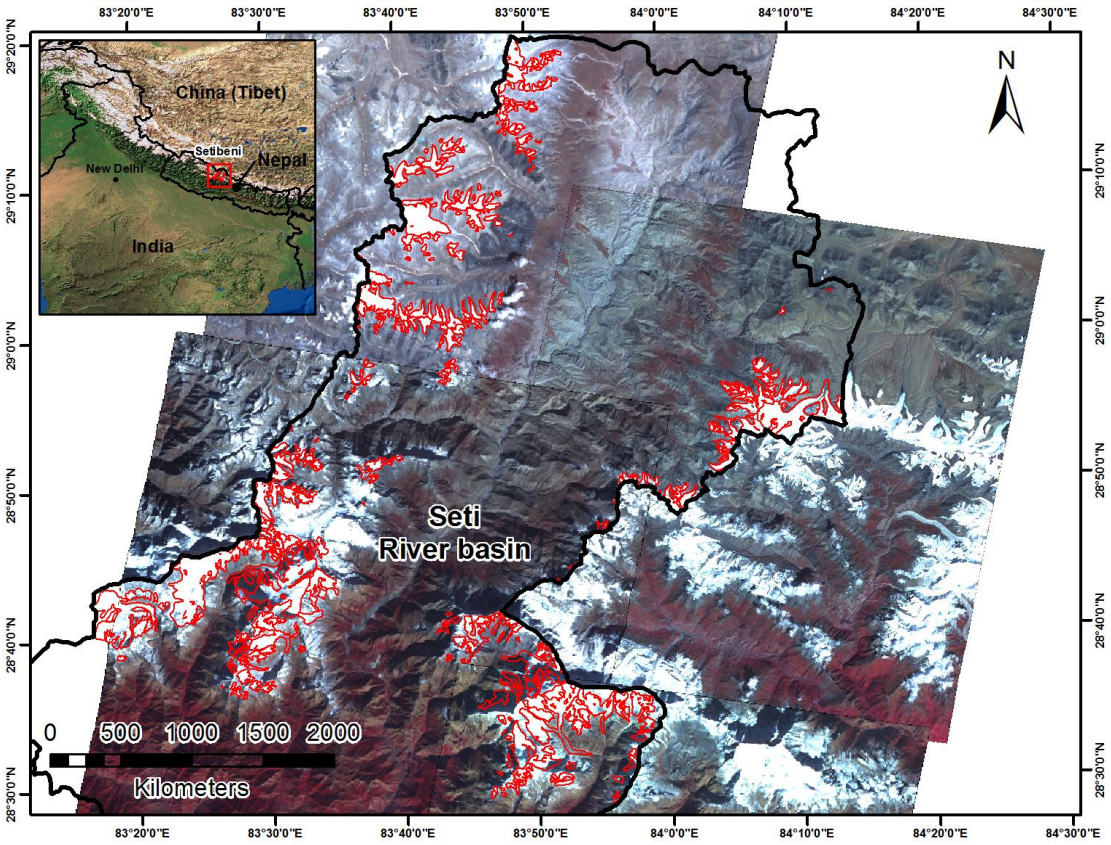


**Figure 1.2: Glaciers selected for the Setibeni study site (outlined in red). Background: Terra ASTER satellite imagery.**

Although it contains a number of large glaciers (five over 20 $km^2$), to the authors knowledge no large scale multi-temporal glacier monitoring studies currently exist for the SB site. In terms of climatic setting, similar to the LT study site, the SB site is dominated by the summer monsoon and experiencing an extended monsoon season in comparison to basins located further west along the Himalayan arc.

### 1.2.3. Nanda Devi

The ND site is located in the Kumaun Himalayas around 100 km east of the GC site. The glaciers of the ND site concentrate around the Nanda Devi peak (7816 m.a.s.l) and cover a surface area of 83 $km^2$ (Figure 1.3). Glaciers included supply meltwater to two separate river basins. On the western side of the Nanda Devi peak, glaciers feed into the Pindar basin, whilst on the north-eastern side glaciers feed the Gori Ganga River which drains into the Kali River basin. Both the Kali and Pindar rivers are tributaries of the Ganges River. The largest glacier of the ND site is the Milam glacier which covers around 54 $km^2$ and is the third largest glacier in the Indian Himalayas. Feeding the Gori Ganga River, Milam glacier originates from two cirques below the Trishul peak (7120m.a.s.l) and includes seven large tributary glaciers. Milam is the most studied out of all the glaciers included in the ND site (Ahmed, 1962; Raj, 2011). Like other glaciers in the ND site, the ablation zone of Milam glacier is covered by debris. Similar to the GC site, ND is influenced by the summer monsoon.

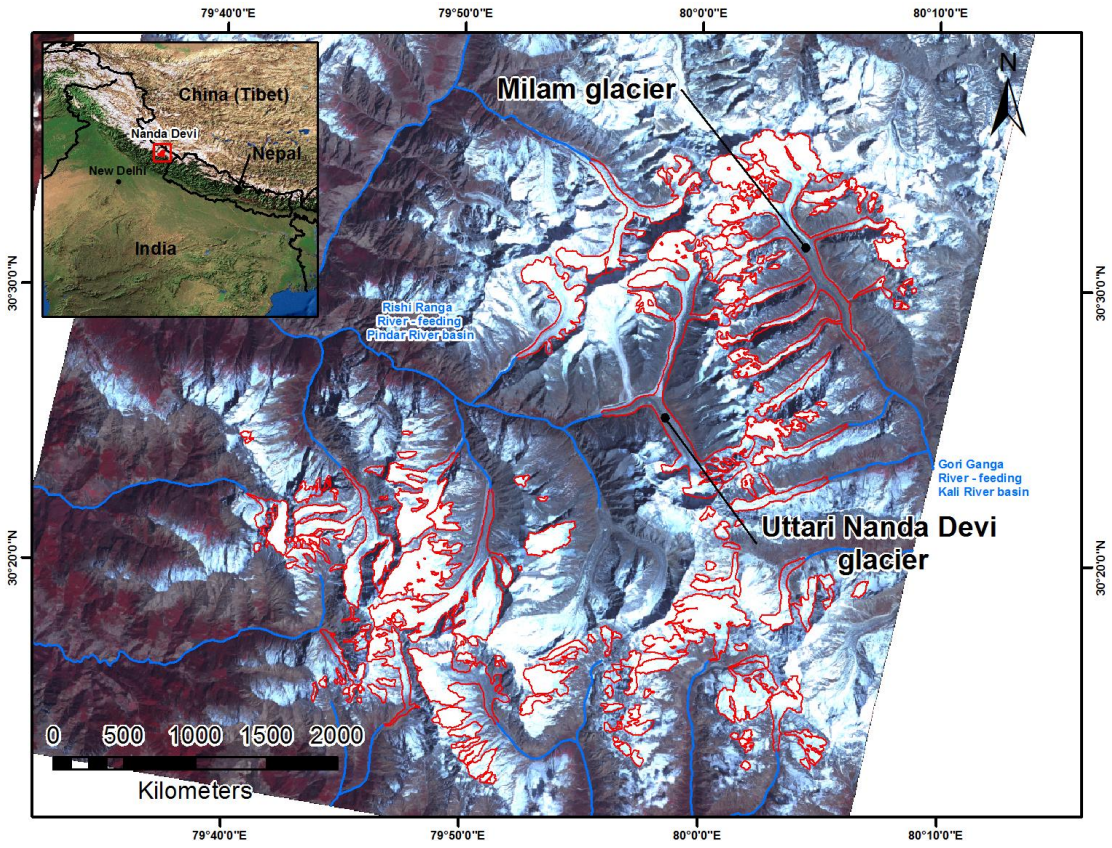


**Figure 1.3: Glaciers selected for the Nanda Devi study site (outlined in red). Background: Terra ASTER satellite imagery.**

### 1.2.4. Gangotri-Chaukhamba

Located in the Garhwal Himalayas, Uttarakhand, India, the GC site includes a portion of glaciated area contained within the upper Bhagirathi River basin (Figure 1.4). The Bhagirathi River is significant in that it is the primary source of the Ganges River. Additionally, the river is dammed at 730 m.a.s.l by the Tehri Dam. Above the Tehri dam the Bhagirathi River basin covers around 5400 km$^2$ with a maximum elevation of 7138 m.a.s.l. Overall, the GC site includes 141 glaciers, equating to 48% of the glaciers contained within the Bhagirathi River basin.

The glaciers included in the GC site are mainly distributed around the Chaukhamba massif and it is from this highly elevated massif that Gangotri glacier originates. As the principle glacier of the GC site, Gangotri is the largest glacier in the Indian Himalayas, covering an area of 182 km$^2$ (Vohra, 2010), and has the most

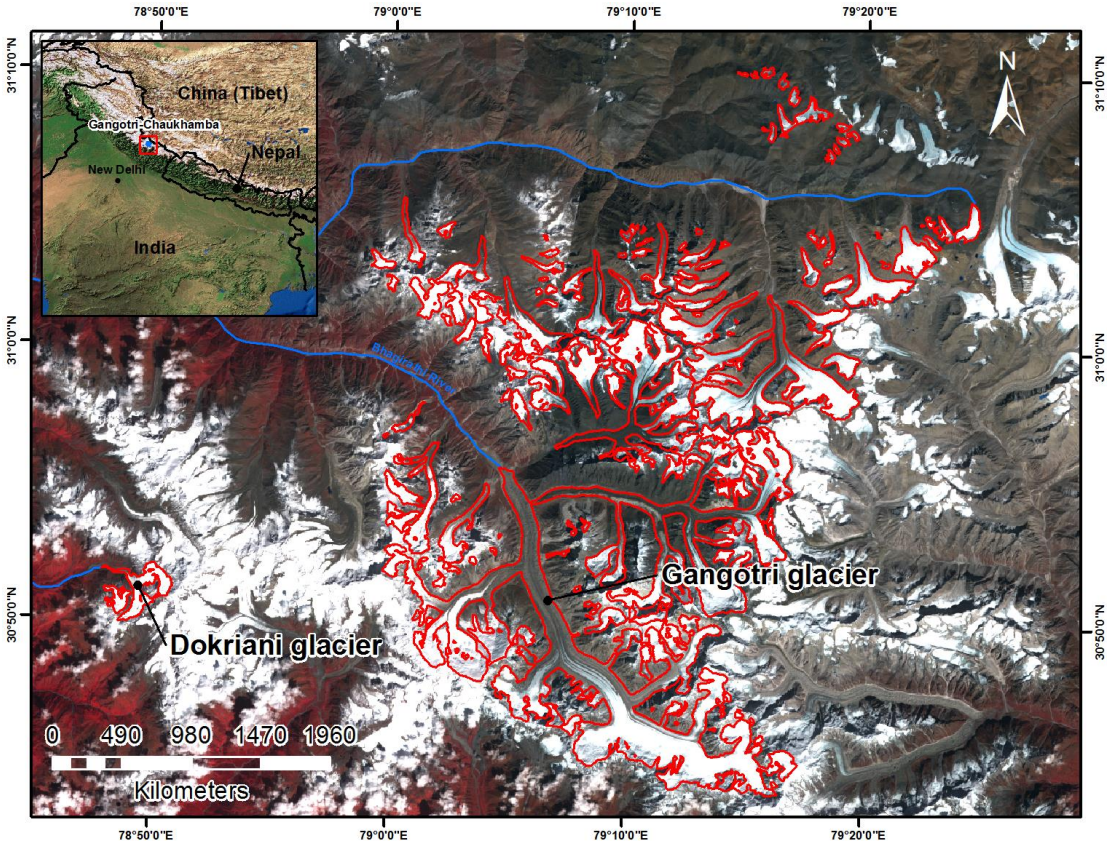


**Figure 1.4: Glaciers selected for the Gangotri-Chaukhamba study site (outlined in red). Background: Terra ASTER satellite imagery.**

comprehensive record of length and area observations of all the glaciers selected in the Uttarakhand region (e.g. Kumar *et al.* 2008; Thayyen *et al*., 2008; Bhambri *et al.*, 2012).

A major feature of the glacierised area within the Bhagirathi basin is the presence of large amounts of supraglacial debris on ablation zones. Of the 20 glaciers studied in the Bhagirathi basin by Bhambri *et al.* (2011), for example, ~26% of the overall ice area was covered with debris. As with the other three study sites in this project, this debris cover influences the sensitivity of glaciers to climatic variations. In terms of climate, the main source of precipitation at the GC site, which falls as snow at high elevation, is the summer monsoon which occurs between June and September (Vohra, 2010). Additionally, large amounts of snowfall also occurs in winter (December-March) supplied by westerly disturbances (Dobhal *et al.*, 2008) (described in chapter 3).

## 2. Corona satellite imagery

With reference to the methodological aims set out in section 1.1, this chapter aims to introduce the Corona image dataset, describe the advantages and limitations of Corona imagery as a mapping tool, discuss the use of Corona imagery by other mapping-based studies and finally set out what is needed to improve the use of Corona imagery as a mapping tool, specifically in the Himalayas. The chapter ends with a statement of methodological objectives for the project.

### 2.1. Corona imagery: Brief history

The Corona satellite program was the United States first space-borne reconnaissance mission, being operational from 1960-1972. Developed to replace the U-2 spy plane missions, the Corona program gathered photographs from space targeted at a number of regions deemed to have strategic military importance at the time, such as Asia, South America, Greenland, Eastern Europe and Northern Africa (Altmaier & Kany, 2002). Regions typically covered by Corona are shown in figure 2.1.

Rather than consisting of a single satellite, the Corona program was made up of a number of individual satellite missions which initially only lasted for a single day but by the end of the program extended for as long as 19 days. Throughout its operational period, the Corona program utilised a number of camera models each of which improved upon the last. Each of these camera models was identifiable through keyhole references (KH) and ranged sequentially from KH-1 to KH-4 (including KH-4A and KH-4B).

Almost all of the imagery collected by the Corona program was recorded on black and white panoramic film, with early missions (KH-1 to KH-3: 1960-1962) achieving ground resolutions of ~8m depending upon atmospheric effects, illumination, and the nature of the target (Campbell, 2006). This relatively high resolution was improved further for later missions with the KH-4, KH-4A and KH-4B camera models

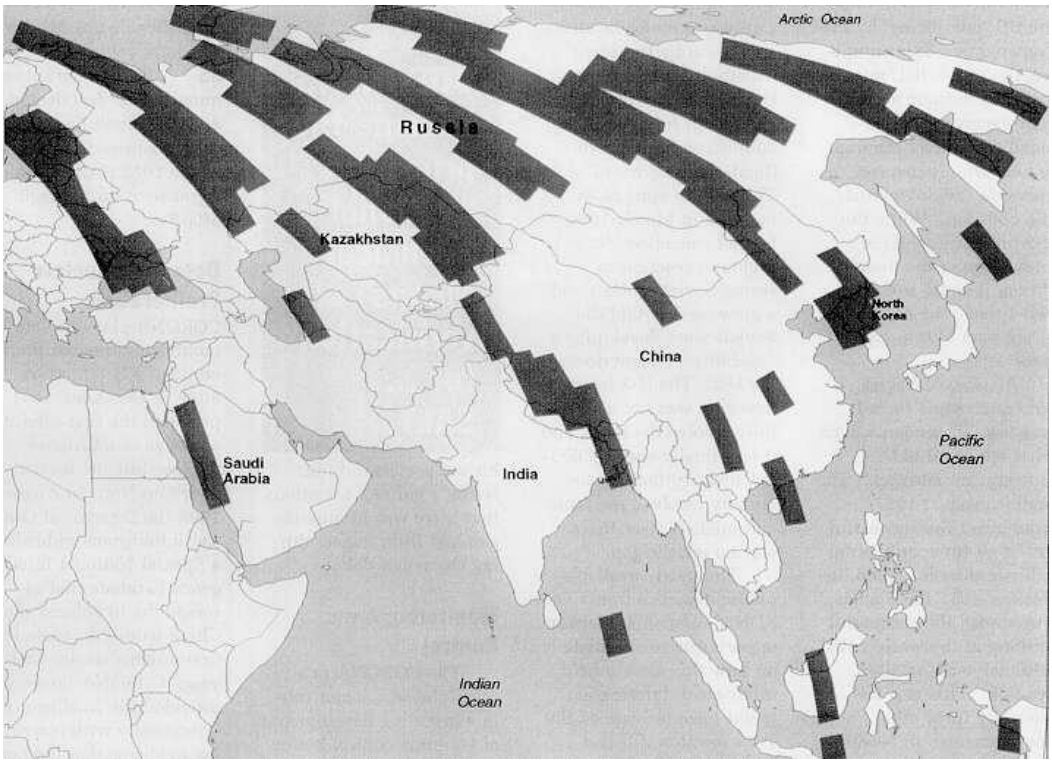


**Figure 2.1: Typical coverage of a KH-4B Corona camera over the Eurasian landmass (from Campbell, 2006).**

achieving resolutions as fine as 1.8 m. MacDonald (1995) summarises the evolution and improvements made to each model in detail.

The KH-4, KH-4A and KH-4B between them acquired the majority of the Corona archive. The technical specifications for each of these later models are shown in table 2.1. These three later camera models were particularly significant in that they captured imagery in stereo, utilising separate forward (For) and Aft facing KH-3 cameras each with a 15° tilt (Figure 2.2). The resulting 30° convergent images allow stereo viewing both in the direction of satellite motion and from any overlapping images taken on adjacent satellite passes (Casana & Cothren, 2008), a capability that was particularly enhanced for the KH-4A and KH-4B models. These stereo Corona images were orientated to the ground with help from index, stellar and horizon cameras built separately into the satellite.

In 1995, the entire Corona archive of over 860,000 images acquired during the 1960-1972 operational period was declassified and subsequently made available to the

**Table 2.1: Technical specifications of the Corona KH-4, KH-4A and KH-4B camera models (Dashora *et al.*, 2007).**

| Data | KH-4 | KH-4A | KH-4B |
|---|---|---|---|
| Time period | 1962-63 | 1963-69 | 1967-72 |
| Camera type | Panoramic | Panoramic | Panoramic |
| Image type | Stereo | Stereo | Stereo |
| Scan angle | 70.16° | 70.16° | 70.16° |
| Stereo angle | 30° | 30° | 30° |
| Focal length (in) | 24 | 24 | 24 |
| Ground Resolution (m) | 3-7.6 | 2.7-7.6 | 1.8-7.6 |
| Film resolution (lines/mm) | 50-100 | 120 | 160 |
| Nominal ground coverage (km) | 15 x 210 to 42 x 580 | 17 x 232 | 14 x 188 |
| Maximum scale | 1:12,000 | 1:7500 | 1:7500 to 1:12,000 |
| Mission life (days) | 6-7 | 4-15 | 19 |
| Nominal orbit altitude (km) | 165-460 | 185 | 150 |
| Image provider | USGS EarthExplorer | USGS EarthExplore | USGS EarthExplorer |
| Price | $30 | $30 | $30 |

public domain. Since being declassified, Corona imagery has become an invaluable source of historical spatial data (pre-dating Landsat imagery in some cases by 20 years) and in many places, such as large areas of the Himalayas, is the only source of inexpensive high-resolution stereo imagery ($30 per image strip). Subsequently, Corona imagery is being increasingly utilised for land-cover change studies in conjunction with more contemporary data sets (e.g. Namara *et al.*, 2009; Bhambri *et al.,* 2012). However, the majority of these studies have not taken advantage of Corona's stereo capabilities (Galiatsatos *et al*., 2008).

## 2.2. Orthorectifying Corona imagery and the extraction of DEMs

ERDAS (2009) define orthorectification as 'the process of removing all geometric distortion inherent in imagery caused by camera/sensor orientation, systematic camera/sensor error, the Earth's curvature, and topographic relief displacement'. The resulting ortho-images represent ground objects in their true, real world x and y positions and therefore have the geometric characteristics of a map. In order to accurately map ground features, such as glaciers, from Corona imagery, and extract DEMs from overlapping stereo image pairs, orthorectification is an essential prerequisite.

The orthorectification of Corona imagery is hindered by the following two factors which have subsequently limited the use of the dataset as a 3-D glacier mapping tool: (1) the existence of large geometric image distortions which are both typical to panoramic imagery (see Slama (1980)) and Corona specific, attributed to Corona's specialised camera setup (Corona cameras, for example, imaged bow-tie shaped areas of the ground that when compressed into a rectangular frame resulted in S-shape distortions running in opposite directions in For and Aft imagery, which increase in significance towards the edges (Casana & Cothren, 2008; Goosens *et al.*, 2006) (see Figure 2.2)); (2) the unavailability of Corona metadata, such as fiducial marks and principle point and ephemeris parameters, which are commonly used to orothorectify aerial photography (Galiatsatos *et al.,*2008).

Importantly, the aforementioned factors hinder the use of the conventional orbital geometry approach applied to orthorectify imagery acquired from various satellite platforms. Orbital geometry models, for example, attempt to define the source, direction and magnitudes of image errors based mainly on satellite orbital characteristics (Toutin, 2004) which are not available for Corona imagery. Despite this limitation, other studies have geometrically corrected Corona imagery using either image transformation or photogrammetry approaches.

The image transformation approach warps a 'slave' image so that it matches the map coordinate locations of a 'master´ image or projection through the use of corresponding GCPs and a mathematical function. The main advantage of this approach is that it is relatively simple, neglecting imaging sensor parameters and their relationship to the ground (e.g. interior and exterior orientations) and instead correcting geometric distortions according to the positional differences of the corresponding ´slave´ and ´master´ GCPs (Mather, 1999). The most commonly used image transformation approach for remotely sensed data is the rubber sheet warping technique which is based on polynomial deformation mathematical functions (Guo Liu & Mason, 2009). Partly overlapping the GC study site, Bhambri *et al.* (2011) used a transformation approach to geometrically correct three Corona image strips for the purpose of planimetric Himalayan glacier mapping. In this case,

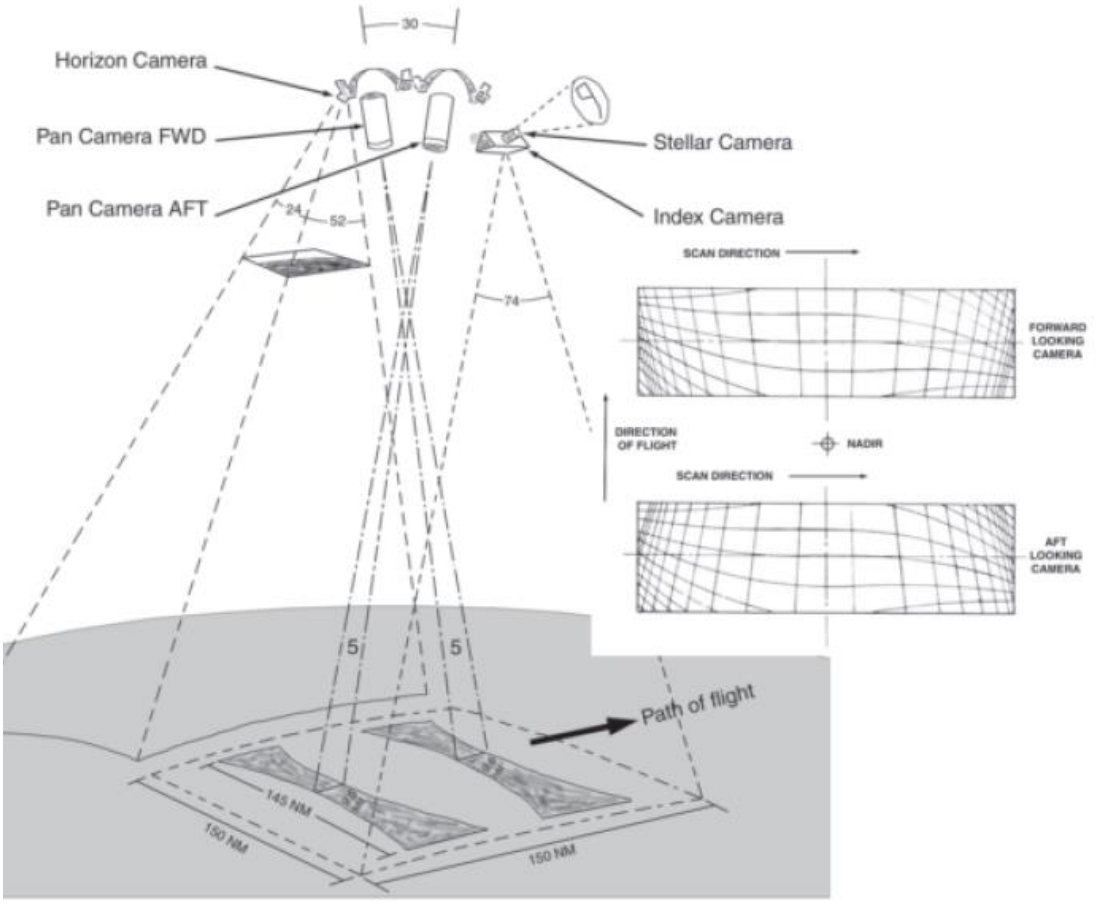


**Figure 2.2: Viewing set up, ground footprint, and relative geometric distortions of a pair of Corona stereo pairs acquired by the KH-4, KH-4A and KH-4B camera models (reproduced from McDonald (1997), Slama *et al.* (1980) and Galiatsatos *et al.* (2008)). NM stands for nautical miles.**

GCPs were sampled from ASTER satellite imagery and resulting relative geometric errors were estimated to <±15 m. However, in order to successfully transform Corona's large geometric distortions, the three image strips utilised had to be divided into 26 separate image subsets, each of which needed to be heavily sampled with GCPs (30-255 GCPs per subset). Furthermore, glacier outlines derived from the corrected Corona subsets could only be directly compared to other satellite-derived outlines outside of highly elevated accumulation zones (suggesting geometric mis-matches).

Grosse *et al.* (2005) also used a transformation approach to geometrically correct two Corona image strips for the purpose of mapping periglacial geomorphology in Siberia, Russia. In this case, 80 GCPs were sampled for each image strip, derived from a

georectified topographic map, resulting in a relative Corona geometric accuracy of ~±17 m. Outside of glaciology, Lorenz (2004) and Challis *et al.* (2004) have also applied image transformations to correct Corona imagery for mapping purposes, using GCPs sampled from Landsat TM and SPOT satellite imagery, respectively.

The aforementioned studies demonstrate the utility of this relatively simple transformation approach for geometrically correcting Corona imagery. However, the drawbacks of the approach, particularly in regards to multi-temporal glacier mapping, are highlighted in Bhambri *et al.* (2011). Although they achieved reasonable geometric accuracies, the approach applied by Bhambri *et al.* (2011) required additional pre-processing steps and the sampling of a large number of GCPs in order to adequately correct Corona distortions. These two factors could be considered as disadvantages when using Corona imagery for large-scale glacier mapping efforts. This study for example, utilised 14 individual Corona image strips.

An additional drawback of the transformation approach is that it only geometrically corrects ‘slave´ imagery relative to horizontal positioning of a ‘master´ image or projection and does not take into account vertical information. Even when correcting Corona imagery relative to an orthorectified reference image, for example, distortion attributed to terrain relief is difficult to remove and the resulting image cannot be classed as orthorectified. Furthermore, without considering camera sensor and flight height information, simple transformation approaches do not provide the framework required to extract DEMs from overlapping Corona stereo pairs. With the aim of using Corona imagery to estimate Himalayan glacier volume change, as well as planimetric glacier change, the image transformation approach would therefore not be an option for this study.

Photogrammetry involves establishing the relationship between the camera/sensor used to capture an image, the image itself, and the ground (ERDAS, 2010). The main advantages of using photogrammetry approaches to correct image datasets are that they consider the image-forming geometry, can handle multiple images at once and integrate information between overlapping regions, and explicitly deal with the third

dimension, elevation (ERDAS, 2010). In addition, the 3-D nature of the rectification process is such that DEMs can be extracted from image stereo-pairs with relative ease and efficiency. For correcting Corona imagery, photogrammetry-based approaches can be broadly divided into rigorous and empirical approaches. The rigorous approach differs from the empirical approach in that it attempts to correct Corona image distortions using exact calculations of all Corona camera parameters. However, aside from focal length which is available through the US National Reconnaissance Office (NRO, 1967), all other camera parameters are unavailable. As a result of this, a number of studies have attempted to calculate the remaining parameters, such as camera scan rate (Madden, 1996), camera pass designation and orbit inclination (Peebles, 1997), start and end camera scan angles (Galiatsatos, 2004), camera orientation angles and horizontal and vertical camera location (McDonald, 1997), using both quantitative and qualitative techniques.

Using the Corona camera parameter calculations published, Galiatsatos *et al.* (2008) attempted to correct a single For and Aft Corona image pair using a rigorous panoramic camera model available within the SocetSet GIS software package. In addition, GCPs were also sampled from a corresponding IKONOS satellite image. Overall, the application of this panoramic model was shown not to be successful and specific image error residuals (compared to IKONOS) were shown to be more than 1000 m. Galiatsatos *et al.* (2008) concluded that the rigorous panoramic camera model available within SocetSet, as with similar models available in other software packages, was not suitable for correcting Corona imagery as it presumed boundaries for camera altitude and incidence angles that cannot work for satellite mounted camera sensors.

Recognising the limitations of the panoramic camera models available, Shin (2003) developed a rigorous panoramic model specifically tailored for the correction of Corona imagery. Through complex mathematical modelling of interior and exterior orientation parameters, Shin (2003) was able to successfully orthorectify Corona imagery to a high degree of accuracy. Applied to two Corona image strips, acquired over the Kangerdlugssuaq outlet glacier in Greenland, this technique resulted in

horizontal RMSE's of less than ±5 m. Schenk *et al.* (2003) and Sohn *et al.* (2004) developed similar rigorous mathematical models specifically designed for geometrically correcting Corona's panoramic distortions. Combining a mathematical camera model with GCPs sampled from aerial photography and a topographic map, Sohn *et al.* (2004), for example, achieved Corona horizontal correction accuracies of less than ±4 m. Importantly, through the precise calculation of Corona's interior and exterior orientation parameters, rigorous approaches also provide the photogrammetric framework needed to extract DEMs from overlapping Corona stereo pairs using the space forward intersection technique. However, for glacier mapping studies, the rigorous approach is limited in that high geometric accuracies are achieved at the expense of time (Galiatsatos, 2004).

Mathematically formulated Corona panoramic models are difficult to develop and have not yet been integrated into commercial GIS and photogrammetric software packages. The development time required for such models would therefore hinder the inclusion of Corona-derived glacier information in large-scale multi-temporal glacier change studies, whose aims are not solely focused on the precise correction of Corona image distortions. Furthermore, the rigorous approaches discussed have not been tested for Corona imagery acquired over high mountainous environments, where the effects of terrain distortion are considerable.

In comparison to rigorous approaches, the empirical photogrammetric approach attempts to correct Corona panoramic distortions using only approximations of camera parameters, derived from the input of known average flight height, focal length and film scanning resolution values and the sampling of GCPs from a map projection. For Corona imagery, the empirical approach consists of the application of non-metric camera frame models (see table 2.2). At best, this approach was shown to orthorectify Corona imagery with horizontal accuracies of ±3 m (Altmaier & Kany, 2002) and ±6 m (Schmidt *et al*., 2001), showing that Corona imagery could be corrected through the use of minimal camera parameter inputs and a camera model available in commercial GIS and photogrammetry software packages.

**Table 2.2: Summary of methods used by selected studies to orthorectify Corona stereo pairs and extract DEMs.**

| Author | Location | Terrain | Method/Software | Ground control (resolution) | Horizontal Accuracy | DEM vertical accuracy |
|---|---|---|---|---|---|---|
| Altmaier & Kany (2002) | Morroco | Mountainous | Photogrammetry: non-metric camera frame model with GCPs & space forward intersection, ERDAS Imagine LPS | Field-based DGPS x,y,z survey (~1 m) | ±3 m | ~±10 m |
| Galiatsatos *et al*. (2008) | Syria | Flat | Photogrammetry: non-metric camera frame model with GCPs & space forward intersection, ERDAS Imagine LPS | Horizontal: IKONOS (4 m) Vertical: Topograhpic map (1:25,000) | n/a | ~±12 m |
| Bolch *et al.* (2008) | Nepal | High mountainous | PCI Geomatic 9.1 & ERDAS Imagine RSG add-on with GCPs | Horizontal: Landsat (30 m) and ASTER satellite imagery (15 m) Vertical: ASTER DEM (30 m) | ~±15 m | ~±18-56 m |
| Casana & Cothren (2008) | Syria | Moderate hills | Photogrammetry: non-metric camera frame model with GCPs & space forward intersection, ERDAS Imagine LPS | Horizontal: SPOT imagery (10 m) Vertical: SRTM (90 m) | n/a | n/a |
| Schmidt *et al.* (2001) | Morroco | Mountainous | Photogrammetry: non-metric camera model with GCPs, Virtuozo 3.1 | Field-based DGPS x,y,z survey (~1 m) | ~±6 m | ~±20-25 m |

The application of the empirical approach by Altmaier & Kany (2002) and Schmidt *et al.* (2001) differed from others in that they utilised field-based DGPS measurements which provided a highly precise 'master' map projection for the non-metric camera frame models bundle block adjustment. Galiatsatos *et al.* (2008) and Casana & Cothren (2008) showed that Corona imagery can also be successfully corrected using non-metric camera frame models combined with GCPs collected from high resolution satellite imagery (IKONOS and SPOT imagery), topographic maps and SRTM data. Additionally, during the progression of this study, Namara *et al.* (2009) utilised a non-metric camera frame model together with GCPs collected from Landsat ETM+ satellite imagery, a topographic map and SRTM data to correct Corona imagery acquired over the Tien Shan Mountains, Kyrgyz Republic (achieving horizontal accuracies of <±30 m). Corona imagery has also been successfully corrected using the RSG software (Remote Sensing Software Package Graz) which is a high cost add-on to ERDAS Imagine and includes photogrammetric processing tools specifically designed for Corona imagery (Bolch *et al*., 2008, see Table 2.2).

However, for application in the Himalayas, the photogrammetric methods described are limited by the following factors which hinder Corona's use as a 3-D glacier mapping tool in this region: (1) they require lengthy development times, making them unfeasible for large scale mapping projects; (2) the extraction of Corona DEMs has not yet been tested in high mountainous regions (excluding the RSG method used by Bolch *et al*. (2008)), orthorectification and extraction of DEMs from stereo imagery is particularly problematic in areas of steep terrain (Kääb, 2005a); (3) they require accurate and precise GCPs acquired from field-based DGPS surveys, expensive high resolution satellite imagery (e.g. IKONOS and SPOT) and detailed topographic maps. In regards to the third factor, the sourcing of GCPs for glaciarised areas of the Himalaya is particularly difficult. DGPS surveys, for example, are often unfeasible due to the remote and harsh nature of the Himalayan terrain, whilst access to accurate topographic maps (outside of Nepal) is also limited.

## 2.3. Summary and methodological objectives

Considering the limitations discussed, in order to improve the usage of Corona imagery as a 3D glacier mapping tool in the Himalaya, there is a need to test and formulate new photogrammetry-based orthorectification/DEM extraction methodologies. Due to time and financial constraints, for this study, methodologies based on the rigorous photogrammetric approach and Corona specific RSG software tool could not be considered. Following on from studies such as Altmaier & Kany (2002), Galiatsatos *et al.* (2008) and Casana & Cothren (2008), this study will utilise the empirically-based photogrammetric non-metric camera frame model available within the ERDAS Imagine LPS software package to both orthorectify Corona image and extract DEMs. Differing from previous studies, this study will test the use of freely available satellite-based GCP source data for orthorectifiying and extracting DEMs in the high mountainous Himalaya. In this regard, multispectral imagery and DEMs available from the ASTER sensor represent ideal options. Multispectral ASTER imagery, for example, has been described as the most suitable satellite image dataset for mapping glacier parameters (Racoviteanu *et al.*, 2008) and is available free for scientific use (through the GLIMS project). Additionally, the ASTER GDEM version 2 (v2) represents a free source of elevation data. Released in 2011, the ASTER GDEM v2 is a higher resolution (30 m) alternative to SRTM elevation data and offers similar vertical accuracies (Tachikawa *et al.*, 2011).

The methodological objectives of the project are to:

- Use an empirically-based photogrammetric non-metric camera frame model approach and ASTER horizontal and vertical reference data to orthorectify Corona imagery, covering areas of the Himalaya, and extract DEMs from overlapping stereo pairs.
- Implement test areas to assess vertical accuracy of Corona DEMs in high mountainous environments.

# 3. Monitoring Himalayan glacier change

With reference to the glaciological aims set out in section 1.1, this chapter aims to introduce the Himalayan region, highlight the importance of Himalayan glaciers and the implications of climate change, describe Himalayan glacier change since the end of the LIA, and discuss the current status of Himalayan glacier monitoring and methods used. The chapter ends with a statement of glaciological objectives for the project.

## 3.1. Himalayas: The abode of ice and snow

The Himalayas, the highest mountain chain on Earth, extend some 3000 km across the Indian subcontinent and cover an area of approximately 7 million $km^2$ (Qin, 2008). Forming a broad arc from the northwest to southeast (75-100°E, 40-25°N), the Himalayan region (also referred to as the Greater Himalayas) encompasses a mountainous area located in parts of Afghanistan, Bangladesh, Bhutan, China, India, Nepal and Pakistan (Figure 3.1). The climate and hydrology of the Himalayan region is dominated by the Asian monsoon. Moving in from the Bay of Bengal, the monsoon is blocked by the Himalayas and forced westerly, causing widespread intense precipitation on the southern side of the main ridge. The onset of this weather system is primarily driven by the springtime heating of the Tibetan Plateau which, creating a land-sea thermal gradient, facilitates the arrival of moisture laden air from the Indian ocean onto the continent (Webster *et al.*, 1998).

Annually the Asian monsoon is responsible for the majority of the Himalayas precipitation, with an estimated 70-80% falling during the summer season (Ueno *et al.*, 2001). However, monsoonal precipitation is highly variable, weakening from east to west and rarely penetrating as far as the Karakorum (Rees & Collins, 2006). Accordingly, average annual rainfall estimates across the foothills of the Himalayas vary from 150 cm in the east to 50 cm in the west (Mall *et al.*, 2006). It is therefore the case that the wetter eastern Himalayas have a prolonged monsoon season from


**Figure 3.1: Extent of the highly mountainous greater Himalayan region including major rivers (taken from Vaux *et al*., 2012).**

June to October, whilst the relatively drier western regions have a much shorter season from July to August (Bahadur, 1993). During winter months westerly disturbances, travelling eastward, deliver further precipitation throughout the Himalayas, causing gales and blizzards on the high peaks (Barry, 1992).

Due to its extreme relief, a large portion of annual precipitation in the Himalayas falls as snow, with a perennial layer forming on summits above 5000 m altitude (Bahadur, 1993). The accumulation of large amounts of snow at high elevation has aided the long-term growth of large numbers of glaciers across the Himalayas, the region representing the most glaciated area outside the polar regions (Dyurgerov & Maier, 2005). Estimates suggest that around 6,475 glaciers currently exist in the Himalayan range alone, covering an area of 8,412 km$^2$ (Tandong *et al.*, 2007). The cold, snowy

and high elevated Himalayan environment is such that many glaciers attain large dimensions and descend for considerable distances to valleys below. In India, whose glacierised area totals ~40,000 $km^2$, the larger principal glaciers, including their lengths, are: Gangotri, 30 km; Zemu, 28 km; Milam, 19 km; and Kedarnath, 14.5 km (Vohra, 2010). Although glaciers are found in the majority of high elevation basins, their distribution across the Himalayan region is uneven, with higher concentrations in western areas than eastern (Geological Survey of India, 1999). This gathering towards the west can mainly be attributed to the varying topography, climate (Dobhal *et al.*, 2008) and the change in latitude.

With over 3,700 $km^3$ of water being stored within Himalayan ice reserves (Qin, 2002; Campbell *et al*., 2005), glaciers are an integral part of the regions hydrological cycle. The release of water from high altitude basins, for example, is strongly regulated by the storing and releasing of water from glaciated areas in relation to long and short term fluctuations in the climate. With recent climate changes, both the importance of glaciers as a downstream water resource and the potential impacts of their shrinkage have become a key area of discussion in the Himalayan region.

### 3.2. Monsoonal control on Himalayan glacier regimes

Monsoonal precipitation over glacierised Himalayan basins plays a complex role in controlling glacio-hydrology (Hasnain, 1999). The presence of cloud cover during the monsoon season coupled with summer snow fall at high elevations, for example, reduces energy available for melting (Figure 3.2 (a.)). These reductions in energy availability subsequently subdue ice melt during the summer months, altering glacier discharge variations (Figure 3.2 (c.)) with respect to those observed in other glacierised mountain regions (Collins & Hasnain, 1995; Hasnain, 1999). This influence on glacier meltwater discharge varies spatially as the monsoon diminishes east to west. Glacier regimes across the Himalayas are similarly influenced by the monsoonal east to west gradient. Thayyen & Gergen (2009) categorise these regimes into; 'Himalayan', encompassing all regions east of Chenab Basin, 'Alpine', found in the far western Himalayas and 'Cold Arid', found in the Ladakh mountain range (Figure 3.3).

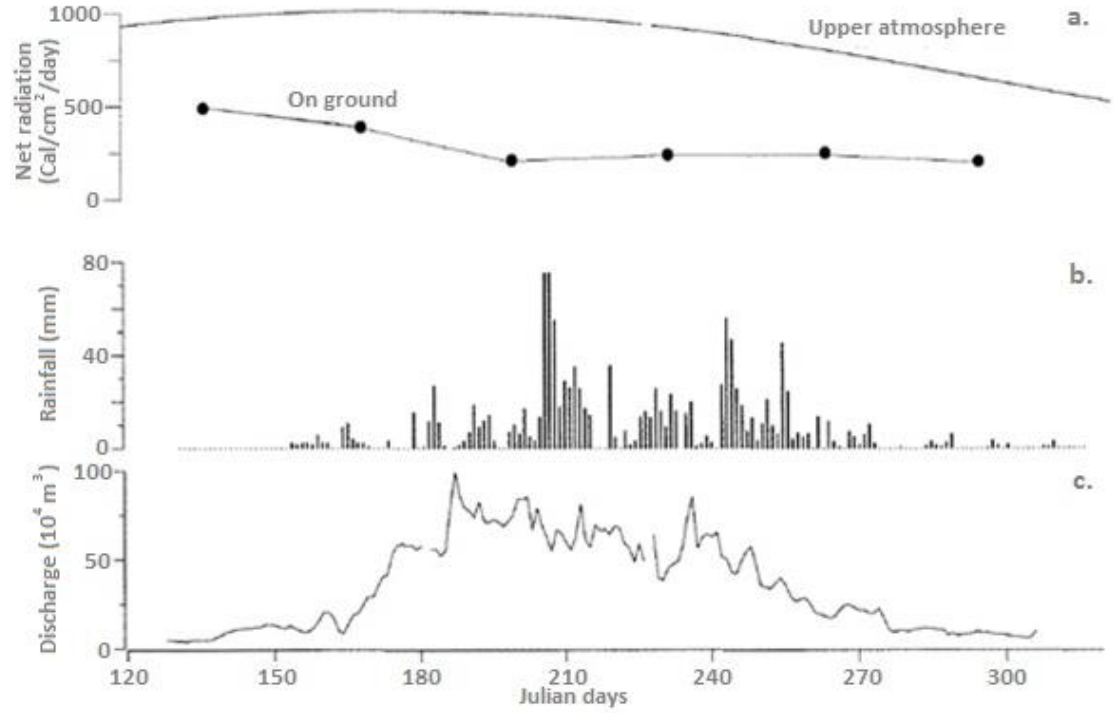


**Figure 3.2: Net radiation (a.), daily rainfall depth (b.) and daily mean discharge (c.) measured in 1994 at the Din Gad River, Garhwal Himalayas, India (Hasnain, 1999). Regulated heavily by glacial melt from high elevations discharge is at its maximum during summer months (c.).**

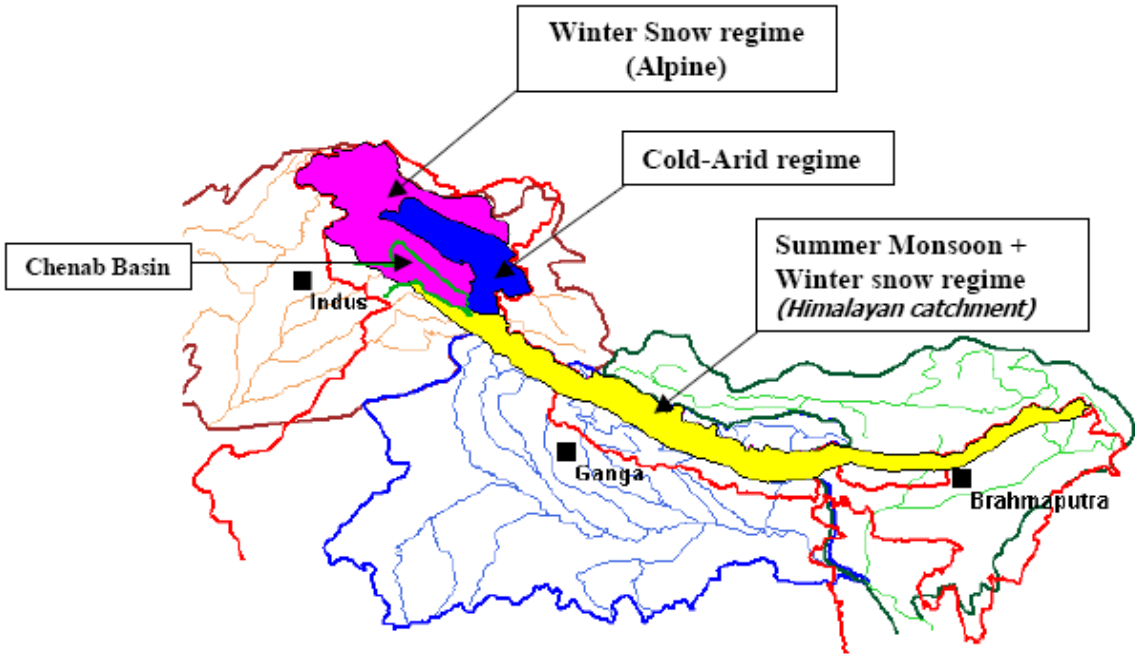


**Figure 3.3: Glacio-hydrological regimes of the Himalayas (Thayyen & Gergen, 2009).**

'Himalayan' regimes exist in areas heavily influenced by the summer monsoon, these glaciers generally being classified as 'summer-accumulation-type' (Ageta & Higuchi, 1984; Vohra, 1981). In comparison, 'Alpine' and 'Cold Arid' regime glaciers located in the west experience winter accumulation, via the winter westerlies, and summer ablation.

### 3.3. Implications of climate change on Himalayan water resources

During the past century, the IPCC (2007) has noted an increase in global surface temperature of 0.76 °C. This increase in global surface temperature has become pronounced since the 1980s and predictions suggest that current rates of warming are unlikely to abate in the near future (IPCC, 2007; Jones *et al*., 2001). Various studies have suggested that warming in the Himalayas has been much greater than the global average. Hasnain (2000) for example, reported that the average air temperature in the Himalayan region has risen by 1°C since the 1970s alone.

The impacts of climate change on Himalayan hydrology are particularly significant. Often referred to as the 'Water Tower of Asia' (Jainchu *et al.*, 2009), the Himalayan region is the source of one of the world's largest supplies of freshwater, providing an estimated $8.6 \times 10^6$ $m^3$ of water annually (Dyurgerov & Maier, 1997). Rivers draining from Himalayan basins deliver large quantities of runoff to the major tributaries of ten of the largest rivers in Asia, making substantial contributions to the water resources of large downstream populations. The basins of the Indus, Ganges and Brahmaputra alone support around 500 million people (WWF, 2005).

Considering the size of the Himalayan ice reserve, the impacts of climate-induced reductions in glacier area and volume on freshwater availability are potentially large. Glacial meltwater draining from the Himalayas supplements runoff at high elevation, derived from precipitation and snow melt, and often represents a significant downstream river flow component (Rees & Collins, 2006; Singh *et al.*, 2008). Not only important in terms of quantity, glacier meltwater also moderates intra-annual variations in river flow (Collins, 2007). The presence of snow and ice within a basin

results in the regulation of runoff in relation to the radiation flux and air temperature (Collins, 2007; Jansson *et al.*, 2003). Hence, even limited ice cover in a mountain basin reduces the variability of annual total runoff with respect to that of annual total precipitation (Kasser, 1959). This moderation of intra-annual river flow variations makes runoff from glaciated mountain basins particularly important as a downstream water resource, as the water provided offsets drought years and dry seasons. It is estimated, for example, that snow and ice melt contribute about 70% of summer flow in the main Ganges, Indus and Kabul rivers during the dry 'shoulder' seasons, before and after the summer monsoon (Kattelmann, 1987; Singh & Bengtsson 2004; Barnett *et al.*, 2005).

With continued climatic warming, rivers draining from glaciated Himalayan basins are likely to undergo a range of changes in response to glacier wastage. Differing through time, these responses have been summarized by Hock *et al.* (2005) for five key discharge variables (Table 3.1). Most notably, specific runoff from glacierised basins in the long-term is expected to decrease as progressive glacier downwasting reduces the surface area of ice over which energy exchange can occur, limiting melt.

**Table 3.1: Summary of discharge characteristics in highly glacierised basins and expected changes as a result of reductions in glacier geometry and prolonged negative mass balance due to climatic warming. Responses are shown both for an initial phase and a later stage when glacier sizes and volumes have been significantly reduced (Hock *et al.*, 2005).**

| **Variable** | **Characteristic** | **Expected change of variable under a warming climate** | |
|---|---|---|---|
| | | *Initial* | *Later stage* |
| Specific runoff | Decrease for positive mass balances<br>Increase for negative mass balances | Increase → | Decrease |
| Seasonal variation | Runoff concentration during melt season | Prolongation of melt season, reduced runoff concentration | |
| Diurnal fluctuation | Pronounced diurnal cyclicity | Increase → | Decrease |
| Year-to-year variability | Glacier compensation effect: reduced variability at moderate glacierization | Increase or decrease depending on initial glacierization | Increase |
| Runoff correlation | Positive correlation with temperature<br>Negative correlation with precipitation | Increase → | Decrease |

### 3.4. Glacier sensitivity to climate change

Changes in energy availability (air temperature being a useful surrogate (Hock, 2003)) and precipitation are generally the main driving forces behind any glacial fluctuation on both a regional and global scale. Energy available for exchange across a given ice surface is governed by the energy balance. Benn & Evans (2010) state the most important components of the energy balance as: (1) shortwave solar radition (*SW*); (2) terrestrial and atmospheric longwave radition (*LW*); (3) sensible heat exchange with the atmosphere (*QH*); (4) latent heat transferred during condensation, evaporation and sublimation (*QE*); (5) heat supplied by rain (*QR*); (6) heat used to change the temperature of the ice (*QT*); and (7) latent heat consumed or released during melting and freezing (*M*). These components make up the energy balance equation:

$$SW + LW + QH + QE + QR - QT - M = 0 \quad (3.1)$$

the sum of which must be zero.

Glacier mass balance refers to the balance between the accumulation of ice mass, primarily via the input of snowfall (as described by Paterson, 1994), and ice ablation, mainly determined by the surface energy balance (Jansson *et al.*, 2003). Positive or negative changes in the energy balance and mass input components have a direct impact on glacier mass balance, leading initially to ice thickening/thinning, followed in turn by a dynamic redistribution of mass via glacier flow, as a glacier tries to regain equilibrium with the altered local climate (Oerlemans, 2001; Lemke *et al.*, 2007). This relationship between specific mass balance (total mass change divided by glacier area) and climate variability, particularly air temperature, has been shown to correlate significantly over distances of several hundred kilometres (Braithwaite & Zhang, 2000; Shöner *et al.*, 2000; Kayastha & Harrison, 2008).

Representing the altitude on a glacier where net ablation and accumulation is balanced, the equilibrium line provides an important indicator of glacier response to climate change (Benn & Lehmkul, 2000). Being closely linked to the zero-degree isotherm and transient snow line, ELAs fluctuate with changes in precipitation, the energy balance, and associated precipitation partitioning (rain/snow), ascending with

decreases in snowfall and/or increases in temperature and vice versa. How an individual glacier responds to movements in ELA and changes in its specific mass balance is known as its climate sensitivity (Oerlemans & Fortuin, 1992). Once the initial geometry of a glacier has been quantified, determining how sensitive it is to a specified climate change is a key element in assessing the scale of subsequent impacts on regional water resources and global sea levels. Climate sensitivities of glaciers are typically calculated by applying unit changes to temperature and precipitation. Benn & Evans (2010), for example, simply define the sensitivity of a glaciers mass balance (B) to a temperature ($C_T$) and precipitation ($C_P$) change of ±1°C and 10%, respectively, as:

$$C_T = \frac{B(+1°C) - B(-1°C)}{2} \quad (3.2a)$$

$$C_P = \frac{B(+10\%) - B(-10\%)}{2} \quad (3.2b)$$

When considering climate sensitivity it is important to view the response of a glaciers specific mass balance three-dimensionally (Adhikari *et al.*, 2009). Along with changes in length and area, a glacier also adjusts ice volume throughout both accumulation and ablation zones in response to climatic changes, altering ice surface elevation. However, the response times of each dimensional variable can differ.

Glacier volume change is viewed as an un-delayed signal of atmospheric conditions (Haeberli, 2004). Glacier volume change can therefore be used as a proxy of mass balance change and is most sensitive to climatic warming (e.g. Baisheng *et al.*, 2003). Unlike volume, the response of glacier length, in particular, lags behind an initial climate change (Figure 3.4). Changes in terminus positions, a factor commonly used to assess glacial fluctuations over a given time period (e.g. Scherler *et al.* (2011)), are therefore not indicative of a current climate setting and instead may reflect previous atmospheric variations. This lag or terminus reaction time is often difficult to quantify due to the complexity of the processes involved during the redistribution of glacial mass as a result of mass balance changes (Oerlemans, 2007). Examining two stages of rapid area reduction for the AX010 glacier in Nepal, Adhikari *et al.* (2009) for example, estimated an 8-13 year terminus response time to climatic changes.

Assuming variations in temperature and precipitation solely control mass balance, glacier fluctuations and sensitivity should vary according to their climatic setting and glacier regime. Attempts to generalize glacier sensitivity in terms of climate, however, are often complicated by contrasting responses within the same region and even adjacent basins to the same atmospheric signals (Furbish & Andrews, 1984; Oerlemans, 2007; Collins, 1998; Raina, 2009). These differential responses are brought about due to the important influence of basin characteristics on individual glacier mass balance. These external factors are superimposed disparately onto a glacier´s typical regional response and often make climate sensitivity basin specific. External factors include, basin hypsometry, elevation range, aspect, relief and ice surface characteristics, amongst others. Glacier size (partly determined by local topography) also influences individual glacier sensitivity to climate change.

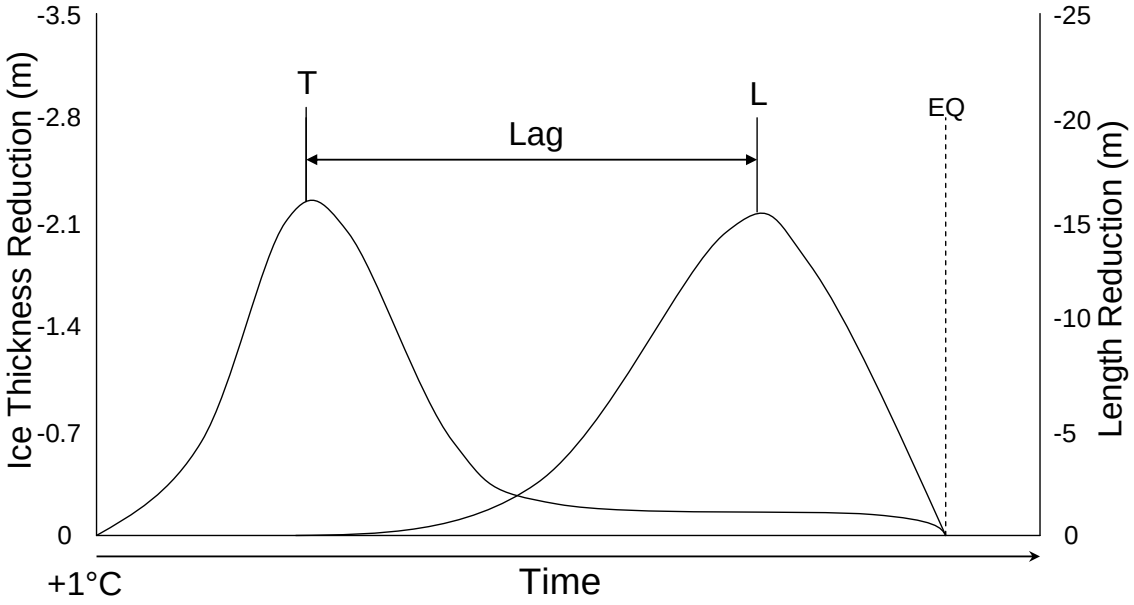


**Figure 3.4: Theoretical temporal response of a theoretical glacier to a 1°C temperature increase (created by author). Glacier thickness (T) reacts to the warming by instantly attempting to regain equilibrium with the local climate (EQ). However, through the process of ice mass redistribution changes in glacier length (L) are delayed, causing the response to lag behind that of thickness. Both response times are governed by local basin climatic and topographic characteristics.**

### 3.4.1. Basin hypsometry

One external factor that plays a particularly important role in controlling the response of glacier mass balance to climatic change is basin hypsometry (e.g. Small, 1995). Hypsometry (the distribution of basin area with elevation) interacts with the ELA, transient snow line and zero-degree isotherm to determine the ablation/accumulation area ratio of a glacier. When the ELA moves as a result of climate change, the extent of accumulation area loss/gain is dependent on the proportion of glacial ice area that lies adjacent to the initial ELA. Therefore, if the ELA passes through a wide portion of ice with a shallow surface slope, a relatively large increment of accumulation area would be lost per unit change in ELA (Small. 1995). A glacier with a wide shallow accumulation area and narrow snout would thus have a different response to the same meteorological inputs than a glacier with a steep accumulation area and broad snout. As a result, basin hypsometry represents an important gauge of how sensitive the individual mass balance of a glacier is to climatic change (Oerlemans *et al.*, 1998).

### 3.4.2. Elevation range

Another basin characteristic that influences glacier mass balance and climate sensitivity is elevation range. Rates of both accumulation and ablation are heavily dependent on altitude, due to the presence of thermal lapse rates in the atmosphere (Benn & Lehmkuhl, 2000). Air temperature, for example, decreases with altitude (~ 0.6°C/100m (Hock, 1999)), reducing energy available to melt. Conversely, precipitation, and the fraction of precipitation falling as snow, increases with altitude (e.g. Daly *et al.*, 1994). In the Karakorum, for example, there can be a 5- to 10-fold increase in precipitation between glacier termini and accumulation zones (Hewitt, 2005). Energy absorption also varies with altitude, as the transition from fresh snow and firn in elevated accumulation zones to bare ice in ablation zones decreases surface albedo down-glacier (Oerlemans & Hoogendoorn, 1989). As a result of these orographic variances in energy-balance components, glaciers originating at higher elevations generally accumulate more mass, enabling them to grow to larger sizes and

flow for further distances down valley (e.g. Ye Baisheng *et al.*, 2003). The relative size of accumulation area of highly elevated glaciers is such that they are subsequently less sensitive to climatic warming and fluctuations in ELA. The relationship between elevation range and glacier size is demonstrated well by Hewitt (2005) for 17 glaciers in the central Karakorum (Figure 3.5). Moreover, Hewitt (2005) suggests it is the extreme elevation of many Karakoram glaciers that may help explain the large-scale glacier expansion that has occurred in this region since the late 1990s. This relationship between elevation range and glacial size, however, is complex and local climatic, topographic and hypsometric factors can offset the positive effect of elevation on glacier mass balance.

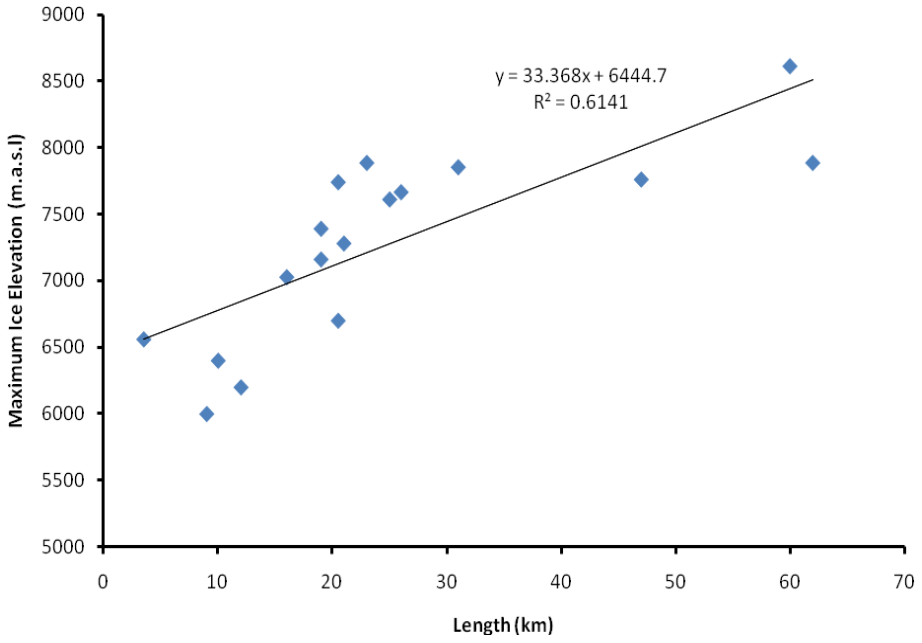


**Figure 3.5: Maximum elevation of 17 glaciers situated in the central Karakorum plotted against their length (data taken from Hewitt (2005)).**

### 3.4.3. Aspect & relief

Glacier basin aspect can influence levels of incoming radiation, precipitation and climate sensitivity. In high mountainous regions of the northern hemisphere, for example, north facing basins receive the least amount of radiation, these being effectively shaded by the local topography (e.g. Ahmad & Rais, 1999). Glaciers situated in such basins benefit from the reduction in energy available to melt and tend to be

less sensitive to climatic variability. Local wind patterns can both enhance or lessen this shading effect by delivering preferential snowfall amounts in lee-side locations and altering levels of sensible heat transfer (Furbish & Andrews, 1984).

The interaction between aspect and wind patterns in high mountainous environments, and their effects on levels of radiation and precipitation, is such that snowline altitudes can often differ between neighbouring basins. In terms of snowfall accumulation, basin relief also plays an important role. High steep valley walls within mountainous basins can act as snow traps increasing glacial accumulation potential through avalanching as well as enhancing any shading effects (Hewitt, 2005). In extreme environments such as the Himalayas where weather systems vary significantly, the effect of aspect, wind patterns and relief is particularly complex and can further add to the variability in climate sensitivity between glaciers in close proximity.

### 3.4.4. Ice surface characteristics

Several ice surface characteristics can impact glacier climate sensitivity, altering key mass balance components. In this respect, supraglacial debris is a particularly important ice surface feature. The influence of supraglacial debris on glacier mass balance is demonstrated by studying mass balance gradients. In straightforward cases mass balance gradients are approximately linear, as glacier ablation rates generally decrease with elevation corresponding to thermal lapse rates and albedo changes (e.g. Schuler *et al*., 2005, Furbish & Andrews, 1984). In such cases, ablation gradients tend to be steeper than accumulation gradients, with glaciers simply being fed by snowfall at higher elevations and losing mass through the melting of clean ice in lower ablation zones (depending on basin hypsometry and elevation range) (Benn & Lehmkuhl, 2000). The presence of supraglacial debris, however, skews the linearity of glacier mass balance gradients, making them unique to the basin in which they are located.

Supraglacial debris has an important influence on mass balance gradients, affecting ablation rates in two ways, these being summed up by Benn & Lehmkuhl (2000). First, where debris cover is thin (< c. 2 cm), ablation rates are often enhanced compared to clean ice, due to the lowering of albedo and the increase in radiation absorption. Hewitt (2005) discusses the relative importance of these thin 'dust' and 'dirt' layers which can increase melt by 40% or more and often cover significant portions of glacier ice. Secondly, where thicker debris cover exists (> c. 2 cm) ablation rates can be lowered. In this instance, due to the diurnal cycles in radiation, the thick debris is unable to acquire sufficient ice melt energy and acts as an insulator (e.g. Mattson *et al.*, 1993; Rezichenko *et al.*, 2010).

In the Himalayas, the overall effect of supraglacial debris on ablation rates is particularly important. The extreme relief of the Himalayas is such that a large amount of glaciers are covered in debris (Kick, 1989; Fujii & Higuchi, 1977) and often entire ablation zones can be affected. Scherler *et al.* (2011), for example, demonstrated the significance of supraglacial debris in the Himalayas, showing that debris cover exceeding a few centimetres considerably reduced frontal recession throughout the region between 2000 and 2008. Frontal reduction was shown to cease for glaciers with >20% surface debris cover. Subsequently, it was concluded that thick and widely distributed supraglacial debris cover slows glacial responses to climate warming and diminishes the role of glaciers as direct indicators of recent climatic change.

The effect of debris cover on mass balance gradients specifically, is well represented by the generalised mass balance curve for Khumbu glacier in Nepal, presented by Inoue (1977) (Figure 3.6). Figure 3.6 demonstrates how the presence of thick supraglacial debris causes a reversal of the ablation gradient, resulting in a distinctly non-linear curve. Referring to the response of glacier geometry to climate change, it is important to note that the presence of thick debris cover in lower ablation zones often results in stagnant terminus regions. Monitoring such debris-covered terminus then becomes an issue, as, although not reducing in area and length, these glaciers may in fact still be downwasting in place (e.g. Bolch *et al.*, 2008). The influence of

debris cover should thus be an important consideration when comparing rates of glacier wastage in the Himalaya to other regions of the globe.

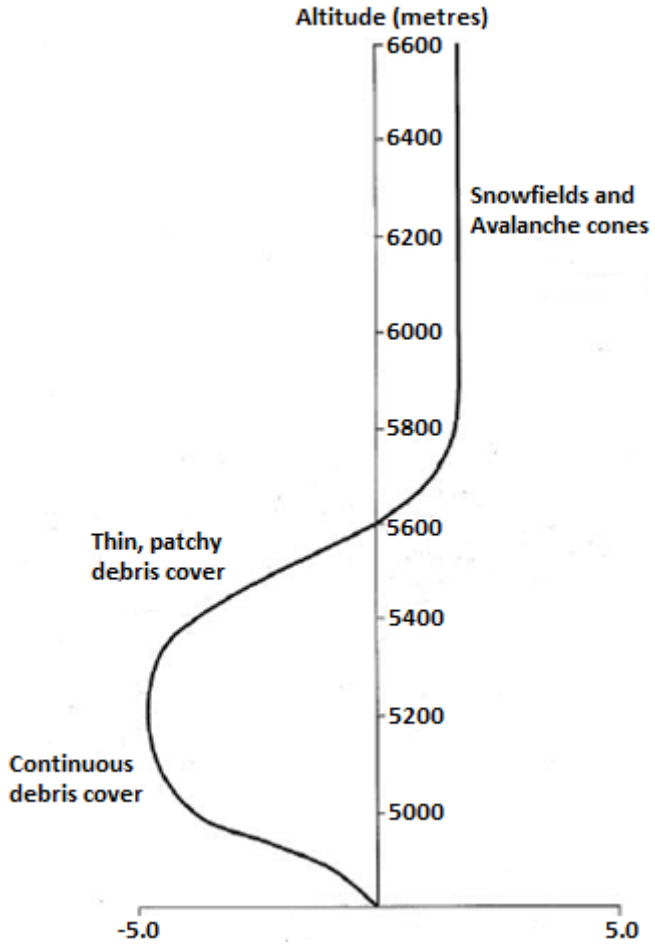


**Figure 3.6: Generalised mass-balance curve for Khumbu glacier, Nepal. The presence of supraglacial debris on ablation zones alters the curve significantly (taken from Inoue, 1977).**

### 3.4.5. Glacier size & climatic sensitivity

The response of glacier geometry to climate change is the culmination of interactions between regional climate, local climate variability and a range of specific basin and ice surface characteristics. The size of a glacier (area, length and volume) is simply a measure of how favourable a particular basin and climate setting is to the formation of long-term glacial ice. Glacier size itself can then be used as a rough gauge of climatic sensitivity.

In general, smaller glaciers are more sensitive and respond faster to climate change

than larger glaciers (e.g. Ye Baisheng *et al.,* 2003; Lemke *et al.*, 2007). This is mainly a function of basin elevation, as smaller glaciers tend to have relatively small areal portions of their accumulation zones available at high elevation to offset rising ELAs. With continued climatic warming over coming decades, small glaciers are therefore liable to disappear in many high mountainous regions, including the Himalayas (IPCC, 2007). However, in terms of the impact on local water resources, it is the changes of larger glaciers that are important, these being relatively less sensitive to climatic change but contributing more meltwater to local drainage systems.

### 3.5. Himalayan glacier change since the end of the LIA

Although not synchronous in amplitude and timing, there has been a general shrinkage of mountain glaciers on a global scale since the end of the LIA (Haeberli & Hoelzle, 2001; Barry, 2006; UNEP & WGMS, 2008). Seen as beginning in the thirteenth and fourteenth centuries and culminating between the mid-sixteenth and mid-nineteenth century, the LIA was 'a period of lower temperatures over most if not all of the globe' (Grove, 1988). In glacierised Himalayan basins, LIAMs are thought by Mayewski & Jeschke (1979) to have been reached between 1850 and 1880 (Mayewski & Jeschke, 1979; Grove, 1988).

The widely reported warming of global air temperatures since ~1850 marked the end of the LIA and the beginning, over the subsequent decades, of a process of wide-scale deglaciation (IPCC, 2007). Of recent concern to the scientific community has been the response of glaciated regions to a second warming phase, which started around 1980. Since 1980, post LIA warming has become notably pronounced (IPCC, 2007). Such increases in air temperature have accelerated the rate of deglaciation significantly, with the majority of monitored glaciers around the world experiencing a considerable further loss in mass and dimension (Dyurgerov, 2003; Khromova *et al.,* 2003; UNEP & WGMS, 2008).

Globally, the increased rate of terrestrial ice mass decline, over the past three decades in particular, has focused attention not only on the subsequent impact on water

availability in high mountainous regions but also on the additional impact on global sea levels. Studies suggest that mountain deglaciation over the last century has already caused sea levels to rise by 0.2-0.4 mm $a^{-1}$, accounting for 20% of the observed change (Warrick *et al.*, 1996; Dyurgerov & Meier, 1997). In addition to the impacts on water resources, the decline in Himalayan ice mass has been singled out as an area of concern in regards to global sea level change contribution (Schubert *et al.*, 2008).

Interest in Himalayan glacial fluctuations heightened in 2007, when the fourth report of the IPCC stated that 'glaciers in the Himalayas are receding faster than in any other part of the world' and that under current warming rates 'the likelihood of them disappearing by the year 2035 and perhaps sooner is very high' (Cruz *et al.*, 2007). Although proved erroneous and later discredited, (Cogley *et al.* (2010), for example highlights that for Himalayan glaciers to disappear by 2035 a 25-fold greater ice mas loss rate from 1999-2035 than that estimated for 1960 to 1999 would be required) the IPCC's report followed several studies suggesting alarming rates of glacial length, area, and volume reductions in the Himalayas (e.g. Dyurgerov & Meier, 2005 (Figure 3.7)). Length observations for the Gangotri glacier (Garhwal Himalaya, India), for example, revealed an 850m retreat from 1971-1996 (Owen & Sharma, 1998) a reduction continuing by ~ 28 m per year up to 2006 (Mall *et al.*, 2006), whilst the nearby Dokriani glacier lost 20% of its volume from 1962-1995, retreating in length by 550 m. Other earlier studies observed similar reduction trends in length. Milam glacier (Kumaun Himalaya, India), for example retreated in length by 1.35 km from 1849-1957 (Vohra, 1981).

Overall, glacier monitoring estimates suggest that around 67% of Himalayan glaciers were retreating in length between 1990 and 2000 (Ageta & Kadota, 1992; Fushimi, 2000). Subsequent attempts to model future changes in ice cover under differing climate scenarios pre-dated the IPCC's 2035 prediction and Qin (2002) concluded, more realistically, that with a 2°C increase in air temperature by 2050 35% of present glaciers will disappear.

More recent monitoring studies have added further detail to the picture of glacial

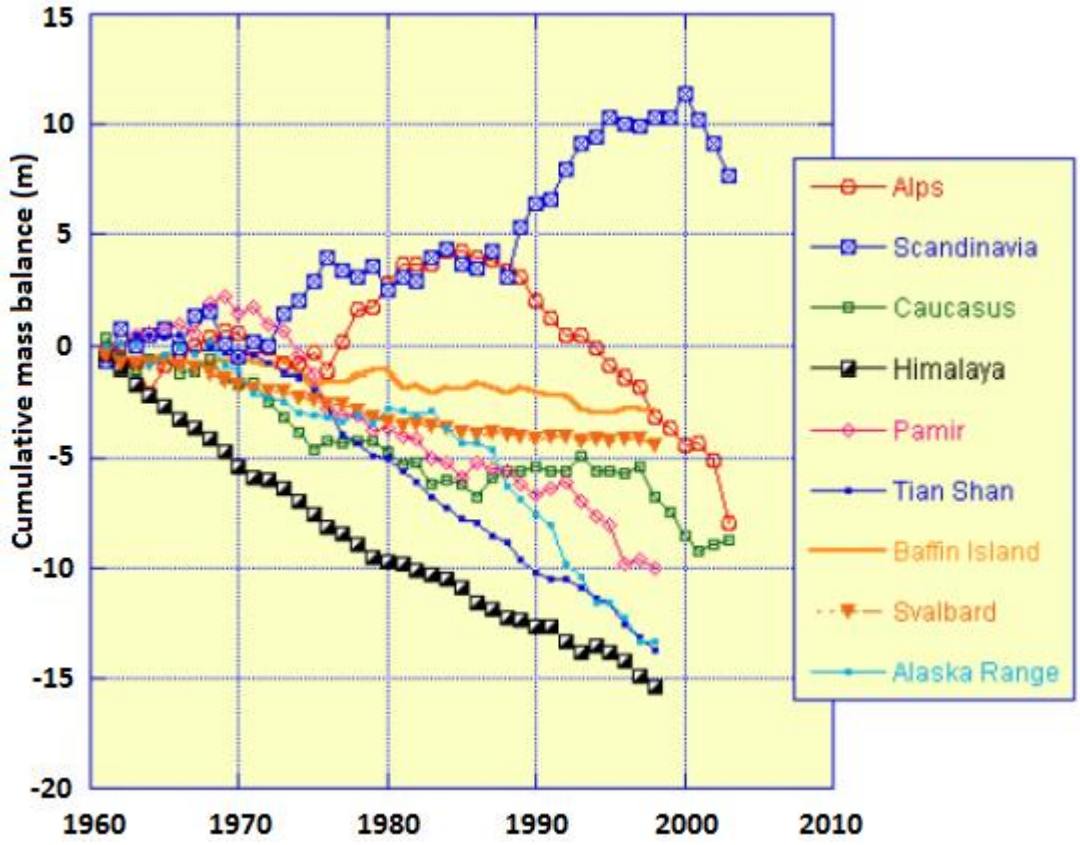


**Figure 3.7: Extensive loss in mass of Himalayan glaciers (black squares) compared to other glacierised regions (Dyurgerov & Meier, 2005).**

wastage throughout the Himalaya. Kulkarni *et al.* (2007) investigated the areal retreat of 466 glaciers in the Chenab, Parbati and Baspa basins (western Himalayas), observing a 21% decrease in area from 1962- ~2001. For another westerly location (Spiti/Lahaul region, Himachal Pradesh), Berthier *et al*. (2007) observed ice mass losses, between 1999 and 2004, that were twice as high as long term (1977-1999) mass balance records available for the Himalayas. In comparison, Bolch *et al*. (2008) observed a more moderate 5% ice area decrease for four glaciers located in the Khumbu Himalaya (Nepal), between 1962 and 2005. In terms of length change, Scherler *et al.* (2011) analysed 255 glaciers located between the Hindu Kush (western) and Bhutan (eastern) between 2000 and 2008, concluding that 65% of the monsoon-influenced glaciers were retreating in length.

### 3.5.1. Himalayan glaciers: Accelerated glacier wastage?

Refuting claims of heightened Himalayan glacier wastage, a report released by the Indian Ministry of Environment and Forests (Raina, 2009) suggested that Himalayan glaciers have not exhibited an abnormal annual ice mass loss over the past decades. Drawing on both published and unpublished studies, the report states that many Himalayan glaciers are stable or have advanced in length in recent years and that areal retreat for some has slowed considerably. The report highlights the Gangotri glacier, which after retreating in length by 22 m $a^{-1}$ from 1934-2003 slowed down significantly during 2004-2005 and since 2007 has been 'practically at a standstill'. Additionally, the report highlights Siachen glacier (Eastern Karakorum Himalaya), which it suggests has only retreated in length marginally in the past 50 years. Observations made by both Kumar *et al.* (2008) and the Birla Institute Technology (WWF, 2009), show similar reductions in the rate of length retreat for Gangotri glacier (Figure 3.8).

Despite being a common measure of glacier health, it is important to note that length

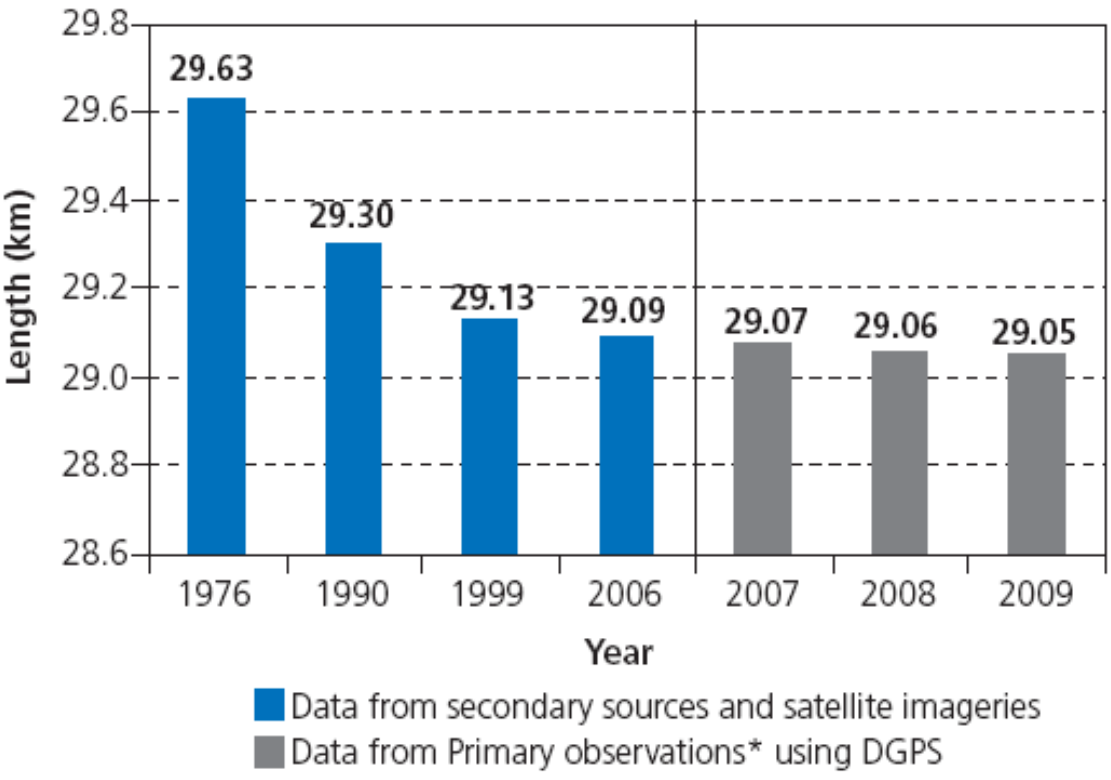


**Figure 3.8: Measured length of Gangotri glacier at different time intervals (WWF, 2009).**

change may not be indicative of the current climatic setting of a glacier. Hence a glacier at standstill may still be downwasting and mass balance observations are therefore more informative. In this regard, a recent mass balance study on 12 glaciers in the Khumbu Himalayas (Bolch *et al.*, 2010) has countered the 'accelerated glacier wastage' assumption, observing a specific mass loss of 0.32 ± 0.8 m $a^{-1}$ w.e. (water equivalent) from ~1970 to 2007, which is not higher than the global average.

In terms of glacier fluctuations, the Karakoram mountain range in particular represents the biggest anomaly. Contrary to the majority of Himalayan glaciers, after declining in area from the 1920s, many larger glaciers in the central Karakorum began a period of areal expansion from the late 1990s that has yet to halt (Hewitt, 1998; Hewitt, 2005; Smiraglia *et al*. 2007). From 2000-2008, for example, Scherler *et al.* (2011) concluded that 58% of studied glaciers (42) in the Karakoram were stable or slowly advancing with a mean rate of about +8±12 m $a^{-1}$. The advancing behaviour of many Karakorum glaciers likely suggests positive mass balance conditions, however, detailed mass balance measurements are currently not available to assess this hypothesis (Hewitt, 2005).

Overall, the mosaic of glacier observations (area, length and mass-balance) currently available across the Himalayan arc portrays a confused picture of varied glacial health. The contrasting behaviour of many Himalayan glaciers, however, highlights the importance of not generalising the effects of climate change across this large region, something which is often done in mass media (e.g. Nelson & Alleyne, 2011). Climatic interactions across the Himalayan region are highly complex and precipitation and air temperatures vary significantly from east to west (Vohra, 1981; Archer & Fowler, 2004; Dobhal *et al.*, 2004; Thayyen *et al.,* 2005)). The response and sensitivity of glaciated areas to climate change throughout the Himalayas is therefore not uniform.

Modelling hypothetical glacier catchments, Rees and Collins (2006), for example, demonstrated that future glacier area reduction will be more rapid in the western Himalayas than the east. Under a warming scenario of 0.06°C $year^{-1}$, total glacier area in western and eastern catchments is shown to reduce to a minimum by the late 2080s

and 2090s, respectively (Figure 3.9). This delay in forecasted deglaciation for eastern catchments is brought about because glacier ice in the eastern Himalayas is protected during the summer months by the accumulation of monsoonal snowfall which, although not offsetting the overall loss of mass, slows the rate of glacier wastage. However, the sensitivity of glaciers to climatic change, especially in the Himalayas, cannot simply be gauged from the spatial variability of metrological conditions over a given area (e.g. monsoonal influence). Other localised non-climatic factors also play a key role in determining glacial response rates to change.

To account for such variability, and accurately assess glacial fluctuations, monitoring in the Himalayas ideally needs to be performed both cross-regionally and on a basin scale, including numerous glaciated areas. To date, such detailed assessments of Himalayan glacier fluctuations are lacking (UNEP, 2009; Bolch *et al.*, 2010). Furthermore, the large-scale observations which are available in the Himalayas tend to focus on changes in glacier length and neglect changes in volume (e.g. Kulkarni *et al.*, 2007; Narama *et al.*, 2009; Scherler *et al.*, 2011), which are a far more

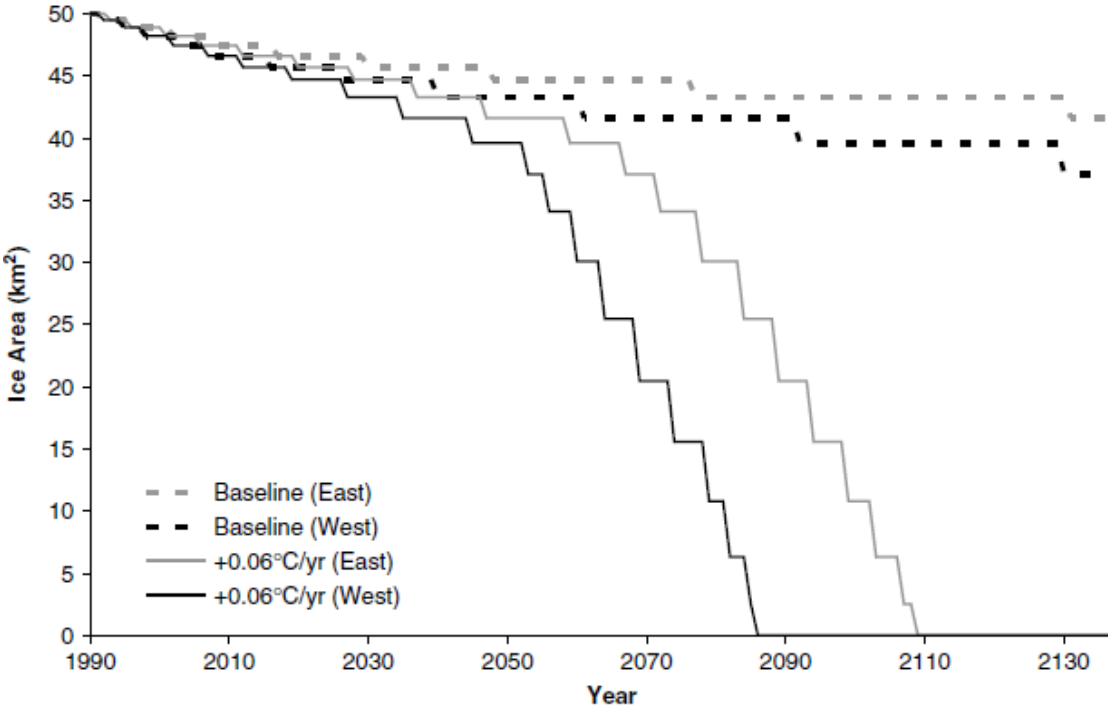


**Figure 3.9: Comparison of decline in glacier area between west (black) and east (grey) for baseline conditions (dashed) and 0.06°C year$^{-1}$ (solid) warming scenario (taken from Rees & Collins, 2006).**

comprehensive assessment of mass balance and overall glacier health (Dyurgerov & Meier, 2005).

### 3.6. Glacier mapping and monitoring in the Himalayas

Glacier monitoring schemes are a valuable tool for the assessment of a number of key issues, such as: (1) the impact of climate change on the cyrosphere; (2) the sustainable management of water resources (most notably in South Asia); (3) the accurate modelling of global and regional hydrology; (4) the increased threat of glacier outburst floods (Mool *et al.*, 2007); and (5) the estimation of glacial contributions to global sea level rises. In comparison to the rest of the world, detailed records of glacial fluctuations in the Himalayas are limited and fail to compare spatially or temporally to those available in the extensively mapped mountainous regions of Europe, North America and Scandinavia (UNEP & WGMS, 2008, Barry, 2006). As a result, relatively little information is available to suitably assess the large-scale evolution of glacierised areas in the Himalayas since the end of the LIA. This lack of detailed and wide-ranging glacier mapping in the Himalayas, although improving, has continued into the twenty-first century and is yet to be fully addressed. Indeed, the study of glaciology as a whole in many parts of the Himalayas has been described as still being in its nascent stage (Srivastava, 2001).

Despite collectively lacking in number, the first basic glacier observations in the Himalayas were documented from around the 1860s onwards. These observations consisted mainly of glacier termini maps and sketches produced using plane-table surveying and heavy theodolites (e.g. Purdon (1861); Godwin-Austen (1864). It was not until the turn of the 20$^{th}$ century that concerted efforts were made to continually measure fluctuations of Himalayan glaciers in order to assess climate/glacier interactions and variability. The first major study of this kind was initiated by the GSI in collaboration with the *Commission International des Glaciers,* monitoring the movements of 12 principle Himalayan glaciers from 1906-1908 (Holland, 1907). However, efforts to continue these systematic monitoring efforts in the following decades were intermittent. A study by Mayewski & Jeschke (1979), investigating

historic glacier fluctuations across the Himalayas, for example, found that length records were available for only 112 glaciers dating back to 1842, repeated measurements for many of these being limited.

For the Indian Himalayas it was not until the early 1960s that the first extensive and detailed maps were produced utilising modern techniques. Covering the Indian Himalayas in their entirety, these maps were produced by the SOI based on aerial photography. However, only a small segment of these maps are available to the public. Although the GSI and SOI continued to survey selected glacier snouts, only three large-scale glacier maps have been produced by the SOI since the 1960s (Chitranshi *et al.*, 2004; Roy, 2001; Dobhal *et al.*, 2004). In comparison, Bhambri & Bolch (2009) note that in Norway, for example, as many as 24 glaciers were mapped more than once on a large-scale between 1952 and 1996.

The lack of detailed topographic surveys for many glaciated areas of the Himalayas has hindered contemporary attempts to quantify long-term glacier change. In addition, the accuracy of many of the Himalayan topographic maps available has also been questioned. Studies by Vohra (1980), Agarwal (2001) and Bhambri & Bolch (2009), for instance, have indicated that the SOI maps available for the Indian Himalaya, for example, contain significant errors concerning the delineation of snow-covered and debris-covered glaciers. Both a lack of appropriate glacier delineation training and the acquisition time of the source aerial imagery (taken during early winter) have been cited as possible reasons for these errors.

Glacier monitoring efforts in the Himalayas have also been hindered by the unavailability of aerial photography. The use of aerial photography has advantages over traditional mapping techniques in that surveys can cover relatively large spatial areas in short periods of time whilst alleviating the need for extensive field work. Additionally, high resolution, often stereoscopic, imagery produced from aerial surveys aid the production of highly detailed topographic glacier maps (e.g. Muller *et al*. (1976) and Ommanney (1980)). However, the availability of aerial photography in

the Himalayas is limited by a number of economic, political and geographic factors (Bhambri & Bolch, 2009).

Derived from the limited topographic maps and aerial photography that do exist for the Himalayas (mainly in Nepal), a number of historic glacier outlines have recently been integrated into the GLIMS project database (see chapter 4). Dating from the 1960s/70s, these GLIMS outlines represent important temporal snapshots of glacier extent during this period. However, in order to quantify temporal change in glacier length and area these outlines need to be compared to other multi-temporal spatial mapping sources. As a result of the limitations discussed, it was not until the 1970s onwards through the introduction of satellite imagery that availability of spatial mapping reference sources for the Himalaya began to increase.

### 3.6.1 Spaceborne imagery: A new era of glacier mapping

The launch of the Landsat 1 satellite in 1972 and the subsequent introduction of digital satellite imagery brought about a new era of remote sensing, one which provided huge potential for mapping and monitoring glacierised regions. Today the number of satellite sensors available with mapping capabilities is large and ever increasing. Satellite platforms offer digital multispectral datasets that have a near-global coverage, are radiometrically calibrated, and are collected repeatedly, making them ideal for prolonged ground feature monitoring. These benefits have been enhanced further through the development of advanced GIS technologies, simplifying image analysis and processing techniques and allowing glacier measurements from satellite imagery to be made using a globally uniform set of methods (Kääb, 2005b.).

Currently, various satellite sensors are available that offer a range of uses as glacier mapping tools (Table 3.2). The majority of these sensors are electro-optical scanners which provide calibrated digital imagery in the visible and near IR regions of the electromagnetic spectrum (Rees & Pellikka, 2010). The degree to which a satellite sensor is suitable for a glacier mapping task is governed by a number of characteristics: (1) spatial resolution - pixel size; (2) spectral resolution – range of radiation

**Table 3.2: Characteristics of satellite used for the remote sensing of glaciers (V= visible, SWIR = shortwave infrared, TIR = thermal).**

| | Low Resolution | High Resolution | | | | Very High Resolution | |
|---|---|---|---|---|---|---|---|
| Satellite | Terra | Landsat 5 | Landsat 7 | Terra | ALOS | IKONOS | GeoEye-1 |
| Sensors | MODIS | TM | ETM+ | ASTER | AVNIR-2 | N/A | N/A |
| Temporal availability | 1999-present | 1985-present | 1999-present | 1999-present | 2006-present | 2000-present | 2008-present |
| Temporal resolution (days) | 1 - 2 | 16 | 16 | 16 | 46 | 5 | <3 |
| Image size (km x km) | 1 x 1.6 x 1 | 185 x 180 | 185 x 180 | 60 x 60 | 35 x 70 | 10 x 10 or 14 x 14 | 15 x 15 |
| Swath width (km) | 2330 | | 185 | 60 | 70 | 11 | 15 |
| Spatial resolution (m) | 250 (V), 500 (SWIR) | 30 (V), 120 (TIR) | 30 (V, SWIR), | 15 (V), 30 (SWIR) | 10 (V) | 0-4 (V) | 0.41-1.65 (V) |
| Cost per full scene (USD) | Free | Free | Free | Free | ~685 | 980* | ~5600 |
| Cost per $km^2$ (USD) | Free | Free | Free | Free * | ~0.27 | 20 | 25 |

*60 USD for non-GLIMS affiliates.

wavelengths detected; (3) spatial coverage – areal coverage of a single image; (4) temporal resolution – satellite orbital revisit time; (5) radiometric resolution – sensitivity of a sensor to reflected radiation; (6) stereo-scopic capabilities – ability to generate DEM from overlapping stereo imagery; and (7) image cost.

One simple way of gauging the suitability of satellite sensors for glacier mapping is by focusing on spatial resolution. In this respect, sensors can be separated into three categories; LR, HR and VHR. LR sensors offer fairly coarse datasets with spatial resolutions of around one kilometre. These include sensors such as AVHRR and MODIS. Due to their poor spatial resolution, sensors such as MODIS are of little use in mapping relatively small mountain glaciers and are more suited to monitoring large-scale land cover changes (e.g. Immerzeel *et al.*, 2009). The main advantage of LR sensors is that in general their poor spatial resolution is compensated by their large coverage (single swath widths of >2000 km) and subsequent short temporal resolutions (~ 1-2 days) allowing large amounts of data to be collected over short time periods.

Several glacier parameters can be measured through the use of satellite data, including; mass balance (Bolch *et al.*, 2010), volume (Bolch *et al.*, 2008), velocity (Kääb, 2005b.), equilibrium line altitude (Zemp *et al.*, 2007), albedo and reflectance (König *et al.*, 2001) amongst others. However, for glacier monitoring, the most common parameter to be mapped and measured from satellite imagery is areal extent (e.g Narama *et al.* (2009) and Bhambri *et al.* (2011)). Individual mountain glaciers can cover areas of <0.001 to >600 $km^2$ with trunk widths varying from <3m to >40m. In order to delineate mountain glaciers, satellite sensors are therefore required to have a spatial resolution of at least 30 m (Rees & Pellika, 2010) and, hence, sensors in the HR and VHR categories are of most use.

The HR category includes satellite sensors with spatial resolutions in the range of 10 m to 100 m. Within this category the Landsat 5 TM and Landsat 7 ETM+ sensors have been the most widely utilised datasets for glacier mapping purposes. Launched in 1982 and 1999 respectively, Landsat TM and ETM+ quickly revolutionised glacier

mapping providing datasets with much improved spatial and spectral resolutions and relatively large spatial coverage. These sensor characteristics, for the first time, enabled glacier parameters to be monitored from space with an adequate level of accuracy and facilitated the rapid compilation of detailed large-scale inventories (e.g. Williams (1986) and Hall *et al.* (1992)). The application of Landsat TM and ETM+ satellite imagery for glacier mapping has been further enhanced by the fact they are now available free of charge.

Since the launch of Landsat 7, many other satellites have become available in the HR category for use within glacier mapping studies. These include satellite systems such as, SPOT, IRS and ALOS. Despite offering improved spatial resolutions, however, the use of many of these sensors on large spatial scales has been limited by the high cost of data per square kilometre. This financial limitation has also hindered the use of VHR sensors. Providing meter and sub-meter resolution imagery, VHR sensors such as IKONOS, Quickbird and Cartosat-1 offer a viable alternative to aerial photography for detailed glacier studies (e.g. Bhambri *et al*., 2011), but for regional studies are limited by their narrow swath widths (Table 3.2) and cost of over 5000 USD per scene.

Currently ASTER sensor, on board the Terra satellite, may be the most suitable for the mapping of glacier parameters and in many cases has begun to supersede the use of the Landsat TM & ETM+ sensors for this purpose (e.g. Taschner & Ranzi, 2002; Kääb *et al.,* 2003; Kääb 2005b.; Svoboda & Paul, 2009; Gjermundsen *et al.,* 2011). Racoviteanu *et al*. (2008) sum up the advantages of ASTER over other sensors. These include ASTER's: (1) spatial resolution of 15 m in VNIR, which is adequate for regional-scale glacier studies; (2) high spectral resolution (3 VNIR bands, 6 mid-IR bands and 5 TIR bands), improving multi-spectral image classification; (3) high resolution along-track stereoscopic vision; and (4) adjustable sensor gain settings providing increased contrast over snow and glacier covered areas. Importantly ASTER imagery is also low cost (0.017 USD per $km^2$) and has become available free of charge to certain scientific organisations (e.g. affiliates of the GLIMS project).

The recent availability and use of spaceborne imagery, particularly from the Landsat (TM & ETM+) and ASTER sensors, has helped increase the number of glaciers being continuously monitored (WGMS, 2011). Only available since the late 1970s, however, high resolution satellite imagery is temporally limited. With the declassification of 1960s Corona imagery (chapter 2) there is an opportunity to extend the observation periods of satellite based glacier monitoring studies by up to 20 years.

### 3.6.2. Satellite-based glacier mapping techniques and their application in the Himalayas

Fundamental to the successful mapping of glacier parameters from satellite imagery is the ability to effectively interpret and classify image content. In general, all remotely sensed images, including those taken by a satellite, contain a matrix of information regarding some physical property of EMR. EMR is associated with radiant energy, which radiates either from the sun, as solar radiation, or the Earth surface, via thermal radiation (Rees & Pallika, 2010). Differentiated by the electromagnetic spectrum, EMR varies in wavelength from very long (hundreds of meters) to very short (nanometres). The majority of passive satellite sensors, such as Landsat ETM+, ASTER and Corona, register reflected EMR in the visible and near IR regions of the electromagnetic spectrum, and do so in the form of a numerical value of radiance (referred to as a pixel DN). Radiance (also referred to as brightness) is a measure of the intensity of radiation in a particular direction and is often specified as a function of wavelength (Rees & Pallika, 2010). Radiance at a sensor is measured for a number of different wavebands selected according to the atmospheric windows that exist in the visible and near IR spectrum (highlighted in Figure 3.10 as atmospheric transmission).

Ground reflectance varies according to a number of factors but is largely dependent on the physical properties of the ground surface material (Lillesand & Kieffer, 2000). A basic assumption of remote sensing is that specific surface materials have a characteristic manner of interacting with incident radiation, which is described by the spectral response of that material (Mather, 1999). As a result, differing surface types reflect specific portions of the electromagnetic spectrum, described by individual

spectral reflection curves. These disparate spectral curves of individual surface types determine their spectral discernibility within satellite imagery.

Accurately interpreting and mapping a particular surface type from satellite imagery depends on individual sensor characteristics. In this respect, spatial and spectral resolutions are two important characteristics. Sensors such as Landsat ETM+ and ASTER are said to provide multispectral data, as they collect EMR information with the use of numerous wavebands. The resulting radiance values from each waveband can be combined with the use of GIS software and then split into corresponding red, blue and green layers that allow the imagery to be viewed as true or false colour composites. In contrast, panchromatic camera systems (such as Corona) simply record total intensity values of radiation falling on each pixel which are displayed in a grey scale.

The spectral curves of various types of snow and glacier ice are described in figure 3.10. 'Clean' glacier ice and snow are characterised by: (1) high reflectivity (attributed to their high albedo) in the visible wavelengths (0.4 - 0.7 µm); (2) medium reflectivity in the near IR (0.8 - 2.5 µm); (3) low reflectivity and high emissivity in the TIR (2.5- 14 µm); and (4) low absorption and high scattering in the microwave region (Racoviteanu *et al.*, 2008; Rees, 2005). In terms of glacier mapping, the spectral uniqueness of ice in the visible and near IR parts of the spectrum in particular, means that in clear weather clean glaciers are relatively easy to identify in LR, HR and VHR satellite imagery.

In order to delineate, and in doing so classify, glacier ice from satellite imagery, two mapping approaches can be utilised. Firstly a manual approach can be adopted which is the most technologically simple form of image classification. Alternatively, a number of automatic approaches have now been developed which have the potential to significantly reduce processing times. Both these approaches will be discussed in relation to measuring glacier geometry in the following two sections.

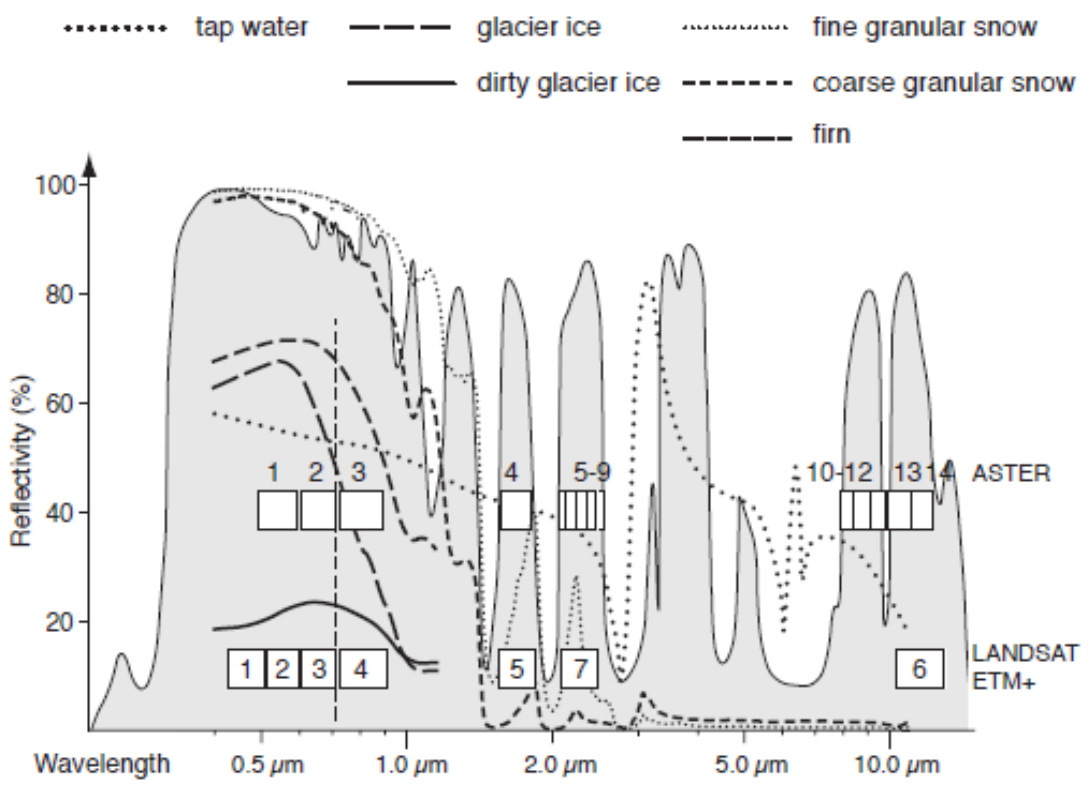


**Figure 3.10: Simplified spectral signatures for water, snow and ice acquired by passive optical sensors (taken from Kääb (2005a.)). Atmospheric transmission (grey region) and Landsat ETM+ and ASTER bands are also shown. Spectral data are taken from ASTER spectral library, Zeng *et al.* (1983), and Hall *et al.* (1988).**

### 3.6.3. Automatic glacier classification

The term classification refers to the process of associating pixels in an image with particular surface material types according to their spectral characteristics (Raup *et al.*, 2007). Broadly there are three types of classification techniques that are commonly used to automatically delineate glacier ice from multispectral satellite imagery. These are: (1) image algebra and segmentation; (2) unsupervised; and (3) supervised classifications. Each of these classification techniques rely on the spectral uniqueness of ice in the visible and near IR portions of the electromagnetic spectrum to distinguish it from surrounding terrain. Table 3.3 summarises the automated classification techniques used by a selection of studies to map glaciers around the world.

**Table 3.3: Summary of automated classification techniques used to map clean and debris-covered glaciers.**

| Clean Glaciers | | | | |
|---|---|---|---|---|
| Author | Classifcation Method | Description | Location | Accuracy (when compared to manual glacier digitization) |
| Paul *et al* (2002) | Band Ratio | Ratio image of Landsat TM bands 4 & 5 with threshold value | Swiss Alps | 97% |
| Albert (2002) | Supervised | Supervised maximum liklihood classification from a Landsat TM false colour composite | Quelccaya Ice Cap, Peru | 90.20% |
| | Unsupervised | Unsupervised classification from a Landsat TM false colour composite | Quelccaya Ice Cap, Peru | 90.60% |
| | Band Ratio | Ratio image of Landsat TM bands 3 & 5 with threshold value of >4.0 | Quelccaya Ice Cap, Peru | 91% |
| | Band Ratio | Ratio image of Landsat TM bands 4 & 5 with threshold value of >3.3 | Quelccaya Ice Cap, Peru | 92% |
| Racoviteanu *et al* (2008) | NDSI | NDSI from SPOT imagery using a threshold of 0.5- 0.6 | Cordillera Blanca, Peru | N/A |
| Bayr *et al* (1994) | Band Ratio | Band ratio of ASTER bands 3 & 4 | Austrian Alps | N/A |
| Sidjak (1999) | Supervised combined with band ratio and NDSI | Supervised maximum liklihood classification from Landsat TM bands 4 & 5 combined with NDSI | Illecillewaet icefield, Canada | N/A |
| Debris-covered glaciers | | | | |
| Author | Classifcation Method | Description | Location | Accuracy (when compared to manual glacier digitization) |
| Paul *et al* (2004) | Band ratio combined with slope threshold | Ratio image of Landsat ETM+ bands 4 & 5 combined with a slope threshold of <24° derived from an ASTER DEM | Swiss Alps | N/A |
| Taschner & Ranzi (2002) | Band ratio combined with thermal threshold | Ratio images from Landsat TM bands 4 & 5 and ASTER bands 3 & 4 combined with ASTER thermal band | Italian Alps | N/A |
| Bolch (2007) | Band ratio combined with curvature threshold | Ratio image of Landsat ETM+ bands 4 & 5 with threshold value of 2 combined with curvature parameters derived from an ASTER DEM | Tien Shan, Kazakhstan | N/A |
| Shukla et al (2010) | Supervised combined with thermal and slope threshold | Tested a number of supervised maximum liklihood classifications from IRS-P6-AWiFS optical data combined with ASTER thermal bands and a topographic map derived DEM. A slope threshold of <15° was ultilised | Chenab basin, Himalayas | 74-89% |
| Buchroitner & Bolch (2007) | Supervised combined with thermal, slope and curvature thresholds | Supervised classification from ASTER optical data combined with slope and curvature thresholds derived from an ASTER DEM | Khumbu Himalaya | 95% |

The image algebra and segmentation classification category refers to the use of individual sensor wave bands within simple algebraic algorithms. For glacier mapping applications, the most common algebraic algorithms in their simplest form are band ratios (R)

$$R_{ij} = \frac{DN_i}{DN_j} \tag{3.3}$$

and normalised differences indices (NDI) (Kääb, 2005a.)

$$NDI_{ij} = \frac{(DN_i - DN_j)}{(DN_i + DN_j)} \tag{3.4}$$

where $DN_i$ and $DN_j$ are digital numbers (radiance values) of two bands *i* and *j* that show high dicernability for the surface category classified with respect to other categories in the image. Band ratios for snow and ice usually involve dividing wave bands in the VNIR by bands in the SWIR (due their high VNIR reflectivity and relatively low SWIR reflectivity). For multispectral ASTER imagery, for example, glacier ratio images have been created by dividing band 3 by band 4 (e.g. Bayr *et al.*, 1994; Paul & Kääb, 2005). Resulting ratio images effectively highlight the pixels assumed to contain either snow or ice. These glacier pixels can then be refined further with use of a threshold value. On a similar premise, the NDSI has also been utilised to automatically classify glaciers from multispectral imagery (see Table 3.3). NDSI is calculated as (VNIR-SWIR) / (VNIR+SWIR) (Racoviteanu *et al.*, 2008), which for ASTER imagery uses band 1 (VNIR) and band 4 (SWIR).

Supervised and unsupervised classifications use the information contained within multispectral imagery slightly differently. Both these techniques utilise pre-defined spectral signatures, each of which are associated with a particular surface type and are usually obtained from a false or true colour composite imagery. For supervised classifications, each of these spectral signatures is defined with the use of operator-selected training areas, covering separate image areas of ice, snow and rock, for example. During unsupervised classifications, this manual selection process is performed automatically with signatures being segmented in concentrations of spectral vectors and then labelled accordingly by the user (Kääb, 2005a.). Using these

pre-defined signatures, images are then separated into glacier and non-glacier classes according to how well individual pixels fit the spectral characteristics of each signature. As well as being applied singularly, a number of studies have combined each of the automatic classification techniques and included further variants in attempts to improve classification efforts (see Table 3.3). For example, in addition to the NDSI, normalised difference water and vegetation index have been used to help eliminate glacier misclassifications (e.g. Huggel *et al.*, 2002; Paul *et al.*, 2002).

Automated glacier classification techniques are now strongly established and represent a standardised approach that can be rapidly applied over large areas (Kääb, 2005a.; Wolken, 2006). Furthermore, for clean glaciers, simple band ratios, for example, have been shown to be particularly robust and almost match results obtained by the manual approach (see Paul *et al.* (2002) in Table 3.3). However, difficulties in the automated mapping of debris-covered glaciers still remain which limit its application in many glacierised regions (Paul *et al.*, 2002; Raup *et al.*, 2007). Supraglacial debris masks the spectral characteristics of ice, reducing its spectral discernability (see Figure 3.10). Having both been derived from valley rock, the resulting spectral response of supraglacial debris is often very similar to surrounding periglacial debris making it difficult to distinguish glacier margins. Consequently, the effectiveness of image algebra, band ratio and supervised/unsupervised techniques, which rely on the spectral uniqueness of ice, is significantly reduced.

In the Himalayas a significant portion of glaciers are debris-covered. As a result, the application of automated technique over large areas has been considerably limited and instead the majority of satellite-based glacier measurements have been derived using manual techniques (Bhambri & Bolch, 2009). Morphometric and thermal parameters, derived from DEMs and thermal satellite bands, have recently been combined with VNIR and SWIR classifications to help delineate debris-covered glaciers (e.g. Shukla *et al.*, 2010; Buchroither & Bolch, 2007) but success has varied. Consequently, automated mapping of debris-covered glaciers from remotely-sensed data still remains challenging.

### 3.6.4. Manual glacier classification

Manual classifications, made through human interpretation, are still regarded as the best tool to accurately delineate glacier margins from satellite imagery (Raup *et al*., 2007; Paul *et al*., 2009). Manual delineation of surface features from satellite imagery is relatively simple and can be undertaken using basic digitization tools available in GIS software packages. The accuracy of this technique is largely dependent on two factors: (1) the characteristics of the satellite imagery being used, such as spatial and spectral resolution; and (2) the glacier mapping knowledge of the user (Kääb, 2005a.).

To aid the manual delineation of glacier boundaries, a number of guidelines and recommendations have been developed by large-scale glacier inventory projects. Table 3.4 lists recommendations put forward by the GLIMS project, for example. These recommendations, to some extent, attempt to standardise what is a very subjective classification technique. Inevitably, however, spectrally indistinguishable features, such as dead ice and supraglacial and periglacial debris, still remain a challenge to manually classify and human error may occur (Bhambri & Bolch, 2009). In comparison to automated technique, the main limitation of manual classification techniques concerns the processing times involved. Unlike automated classifications that can be applied rapidly to imagery, the nature of the manual approach is such that each glacier in an area of interest needs to be individually delineated, which for large areas can be time-consuming.

**Table 3.4: Basic recommendations set out by the GLIMS project for the delineation of glaciers from satellite imagery (taken from Racoviteanu *et al.*, 2009).**

| GLIMS Recommendations | | |
|---|---|---|
| Glacier definition | Ice divides | Debris-covered ice |
| Tailored to remote sensing 'a glacier or perennial snow mass consists of a body of ice and snow that is observed at the end of the melt season. This includes all tributaries and connected feeders that contribute ice to the main glacier, plus all debris-covered parts of it. Excluded is all exposed ground, including nunataks.'<br><br>Bodies of ice above the bergschrung that are connected to the glacier should be considered part of the glacier, because they contribute snow (through avalanches ) and ice to the glacier<br><br>A stagnant ice mass that is still in contact with a glacier is part of the glacier, even if it supports vegetation.<br><br>If snowfields are identifiable, they should be disconnected from the main glacier<br><br>Ice avalanche cones below a glacier terminus (dry-calving) are not part of the glacier. | If there is no flow between separate parts of a contiguous ice mass, the parts should, in general, be treated as distinct units, separated at the topographic divide.<br><br>Any steep rock walls that avalanche snow onto a glacier but do not retain snow themselves should not be included as part of a glacier | All debris-covered ice must be included even if covered with vegetation. |

### 3.6.5. DEMs and the measurement of glacier volume

DEMs consist of a matrix of values that describe the three-dimensional position of surface and sub-surface objects (Kääb, 2005a.). Due to their increasing availability both regionally and globally, DEMs now represent a valuable tool for a range of geoscience applications. In regards to high mountainous environments these include, amongst others, visualising 3D environments, analysing terrain characteristics, orthorectifying satellite imagery, classifying surface types, and modelling geomorphic processes (e.g. Wilson & Gallant, 2000; Shukla *et al.*, 2010; Etzelmüller & Björnsson, 2000).

For large-scale mapping of high mountainous environments, spaceborne DEMs now offer a number of advantages over terrestrial and airborne alternatives. In addition to their availability over large areas, spaceborne DEMs are now readily accessible and, in some instances, can be acquired free of charge. Spaceborne DEMs are mainly prepared using the following methods:

- Satellite stereo imagery: DEMs are generated from image stereo pairs using photogrammetric techniques to extract 3D data points (stereo satellite sensors include ASTER, SPOT and ALOS, amongst others).

- Interferometric SAR: Interferometric synthetic aperture radar (InSAR) uses the phase difference between two or more images acquired at slightly different positions in space to characterise scene topography (see Hanssen, 2001 and Høgda *et al.*, 2011) (e.g. SRTM global DEM).

- LiDAR and Radar altimetry: Both LiDAR and Radar altimetry determine terrain heights from the travel time of a nadir-looking laser or microwave beam, respectively (Kääb, 2005a.).

In addition to spaceborne methods, topographic maps can also be a cost-effective source of large-scale elevation information from high mountainous environments. The usefulness of this source however, relies heavily on the availability of good quality maps, which for many parts of the Himalayas, for example, are lacking.

For glaciological studies, DEMs have been utilised to create hypsometric maps (e.g. Brockelhurst & Whipple, 2004), model glacier flow parameters (e.g. Kumar *et al.*, 2011), and most importantly estimate glacier volume change. Traditionally, glacier volume and mass balance change is measured using the direct glaciological method (see Kaser *et al.* (2002) and Hagg *et al.* (2004)). Due to their high temporal and spatial availability, many studies are now using DEMs to estimate glacier volume/mass balance change via the indirect geodetic method. The geodetic approach consists of measuring elevation changes over time ($\delta h/\delta t$) from various DEMs constructed over a glaciers surface (Racoviteanu *et al.*, 2008). Over the past five decades, this approach has mainly been performed by subtracting older DEMs, obtained from historical maps

or airborne stereo imagery, from newer DEMs obtained from more contemporary airborne stereo imagery. However, more recently, an increasing number of studies are utilising DEMs obtained from spaceborne sensors to geodetically estimate volume changes, due to the advantages described previously (e.g. SPOT: Berthier *et al.* (2004) SRTM: Li *et al.* 2011, ASTER: Kääb (2008)).

There are two approaches to estimating glacier change from geodetically derived elevation ice surface changes. Firstly, if elevation changes are computed pixel by pixel, the elevation differences are multiplied by the pixel resolution to give volumetric changes per pixel (e.g. Berthier *et al.*, 2010). Secondly, a hypsometric approach can be taken whereby the average elevation change is multiplied with glacier area to obtain overall volume change (e.g. Nuth *et al*., 2010). Volume change estimates for both of these approaches can be converted into mass balance by multiplying them with the density of ice (Racoviteanu *et al.*, 2008). In most instances the density of ice is assumed to be ~900kg/$m^3$ (Arendt *et al.*, 2002), this value can vary considerably, however (see Paterson, 1994.

In regions where direct glacier mass-balance measurements are lacking, geodetic methods can offer an invaluable source of volume change information. In the Himalayas in particular, the application of geodetic techniques has increased the amount of mass balance data available for individual glaciers. However, the relative accuracy of volume and mass-balance changes that have been estimated via the geodetic technique still remains an issue of concern. Where comparisons with field data exist, and high resolution DEMs have been used, some studies have demonstrated good agreement between geodetic and direct glaciological estimations of mass-balance change (e.g. Hagg *et al.*, 2004). However, the accuracy of volume estimations obtained via the geodetic technique is largely dependent on the DEM source and the DEM extraction method. Stereo-imagery produced by the spaceborne ALOS PRISM sensor, for example, can be used to extract DEMs with a vertical accuracy of ~±5 m (EORS, 2007). Other VHR satellite sensors such as GeoEye-1, Quickbird, IKONOS offer DEM products with similarly high vertical accuracies.

Although being the preferable choice, the applicability of DEMs produced by VHR satellite sensors for large glacier monitoring projects is limited considerably by their high cost. One of the more economical sources of satellite data available is the ASTER sensor. ASTER DEMs have been utilised in a number of geodetic glacier volume studies and are the primary source of elevation data for the GLIMS project (Kargel *et al.*, 2005; Raup *et al.*, 2007). However, the vertical accuracy of ASTER DEMs has been reported to vary from ±15 to ±60 m (Toutin, 2008; Fujisada, 2005), error magnitudes which for short-scale studies may exceed any temporal changes in glacier surface elevation.

In addition to ASTER stereo imagery, the SRTM and ASTER GDEMs now represent a free source of elevation data. Released in 2000, the 90 x 90 m SRTM near global DEM, in particular, has been utilised by many glacier volume-change studies, providing a base dataset to compare to other DEM products (Paul and Haeberli, 2008; Larson *et al.*, 2007). The vertical accuracy of SRTM data has been reported to range from ±10 m to ±16 m (Nuth & Kääb, 2010; Rodiguez, 2006) which makes it suitable for monitoring long term surface changes. However, in many high mountainous regions SRTM is limited by the presence of data voids resulting from topographic shadowing errors and a number of InSAR specific processing artefacts (Reuteral *et al*., 2007; Kervyn, 2001) (Figure 3.11).

Created through the merging (via stereo-correlation) of ASTER stereo images acquired from 2000-2008, the ASTER GDEM represented a higher resolution alternative (30 m) to SRTM, filling many of the SRTM data voids. Despite these improvements, however, in comparison to SRTM, ASTER GDEM elevation errors in high mountainous regions are often higher, with RMSE's ranging from ±5-50 m (METI/NASA/USGS, 2009)). As a result, many studies suggest SRTM is still the superior product for glaciological applications (Nuth & Kääb, 2010; Xing, 2011). The release of ASTER GDEM version 2 in October 2011, however, may have changed this view, with initial studies reporting improved vertical RMSE's of ±12 m (Tachikawa *et al.*, 2011).

Overall, elevation errors associated with all cost-effective spaceborne DEM sources (i.e. ASTER, SRTM and ASTER GDEM) are generally quite large, this being their main

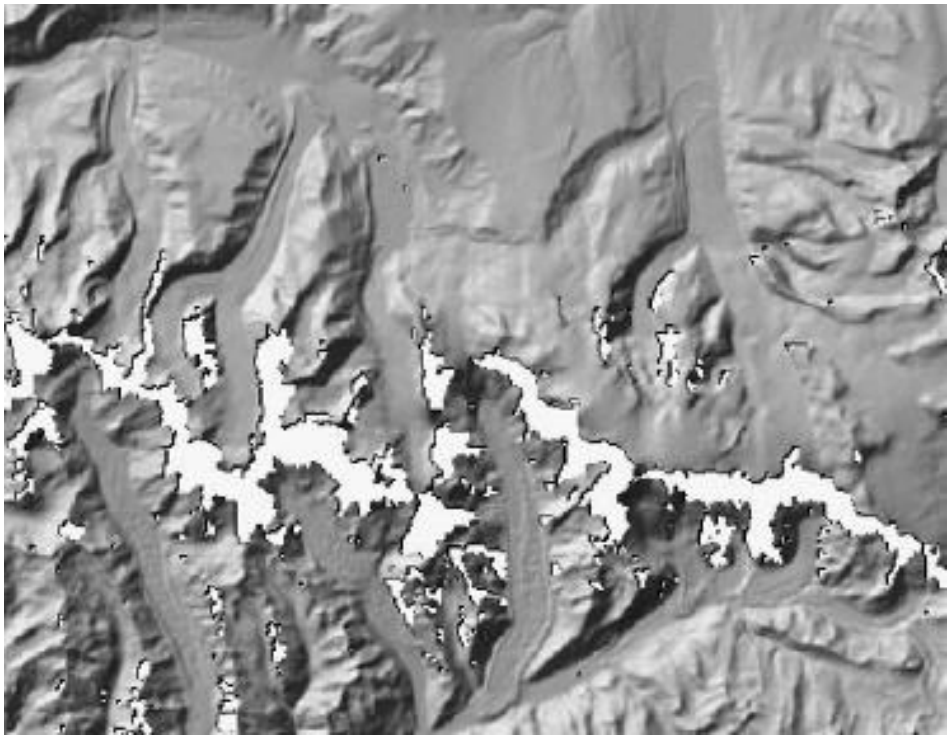

**Figure 3.11: SRTM hillshade image of a glaciated portion of the Bhutan Himalayas. White regions indicate voids in the data (taken from Kääb, 2005b.).**

limitation. The sources of these elevation errors for InSAR and stereoscopic derived DEMs are summarised in table 3.5. The problem of error is accentuated further when DEMs from various sources are combined during DEM differencing. Any errors in the source DEMs propagate with each arithmetic operation performed. Errors in the derived differences are therefore larger than in the original. The total RMSE for any elevation change $\Delta h$, for example, can be estimated from the RMSE of each of the input DEMs (Kääb, 2005a.; Etzelmüller, 2000):

$$(\text{RMSE } \Delta h)^2 = (\text{RMSE } h_1)^2 + (\text{RMSE } h_2) \qquad (3.5)$$

DEM errors are also difficult to accurately quantify. In equation 3.5, individual DEM error is quantified with the use of total RMSE of residuals. However, this technique requires an elevation reference source that is assumed to be accurate. Ideally, this reference data would be obtained either from highly accurate DGPS measurements or high quality aerial stereo data (Kääb, 2005a.).

As a consequence of the factors discussed, many glacier volume change studies have numerous errors built in to them at each stage of the geodetic process. Some studies

do not correct for these errors (e.g. Sund *et al.*, 2009; Muskett *et al.*, 2009), meaning the resulting volume change estimates may be significantly biased. Other studies have applied a number of elevation corrections using various statistical methods (Nuth & Kääb, 2010; Berthier *et al.*, 2010; Peduzzi, 2010). However, due to the magnitude of error associated with many DEM sources it is currently recommended that the geodetic method is only used for estimating changes in glacier mass balance at decadal scales (Bamber & Rivera, 2007; Hagg *et al*., 2004).

Similar to satellite imagery, satellite-based DEMs are also temporally limited, the first being produced from the SPOT-1 satellite launched in 1986. For many mountainous regions, however, this date is brought forward to 1999 with the availability of the near global ASTER stereo imagery and SRTM data. This temporal limitation hinders satellite-based geodetic glacier volume change studies and highlights the importance of the DEMS derived from declassified 1960s Corona stereo imagery.

**Table 3.5: Sources of error in Stereo- and InSAR-derived DEMs. SRTM and ASTER based DEMS are used as an example (taken from Nuth & Kääb (2010), Kääb (2005a) and Strozzi *et al.* (2003)).**

| ASTER DEMs (Stereo Imagery) | SRTM (InSAR) |
|---|---|
| Orientation of stereo-pairs: Horizontal and vertical errors present in the GCP and tie point reference sources effect the quality of the triangulation process and thus the ability of matching algorithms to locate corresponding image points.<br><br>Image quality: Cloud cover, poor contrast and shadows degrade the stereo image matching process.<br><br>Topography: Topographic distortion degrades the stereo image matching process, particularly for steep slopes and sharp mountain peaks.<br><br>GCP distribution: Uneven GCP distribution within stereo pairs can cause elevational bias in areas of clustering.<br><br>Techniques: Stereo image point matching algorithms are each associated with some level of error. | Voids present in SRTM data due to radar shadowing, layover, foreshortening and insufficient interferometric coherence. These data gaps are found mainly in mountainous areas on east facing slopes which correspond to back slopes of SAR illumination<br><br>Penetration of C-band radar waves into snow and ice.<br><br>Acquisition month: SRTM data acquired during the accumulation season in the mid-latitudes and the outer tropics. Consequently SRTM-derived elevations over Himalayas may be overestimated. |

### 3.6.6. Satellite-based Himalayan glacier monitoring studies and their findings

With the increase in availability of satellite imagery since the 1970s the number of glacier change studies conducted in the Himalayas has gradually increased. This section summarises existing large-scale and long term glacier area, length and volume change studies covering the main Himalayan arc with use of satellite data. Table 3.6 and figure 3.12 describe the existing large-scale glacier area change and their spatial distribution. What is clear from figure 3.12 is that the sample of glacier area change measurements across the main Himalayan arc is relatively sparse. Overall, only six large-scale glacier area change studies exist, one of which includes only 4 glaciers. In total, these studies include around 1500 glaciers (estimating that Shrestha & Joshi (2009) included ~400 glaciers), a small proportion when considering the Indian Himalayas alone is reported to contain ~9600 glaciers (Raina & Srivastava, 2008).

Monitoring glacier changes from the 1960/70s up to 2010, the studies presented in table 3.6 reveal glacier area reductions varying from 0.12% $a^{-1}$ (Bolch *et al*., 2008; Bhambri *et al*., 2011) to 0.53% $a^{-1}$ (Kulkarni *et al*., 2007). These glacier observations to some extent support the assumptions of Rees & Collins (2006), who suggest that the summer monsoon may subdue glacier wastage in the eastern Himalayas. Figure 3.12, for example, shows that glacier area reduction in the easterly located Khumbu region (e.g. Bolch *et al*., 2008): -5.3%, 1962-2005) is considerably less than in the westerly located Chenab, Parbati and Baspa basins (e.g. Kulkarni *et al*. (2007): -21%, 1962-2001). However, this east-west assumption may be overly simplified. The highest rate of glacier area reduction for example, has been estimated for the Langtang basin, which is relatively close in proximity to the easterly located Khumbu region in Nepal.

The current inadequacies in Himalayan glacier monitoring are particularly demonstrated when considering the number of geodetic glacier volume change measurements available in the region (Table 3.7 and Figure 3.13). As discussed, changes in glacier volume are seen as a direct and immediate signal of mass balance change and therefore are the most valuable indicator of glacier health (Haeberli, 2004). However, to date, only five glacier change studies have measured geodetic

**Table 3.6: Glacier area change studies performed on the main Himalayan arc and their findings (Map Ref. refers to figure 3.12).**

| Author | Map Ref. | Location | Data used and spatial resolution/scale | Horizontal error | No./Size of glaciers studied | Glacier Area change (%) |
|---|---|---|---|---|---|---|
| Kulkarni & Alex (2003) | 1 | Baspa basin, India | SOI topographic map - 1:50,000<br>IRS LISS-111- 23.5m<br>IRS PAN- 5.8m | N/A | 19 | 1962-2001 - 19% |
| Kulkarni *et al* (2007) | 2 | Chenab, Parbati and Baspa basins, India | SOI topographic map - 1:50,000<br>IRS LISS-III - 23.5m<br>IRS LISS-IV - 5m<br>Landsat TM - 30m | N/A | 466 | 1962-2001 - 21%<br>Large glaciers - 12%<br>Small glaciers - 38% |
| Bolch *et al* (2008) | 3 | Khumbu Himal, Nepal | Corona KH4 - 8m<br>ASTER - 15m | ~24m | 4 | 1962-2005 - 5.3% ±2% |
| Shrestha & Joshi (2009) | 4 | Khumbu and Langtang region, Nepal | Landsat MSS - 57m<br>Landsat ETM+ - 30m | N/A | Langtang - 230km$^2$<br>Khumbu - 583km$^2$ | 1976-2000<br>Langtang - 28%<br>Khumbu - 4.83% |
| Bhambri *et al* (2011) | 5 | Garhwal Himalaya | Corona KH4A - 8m<br>ASTER - 15m | ~12m | 86 | 1968-2006 - 4.6% ±2.8% |
| Schimdt & Nüsser (2012) | 6 | Kang Yatze Massif, Ladakh, India | Corona KH4A - 8m<br>SPOT-5 - 2.5m<br>Landsat TM - 30m | ~30m | 121 | 1969-2010 - 14% |

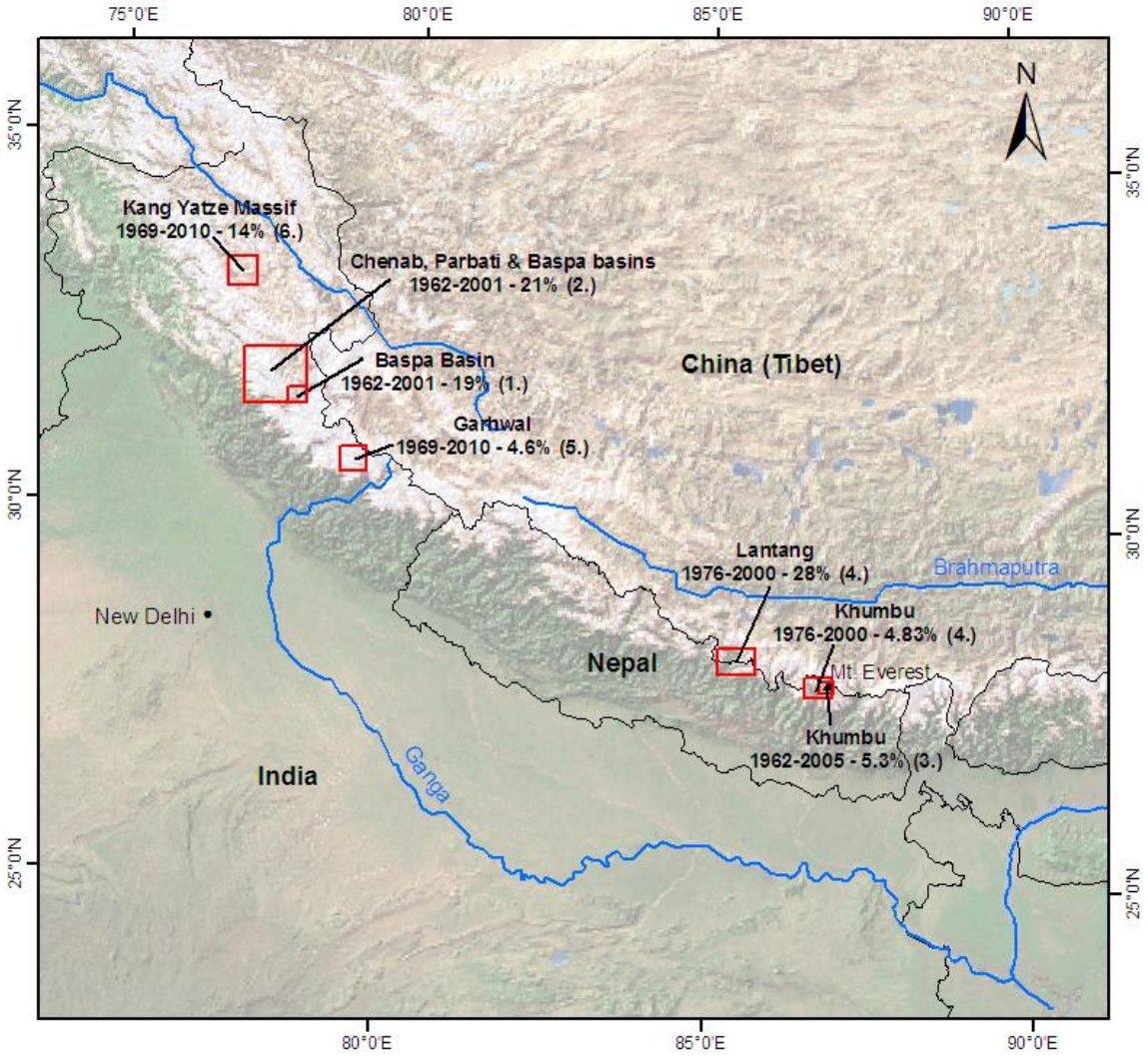


**Figure 3.12: Spatial distribution of area change studies conducted on the main Himalayan arc and their findings. Reference numbers (in brackets) refer to table 3.6.**

**Table 3.7: Glacier volume change studies performed on the main Himalayan arc and their findings (Map Ref. refers to figure 3.13).**

| Author | Map Ref. | Location | DEM source | Vertical accuracy | Volume/elevation change | Volume/elevation change accuracy |
|---|---|---|---|---|---|---|
| Bahuguna *et al* (2007) | 1 | Garhwal Himalaya | Topographic map IRS 1C & 1D Pan | IRS 1C & 1D Pan - ±15m | 15-150m surface lowering of the Gangotri snout from 1962-2000 | ±15m |
| Berthier *et al* (2007) | 2 | Spiti/Lahaul region Himachal Pradesh (India) | SRTM, SPOT 5 | SRTM - ±18m<br>SPOT 5 - ±25m | Overall specific mass balance of -0.7 to -0.85 m/a w.e. for 915 $km^2$ of glaciers (1999-2004) | ±0.05 m/a |
| Bolch *et al* (2008) | 3 | Khumbu Himalayas | ASTER, Corona KH4 | ASTER - ±30M<br>Corona KH4 - ±56m | Studied 5 debris-covered tongues. Found average surface lowering of -13.3m and volume loss of 192.1 x $10^6m^3$ from 1962-2005. | Surface lowering - ±9.6m<br>Volume loss - ±138.7 x$10^6m^3$ |
| Bolch *et al* (2010) | 4 | Mt. Everest region, Nepal | Corona, Aerial photo's, ASTER, Cartosat-1 | Corona 1962 KH4 - ±19.8m<br>Corona 1970 KH4B - ±18.8m<br>Aerial DEM - ±10.1m<br>ASTER - ±10.1 Cartosat 1 - ± 19.2m (compared to SRTM) | Studied 12 glaciers:<br>1970-2007 - Av. Surface lowering -13.3m, Specific mass balance -0.32m/a w.e. 2002-2007 - Av. Surface lowering -4.4m, Specific mass balance -0.79m/a w.e. | 1970-2007 - Av. Surface lowering ±2.5m, Specific mass balance ±0.08m/a w.e. 2002-2007 - Av. Surface lowering ±2.6m, Specific mass balance ±0.42m/a w.e. |
| Nuimura *et al* (2012) | 5 | Khumbu region, Nepal | DGPS, Topo-map, SRTM, ASTER | DGPS - ±17m<br>Topo-map - ±14m<br>SRTM - ±10.8M<br>ASTER - ~±13m | Studied 10 glaciers:<br>1992-2008 - Av. Surface lowering -0.47m/a, Specific mass balance -0.26m/a w.e.<br>2000-2008 - Specific mass balance -0.45m/a w.e. | 1992-2008 - Av. Surface lowering ±0.27m/a, Specific mass balance ±0.24<br>2000-2008 - Specific mass balance ±0.27m/a w.e. |

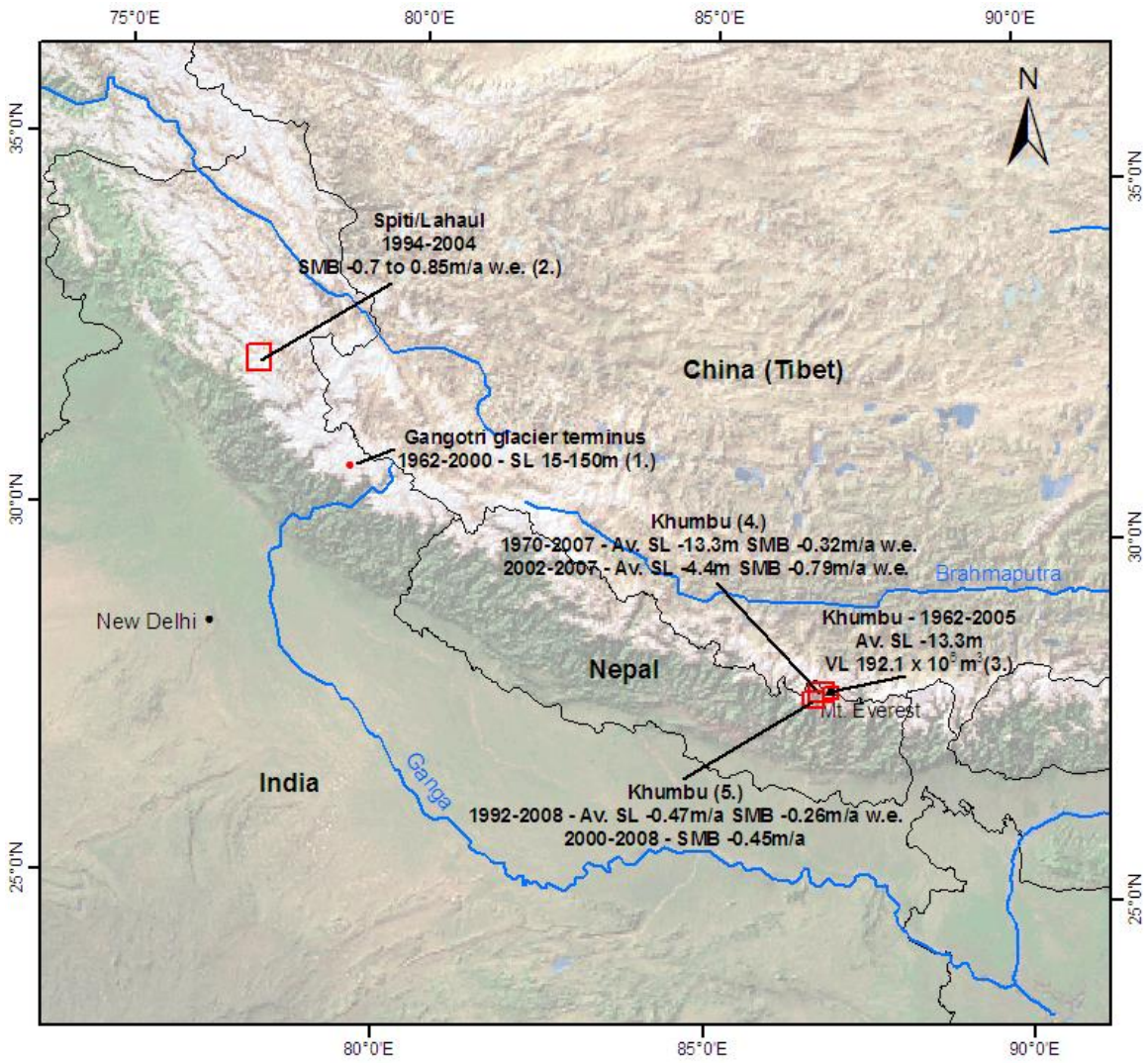


**Figure 3.13: Spatial distribution of volume change studies conducted on the main Himalayan arc and their findings. Reference numbers (in brackets) refer to table 3.7.**

volume changes in the Himalayas, including only around 100 glaciers. Of these five volume change studies, three are centred on the Khumbu region of Nepal (see Figure 3.13).

Due to the limited sample, determining the spatial pattern of glacier volume change across the Himalayas is again difficult. Looking at volume measurements from east to west, there is some suggestion of spatial variability in glacier volume change. For example, Nuimura *et al.* (2012) estimated specific mass balances of -0.26 m $a^{-1}$ w.e. from 1992-2008 for glaciers in the Khumbu region (eastern Himalayas), whilst Berthier *et al.* (2007) estimated specific mass balances of 0.7-0.85 m $a^{-1}$ w.e. for glaciers in the Spiti region (western Himalayas). However, these two studies are difficult to compare,

as the sample number, size and topography of the glaciers studied differs considerably. In terms of temporal patterns, for the Khumbu region there is some suggestion that the rate of volume loss may have increased during the 2000s, as demonstrated by Bolch *et al.* (2010) and Nuimura *et al.* (2012) (see Table 3.17). However, again this is only for one small region of the Himalayas.

Of all the geometric glacier changes monitored in the Himalayas, length is the most represented spatially. A recent study by Scherler *et al.* (2011), for example, studied length changes for 269 glaciers spread over several locations from Sikkim (eastern Himalayas) to the Hindu Kush (western Himalayas) (see Figure 3.14). Although still a relatively small sample, the spatial distribution of the glaciers included in this study is such that an overall length change trend across the Himalayan arc over the 8-year study can be assessed. Analysis of the findings of Scherler *et al.* (2011) (summarised in Table 3.8 and Figure 3.14) reveals that glacier length reduction on the south side of the Himalayan ridge is larger in the western regions than the central and eastern regions. Again, this suggests that glacier sensitivity to recent climatic changes in the eastern regions is heightened compared to more westerly regions. However, this increased rate of glacier length reduction in westerly regions does not continue through to the Karakorum and Hindu Kush regions where many glaciers have recently undergone areal expansions (e.g. Hewitt, 2005).

**Table 3.8: Summary of the length change measurements made by Scherler *et al.* (2011).**

| Location | Time scale | No. of glaciers | Av. glacier size ($km^2$) | Av. mean annual frontal change (m/a) | Uncertainty |
|---|---|---|---|---|---|
| Hindu Kush | 2000-2008 | 19 | 22.5 | -5.83 | ~10m/a |
| Karakorum | | 42 | 73.6 | -2.92 | |
| Western Himalaya | | 64 | 17.9 | -11.95 | |
| Central Himalaya (North facing) | | 72 | 13.4 | -12.56 | |
| Central Himalaya (South facing) | | 72 | 16.8 | -8.91 | |

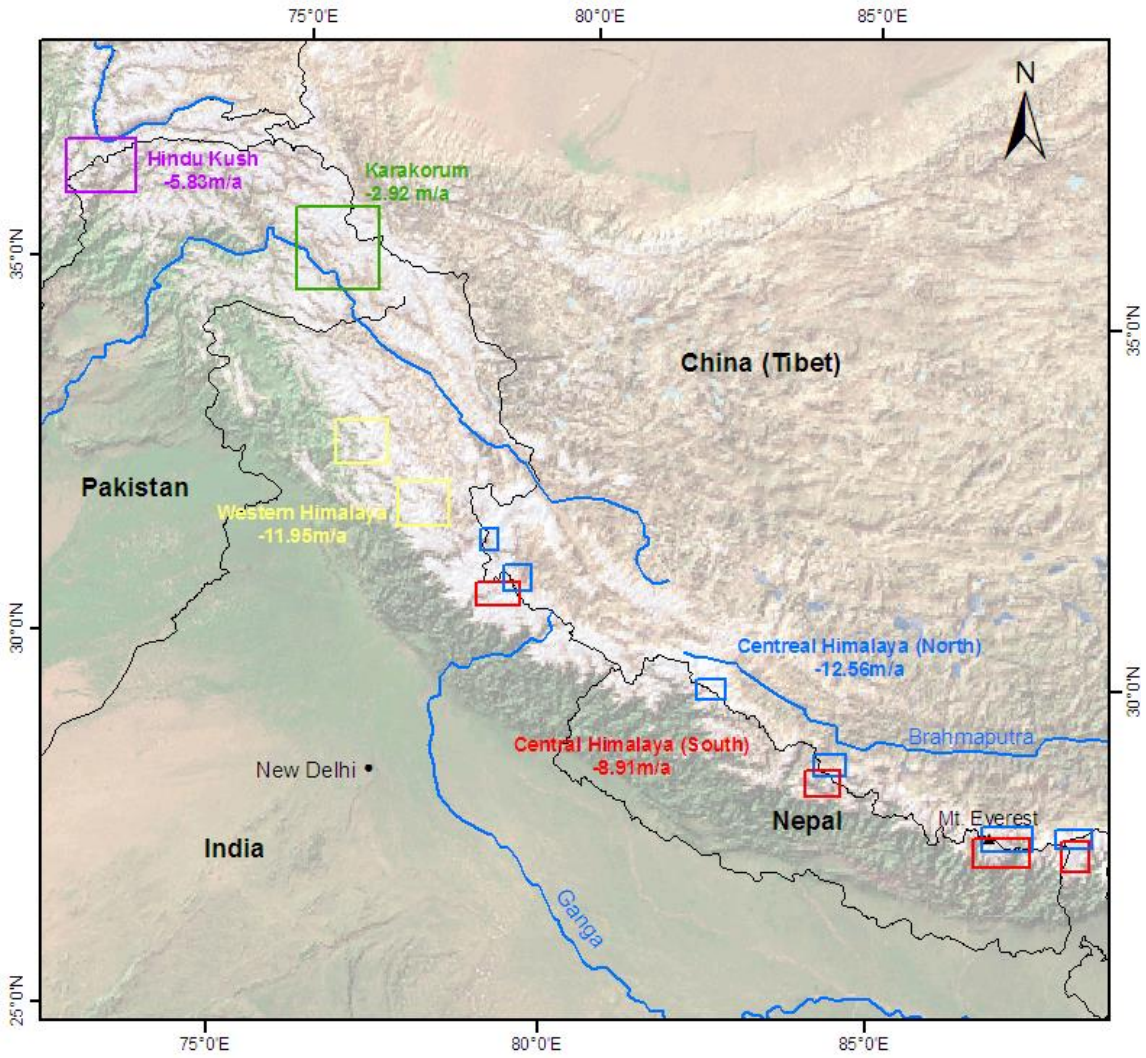


**Figure 3.14: Spatial distribution of glacierised sites used by Scherler *et al.* (2011) to monitor the rate of frontal recession of 269 glaciers, from 2000-2008.**

## 3.7 Summary and glaciological objectives

Himalayan glaciers represent an important water resource for a downstream population of over 500 million people and are currently contributing to ongoing global sea level rise. Despite their importance, Himalayan glacier area, length and volume reductions, initiated by climate changes since the end of the LIA, are yet to be fully understood. Glacier monitoring efforts aimed at improving the understandings of Himalayan glacier change are currently both spatially and temporally limited. In this regard, glacier volume change information is particularly lacking. These Himalayan glacier monitoring limitations have been partly brought about because of: (1) the unavailability of historic topographic maps and aerial photography for many areas of the Himalayas; and (2) the unavailability of high resolution imagery and DEMs from

satellite platforms pre-1972 and pre-1989, respectively. In practice, Himalayan glacier mapping from satellite imagery, specifically, is also hindered by the existence of debris on the surface of many glaciers which masks ice boundaries. GLIMs glacier outlines available for areas of Nepal dated from the 1960/70s and 1960s Corona stereo imagery now represent new glacier mapping tools which could potentially help reduce temporal and spatial Himalayan glacier monitoring limitations and improve the understanding of Himalayan glacier change over the past 40-50 years.

The glaciological aims of the project are to:

- Utilise historic GLIMS glacier outlines in comparison with those manually delineated from more contemporary ASTER satellite imagery to quantify glacier area and length change between the 1960/70s and 2000s in the LT and SB study sites, Nepalese Himalaya.
- Utilise glacier outlines manually delineated from 1960s Corona imagery in comparison with those manually delineated from more contemporary ASTER satellite imagery to quantify glacier area and length change between the 1960s and 2000s in the LT and SB study sites, Indian Himalaya.
- Quantify geodetic volume change for selected glaciers in the GC and ND study sites, Indian Himalaya, through comparing 1960s Corona DEMs with the ASTER GDEM compiled in the 2000s.
- Utilise the ASTER GDEM to analyse the hypsometry of ice area change at the GC, ND, SB and LT study sites between the 1960s and 2000s
- Test the accuracy of the manual glacier outline delineation approach for selected debris-covered Himalayan glaciers.
- Qualitatively assess the accuracy of the GLIMS glacier outlines used with reference to ortho-ASTER imagery and the manually derived glacier outlines utilised at the SB and LT study sites.

## 4. Satellite data & GLIMS glacier outlines

This chapter outlines the Corona, ASTER and GLIMS glacier outline geospatial data used in this study in order to fulfil the aims set out in chapter 1.

### 4.1. Corona data

A description of the Corona sensor is given in chapter 2. For this project, 14 digital Corona image strips, pre-scanned directly from filmstrips at 7 $\mu$m, were purchased from the USGS's Earthexplorer web-interface (http://earthexplorer.usgs.gov), 6 for the ND site and 8 for the GC site (see Table 4.1). Prior to purchasing, each image strip is cut into four sub-sets (a, b, c, d) by the USGS. In total, this project used 21 sub-sets, 11 For camera sub-sets and 10 Aft camera subsets (10 stereo pairs).

**Table 4.1: Corona image strips used for the GC and ND study sites. Image ID: df – 'For' camera strip; da – 'Aft' camera strip; ### - image strip number ID; a, b, c, d: Camera strip sub-set.**

| Study site | For image ID | Aft image ID | No. of image strips | Year |
|---|---|---|---|---|
| Gangotri-Chaukhamba | df106d | da106a | 8 | 24/09/1965 |
| | df107c | da107a | | |
| | df107d | da108a | | |
| | df108d | da109a | | |
| | df109d | | | |
| Nanda Devi | df110b | da110b | 6 | 27/09/1968 |
| | df110c | da110c | | |
| | df111b | da111b | | |
| | df111c | da111c | | |
| | df112b | da112b | | |
| | df112c | da112c | | |

### 4.2. ASTER satellite imagery

ASTER is an imaging sensor that was launched on board NASA's Terra satellite in December, 1999. ASTER collects data in 14 spectral channels, ranging in spatial resolution from 15 m in the VNIR to 30 m in the SWIR, and 90 m in the TIR. Sensor characteristics are summarised in table 4.2.

The relatively low resolution in VNIR makes ASTER of particular use for, amongst

**Table 4.2: ASTER satellite sensor characteristics.**

| | |
|---|---|
| Satellite | TERRA |
| Sensor | ASTER |
| Temporal availability | 1999-present |
| Temporal resolution (days | 16 |
| Image size (km x km) | 60 x 60 |
| Swath width (km) | 60 |
| Cost per full scene (USD)* | 60 |
| Cost per $km^2$ (USD)* | 0.02 |

***free of charge for GLIMS affiliates**

other things, a number of land-cover change applications including the monitoring of glacier parameters (e.g. Paul & Svoboda, 2009; Bhambri *et al.*, 2011; Gjermundsen *et al.*, 2011). The use of ASTER data for such applications is aided by the low cost of the imagery ($60 per scene). Affiliates of the GLIMS project (such as the author) are able to acquire imagery of glacierised regions free of charge (Racoviteanu *et al.*, 2008). The level 3 processed ortho-ASTER imagery utilised in this study was downloaded from NASA's Reverb web-interface (http://reverb.echo.nasa.gov/reverb/), projected in the UTM coordinate system, WGS84 datum (Grid 44 South), and are listed in table 4.3. The horizontal accuracy of this product is estimated to be ~±50 m (Iwasaki, 2005; Fujisada, 2005).

In addition to multispectral imagery, the ASTER sensor also provides stereo coverage through the use of a backward pointing telescope that acquires imagery in channel 3 (3B). Tilted 27.6° from the nadir telescope (3N), the backward pointing telescope acquires an along-track nadir-matching image approximately 60 seconds after a given nadir image (Figure 4.1). The resulting image stereo pair can then be used to generate DEMs.

**Table 4.3: ASTER scenes used for each of the study sites.**

| Study Site | Scene ID | Date |
|---|---|---|
| Gangotri-Chaukhamba | AST14DMO_0030902001054213_20111028032432_27334 | 09/09/2001 |
| NandaDevi | AST14DMO_00303182004052957_20120116204909_14717 | 18/04/2004 |
| Setibeni | AST14DMO_00310052003051133_20111219051537_18869 | 05/10/2003 |
| | AST14DMO_00310052003051125_20111206062303_27073 | 05/10/2003 |
| | AST14DMO_00304212004051735_20111206062303_27076 | 21/04/2004 |
| | AST14DMO_00302102004051215_20111206062303_27061 | 10/02/2004 |
| | AST14DMO_00312262007051748_20111206062303_27068 | 26/12/2007 |
| Langtang | AST14DMO_00310282000052506_20111121032958_19655 | 28/10/2000 |
| | AST14DMO_00310242001051047_20111130122216_15918 | 24/10/2001 |
| | AST14DMO_00310302003050529_20111121032958_19669 | 30/10/2003 |

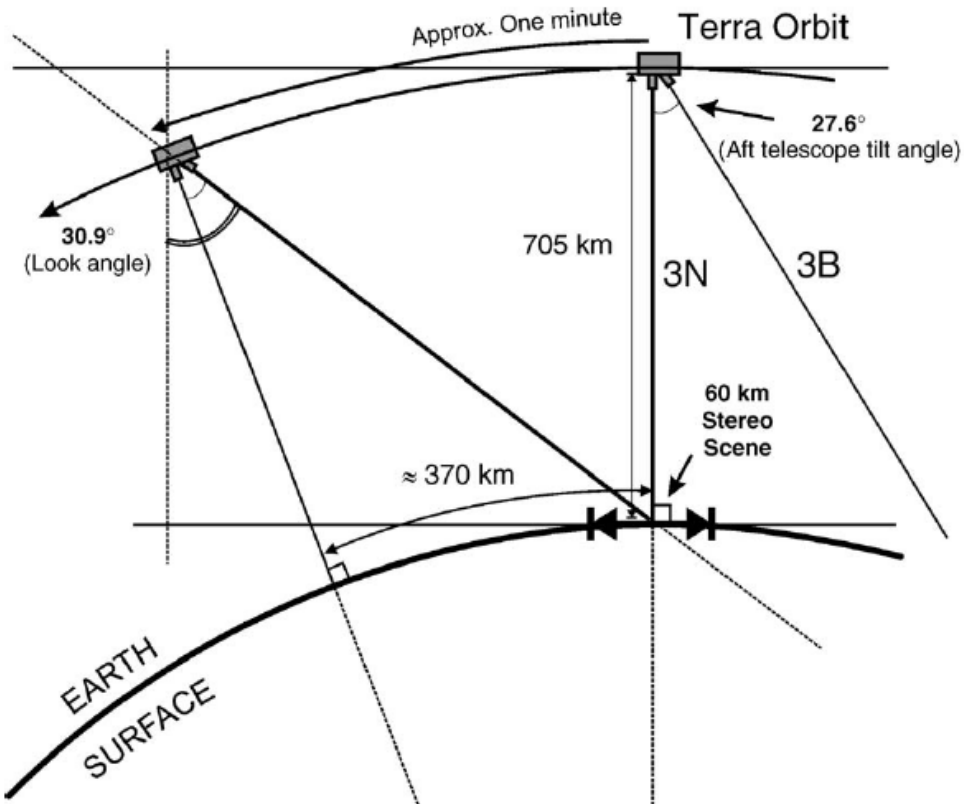


**Figure 4.1: Imaging geometry for ASTER along-track stereo (taken from Hirano *et al.*, 2003).**

## 4.3. ASTER GDEM data

In 2009, NASA and METI of Japan released the first version of the ASTER GDEM to users worldwide at no charge, as a contribution to the Global Earth Observing System of Systems. Offering an alternative to the 90 m resolution SRTM DEM product, the ASTER GDEM consists of 22,600 30m resolution tiles, covering land surfaces between 83°N and 83°S latitude (METI/NASA/USGS, 2011).

The ASTER GDEM version 1 was produced through the automated processing of over 1.2 million ASTER stereo pairs collected globally from 2000 to 2008. The creation of an individual ASTER GDEM tile involved seven levels of processing: (1) production of 1,264,118 individual ASTER scene-based DEMs; (2) removal of cloud obscured pixels; (3) stacking of all cloud-screened DEMs; (4) Removal of residuals/outliers; (5) Averaging of stacked pixels; (6) Replacement of remaining residuals with elevations from other DEMs (e.g. SRTM); and (7) Partitioning in to 1° -by- 1° tiles.

In 2011, the ASTER GDEM was improved with the release of version 2 (v2). ASTER GDEM v2 included the compilation of additional ASTER stereo scenes collected from 2008 to 2010. Additionally, improved masking, merging and correlation techniques were introduced to reduce elevation artefacts. Subsequently, a 5 m overall bias observed in GDEM v1 was removed and the overall accuracy was improved from ~20m vertically and 120 m horizontally to ~±17 m and ±75 m, respectively (Tachikawa *et al.*, 2011). The ASTER GDEM v2 tiles acquired for this project were downloaded from NASA's Reverb web-interface, projected in the geographic coordinate system WGS 1984, and are listed in table 4.4.

**Table 4.4: ASTER GDEM tiles used for each study site.**

| Study Site | ASTER GDEM tile |
|---|---|
| Gangotri-Chaukhamba | ASTGTM2_N31E079 |
| | ASTGTM2_N31E078 |
| | ASTGTM2_N30E079 |
| | ASTGTM2_N30E078 |
| Nanda Devi | ASTGTM2_N30E080 |
| | ASTGTM2_N30E079 |
| Setibeni | ASTGTM2_N29E084 |
| | ASTGTM2_N29E083 |
| | ASTGTM2_N28E084 |
| | ASTGTM2_N28E083 |
| Langtang | ASTGTM2_N28E085 |
| | ASTGTM2_N28E084 |

## 4.4. GLIMS glacier outlines

Launched in 1995, in close co-operation with the US NSIDC and the WGMS, the GLIMS project aims to generate a global snapshot of digital glacier extent and change

information with the use of satellite data (Raup *et al.*, 2007; Racoviteanu *et al.*, 2009). Bringing together the resources of universities and research institutes from 27 countries, the main product of the GLIMS project is the GLIMS glacier database which is freely available through a map-based website interface accessible at http://www.glims.org.

The GLIMS database contains vectorized glacier outlines and information on individual glacier parameters such as glacier area, length, centrelines, snow lines, elevation, hypsometry and, where possible, ice volume. As of July 2012, the GLIMS database contained outlines from approximately 96,727 glacier entities, covering an area of over 260,000 $km^2$ (GLIMS, 2011). Despite this, there still remains a significant gap within the GLIMS inventory for glacierised areas of the Indian and Pakistan Himalayas, Canadian Cordillera, South America, the Canadian Arctic and Alaska. These five regions account for ~90% of the glaciers still to be inventoried worldwide (Ohmura, 2009). The characteristics of the glacier outlines extracted from the GLIMS database for use within this project are listed in table 4.5.

**Table 4.5: Characteristics of the glacier outlines extracted from the GLIMS database for use within this project.**

| Study site | Date | No. Glaciers | Measurement source | Total glaciers |
|---|---|---|---|---|
| Setibeni | 1959 | 1 | Topographic maps and aerial photography | 238 |
| | 1963 | 44 | | |
| | 1967 | 62 | | |
| | 1970 | 2 | | |
| | 1974 | 36 | | |
| | 1975 | 93 | | |
| Langtang | 1965 | 25 | Topographic maps and aerial photography | 274 |
| | 1966 | 16 | | |
| | 1974 | 226 | | |
| | 1975 | 5 | | |
| | 1978 | 2 | | |

## 5. Processing satellite imagery for quantification of glacier change

This chapter aims to describe the procedures undertaken to enable glacier area, length and volume changes to be quantified with the use of Corona and ASTER data. These procedures have been set out schematically in figure 5.1 and the chapter follows the workflow structure shown. Additionally, this chapter also describes the integration process of the GLIMS glacier outlines used at the SB and LT study sites.

Section 5.3, in particular, is central to this chapter and the study as a whole, describing the novel methodological approach developed and implemented to orthorectify Corona imagery and extract DEMs in accordance with the aims set out in chapter 1.

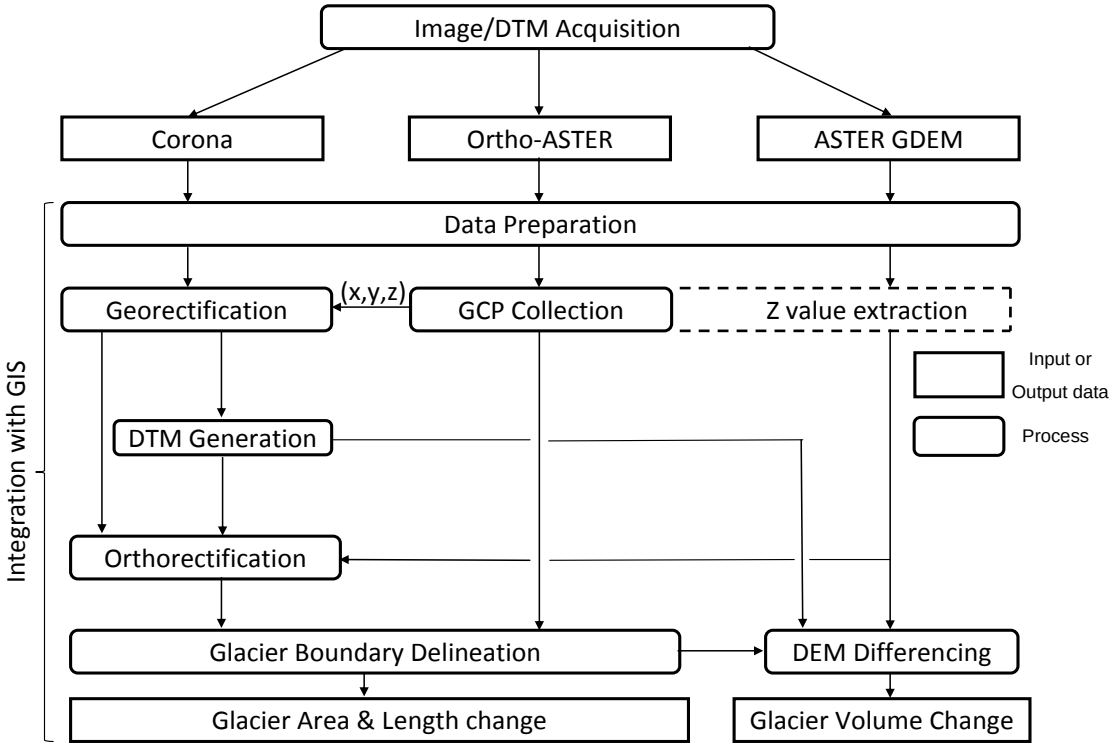


**Figure 5.1: Schematic workflow for calculating glacier area, length and volume change from satellite data.**

## 5.1. Image and DEM acquisition

Referring to the ability to clearly identify ground features, image quality was the main acquisition consideration when selecting Corona and ASTER imagery for this study. Factors affecting image quality for glacier mapping studies include: (1) cloud cover and haze; (2) topographic shadowing; and (3) snow cover. Importantly, each of these image quality factors can also induce errors onto satellite-derived DEMs by inhibiting tie point and GCP sampling, and the image matching process. In regards to the ortho-ASTER imagery used, for example, which were automatically orthorectified by their inherent DEMs, the presence of cloud-cover, topographic shadowing or extensive snow cover often resulted in the presence of large geometric image skews visible in figure 5.2. Overall, the presence of cloud and snow cover within imagery acquired for the Himalayas played a significant role in the elimination of many possible study sites for this project.


**Figure 5.2: The effect of cloud-cover on the geo-location of ground features in an ortho-ASTER image of a portion of the Uttarakhand Himalayas, India captured on 11th September 2001 (a.), relative to those in a cloud-free orth-ASTER image of the same area captured on 13th October 2001. A horizontal shift of ~300 m is visible in the main tributary trunk of the central glacier.**

## 5.2. Data preparation

The preparation procedures undertaken for each dataset used in this study are set out schematically in figure 5.3 (this being an expansion of the data preparation step in Figure 5.1). Preparation of the Corona dataset involved the clipping of image subsets from each of the image strips used. This image subsetting procedure was undertaken to remove areas of distortion commonly found towards the edges of Corona imagery (caused by the panoramic camera setup) (McDonald, 1997). Removal of these areas helps to improve orthorecitification and DEM extraction procedures by excluding potential sources of error. Here, this subsetting procedure was performed using the 'Subset' tool available in ERDAS Imagine.

For the ortho-ASTER images used in this study, preparation was aimed at improving functionality during later pre-processing and processing stages. Preparation included: (1) creation of false-colour composites through the combination of VNIR bands to aid glacier identification; and (2) mosaicking of neighbouring image scenes to aid the GCP and tie point collection process. Both these tasks were completed using the 'Layer stacking' and 'Mosaic Pro' tools available in ERDAS Imagine.

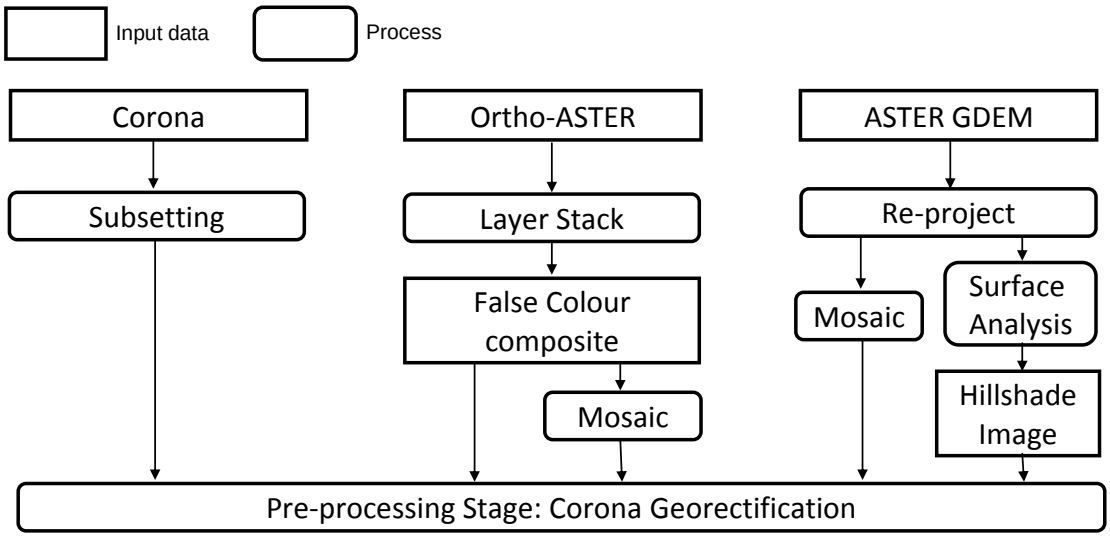


**Figure 5.3: Schematic workflow of the data preparation stage for each dataset prior to pre-processing.**

Preparation of the ASTER GDEM v2 tiles utilised involved transforming the datasets projection from the geographic coordinate system WGS 1984 to the UTM projected coordinate system (Grid 44 South, WGS 1984 datum), the latter being the base projection for all geospatial datasets used in this study. This transformation procedure was performed using the 'Re-project' tool available in ArcGIS. In addition to the projection transformations, hillshade images were also created for each ASTER GDEM tile using the 'Hillshade' tool available in ArcGIS. Hillshading tools work by adding a shading effect onto the surface of a DEM, assuming a pre-set illumination angle, highlighting mountain ridges and valley bottoms (Figure 5.4). This shading creates a 3-D effect without changing the 2-D perspective, aiding glacier mapping procedures (Figure 5.4).

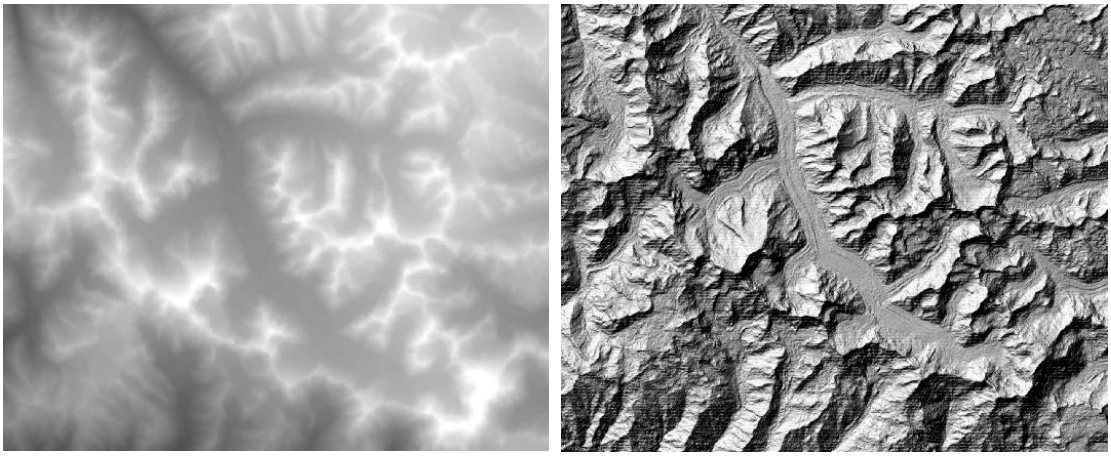

**Figure 5.4: ASTER GDEM tiles are initially symbolised by a matrix of brightness values (corresponding to the elevation value of each pixel and the overall elevation range) which make it difficult to distinguish terrain details (left image). By adding a hillshade effect, terrain variations are highlighted creating a faux 3-D perspective.**

## 5.3. Pre-processing

The pre-processing section was central to the study as whole and describes the methods implemented in order to orthorectify Corona imagery and extract Corona DEMs, using an empirically-based photogrammetry non-metric camera frame model and ASTER horizontal and vertical reference data. This process can be roughly divided into three stages: (1) Corona image georectification; (2) Corona image

orthorectification; and (3) DEM extraction from Corona image stereo pairs. The following three sections detail these stages accordingly.

### 5.3.1. Georectification of Corona imagery using a non-metric camera frame model

Georectification, or geometric correction, is the process of transforming raw satellite imagery so that it has the scale and projection properties of a map (Mather, 1999). A map is defined as '…a graphic representation on a plane surface of the Earth's surface or part of it, showing its geographical features. These are positioned according to pre-established geodetic control, grids, projections and scales' (Steigler, 1978). However, unlike orthorectification, georectification does not correct image distortion errors induced by topographic relief.

All remotely sensed images in their raw state contain large geometric errors which must be either eliminated or minimised during the georectification process, for them to fit a given map projection. Sources of geometric error in satellite imagery can broadly be described as systematic (caused by the acquisition system) and un-systematic (related to the area of observation) (see Toutin, 2004). Such errors present themselves un-equally within imagery as geometric distortions. Corona imagery, in particular, contains large distortions specific to the panoramic camera system used (see chapter 2).

The Corona images used in this project, which initially lacked any spatial reference information, were georectified and then orthorectified using a photogrammetric non-metric camera frame model available in the ERDAS Imagine LPS software package. As with all photogrammetric approaches, the relationship between the camera/sensor used to capture an image, the image itself, and the ground need to be defined using: (1) exterior orientation image parameters for an image; (2) interior orientation for image parameters; and (3) a projected coordinate system (obtained through the collection of GCPs). Here, GCPs were collected from ortho-ASTER images and therefore the WGS 1984 UTM projected coordinate system was used as the reference projection. Calculation of interior orientation parameters allows for the

initial pixel coordinate system (represented simply by an array of column and row values) of an image to be transformed in relation to the internal geometry of a camera or sensor (represented by image space x, y, and z coordinates). Sensor variables estimated during this process include focal length, principle point, fiducial marks and lens pattern distortion.

In comparison, exterior orientation image parameters include sensor angle data (camera axis at the time of exposure, defined in terms of the angles of rotation (ώ, ϕ and κ)) and exposure station positional data, in terms of the three-dimensional coordinates of the perspective centre ($X_0$, $Y_0$ and $Z_0$) (Ghosh, 2005). Using GCPs exterior parameters can be mathematical estimated by solving collinearity condition equations. Collinearity conditions generally state that the exposure station, image point and corresponding ground point should lie in one straight line at the instant of exposure (ERDAS, 2010). Once the exterior and interior parameters are known, space forward intersection can be performed to determine the ground coordinates of unknown image points with reference to the GCP map projection used. In addition to x and y coordinates, space forward intersection also determines z values for overlapping stereo-image pairs.

The following sections describe the use of a non-metric camera frame model, available in ERDAS Imagine LPS, to georectify Corona imagery through the estimation of interior and exterior orientation image parameters. Here, the Corona For and Aft imagery acquired for the GC and ND study sites were georectified together as image batches. The GC batch contained 8 images strips, whilst the ND contained 6.

#### 5.3.1.1. Estimating Corona interior orientation image parameters

Interior orientation image parameters were automatically estimated for each Corona image strip contained within a batch using the following input variables: (1) a reference coordinate system – obtained from the ortho-ASTER data; (2) known camera parameters – for Corona imagery only average flying height and focal length are known (609.602 mm and 185,000 km, respectively (NRO, 1967; Dashora *et al.*,

2007)); and (3) camera filmstrip scanning resolution – 7 $\mu$m. These initial interior estimates were later altered by the bundle block adjustment which was used to estimate exterior orientation image parameters.

#### 5.3.1.2. Estimating exterior orientation

Corona exterior orientation image parameters were estimated by the non-metric camera frame model through the use of (1) horizontal GCP coordinates acquired from ortho-ASTER imagery and corresponding vertical coordinates acquired from the ASTER GDEM, (2) image tie points – connecting image features between overlapping image strips within each study site batch, and (3) a bundle block adjustment – which solved the collinearity equations. These factors are described and discussed in the following three sections.

#### 5.3.1.3. GCP sampling

A GCP is defined as an easily recognisable feature than can be located accurately on a 'master' map projected image and corresponding ´slave' image (Mather, 1999). Through registering Corona imagery to the 'master' ASTER datasets the geometric correction process here is not based on an absolute coordinate system. Any geometric error introduced to the Corona imagery during orthorecitifaction will therefore be added on to those already present within the ASTER reference data (see chapter 4). When identifying GCPs from a 'master' and 'slave' image Mather (1999) suggests that three main factors should be considered: (1) The size of the sample needed in relation to the level of accuracy sought, (2) the spatial distribution of the GCPs, and (3) the accuracy with which they are located. In terms of sample size, the non-metric camera frame model used requires at least three full x, y and z GCPs for estimation of exterior orientation parameters of a single image (ERDAS, 2009. In reality, however, to achieve a satisfactory level of accuracy with Corona imagery a greater number of GCPs is needed.

Bolch *et al.* (2008) and Namara *et al.* (2009) conducted similar glacier change studies utilising Corona data from the 1960s. Bolch *et al*. (2008) used a topographic map to collect >100 GCPs for the correction of three Corona strips and achieved a horizontal accuracy of ~±15 m. Namara *et al.* (2009) used a topographic map and Landsat data to collect 50-100 GCPs to correct four Corona strips achieving a horizontal accuracy of <±30 m. In this case, the aim was to achieve a horizontal accuracy of within one pixel of the horizontal reference source (~±15 m) and in total around 50 GCPs were collected for each Corona strip within a batch.

In terms of spatial distribution, it is recommended that GCPs are evenly distributed across a 'slave' image to ensure the accurate estimation of exterior orientation parameters and unbiased correction of image distortions (ERDAS, 2009). Mather (1995) states that GCP distribution should represent a two-dimensional pattern, hence, (1) linear GCP transects and (2) GCP clustering should be avoided. In line with these recommendations, the following six-step GCP sampling strategy was devised in an attempt to limit orthorecitifcation errors:

**1.** Locate GCPs in the top four corners of the first Corona image strip selected in a batch. This in theory helped define the geometric scale of the overall image strip in relation to the reference coordinate system during the bundle block adjustment process.

**2.** Begin to locate GCPs at equal intervals across each edge of the image strip. This helped the bundle block adjustment process to accurately define geometric relationships between 'slave' and 'master' images.

**3.** Fill in the empty central portions of the image strip with GCPs from left to right.

**4.** Load the next 'slave' image in a batch and then repeat the first three steps.

**5.** Once two 'slave' images have been sampled, identify GCPs that are located within areas of image overlap following the same steps – corners, edges and then centres.

**6.** Repeat first 5 steps until all images in a batch, and their respective areas of overlap, have been fully sampled.

The aim of this six-step strategy was to develop a strong geometric network of observations for each study site image batch, providing a template for the

subsequent bundle lock adjustment process. Figure 5.5 depicts an idealised GCP configuration. However, in practice this strategy was often hindered (see Figure 5.6) by a number of issues discussed in chapter 6. To define z values for each GCP point sampled, ERDAS Imagine LPS's 'Update Z values' tool was used to automatically extract elevation values from the reference ASTER GDEM corresponding to the GCP x,y coordinates.

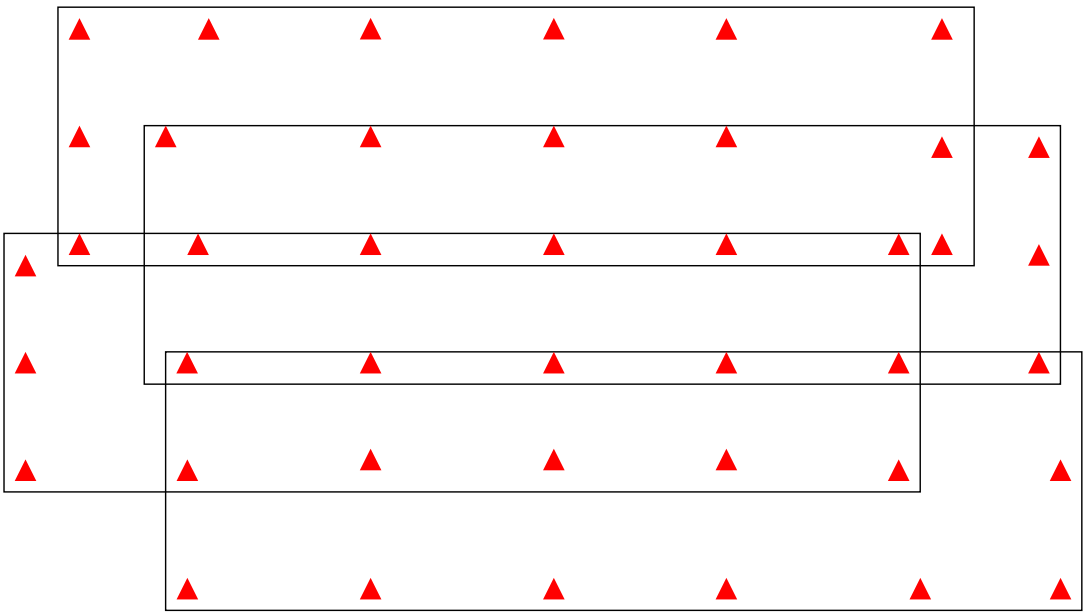

**Figure 5.5: Idealised GCP configuration for a block of four overlapping Corona images.**

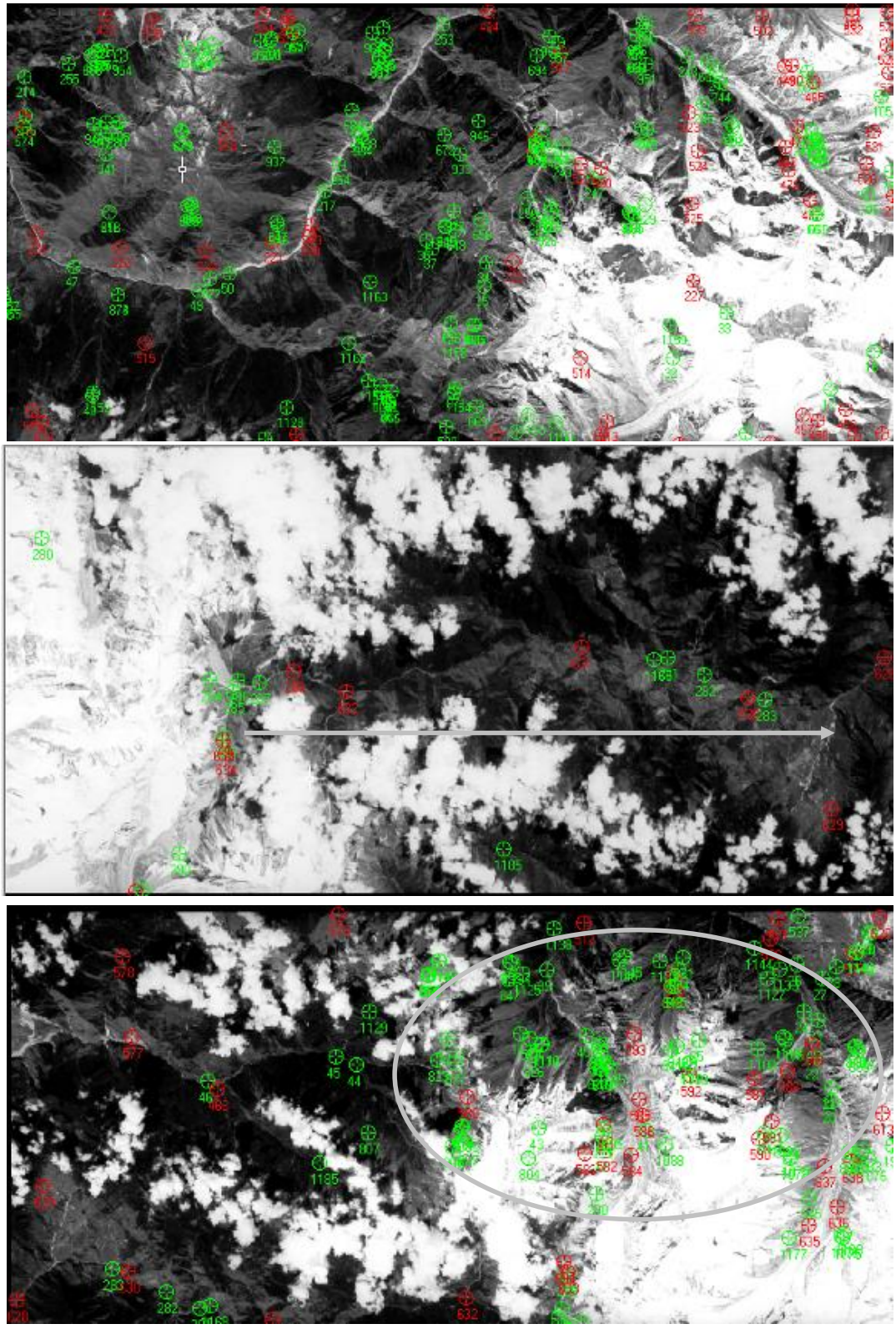

**Figure 5.6: Three examples of the spatial distribution of GCPs (marked green) identified on Corona strips in the Milam block. The top image represents a relatively well distributed sample, the middle image represents a one dimensional GCP transect (labelled with an arrow) and the bottom image is an example of GCP clustering (circled).**

#### 5.3.1.4. Tie point sampling

Tie points connect corresponding feature points between overlapping image strips contained within a batch and are a necessary input for the subsequent bundle block adjustment process (ERDAS, 2009). Typically, at least nine tie points should be identified for each image overlap, in addition to GCPs, in order for exterior parameters to be estimated by the non-metric camera frame model. However, much like GCPs, it is recommended that as many tie points are used as possible to help minimise and better distribute error throughout the network of observations (Khoshelham, 2009; ERDAS, 2009).

The tie point sampling strategy implemented was similar to that utilised for the GCPs, only this time being (1) confined to image overlap areas and (2) within the confines of GCP configurations, in order to improve bundle block adjustment accuracy (ERDAS, 2009). Overall, the comparatively high resolution of the Corona image strips made tie point sampling less challenging than the ASTER-dependant GCP sampling procedure and in total 20-100 tie points were manually selected depending on image overlap size. However, in addition to image quality issues, such as snow/cloud cover and poor image contrast, tie point sampling was often limited by the varying radiometric quality of Corona For and Aft imagery (Figure 5.7).

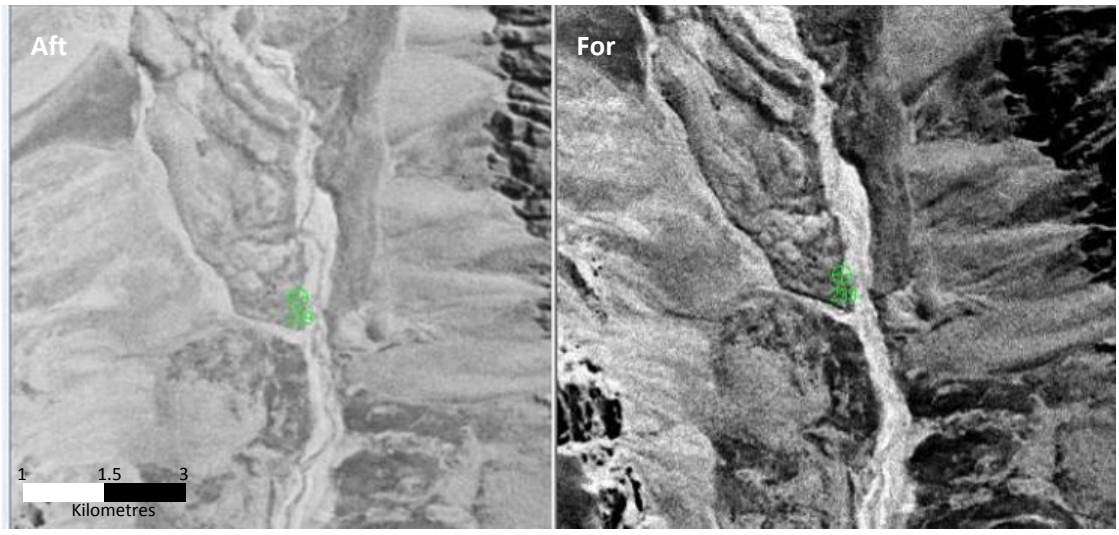


**Figure 5.7: Difference in radiometric contrast between Corona For and Aft image pairs.**

**5.3.1.5. Bundle block adjustment**

Prior to bundle block adjustment, each Corona image contained within a batch included a number of GCPs, whose x, y, and z coordinates were known, and a series of tie points, tying together overlapping image areas. Using these GCP/tie point image points and the previously estimated interior orientation, exterior orientation parameters for each image in a batch were reconstructed using a bundle block adjustment. As summarised by ERDAS (2009), a bundle block adjustment is a mathematical technique that simultaneously computes the following variables for a block of images: (1) the position (x, y, z) and orientation (Omega, Phi, Kappa) of each image as they existed at the time of image capture; (2) the x, y and z coordinates of tie points collected throughout a block, including their accuracy; and (3) the final interior orientation parameters of each image in a block, and their accuracy. Additionally, GCP coordinates are adjusted accordingly and resulting residuals are provided. Any error identified during this process, associated with image distortions and GCP/tie point error, is minimised and effectively distributed across the network of observations.

The workings of the bundle block adjustment are centred on solving collinearity equations. For each GCP measured, two collinearity equations have to be formulated, one for the x ground coordinate and one for the y. This doubles to four if a GCP has been measured on an area of overlap between two images. Similarly, for each tie point measured another four collinearity equations have to be formulated (two for each set of potential coordinates on the overlapping images). A typical Corona stereo pair in this project contained ~30 GCPs and ~80 tie points. Therefore, if a bundle block adjustment was applied solely to one stereo-pair around 440 individual collinearity equations would be formulated, neglecting GCPs located outside the area of overlap.

In addition to the 440 collinearity equations formulated for this hypothetical example, there would be 252 unknown values. These unknowns would include six exterior orientation parameters, for each image in the stereo-pair, and x, y, and z

values for each tie point. In order to estimate the collinearity equation unknowns during a bundle block adjustment, a least squares adjustment approach is utilised. The least squares approach estimates unknown parameters by working through a number of correction iterations (defined by the user) until a solution is found that minimizes the residuals or error associated with the image input data (ERDAS, 2009). Residuals, in this respect, are derived from the difference between the measured (GCPs and tie points) and computed value for any measurement in a block (ERDAS, 2009).

Figure 5.8 depicts the bundle block adjustment process, with collinearity establishing the relationship between the camera/sensor, two stereo images and the ground. GCP and tie point coordinates are altered and estimated, respectively, according to where a particular light ray intersects with the image space and in the camera interior and exterior orientation parameters. In terms of estimating unknown z values, the orientation parameters of both images are taken into account (Figure 5.9). In ERDAS Imagine LPS, as with other photogrammetry software, the process of performing a bundle block adjustment is referred to as aerial triangulation.

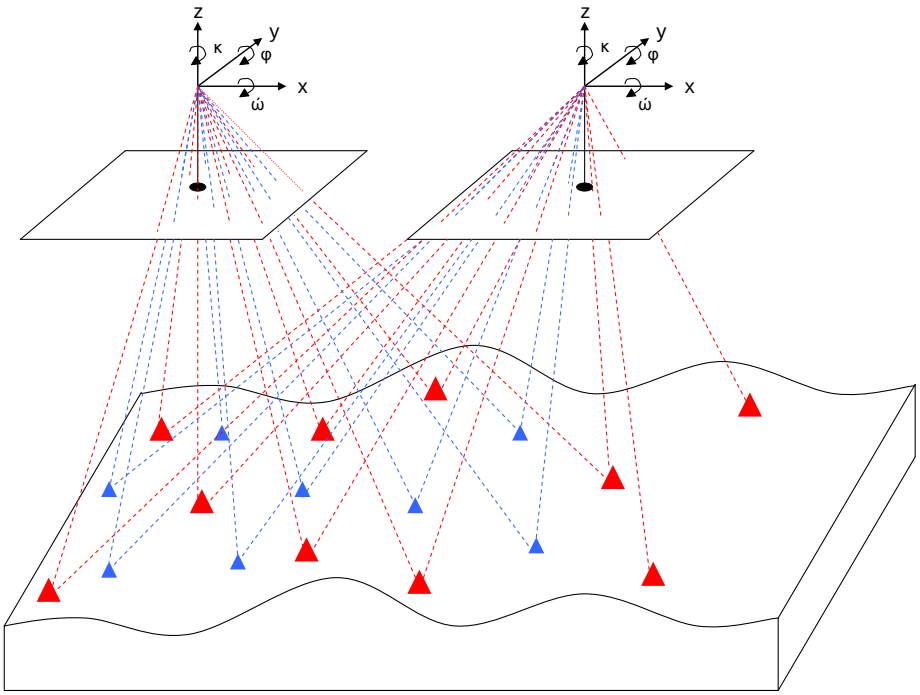


**Figure 5.8: Enforced collinearity between GCPs (red) and tie points (blue) located on an overlapping stereo-pair during a bundle block adjustment.**

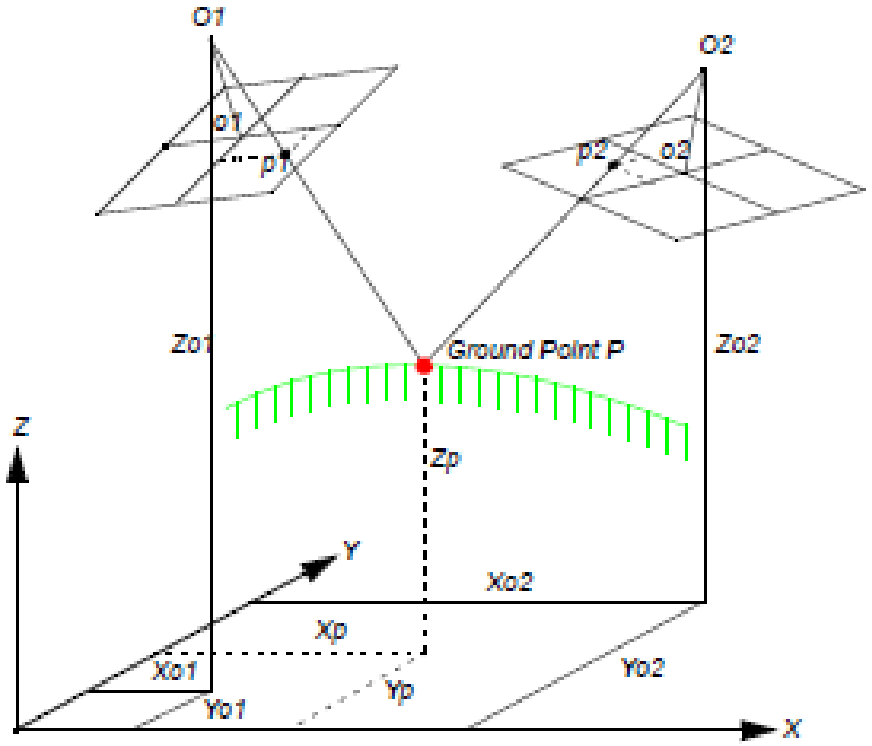


**Figure 5.9: Using the collinearity equations, the exterior orientation parameters (O1 and O2) along with the image coordinates measurements of point p1 on image 1 and point p2 on image 2 are input to compute Xp, Yp, and Zp coordinates of ground point P using the space forward intersection technique (taken from ERDAS, 2009).**

The process of producing an optimised triangulation result involved a repetitive multi-stepped workflow which included two key decision points. The first decision point involved gauging when a triangulation was optimised in relation to its particular set of input points (GCPs and tie points) and triangulation parameters (statistical weights). The second decision point involved analysing the first of the end products (an extracted Corona DEM) and deciding (1) whether it could be improved and (2) what triangulation parameters needed to be altered. Both of these decisions are discussed in more detail later. This workflow is represented in figure 5.10.

Prior to running aerial triangulations, ERDAS Imagine LPS allows the user to tailor the process, according to data quality, by setting a number of statistical parameters. In this case, the accuracy and precision of GCP coordinates was the main data quality issue, due to the image resolution disparity between the Corona and ASTER imagery. A GCP location error of one ortho-ASTER pixel, for example, equates to a possible

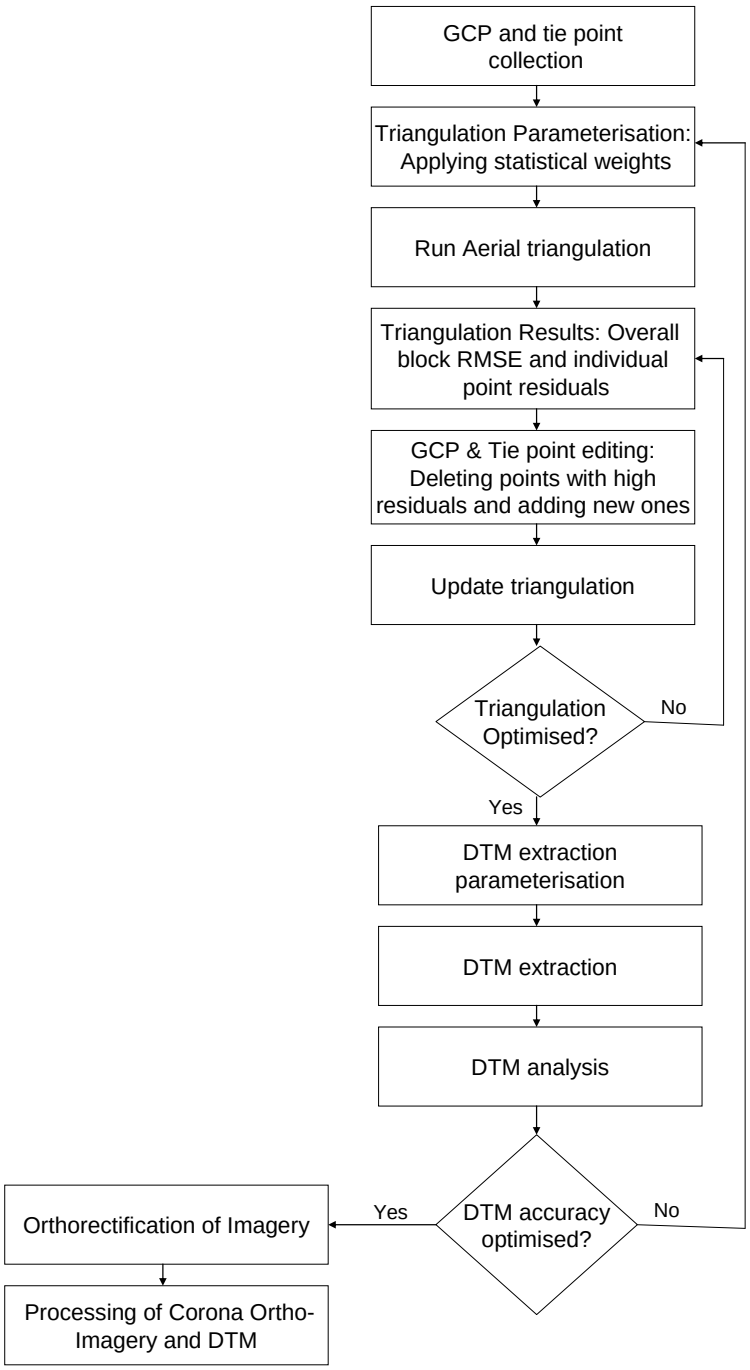


**Figure 5.10: Schematic workflow for optimising the aerial triangulation and the accuracy of output data.**

error of over 8 Corona pixels. To account for this GCP error, as well as others, standard deviation values, referred to as statistical weights, can be pre-set. These weights govern the amount of allowable error which can be attributed and distributed to image (GCP and tie point locations on a given Corona image) and ground points (GCP locations on the 'master' ortho-ASTER image) (Figure 5.11) (ERDAS, 2009). Due to the disparity in the spatial resolutions of the datasets used, the amount of statistical weight applied to image points and 'master' GCP coordinates and the subsequent impact on triangulation results was analysed. ERDAS (2009) recommend that statistical weight values no larger than 1 should be applied to GCP/tie point locations (ERDAS, 2009), these values referring to pixels of the slave Corona image.

The process of altering the statistical weights for image points and 'master' GCPs involved running numerous aerial triangulations, changing respective standard deviation values each time to optimise results. In terms of assigning image point

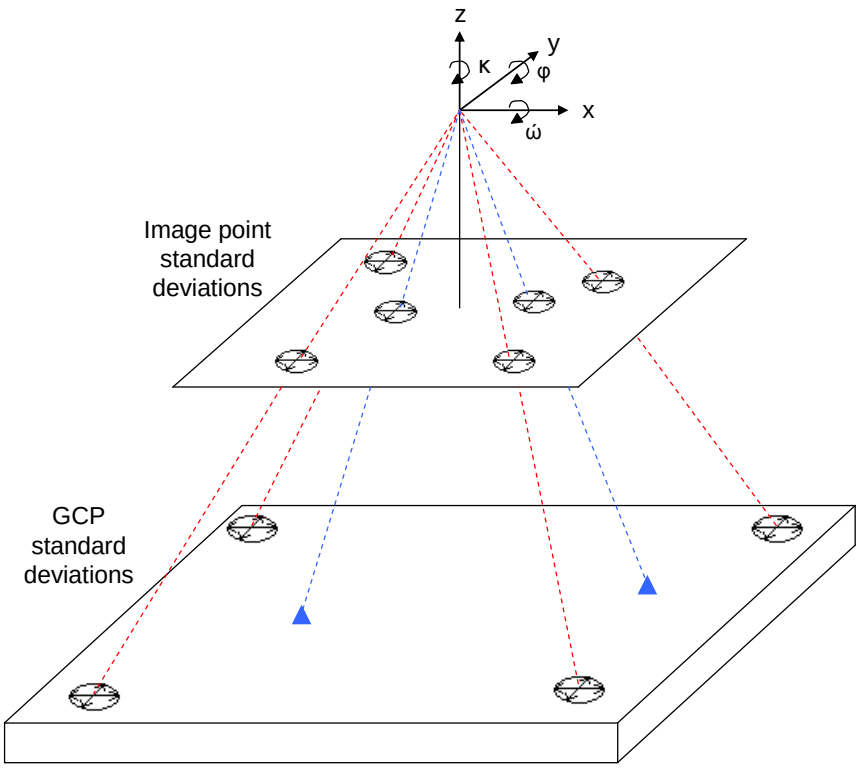


**Figure 5.11: By assigning statistical weights or standard deviations to the image points and GCPs the collinearity equations are given a margin of error in which they can fluctuate in order to be solved.**

weights, standard deviation values were applied equally to both the x and y coordinates. Initially, high standard deviations were tested (1 pixel), in accordance to the data accuracy and precision issues discussed. However, after several triangulations it was found that, irrespective of the GCP weights, any value >0.5 resulted in a highly un-stable triangulation and inaccurate image orientations. Consequently, lower standard deviation values of ~0.3 were tested.

For 'master' GCPs locations, three options are available: (1) fixed x, y, z coordinates, this option is discouraged as any error estimated during the triangulation process will be distributed purely through the exterior orientation parameters, since it is not allowed to propagate throughout the block GCPs (ERDAS, 2009). When applied here, the fixed option resulted in high triangulation RMSE's which could not be reduced. (2) Different x, y, z weighted values. This option initially seemed preferable, allowing the coarser spatial resolution of the ASTER GDEM to be accounted for by applying larger z coordinate weighed values. However, when different x, y, z values were tested, this again resulted in fairly high triangulation RMSEs and subsequently the georectified Corona imagery and extracted Corona DEMs contained errors. (3) Same x, y, z weighted values. The application of uniform x, y, z weighted values generally produced more stable results compared to the previous options. Testing was initially confined to weighted values <1. In the end, triangulation RMSEs were optimised with the use of the same weighted value of 1.

Throughout the data 'optimising' process, depicted in figure 5.10, numerous aerial triangulations were performed, each testing slightly different parameters and input points (GCPs and tie points). Following each triangulation, a summary report was provided listing the following accuracy measures: (1) total RMSE of the solution, describing the standard deviation of all image coordinate residuals and ground coordinate residuals. Image and ground residuals, in this respect, are the differences between the coordinate values of measured points (including GCPs and tie points) and the newly computed coordinate values of the resulting rectified image. Here, all residuals were measured in Corona pixels, with a residual of 1 equalling 1.8 m. (2) The RMSE for all measured ground and image points in the x, y, z and x, y directions,

respectively. (3) Individual x, y, z and x, y residuals for each ground and image point measured, including individual point RMSEs (report).

An important concept to understand prior to analysing a triangulation summary and report is the difference between image coordinate residuals and ground coordinate residuals. Residuals can only be calculated where a computed point can be subtracted from a measured point. Therefore, residuals for GCPs and tie points can be calculated on the newly rectified Corona image in the x and y directions, these being the image coordinate residuals, and for altered reference GCPs in the x, y and z directions, these being the ground coordinate residuals. As tie points were not physically measured on the ground, these are not included in the ground coordinate residual calculations (see Figure 5.12).

The process of analysing and editing the triangulation results focused primarily on reducing the total RMSE. Prior to triangulation, it was decided that the accuracy of Corona triangulation should at least be within one pixel of x and y reference source. This would equate to x, y residuals of ~8.33 and z residuals of ~16.66, assuming a Corona pixel value of 1.8 m. Such residual results would equate to a total RMSE of ~11.1. The editing process began by first deleting any individual image and ground

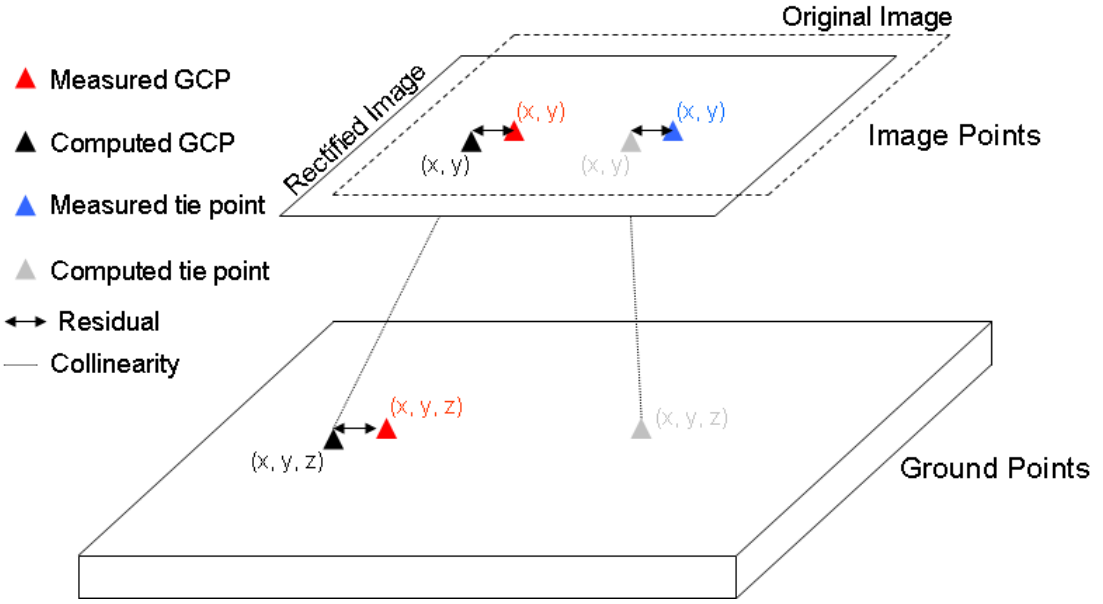


**Figure 5.12: Image and ground coordinate residuals represented within triangulation results.**

points within the triangulation report that exhibited excessively high residuals and RMSEs. Next, points were deleted that exceeded the specified x, y and z accuracy limits. For tie point residuals, the accuracy limit was reduced to 1, in line with the one pixel specification (as these were measured on the Corona images). During the editing procedure it was important to maintain a sufficient sample size and distribution of both GCPs and tie points. If too many GCPs were deleted, the total RMSE would increase, as the reduced point residuals would be offset by increased error in the estimation of interior and exterior orientation parameters. A similar increase in RMSE would also occur if key GCPs were deleted, such as those located in image corners or within image overlap areas. Once a triangulation was optimised for a particular set of input points, accuracy was then analysed in the first of the output products, the extracted Corona DEMs.

### 5.3.2 Corona orthorectification

Once interior and exterior orientation image parameters had been estimated and optimised, each Corona image strip could then be orthorectified. During the bundle block adjustment process described, geometric distortions attributed to the Corona camera/sensor are corrected. Additionally, topographic relief displacement was considered through the use of GCP and tie point x, y and z coordinates, measured from ortho-ASTER imagery and ASTER GDEM. However, these GCP/tie points only represented the initial framework of the orthrectification process, and for the effects of topographic relief displacement to be fully removed from each Corona image strip, a base DEM had to be applied during the final step of resampling of the imagery. Ideally, the Corona DEMs extracted from each study site batch would provide this base. However, due to its complete coverage and standardized accuracy, in this case the ASTER GDEM was utilised as the base DEM.

Ortho-images are created by ERDAS Imagine LPS through a process of resampling. The resampling process involved the creation of new orthorectifed image pixel grids. These grids were derived from each raw Corona image through a transformation calculation that combined both the base DEMs x, y and z information and the bundle

block adjustment results. In this case, the pixel size of the new grids corresponded to the spatial resolution of the original Corona imagery (1.8 m). Once this grid was created, location coordinates of each pixel centre were calculated (x, y) and then inversely transformed into the column and row coordinates of the original raw imagery (c, r). These column and row coordinates then represent the position in the uncorrected raw imagery of the new orthorectified pixel centres. A resampling method is then used to assign an x, y point from the orthorectified grid and a brightness value interpolated from the uncorrected raw image. In this case, resampling was performed using the nearest neighbour method (depicted in figure 5.13), as this method does not alter the brightness values obtained from the raw image. Once resampled, each orthorectified Corona image was projected to the WGS 1984 UTM coordinate system.

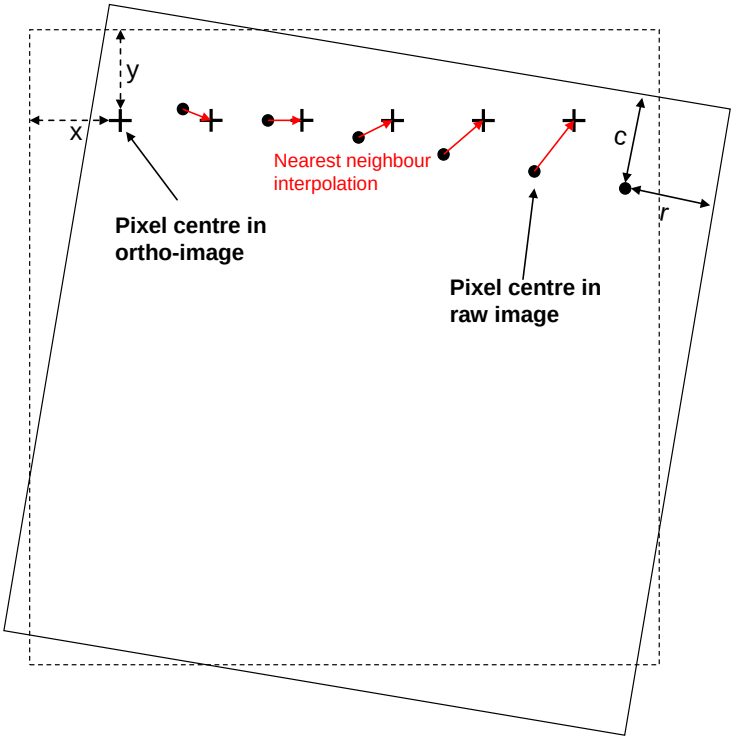


**Figure 5.13: Once the pixel centres from a new ortho-image (dashed box) had been transformed into c, r locations in the raw image, a nearest neighbour interpolation method was used to assign the new ortho-image brightness values from the raw image. The nearest neighbour method simply uses the value of the closest pixel centre to assign to the output pixel value (depicted by the red arrows). Here, only one row of pixel centres is present. The spacing between the raw image and ortho image pixels is defined by their respective coordinate systems. In terms of the ortho-image x and y coordinates, these are fully geometrically corrected within a specified map projection.**

### 5.3.3. Extracting DEMs from Corona stereo pairs

Once the interior and exterior orientation parameters had been estimated for each batch of Corona images during aerial triangulation, DEMs could then be extracted from stereo image pairs using the ATE module in ERDAS Imagine LPS. The ATE DEM extraction process involves three steps, summarised from Leica Geosystems (2006). Firstly, image matching takes place. The initial stage of the image matching process involves a series of interest points being identified on each overlapping image contained within a batch. An interest point is a point within an image that exhibits sufficient grey level variation and contrast in the x and y direction. In this case, an interest point would refer to a well defined ground feature, such as the corner of a river junction or a mountain peak, that is illuminated on one side and in shadow on the other.

Once interest points have been identified on all overlapping images in a batch, ATE then attempts to match corresponding points that refer to the same ground feature on two or more overlapping images. This interest point matching is performed using a correlation window, which exists on a reference image (assigned by ATE) and a search window, which exists on any overlapping images. These interest point windows systematically work through all points identified within a batch and measure the degree of similarity between overlapping points by calculating cross-correlation coefficients (ranging from 1 (excellent) to 0). Successful interest point pairing relates to how well image pairs have been orientated during aerial triangulation. To improve interest point matching success, ATE includes a number of pre-set matching strategies that are tailored to a range of terrain types. Here, the High Mountains matching strategy was applied to each Corona DEM extraction process undertaken.

The second step of the DEM extraction process involves determining ground point coordinates. Once correlation coefficients have been computed for each matching image point within a block, statistical tests are used within ATE to determine a final set of image points that relate to surface ground features. Each of these final points

are then given a set of row and column pixel coordinates, one for each image within an image pair. The final DEM extraction process involves the conversion of these pixel coordinates into full 3D coordinates. This conversion is performed using the space forward intersection technique (depicted previously in Figure 5.9) and interior and exterior orientation information available from the previous triangulation. Each resulting 3D coordinate, referred to individually as a mass point, is then used during DEM construction, the third step of the extraction process.

Prior to DEM extraction, LPS ATE allows users to set a number of extraction and accuracy properties to help improve the overall quality. One of the most important tools, in this respect, allows users to manually delineate image areas to be excluded from the DEM extraction process. In practice, this meant that image quality features, such as clouds and areas of poor contrast, could be removed from resulting DEMs (Figure 5.14). The final step of the extraction process was to set the output characteristics of the resulting DEMs. Here, Corona DEMs were produced in 30 m raster formats, matching the resolution of the ASTER GDEM.

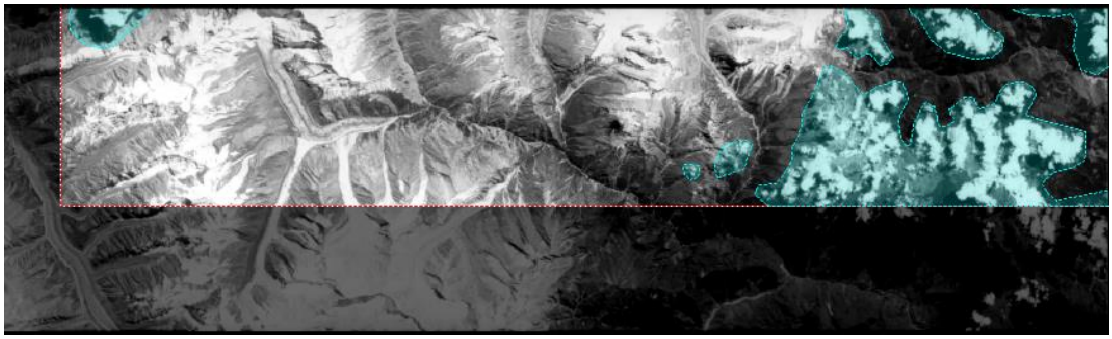

**Figure 5.14: Polygon regions (highlighted in blue) delineating areas of cloud on the overlap area of a Corona image strip (dashed red box). Areas within the region polygons are excluded from the DEM extraction process.**

### 5.3.3.1. Corona DEM accuracy assessment

Post DEM extraction, a number of analysis procedures were undertaken in order to assess DEM accuracy, quality and optimisation (see Figure 5.10). The initial step in the accuracy assessment of the DEMs produced was to analyse the resulting

accuracy report. Similar to the aerial triangulation process, an accuracy report is compiled by ATE for each DEM extracted. These DEM extraction reports contain the following accuracy information (taken from Lieca Geosystems, 2006). (1) DEM mass point quality: Stating the correlation coefficient values of each point. (2) Global vertical and horizontal accuracy: Describing the vertical and horizontal accuracy of the 3D mass point information in comparison to SRTM data. (3) Block GCP and tie point accuracy: Comparing the GCP and tie point x, y, z coordinates to the corresponding 3D mass points extracted. (4) Reference DEM accuracy: Comparing ASTER GDEM coordinates to the corresponding 3D mass points extracted. For the latter three points, mass point accuracy indices are given, including RMSE and mean error, amongst others.

The DEM accuracy analysis performed focused mainly on mean error and total RMSE values of the block GCP and tie point, and reference DEM accuracy sub-reports. For each of these sub-reports, the aim was to minimize the accuracy values. In terms of RMSE, Lieca Geosystems (2006) suggests that values should be within two magnitudes of the original pixel size of the input imagery, which for Corona imagery would be around 3.6 m. However, in light of the significant distortions present in Corona imagery, this target value of 3.6 m was seen as optimistic.

Residual error in the Corona DEMs, when compared to ASTER GDEM and SRTM elevations, in many ways was an inherent feature because of (1) the higher resolution of Corona imagery and (2) the natural surface elevation difference of glacierised portions of the Corona DEMs in the 1960s. Due to this, the use of RMSE values as a sole gauge of Corona DEM accuracy was limited. Therefore, a number of manual DEM inspections were also performed using various GIS based tools. These manual inspections focused on identifying irregular surface features within the resulting DEMs, and locating any areas where surface elevation differences were large in comparison to the ASTER GDEM. Once identified, attempts could be made to rectify such errors during the triangulation or DEM extraction parameterisation process. Additionally, the DEMs were analysed in relation to the following project specific DEM criteria: (1) DEM glacier surface geometry should conform to that of a

glacier, e.g. relatively flat (maybe slightly convex or concave); and (2) elevation errors in flat non-glacierised portions of the DEM should be minimal when compared to the reference ASTER GDEM.

The manual inspection process included the use of Corona DEM contour maps (produced using the ArcGIS software package) and ArcGlobe (module included within ArcGIS). ArcGlobe was used to analyse each extracted Corona DEM in 3D. The ability to view entire Corona DEMs three dimensionally aided the analysis process allowing elevation irregularities, visible as large peaks and troughs on the DEM surface, to be quickly identified (see Figure 5.15).

To assess the accuracy of non-glaciated flat valley bottoms (with reference to the methodological objectives), a number of checkpoint elevations were sampled from the Corona DEMs and compared to the ASTER GDEM. After manually delineating test

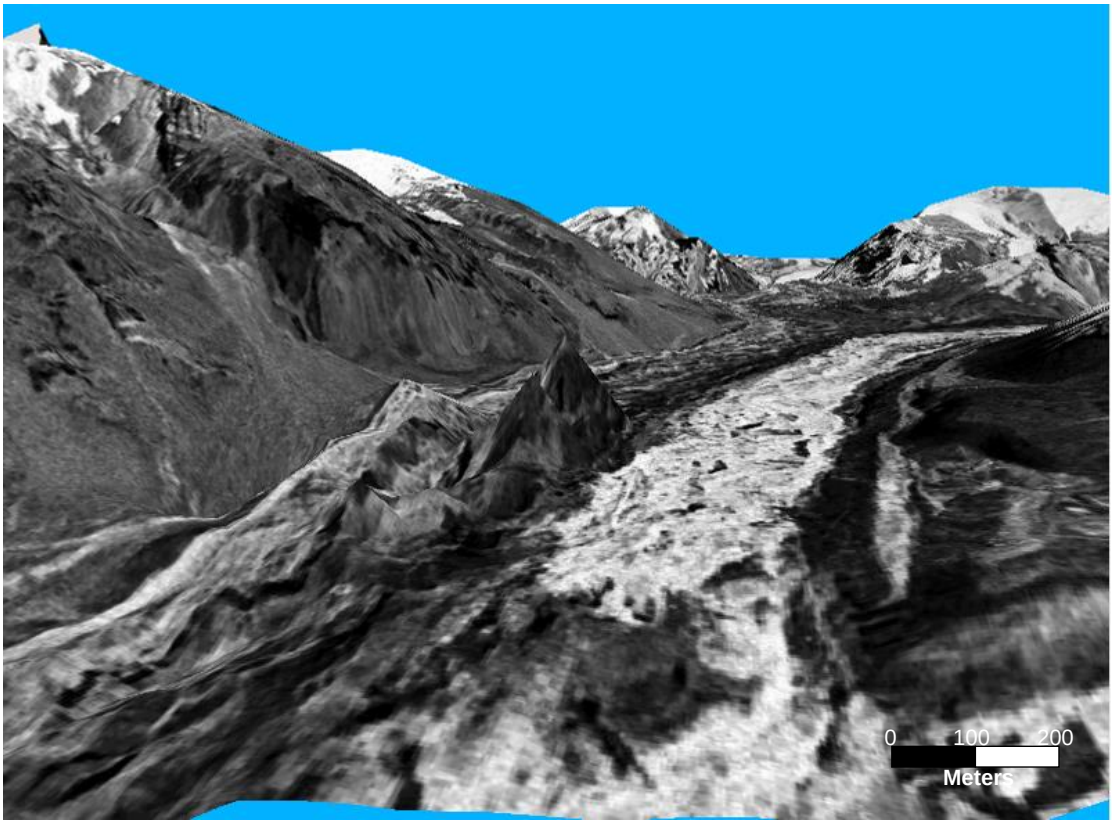


**Figure 5.15: 3D view of the Chaturangi glacier, Uttarakhand, India. By overlaying Corona ortho-images onto corresponding Corona DEMs, regions of error, visible in the form of irregular peaks and troughs (in the centre of the image), can be identified.**

areas, located in close proximity to glaciers selected from the GC and ND study sites (using the glacier boundary delineation technique described in section 5.4.1.), the 'Generate Random Point' tool available within the ArcGIS Hawths Tool extension package (downloaded from www.spatialecolog.com) was used to generate elevation checkpoints. Once generated, elevation values were extracted from both the Corona DEMs and the ASTER GDEM. These corresponding elevation values were then subtracted to analyse elevation differences. In total, 200 checkpoints were used for each valley bottom location selected.

Additionally, the Gangotri glacier basin (included within the GC study site) was chosen for a detailed accuracy assessment of all non-glaciated areas. This analysis aimed to assess the influence of the steep mountainous terrain on Corona DEM error and considered basin slope, elevation and aspect. Using the same procedure applied for the valley bottom analysis, in total 1000 elevation checkpoints were compared between the GC Corona DEM and the ASTER GDEM. Slope and aspect values were extracted for each checkpoint location using slope and aspect raster datasets generated from the ASTER GDEM using tools available within ArcGIS. Both the valley bottom and Gangotri basin accuracy tests were performed using the final optimised Corona DEMs.

For the glaciers sampled at each study site, Corona DEM and ASTER GDEM differencing (described in section 5.4.2.) was also performed in order to identify erroneous Corona elevations. In such areas, it was assumed the surface lowering would have occurred over the past 40 years and that this lowering would be considerably greater for glacier ablation zones. The knowledge acquired during the accuracy assessments performed was ultimately fed back into the aerial triangulation and DEM extraction process, and parameters for both were often changed accordingly until an optimal solution was found. Most notably, additional GCP and tie points were often added to the block and existing points altered in regions that exhibited large errors.

## 5.4. Processing: Quantifying glacier length, area and volume change

The processing of the ortho-Corona and ortho-ASTER imagery involved quantifying areal and length changes for the glaciers selected within each of the four study areas. For the Corona and ASTER GDEM elevation datasets, processing this involved quantifying changes in glacier volume. The methodology used to perform these tasks is described in the following two sections.

### 5.4.1. Manual glacier boundary delineation and the quantification of glacier area and length change

For the GC and ND study sites, glacier boundaries were manually delineated and compared from the 1960s Corona ortho-images and 2000s ortho-ASTER imagery. For the SB and LT study sites, glacier boundaries were manually delineated from the 2000s ortho-ASTER imagery only, these being compared to the 1960/70s glacier outlines available within the GLIMS glacier database. The process used to manually delineate glaciers from the ortho-Corona and ortho-ASTER imagery, and subsequently quantify areal and length changes, can be split up into three stages (all of which were performed using the ArcGIS software package).

(1) Vector shapefiles were created for each manual delineation observation date and were assigned to the WGS 1984 UTM map projection. (2) Once created, each shapefile was populated by point locations (known as vertex), manually measured to create a number of individual polygon features delineating glaciers sampled from the ortho-Corona and ortho-ASTER imagery. Here, glacier delineation was performed at high spatial scale in order to differentiate glacier ice from the surrounding terrain on a pixel-by-pixel basis (e.g. ~ 1:1,900 scale). During delineation, an identification value was added to the Corona, ASTER, and GLIMS shapefile attribute tables so that matching glacier polygons could be compared during the third stage.

The third step involved quantification of areal and length change between the 1960s Corona glaciers, 1960/70s GLIMs glaciers (SB and LT) and the 2000s ASTER glaciers

were applicable. Individual planimetric glacier areas were calculated using the 'Calculate Geometry' tool in ArcGIS, based on the map projection assigned to the glacier shapefiles. These area data were then exported into Microsoft Excel, where the ASTER and Corona, and ASTER and GLIMS glacier polygon areas were subtracted, respectively, quantifying areal change. Calculation of glacier length change for each respective glacier polygon pair was performed manually using the 'Measure Distance' tool in ArcGIS. Length change was measured at a single point along the frontal margins of each glacier sampled, located with reference to the central flow line.

The accuracy of glacier delineation from both image datasets was largely dependent on individual user knowledge in regards to glacier mapping. In this case, the mapping recommendations of the GLIMS project (Racoviteanu *et al.*, 2009) were adhered to where possible. Delineating debris covered ice, which was present on the majority of the glaciers sampled, was particularly challenging. To aid this process morphological features, indicative of active ice and ice flow, were identified in an attempt to distinguish glacier boundaries. These morphological features included flow lines, crevasses and ablation features (e.g. melt ponds and proglacial streams). Identified features were compared in both the ASTER and higher resolution Corona ortho-imagery. Any visual evidence of temporal glacier area, length and volume loss identified in the corresponding imagery was also used to help the delineation process.

### 5.4.2. DEM differencing and the quantification of glacier volume change

To quantifying glacier volume change for selected glaciers in the GC and ND study sites, the ASTER GDEM was subtracted from the corresponding Corona DEMs, resulting in raster output files of positive and negative values. This procedure was performed used the 'Raster Calculator´ tool in ArcGIS. Positive values in this instance represented surface lowering. It was assumed that surface changes in non-glaciated regions would be minimal and that positive values would be present in glaciated areas, demonstrating losses in ice volume (Figure 5.16). Next, a subset of glaciated

areas was created from each DEM difference raster output using the manually delineated glacier boundaries as masks. This procedure was performed using the extract by mask function in ArcGIS. Glacier volume change was then calculated for individual glaciers by multiplying the average ice elevation change by individual planimetric area (Racoviteanu *et al*., 2008).

To analyse individual glacier surface changes further, a number of transects were used to compare corresponding surface elevations between the Corona DEMs and the ASTER GDEM. Working within ArcGIS, each transect was manually created as a 3-D polyline. Overall, four width transects were created for each glacier selected, placed at intervals running across the main trunk. Additionally, a single length transect was created for each selected glacier, running centrally down the main trunk from the maximum to minimum elevation. Elevation values were extracted from the Corona DEMs and ASTER GDEM across each transect created, at corresponding 25 m intervals, and compared.

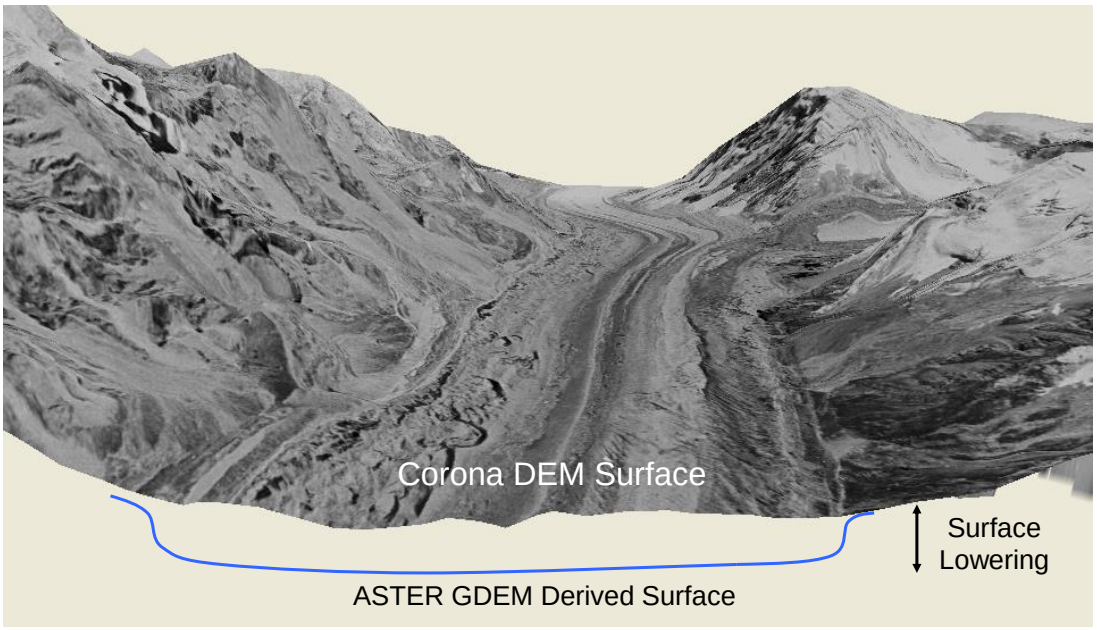


**Figure 5.16: 3D view of the Chaturangi glacier, Uttarakhand, India, created by overlaying Corona ortho-images onto corresponding Corona DEMs within ArcGlobe. Possible ice surface lowering was calculated by subtracting the ASTER GDEM from the corresponding Corona DEMs.**

### 5.4.3. Processing GLIMS glacier outlines and quantification of glacier change.

The 1960/70s GLIMS glaciers selected for the SB and LT study sites were downloaded from the GLIMS database in shapefile format. Within this shapefile, each separate glacier was represented by a vectorised polygon outline feature and a number of individual internal rock polygon features. Together with the polygon geospatial reference information of each glacier, the GLIMS shapefile also included descriptive information referring to the mapping source of the polygons and the acquisition dates, amongst others. The downloaded GLIMS shapefile was initially referenced to the WGS 1984 global coordinate system and was therefore re-projected into the WGS 1984 UTM projected coordinate system prior to processing. In order for the GLIMS glacier polygons to be comparable to manually derived glacier outlines delineated from ortho-ASTER imagery at the SB and LT study sites, internal rock features were first excluded. Initially, the GLIMS glacier outline polygons included all areas within the glaciers boundaries, including any internal rock outcrops. For each GLIMS glacier sampled, internal rock outcrops were represented by separate polygon features (see Figure 5.17). To clip all regions of internal rock out of the glacier polygons, the erase function available within the ArcGIS 'Xtool Pro' add-on tool was therefore used, applying the internal rock polygons as a mask.

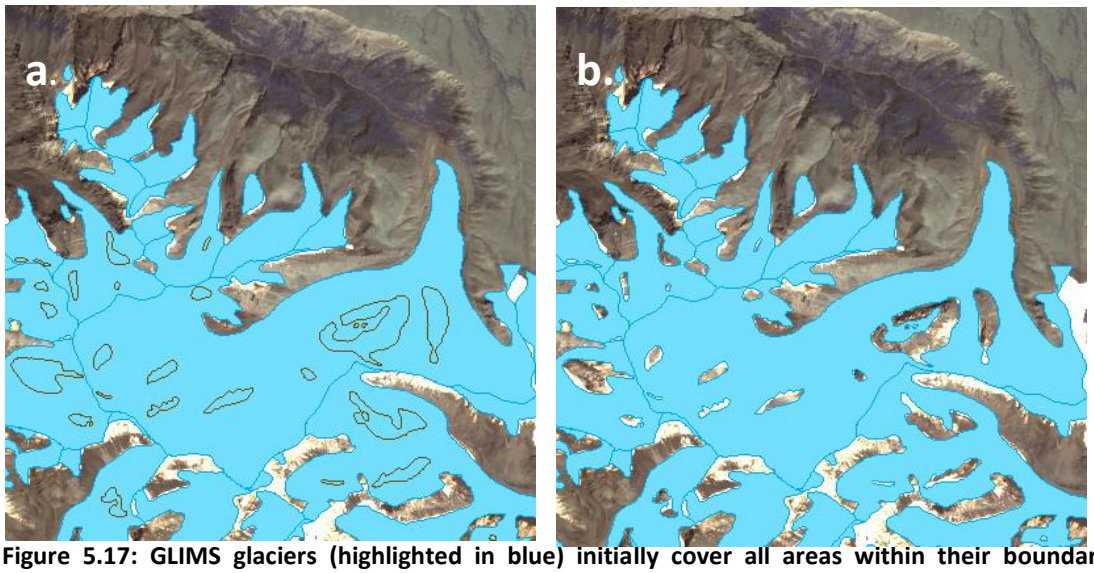


**Figure 5.17: GLIMS glaciers (highlighted in blue) initially cover all areas within their boundary including rock outcrops (outlined in brown) (a.). The internal rock polygons are used to remove such areas out of the GLIMS glacier polygons (b.).**

Once the internal rock outcrops had been removed from each of the GLIMS glacier polygons, glacier area and length change could be quantified in relation to glacier outlines manually delineated from ortho-ASTER at the SB and LT study sites (using the methods described in section 5.4.1.).

### 5.4.4. Hypsometric glacier area analysis

The hypsometric glacier area analysis at each of the four study sites was separated into six stages, each of which will be described in the following sub-sections and are indicated within figure 5.18.

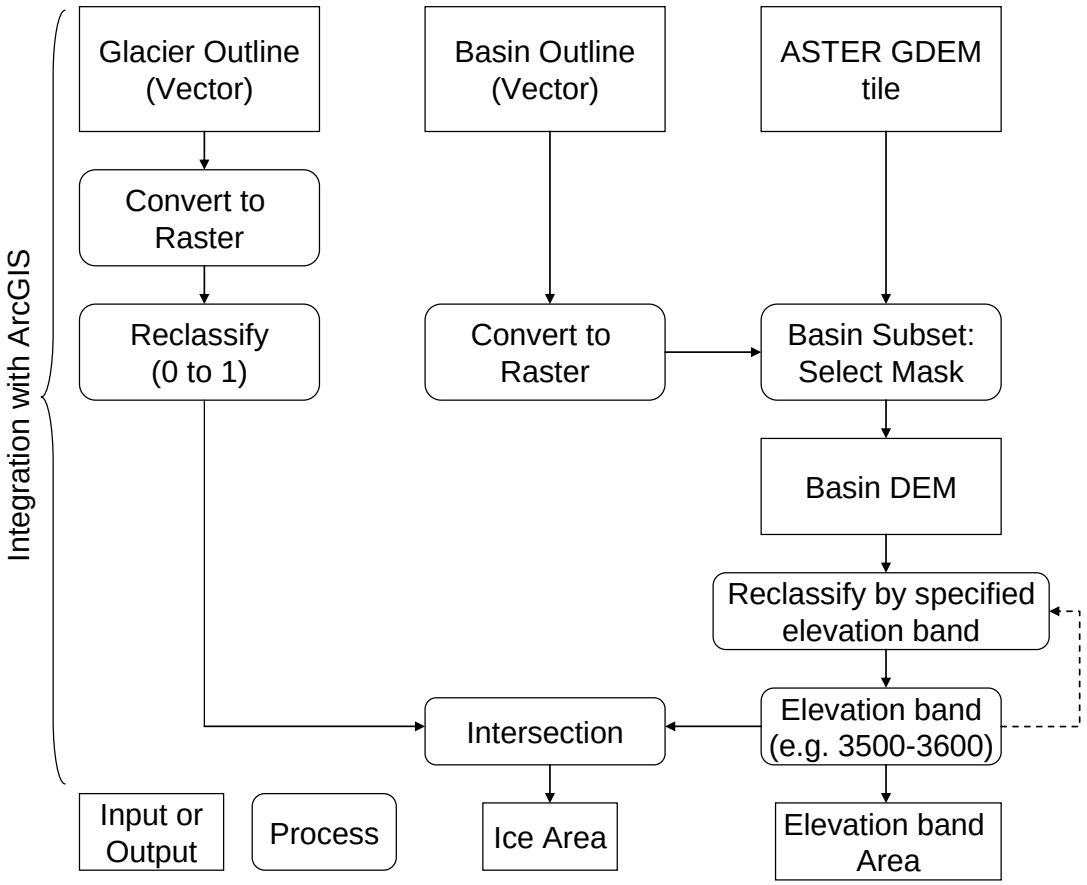


**Figure 5.18: Schematic workflow for calculating glaciated and non-glaciated area by elevation in a specified basin.**

#### 5.4.4.1. Basin delineation, raster conversion and reclassification

The input for the hypsometric analysis process was the glacier outlines delineated for each study site and the corresponding ASTER GDEM tile. Additionally, four basin outlines were also manually delineated (using the same method applied for the glacier outlines) encompassing all the selected glaciers at each study site. Initially, the basin and glacier outlines represented vectorised shapefile polygon features. In order to utilise these two datasets in the 'Raster Calculator' in ArcGIS (used during the basin extraction and intersection procedures) each polygon feature needed to be converted into a raster format. This conversion process was performed using the Spatial Analyst 'Feature to Raster' tool in ArcGIS. To aid the pixel intersection stage, the newly created glacier and basin raster datasets were assigned a 30 m pixel size (to match the ASTER GDEM). Once converted to raster formats, the glacier outlines required an additional reclassification step. In order for the raster glacier outlines to be later intersected with the individual elevation bands, the glacier pixels were reclassified from the value 0 to the value of 1. This pixel reclassification was performed manually using the Spatial Analyst 'Reclassify' tool in ArcGIS.

#### 5.4.4.2. ASTER GDEM study site basin subset and elevation band classification

To extract basin subsets from the ASTER GDEM for each study site, the select by mask function (Eq. (5.1)) was used within the 'Raster Calculator' available in ArcGIS. Here, the manually delineated basin outlines were used as subset masks, where InRas1 was the ASTER GDEM tile, InRas2 the rastered basin outline and OutRas the subsequent basin subset.

$$OutRas = SelectMask(InRas1, InRas2) \quad (5.1)$$

Once a subset basin DEM had been created for each study site, individual pixels within this subset were divided by elevation band through a process of binary reclassification. In this case 100 m elevation bands were utilised. In order to divide

the DEM, all pixels (each with a specific elevation value) within a specified elevation range (e.g. 5000-5100) needed to be assigned a value of 1 with all others given a value of 0.

Pixel reclassification involved manually defining elevation classes using the Spatial Analyst 'Reclassify' tool in ArcGIS. A DEM consists of a matrix of pixel elevation values whose statistical distribution can be represented by a histogram. By manually inserting separate classes, these pixels can be segregated into separate groups, which can then be assigned a different pixel value. In this case, 3 classes were used. For example, when a 5000-5100 elevation band was segregated, the first class was assigned as 5000, the second as 5100 and the third was the maximum elevation for the basin. This example would distribute pixel values into 3 groups; minimum-5000, 5000-5100 and 5100-maximum. Once distributed in this way, a value of 0 was assigned to all pixels in the minimum-5000 and 5100-maximum groups and a value of 1 to all pixels in the 5000-5100 group. The subsequent raster dataset would highlight all pixels within the 5000-5100 range and allow the number of pixels in that particular elevation band to be quantified. This process of reclassification by elevation was repeated for each 100 m elevation interval within the four basins.

#### 5.4.4.3. Elevation band and glacier area intersection

After reclassification, each 100 m elevation band within a basin was then individually combined (or intersected) with the reclassified glacier outlines. This intersection subsequently allowed the number of glacier pixels overlapping with each specific elevation band to be quantified. To perform the intersection procedure, a simple expression was executed in the 'Raster Calculator' of ArGIS, whereby an individual raster elevation band was multiplied together with the reclassified glacier outline creating a new intersection raster. Through executing this expression, pixels in both datasets that shared the same spatial location were multiplied together. Importantly, as both the glacier and elevation band pixels had been assigned the value of 1, the resulting intersection raster only highlighted glacier pixels that were located within that specific elevation band (because 1 x 1 = 1 and 0 x 1 = 0) (Figure 5.19). The

intersection process was repeated for every elevation band that contained ice area at each study site basin.

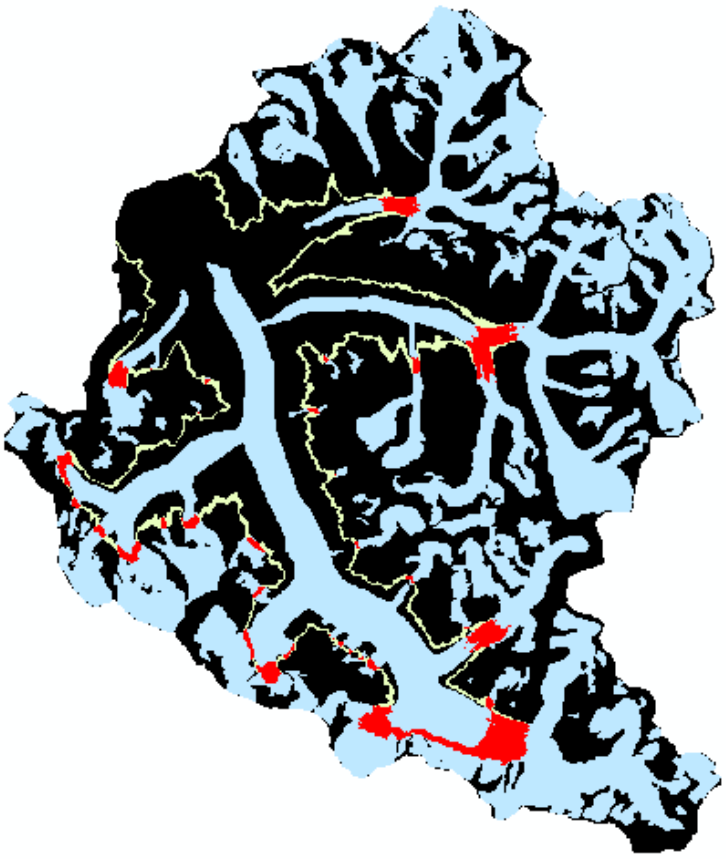

**Figure 5.19: Intersection between the 5000-5100 elevation band and ice pixels in the Gangotri basin (subset of GC study site). Ice pixels within elevation band are indicated in red.**

#### 5.4.4.4. Calculation of glaciated and non-glaciated area

Once an intersection raster had been created for every elevation band containing glacier ice area at all four study sites, the glaciated and non-glaciated area for each band could be calculated with relation to the number of pixels. Within each intersection raster ice pixels were assigned a value of 1. Areal coverage could therefore be quantified by multiplying the area of an individual pixel (in this case 30 x 30 m) by the total number of glacier pixels in a specified elevation band. To calculate non-glaciated area the number of glacier pixels in an individual elevation band was simply subtracted from the total number of pixels in that band.

### 5.4.5. Topographic analysis: Minimum, maximum & median glacier elevation

Glaciers delineated at each study site were also analysed in regards to individual elevation characteristics. This topographical analysis was performed by extracting information from the ASTER GDEM for each manually delineated glacier outline using the 'Zonal Statistics' tool in ArcGIS. The zonal statistics tool automatically calculated elevation statistical values for each glacier outline, including minimum, maximum, and median.

## 6. Results & discussion: Corona orthorectification & DEM extraction

This chapter presents the results of the Corona orthorectification and Corona DEM extraction process described in chapter 5. Utilising the extracted Corona DEMs, this chapter also presents the results of the DEM differencing procedure undertaken and the quantification of ice surface elevation/volume change for selected glaciers. The chapter ends with a detailed discussion about the implications of the aforementioned procedures and the results presented.

### 6.1. Corona orthorectification using a non-metric camera frame model and ASTER reference data

Utilising the photogrammetric non-metric camera frame model described in chapter 5, raw Corona imagery was orthorecitifed at both the GC and ND study sites. The resulting accuracy of the Corona ortho-rectification process is presented in table 6.1. The aim of the Corona orthorectification process was to achieve a geometric accuracy of within 1 pixel of the ortho-ASTER reference source (15 m). This aim was achieved for the GC Corona imagery, which was orthorectified with a horizontal RMSE of ±7.5 m. In comparison, the ND Corona imagery only marginally exceeded the 15 m aim, having been orthorectified with a horizontal RMSE of ±16.7 m.

Overall, despite the large difference between the spatial resolution of both ortho-ASTER (15 m) and Corona imagery (1.8 m), the success of the Corona orthorectification process meant that glacier outlines delineated from each spatial dataset could be geometrically compared, with the horizontal accuracy achieved matching that

**Table 6.1: Corona geometric accuracy relative to ortho-ASTER imagery.**

| Study site | $RMSE_{xy}$ (Pixels) | Absolute error (m) |
|---|---|---|
| Gangotri Chaukhamba | 4.17 | ±7.5 |
| Nanda Devi | 9.29 | ±16.7 |

reported by other glacier mapping studies (see Table 2.2, Chapter 2). The error attributed to the glacier area and length change observations derived from the Corona and ortho-ASTER imagery is assessed in chapter 7.

Importantly, the horizontal RMSE values for both the GC and ND Corona imagery represent the overall bundle block adjustment accuracy of an entire image batch. After visual comparison with the ortho-ASTER imagery, it was evident that spatial accuracy across each batch varied according to the size and distribution of GCPs sampled. In both the GC and ND Corona image batches, GCPs tended to cluster around glacierised regions. The geometric accuracy of the glacierised regions within the Corona imagery was therefore often greater than the overall RMSE reported, the spatial correspondence between ortho-ASTER and Corona imagery in such areas being particularly high. An example of this high level of geometric correspondence in glacierised regions is presented in figure 6.1.

In contrast, for image areas that were poorly sampled with GCPs, geometric accuracy declined, resulting in spatial mis-matches between image features in the Corona and ortho-ASTER imagery. These spatial mis-matches, although limited overall, were most

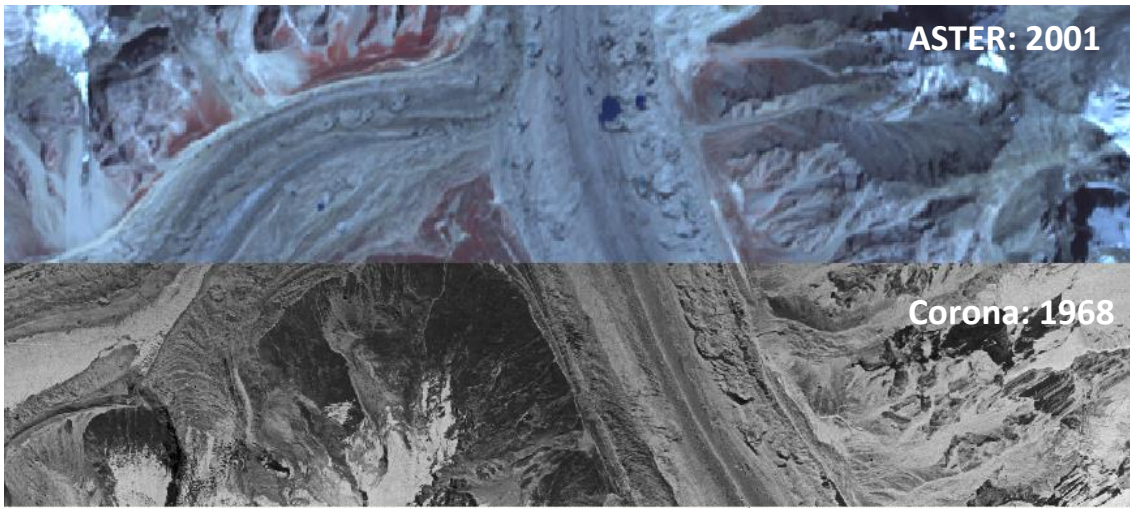


**Figure 6.1: Comparison of the spatial geometries of the ortho-ASTER and Corona imagery used to delineate glaciers in the GC site. Imagery is focused on the central portions of the Gangotri glacier.**

common for areas at higher elevations where GCP sampling was difficult, particularly within the ND Corona image batch. Corona glacier outlines delineated in these areas often appear displaced in relation to ASTER derived outlines (see Figure 6.2).

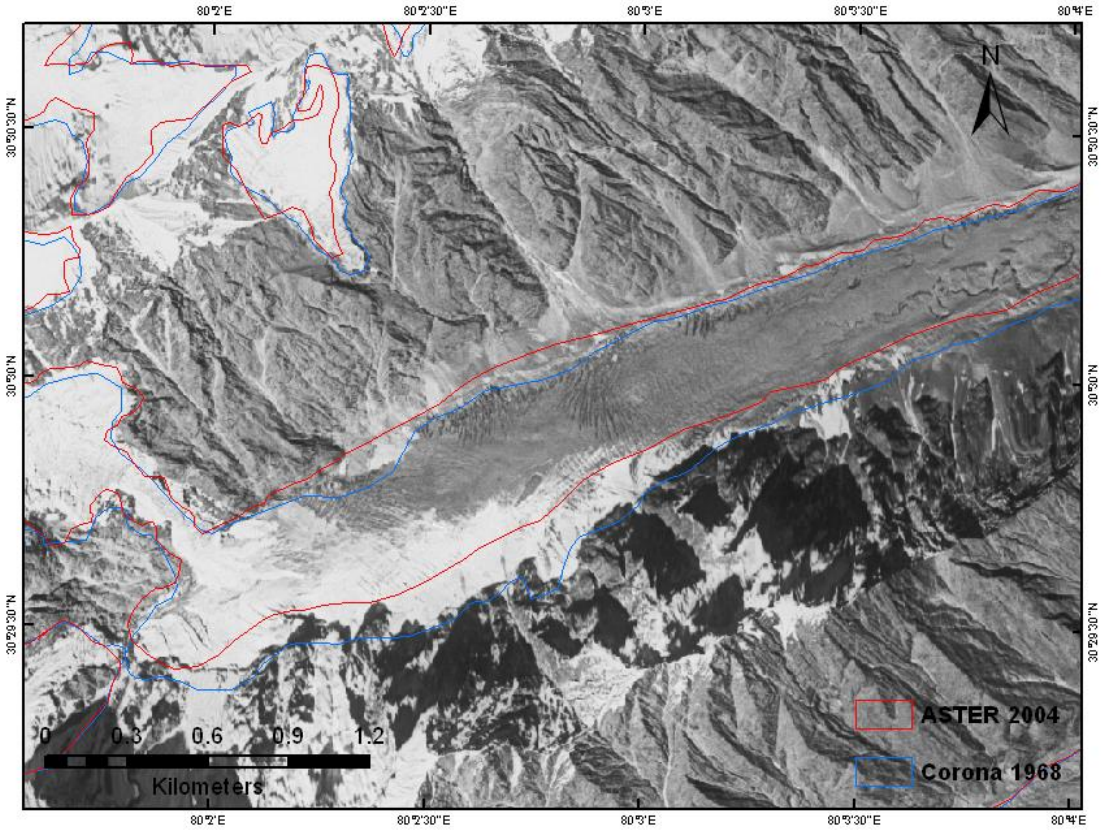


**Figure 6.2: Geometric errors in the positioning of Corona glacier outlines (blue) in respect to ASTER outlines (red) at a high elevation tributary of the Milam glacier.**

## 6.2. Corona DEM Extraction

By comparison with the Corona orthorectification process, the Corona DEM extraction process was more challenging. The extent of the challenges encountered meant that the expectations placed upon these 3-D datasets, in terms of quantifying glacier volume change, were greatly reduced. Overall, due to the magnitude of the elevation errors present, neither of the GC and ND Corona DEMs could be used to assess surface lowering and volume change over entire glaciers, as planned. However, after analysing glacier surface topographies, elevation differences at former 1960s glacier termini, and elevation errors of flat valley bottoms, it was shown that for a selected number of glaciers, the Corona DEMs could be used to assess surface lowering in lower

ablation zones. These glaciers were located in regions of each Corona DEM that were particularly well sampled in terms of GCPs and tie points.

Four glaciers were selected from the GC and ND Corona DEMs for surface analysis. These included Gangotri glacier from the GC site and Milam, Uttari Nanda Devi and Nanda Devi 1 glacier from the ND site. These four glaciers were selected against the following criteria: (1) ice surface lowering showed a typical ablation pattern (i.e. decreasing with ice elevation), (2) surface lowering was evident within the boundaries of former 1960 ice termini, and (3) elevation errors of valley bottoms close to the 1960 ice termini were low in comparison to the level of surface lowering measured. To analyse ice surface changes, the 1960s lower ablation zone of each glacier selected was clipped out of the Corona DEMs. These clipped glacier snouts then analysed using the methods described in section 5.4.2. In order to explain why the use of Corona DEMs was changed, the results of the overall vertical accuracy assessments will be addressed first, followed by the accuracy assessment of the glacier snouts and the results of the glacier snout surface analysis.

### 6.2.1. Overall vertical accuracy: Corona DEMs

The overall accuracy of the two DEMs extracted from the GC and NC Corona stereo image pairs is presented in table 6.2. It is important to note that each of the measures of accuracy presented in table 6.2 do not represent absolute elevation accuracy at each site but instead represent accuracy relative to that of the elevation reference source (ASTER GDEM, see Chapter 4). Table 6.2 reveals that the overall elevation errors in both the GC and ND DEMs are large, with RMSEs equating to ±343.13 m and ±489.94 m, respectively. Although these errors reduce when measured for user defined GCPs taken from the bundle block adjustment (measured on stable non-glaciated terrain), the magnitude of both would suggest that their use for assessing glacier volume change would be limited.

In addition to the measures of accuracy shown in table 6.2, table 6.3 presents mass

**Table 6.2: Overall vertical accuracy characteristics for the GC and ND Corona DEMs.**

| | | Corona DEMs | | | |
|---|---|---|---|---|---|
| | | Gangotri Chaukhamba | No. of elevation points checked | Nanda Devi | No. of elevation points checked |
| Overall accuracy (m) | Minimum | -3629.25 | 212002 | -5000.33 | 205950 |
| | Maximum | 3688.8 | | 2888.03 | |
| | Mean | 17.22 | | -118.01 | |
| | RMSE | 343.13 | | 489.94 | |
| User defined GCP to DEM accuracy (m) | Minimum | -918.71 | 169 | -1694.5 | 64 |
| | Maximum | 766.89 | | 254.38 | |
| | Mean | -27.96 | | -69.25 | |
| | RMSE | 179.04 | | 275.47 | |
| ATE-defined reference DEM to DEM accuracy (m) | Minimum | -3629.25 | 211509 | -5000.33 | 205886 |
| | Maximum | 3688.8 | | 2888.03 | |
| | Mean | 17.31 | | -118.02 | |
| | RMSE | 343.4 | | 489.99 | |

point quality for each of the DEMs extracted. Used as an indicator of the success of the initial image matching stage of the DEM extraction process, a large percentage of excellent points (points with correlation coefficients of 0.85-1) is usually a feature of a good quality DEM. In this case, the majority of the image points matched between each stereo image pair of the DEMs extracted were classed as fair, which coincides with the high level of error found in both. However, in contrast to their respective RMSEs, the ND Corona DEM is shown to have a higher percentage of its image point matches classed as excellent.

In Figure 6.3 and 6.4 Corona- and ASTER-derived shaded relief images for the GC and ND study sites are presented. In contrast to the smooth topographic features visible in the ASTER GDEM (Figure 6.3 and 6.4), elevation errors are identifiable on the surface of each of the Corona DEMs as uneven and textured patches. Further analysis of the Corona DEMs also reveals that elevation errors tend to occur on steep sided

**Table 6.3: Corona DEM mass point quality for the GC and ND study sites (see section 5.3.3 for information on mass point quality classification).**

| Mass Point Quality | Gangotri Chaukhamba (%) | Nanda Devi (%) |
|---|---|---|
| Excellent (1-0.85) | 24.49 | 27.25 |
| Good (0.85-0.7) | 27.19 | 33.16 |
| Fair (0.7-0.5) | 48.31 | 39.57 |

slopes and in areas of particularly high elevation, suggesting a link between DEM error and surface topography. Additionally, errors are visible at the edges of adjacent image stereo-pairs and in areas of triple image overlap, indicating problems related to the image orientation process.

Looking at the effect of the bundle block adjustment on the DEM extraction process, it is clear that the size and distribution of GCPs sampled had an impact on the level of error. From table 6.2, for example, it can be seen that the GC DEM, which has the lowest measurable error, has a larger number of user defined GCPs. Also, stereo image pairs that have a low number of GCPs tend to show irregular elevation errors by comparison with adjacent pairs. This stereo pair irregularity is visible towards the bottom of figure 6.5 as a large strip of relatively elevated surface. Additionally, areas that were difficult to sample, such as densely vegetated low lands and snow and ice covered high mountain slopes, also showed high levels of error.

In figure 6.5 and 6.6, the spatial distribution of surface changes, derived from the comparison of Corona and ASTER GDEM elevations, is shown for both the ND and GC sites. For the GC site, the surface of the Corona DEM is generally lower in comparison to the ASTER GDEM (Figure 6.6). Additionally, the spatial distribution of surface changes in figure 6.6 suggests a possible link between elevation error and slope aspect, with a number of erroneous elevation gains being visible on south facing slopes.

Surface lowering, with respect to the ASTER GDEM, is far less prominent in the ND Corona DEM (Figure 6.5). Here, large sections are significantly elevated compared to the ASTER GDEM. Overall, the ND Corona DEM contains a number of large elevation errors that correspond well to the placing and overlapping of stereo image pairs used

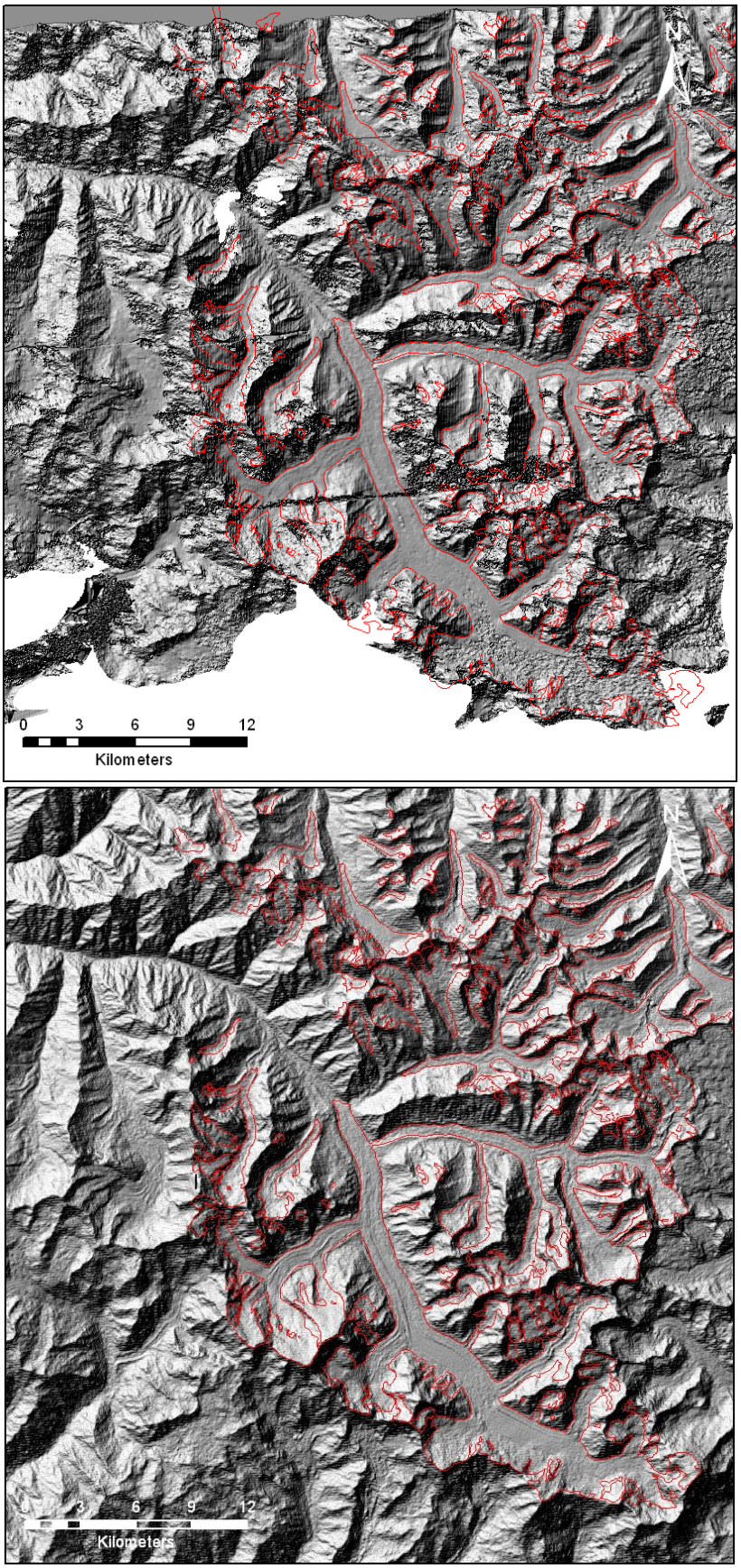


**Figure 6.3: Comparison of the surface topographies of the GC Corona DEM (above) and ASTER GDEM (below) highlighted through use of a hill shading effect.**

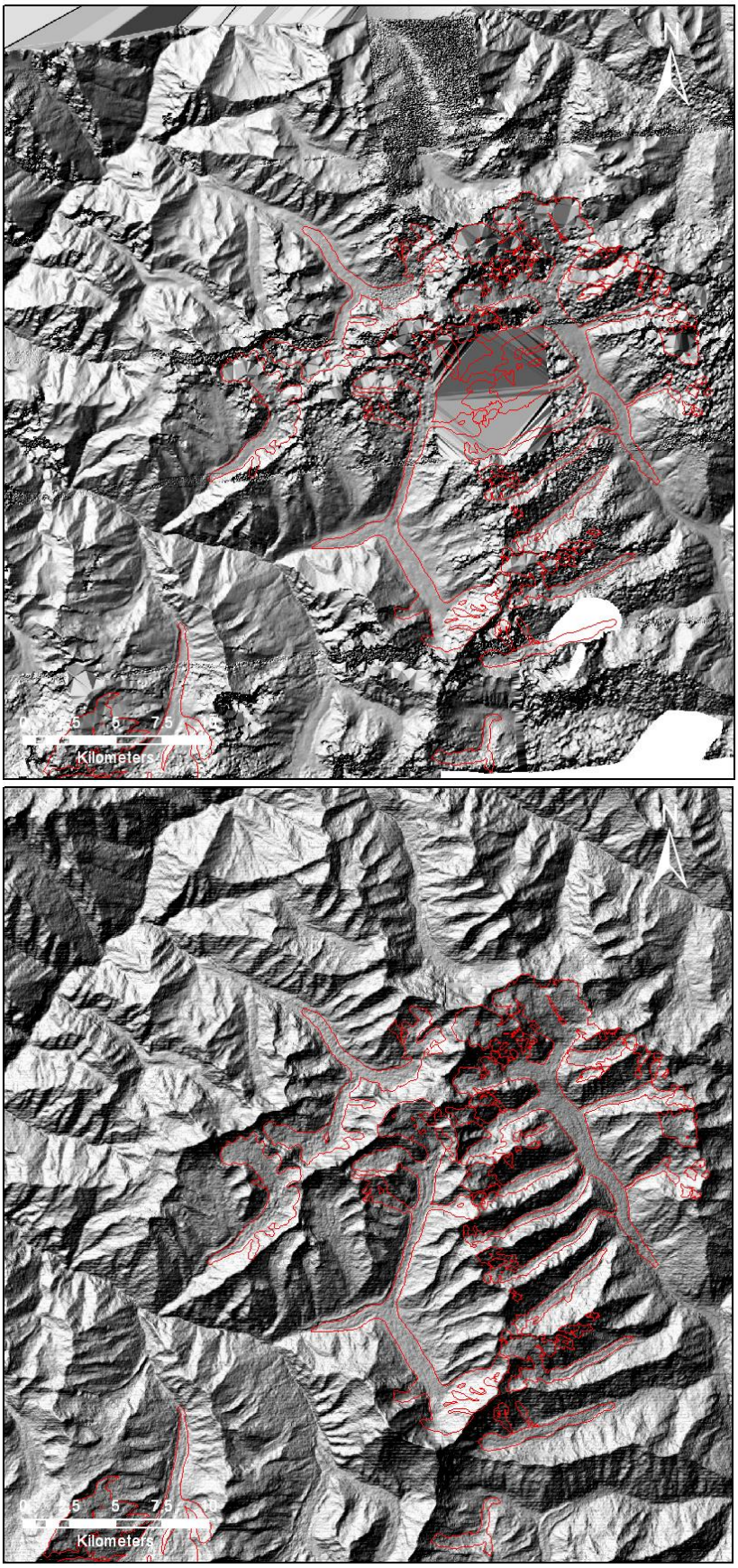


**Figure 6.4: Comparison of the surface topographies of the ND Corona DEM (above) and ASTER GDEM (below) highlighted through use of a hill shading effect.**

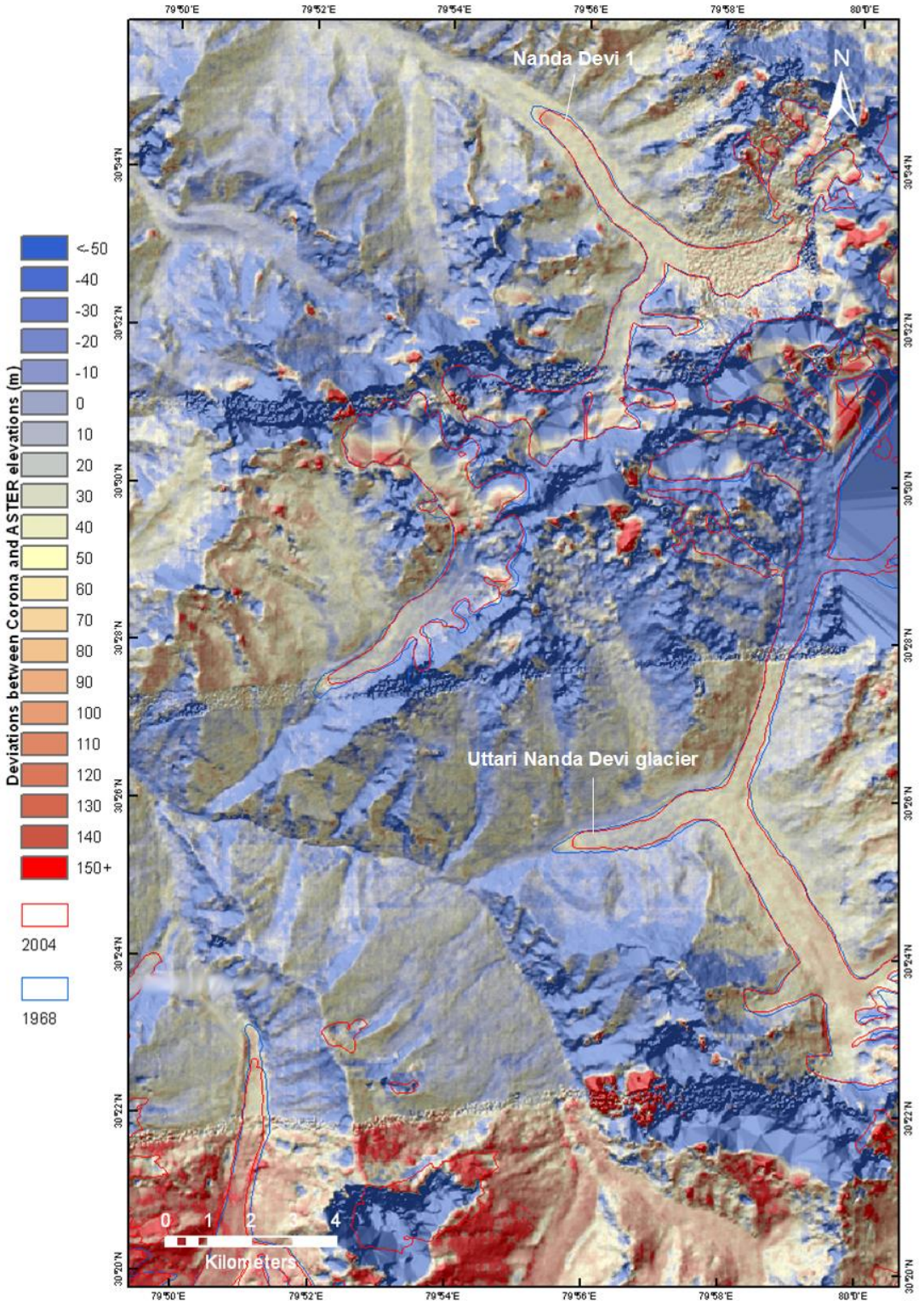


**Figure 6.5: Deviations in the surface of the ND Corona DEM (centred on eastern side of study area), relative to the ASTER GDEM. Positive values reveal surface lowering between 1965 and 2000s.**

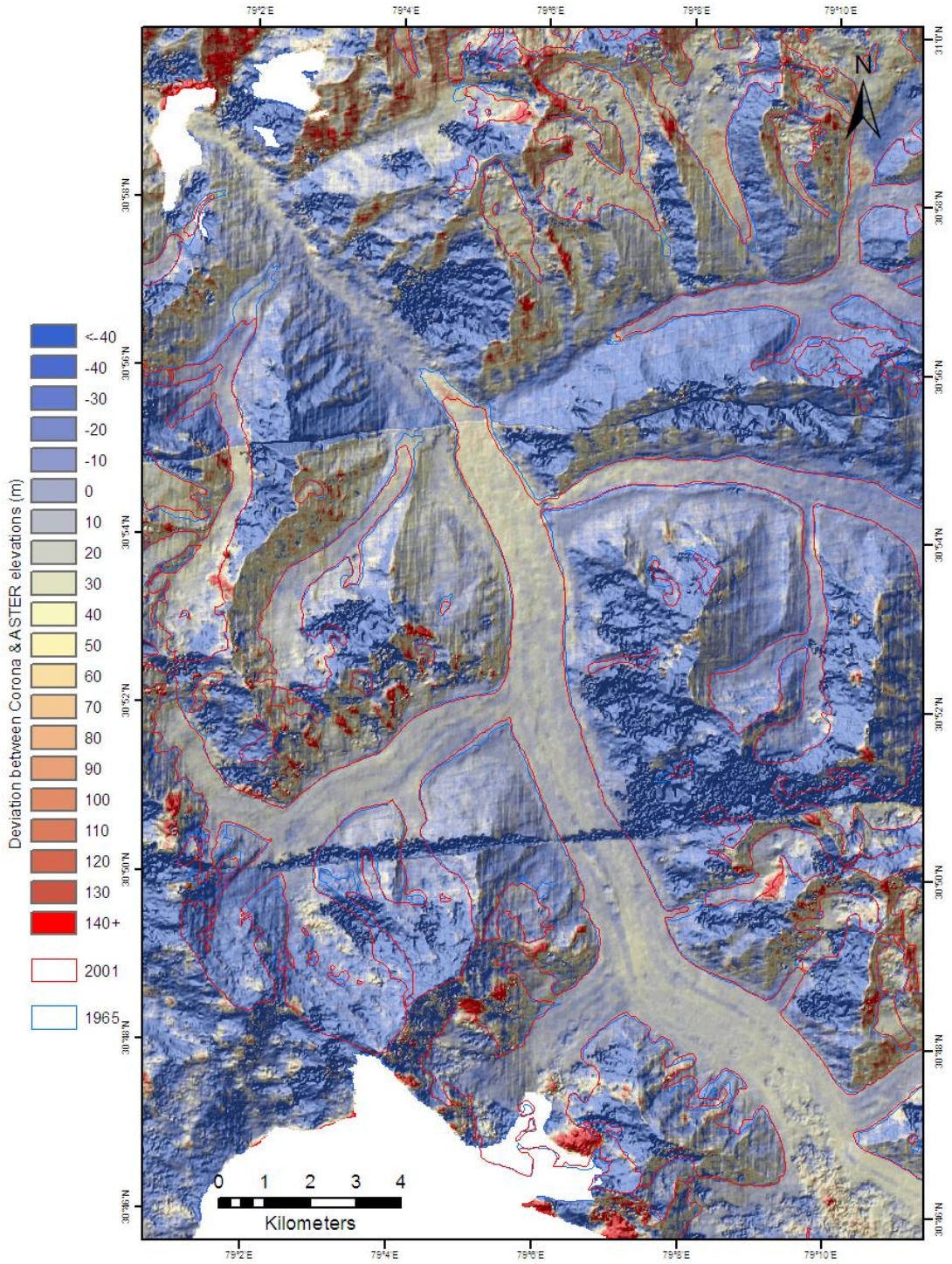


**Figure 6.6: Deviations in the surface of the GC Corona DEM (centred on Gangotri glacier), relative to the ASTER GDEM. Positive values reveal surface lowering between 1965 and 2000s.**

during the bundle block adjustment. Therefore, it is likely that the errors within this Corona DEM are attributed to problems with tie point and GCP sampling problems.

### 6.2.2. Vertical accuracy test: Gangotri basin

The results of the manual accuracy assessment performed on the GC Corona DEM for non-glaciated portions of the Gangotri glacier basin (described in section 5.3.3.1) are shown in table 6.4. Overall, the Gangotri glacier basin, shown in figure 6.6, represented the most sampled glacierised basin in terms of GCPs and tie points for both the GC and ND sites. Therefore, the elevation errors present within this test basin are least likely to have been caused by poor sampling, and instead may highlight other factors influencing error. Results of the manual accuracy assessment indicate a reduced minimum, maximum and RMSE error. However, the magnitude of each of these error values is still large. The manual assessment also confirms lowering of the Corona DEM in this area compared to the ASTER GDEM with the average elevation difference being -90.29 m.

Analysis of the location of each of the 1000 points measured during the manual assessment, in terms of slope aspect and their respective elevation errors, reveals that elevation errors are larger for North-west, West, South-west, and South facing slopes (see Figure 6.7). The smallest elevation differences between the Corona DEM and ASTER GDEM were located on North-east and East facing slopes. The large disparity of elevation errors measured on North-west to South and South-east to North facing slopes suggests that slope aspect has an impact on the DEM extraction process.

**Table 6.4: Vertical accuracy characteristics for non-glaciated portions of the Gangotri basin manual test site.**

| | Elevation error (m) | No. of elevation points checked |
|---|---|---|
| Minimum | -2080.14 | 1000 |
| Maximum | 432.34 | |
| Mean | -90.29 | |
| RMSE | 239.88 | |

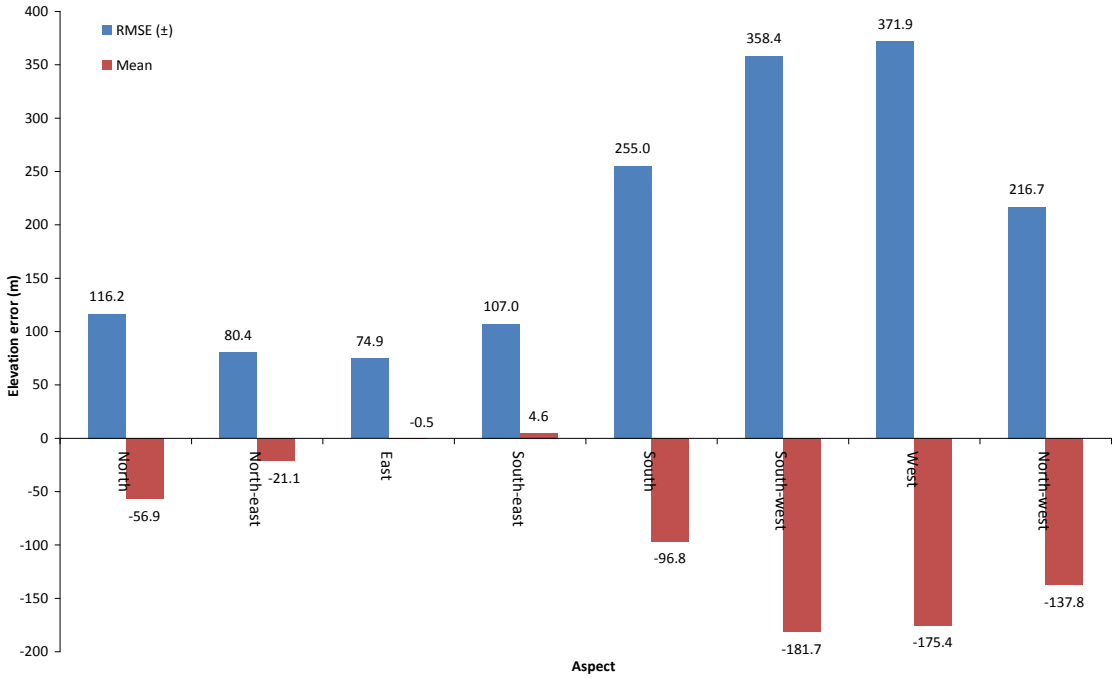


**Figure 6.7: Elevation differences of 1000 test points located in the non-glaciated portions of Gangotri basin in relation to slope aspect.**

Although results indicate that the overall accuracies of both the Corona DEMs is poor, relative to the ASTER GDEM, visual inspection of the DEMs revealed evidence that for certain areas surface topographies had been correctly extracted. The surface topography of the GC Corona DEM, in particular, shows a good deal of similarity to those of the ASTER GDEM. The topography of the Gangotri glacier is a good example of this comparability (Figure 6.8). Additionally, some glaciated areas covered by the GC and ND Corona DEMs show up clearly as having experienced surface lowering, particularly within 1960s terminus regions. Gangotri glacier, for example, is shown to have experienced surface lowering in ablation zones between 1965 and 2001. This ice surface lowering, occurring within the 1965 extent of Gangotri, is most prominent in terminus regions where large elevation losses correspond well to the ice area that had disappeared by 2001.


**Figure 6.8: Comparison of the surface topography of the main Gangotri trunk in the GC Corona DEM and ASTER GDEM.**

### 6.2.3. Vertical accuracy test: Valley bottoms

To assess the accuracy of ice surface lowering identified at the lower regions of the Gangotri, Milam, Uttari Nanda, Nanda Devi 1 glaciers, elevation differences between the Corona DEMs and ASTER GDEM for the non-glaciated valley bottoms adjoining

each selected glacier were analysed using the method described in section 5.3.3.1. The location and extent of these accuracy tests are shown in figure 6.9 and 6.10.

The results of each valley bottom accuracy test are presented in table 6.5. Compared to that of the entire GC and ND Corona DEMs, the minimum, maximum, mean and RMSE values of the elevation differences measured at each of the test sites are shown to have reduced. The RMSE values, in particular, are all shown to be <±30 m. Additionally, the correlation between Corona DEM and ASTER GDEM elevations is high at each of the test sites used, with $R^2$ values, ranging from 0.84 to 0.99. Figure 6.11 shows an example of the correlation obtained at the Gangotri test site. Overall, the results of the accuracy assessments demonstrate that, for some relatively flat regions of the high mountainous terrain modelled, the accuracy of Corona DEM elevations is

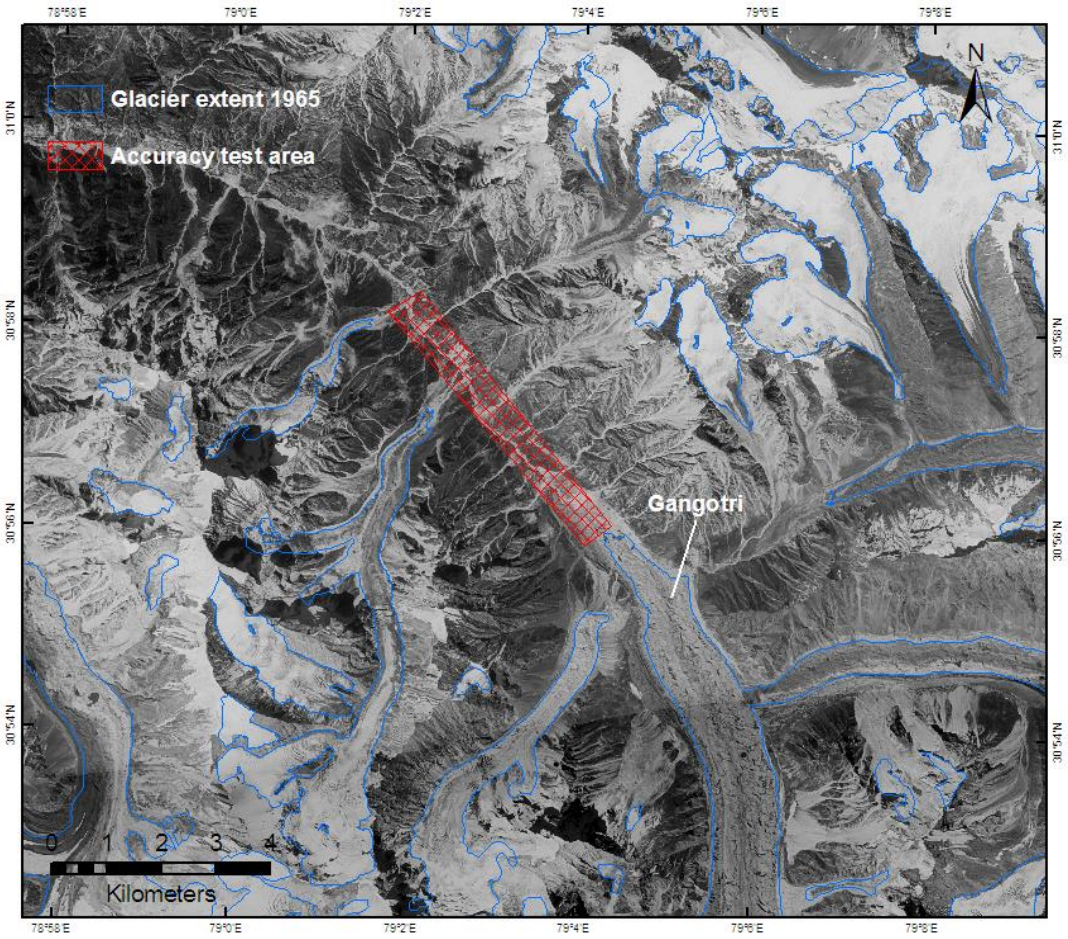


**Figure 6.9: Location of the elevation accuracy test site at the non-glaciated valley adjoining the Gangotri glacier. Background image: Corona, 24th Sep. 1965.**

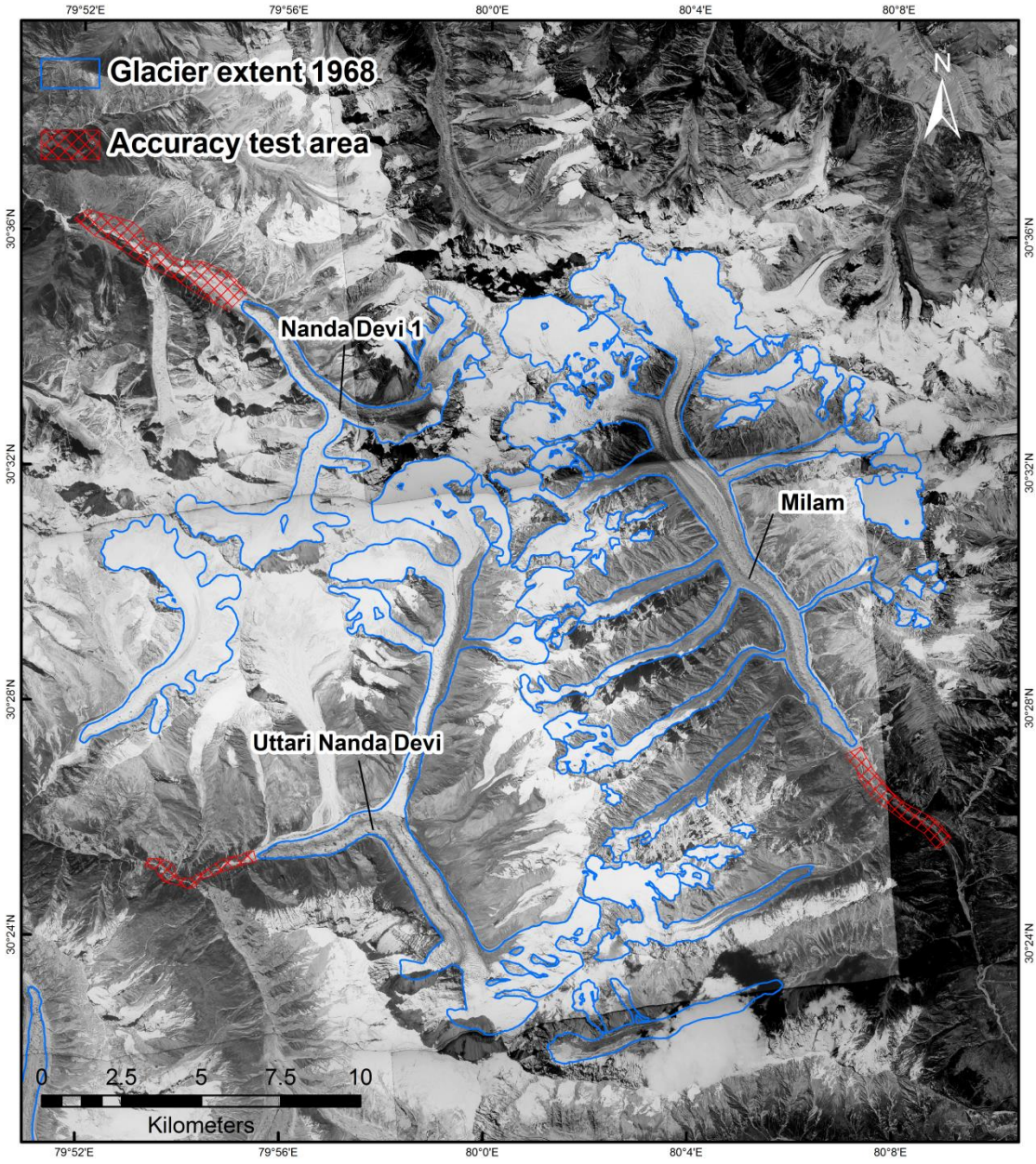


**Figure 6.10: Location of the elevation accuracy tests sites in the non-glaciated valley adjoining the Milam, Uttari Nanda Devi and Nanda Devi 1 glaciers. Background image: Corona, 27th Sep. 1968.**

**Table 6.5: Elevation difference statistics between the Corona DEMs and the ASTER GDEM at each accuracy test site.**

| Accuracy measure | Elevation error (m) | | | | No. of elevation points checked |
|---|---|---|---|---|---|
| | Gangotri | Milam | Uttari Nanda Devi | Nanda Devi 1 | |
| Minimum | -72 | -31 | -39 | -56 | 200 each |
| Maximum | 87 | 106 | 84 | 45 | |
| Mean | 9 | -1 | 15 | -19 | |
| RMSE | ±26.36 | ±26.93 | ±27.27 | ±27.72 | |

improved. Following the assumption that elevation errors increase according to slope, it would therefore be reasonable to suggest that the Corona glacier snout elevations nearby to each test site might exhibit similar respective vertical accuracies. The lower portions of each glacier, for example, effectively flatten the terrain between adjacent valley sides and are characterised by low slope gradients (around 24°).

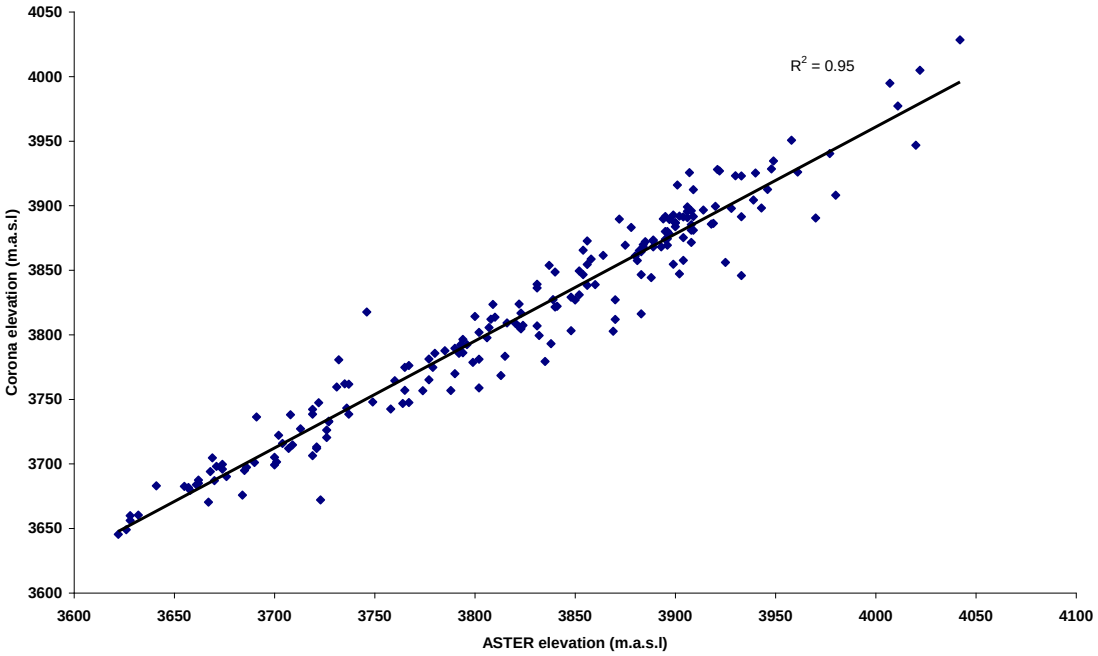


**Figure 6.11: Elevation of 200 points located at the Gangotri accuracy test site extracted in both the GC Corona DEM and the ASTER GDEM.**

## 6.3. Glacier snout volume and surface change derived from Corona DEMs

### 6.3.1 Gangotri Chaukhamba

Figure 6.12 shows the spatial distribution of surface changes derived from the comparison of Corona and ASTER GDEM elevations for the snout regions of Gangotri glacier. Despite the Corona DEM being generally lower than the ASTER GDEM, the portions of the DEM corresponding to the glaciated extent of Gangotri glacier in 1965 show up clearly as having experienced surface lowering, suggesting that glacier downwasting may have occurred. This surface lowering is particularly prominent in the 1965 terminus regions, where large elevation differences correspond to ice areas that had disappeared by 2001.

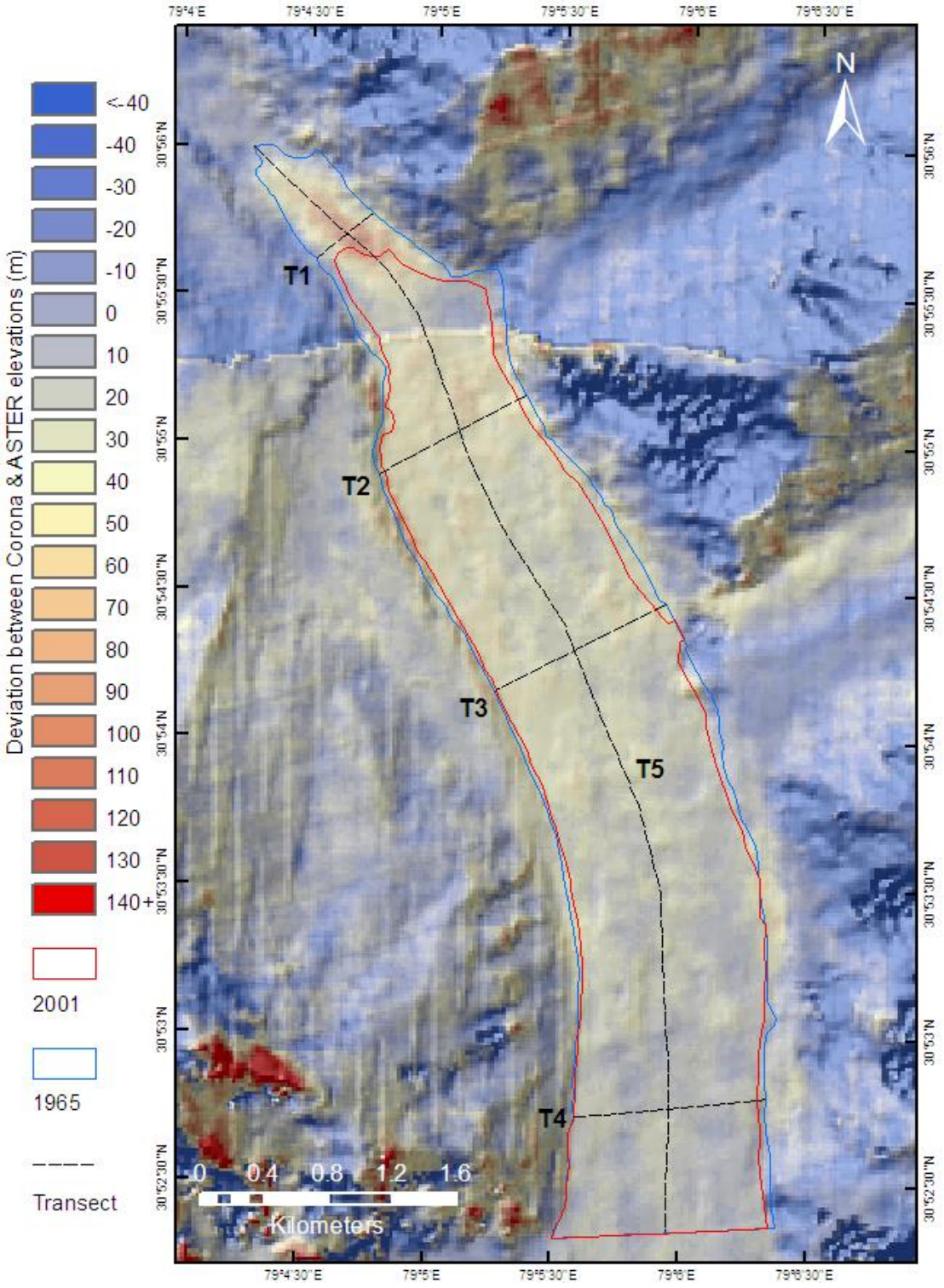


**Figure 6.12: Deviations in the surface of the GC Corona DEM (centred on Gangotri snout), relative to the ASTER GDEM. Positive values reveal surface lowering between 1965 and 2000s. In addition to the positions of 1965 and 2001 glacier outlines the location of five elevation transects are shown.**

Analysis of the surface changes at the lower portions of Gangotri glacier from 1965-2001 reveal that on average the ice surface has lowered by 27.31 m, equating to a volume loss of 210.4 x $10^6$ $m^3$ (see Table 6.6). However, this average surface lowering does not exceed the errors estimated for nearby flat regions. In contrast to this, surface lowering close to the 1965 terminus is considerably larger than the errors stated. The results of each of the five elevation transects, shown in figure 6.13 and 6.14, show a typical pattern of glacier downwasting, with surface lowering being largest in terminus regions and then reducing as elevation increases. This decrease of surface lowering with elevation is shown particularly well in figure 6.15. Although unsurprising in terms of glacier change characteristics, the presence of this pattern gives support to the accuracy of the Corona DEM ice surface.

The large surface lowering shown at the now ice-free 1965 glacier terminus region suggests that elevation extraction in this region may have been successful. This is demonstrated further in figure 6.14 and 6.15. In figure 6.14, for example, the minimum Corona surface elevation is seen to closely match that of the ice-free valley bottom in the 2000s. Above this point, the Corona DEM surface then increases (around 3900 m.a.s.l) suggesting the presence of the 1965 ice terminus. In contrast the ice surface represented by the ASTER GDEM is shown to begin ~3940 m.a.s.l.

**Table 6.6: Surface lowering statistics, volume change and estimated valley bottom accuracy for the Gangotri snout.**

| | **Surface lowering (m)** | **$RMSE_Z$ (m)** | **Volume loss ($m^3$)** |
|---|---|---|---|
| **Minimum** | -8.1 | 26.36 | 210.4 x $10^6$ |
| **Maximum** | 110.77 | | |
| **Mean** | 27.31 | | |

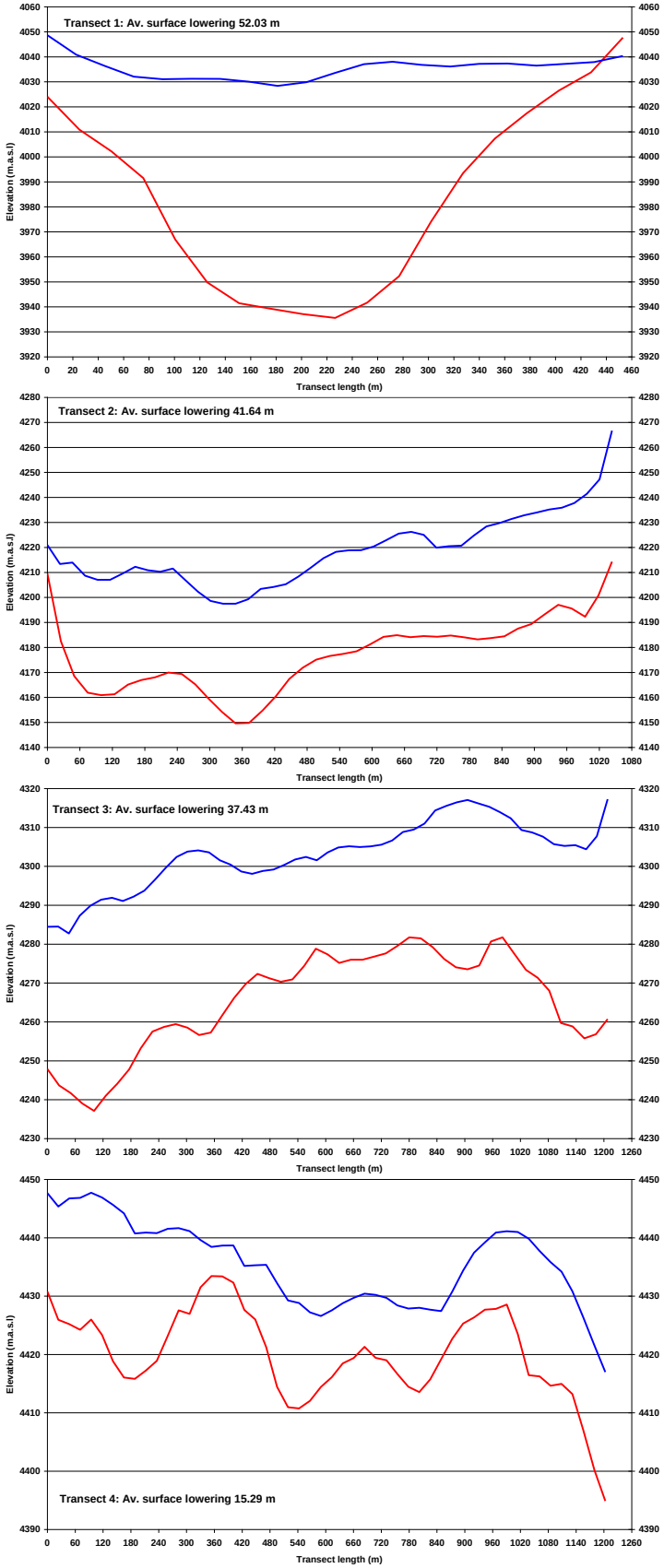


**Figure 6.13: Comparison of Corona DEM (blue) and ASTER GDEM (red) elevation across transects 1-4 on Gangotri snout.**

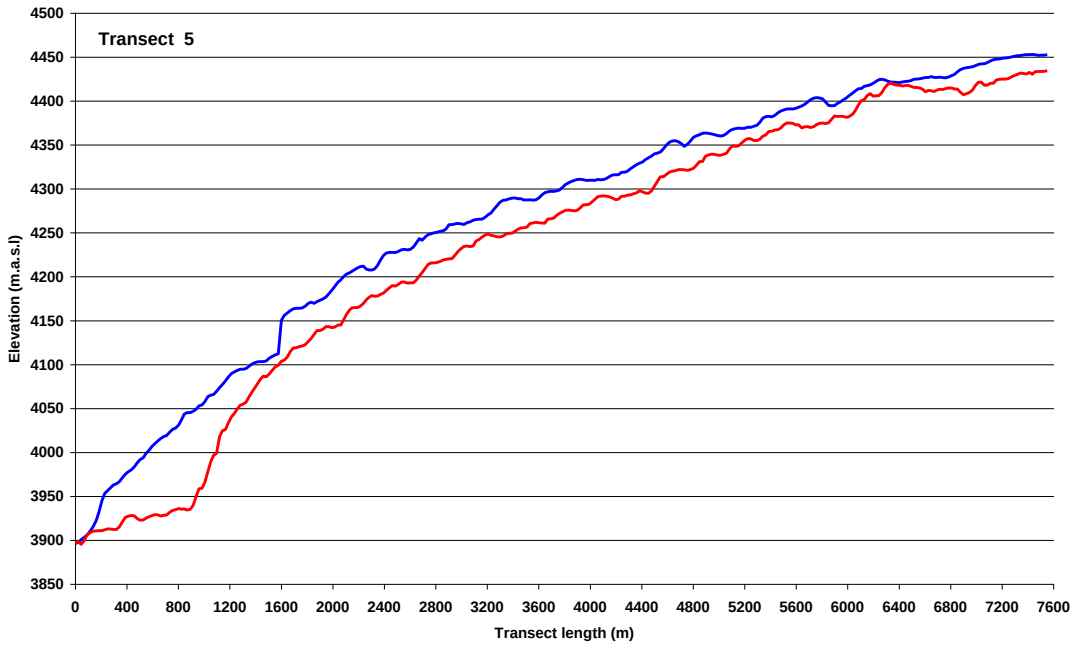


**Figure 6.14: Comparison of Corona DEM (blue) and ASTER GDEM (red) elevations across the length transect (transect 5) on Gangotri snout.**

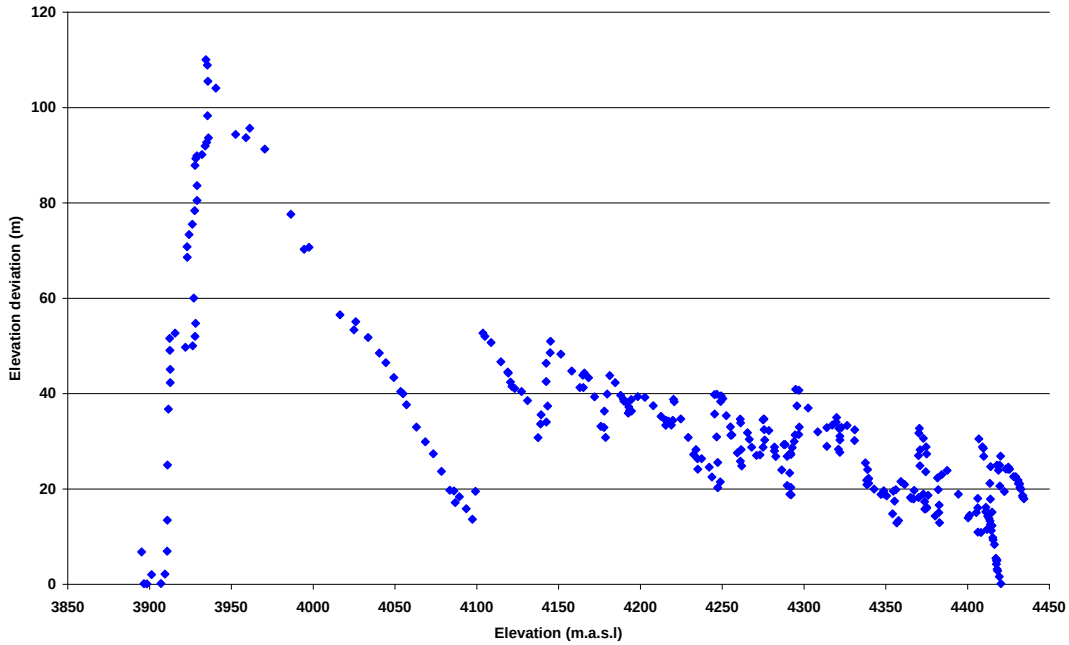


**Figure 6.15: Differences in Corona DEM and ASTER GDEM elevations across transect 5 on Gangotri snout.**

The surface differences between the Corona DEM and ASTER GDEM at Gangotri glacier are well highlighted by the four elevation transects presented in figure 6.13. Transect 1 is of particular interest, with the typical deglaciated U-shape valley represented in the ASTER GDEM contrasting the possible 1965 ice surface topography represented in the Corona DEM. Notably, the average ice surface lowering shown for transects 1 to 3 is higher than the RMSEs estimated for the adjacent elevation accuracy test site.

### 6.3.2. Nanda Devi

The elevation differences between the ND Corona DEM and the ASTER GDEM at the lower portions of the Milam, Uttari Nanda Devi and Nanda Devi 1 glaciers are presented in table 6.7. Each of the three glaciers included at the ND site are shown to have experienced surface lowering since 1968, which in terminus regions exceed errors estimated for nearby test sites. However, in terms of mean surface lowering only two glaciers, Milam and Nanda Devi 1, exceed their errors estimates considerably. The location of these four glaciers is presented in the previous section (Figure 6.10).

Overall, Milam glacier is shown to have experienced the largest surface lowering of the three glaciers selected at the ND study site. Similar to Gangotri glacier, the lower portions of Milam are shown to have experienced a typical pattern of glacier downwasting with surface lowering being largest in 1968 terminus regions and reducing with elevation (see Figures 6.16-6.18). The spatial distribution of surface elevation changes estimated for the lower regions of Milam glacier is shown in Figure

**Table 6.7: Surface lowering statistics, volume change and estimated valley bottom accuracy for the Milam, Uttari Nanda Devi, Nanda Devi 1 and Nanda Devi 2 snouts.**

| Glacier Snout | Surface lowering (m) | | | $RMSE_Z$ (m) | Volume loss ($m^3$) |
|---|---|---|---|---|---|
| | Minimum | Maximum | Mean | | |
| Milam | 3.25 | 142.28 | 66.73 | 26.93 | $153.9 \times 10^6$ |
| Uttari Nanda Devi | -45.3 | 86.88 | 23.81 | 27.28 | $55.3 \times 10^6$ |
| Nanda Devi 1 | 14.49 | 109.61 | 48.97 | 27.73 | $126.3 \times 10^6$ |

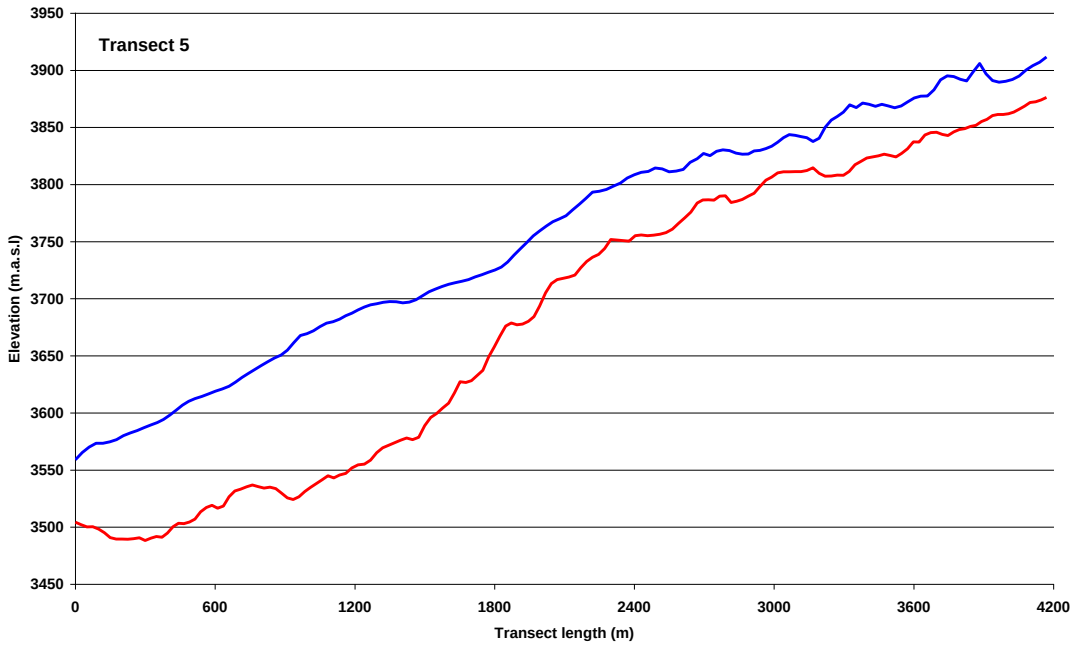


**Figure 6.16: Comparison of Corona DEM (blue) and ASTER GDEM (red) elevations across the length transect (transect 5) on Milam snout.**

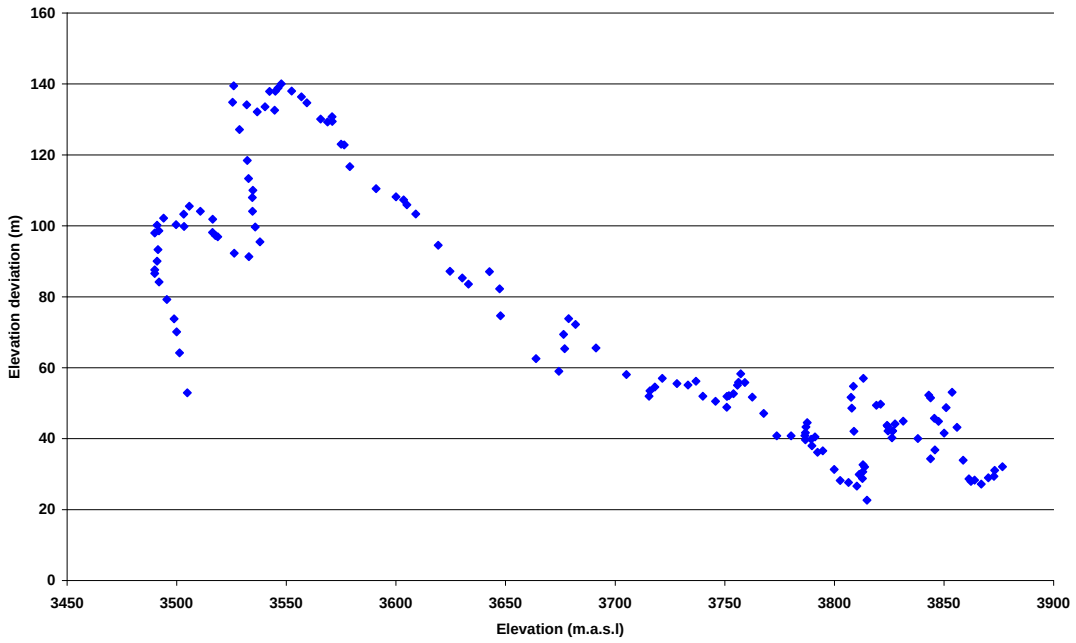


**Figure 6.17: Differences in Corona DEM and ASTER GDEM elevations across transect 5 on Milam snout.**

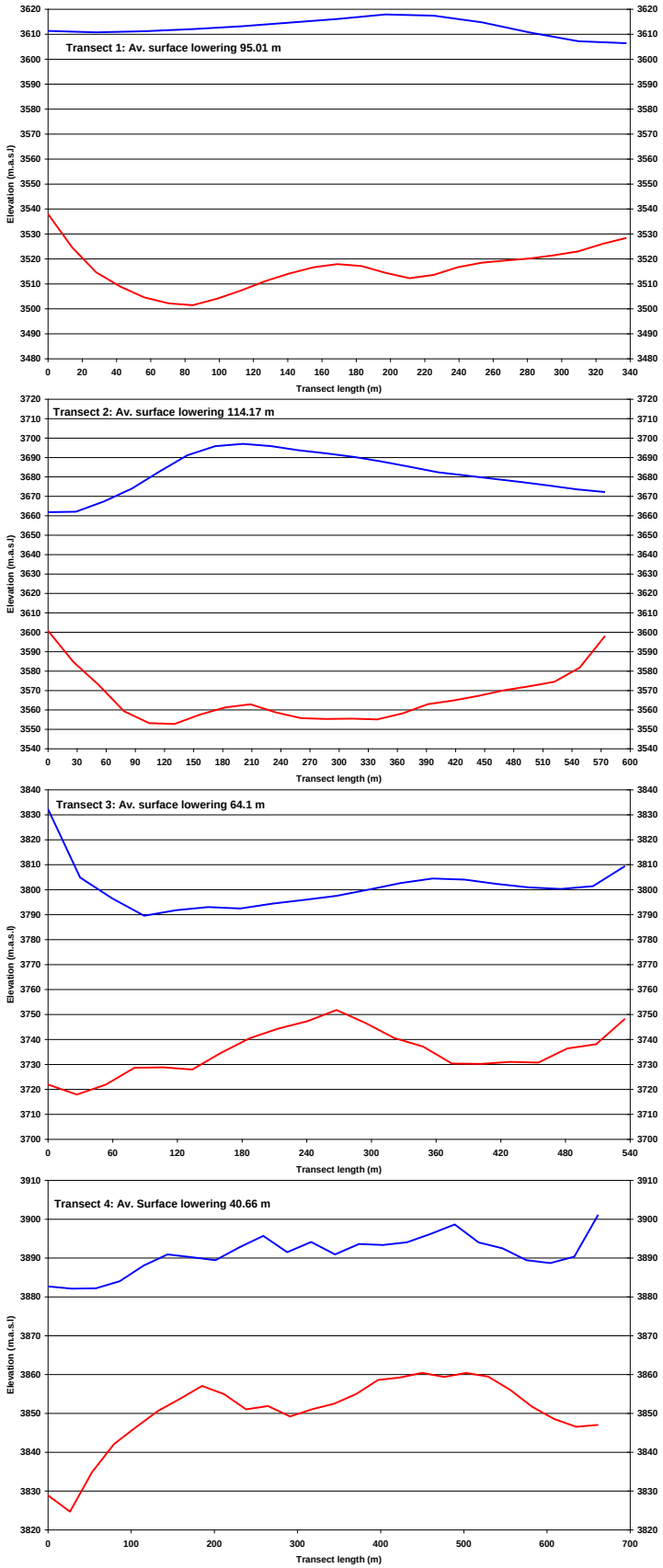


**Figure 6.18: Deviations in the surface of the ND Corona DEM (centred on eastern side of study area), relative to the ASTER GDEM. Positive values reveal surface lowering between 1965 and 2000s.**

6.19. Despite the surface of the Corona DEM being both moderately lower and higher on adjacent east and west facing slopes, compared to the ASTER GDEM, surface lowering is pronounced for areas which correspond to the extent of Milam glacier in 1968. Surface lowering estimated for the 1968 terminus region is particularly pronounced, highlighted by the contrasting Corona-ASTER surface topographies shown in figure 6.16 and 6.18, reaching maximums of 142.38 m. Analysis of the four glacier width transects placed along Milam glacier, shown in figure 6.18, reveals that elevation differences at each exceeded vertical errors estimated at adjacent non-glaciated valley bottoms (±26.93 m).

The spatial distribution of surface elevation changes at the Uttari Nanda Devi and Nanda Devi 1 glaciers is shown in figures 6.20 and 6.21, respectively. Similar to that shown for Milam glacier, surface lowering estimated at each of these two glaciers corresponded well with ice extents delineated for 1968. Maximum surface lowering for terminus regions of the Uttari Nanda Devi and Nanda Devi 1 glaciers was again shown to be pronounced (ranging from 86 m to 109 m) and exceeded errors estimated for nearby valley bottoms (~±27m).

As with Gangotri and Milam glacier, surface lowering estimated for Nanda Devi 1 was shown to exhibit a typical pattern of glacier wastage, being largest at terminus regions and reducing with elevation (see Figure 6.22 & 6.23). Additionally, surface differences identified at each width transect exceed vertical errors estimated for the adjacent valley bottoms (Figure 6.24). In contrast, surfacing lowering at Uttari Nanda Devi glacier did not exhibit a typical pattern of glacier wastage. Although shown to be pronounced for 1968 terminus regions, at higher elevations surface lowering varied considerably and did not exceed error estimated for the adjacent valley bottoms (see Figure 6.25-6.27). These surface change characteristics shown for Uttari Nanda Devi glacier may be indicative of elevation errors, possibly induced by: (1) image wide GCP sampling issues - less than half the number of GCPs were sampled in the ND Corona image batch in comparison to the GC Corona image batch; (2) localised GCP sampling issues - GCPs were often sampled in valley bottom locations adjacent to glacier snouts

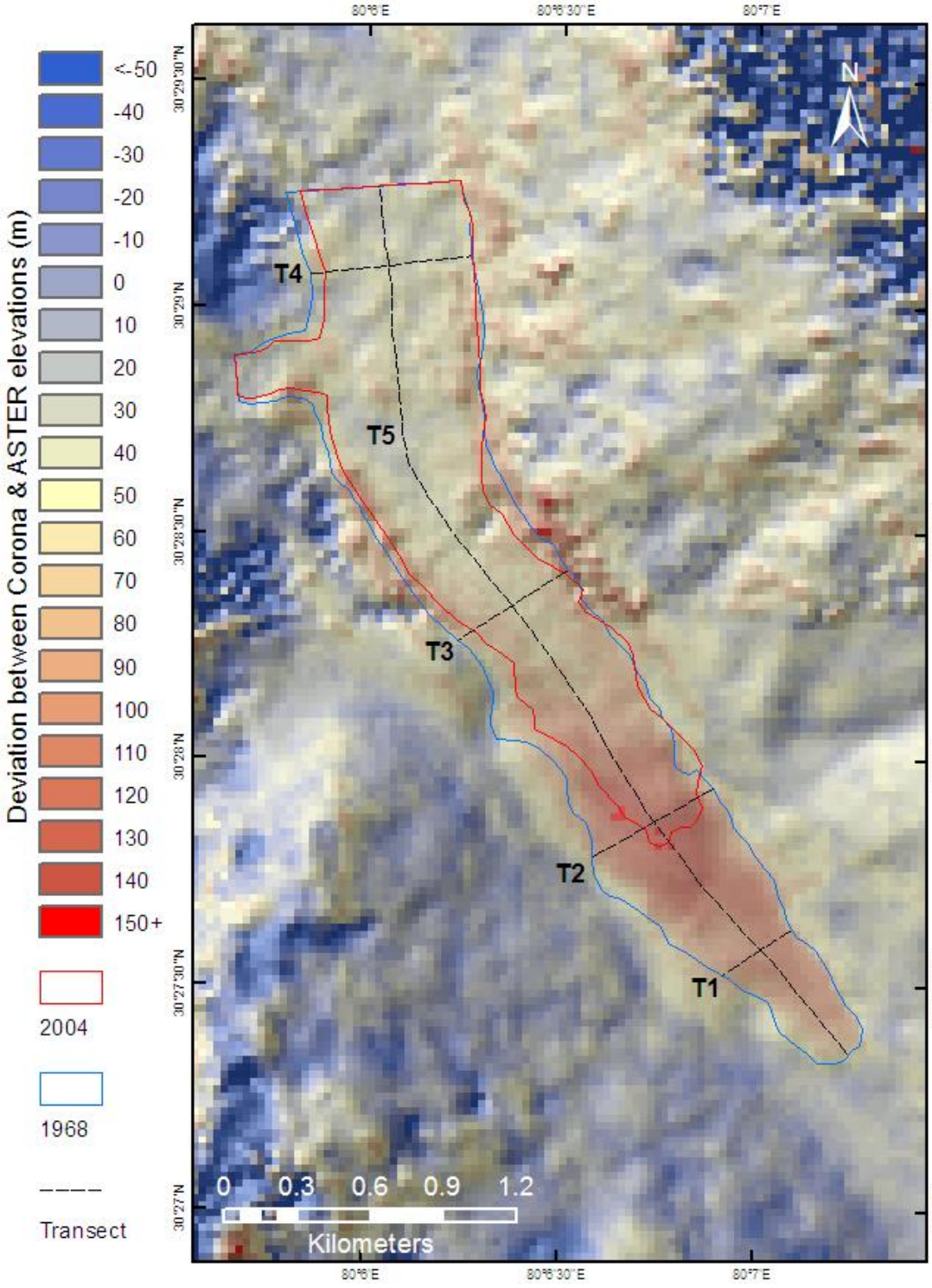


**Figure 6.19: Deviations in the surface of the ND Corona DEM (centred on Milam snout), relative to the ASTER GDEM. Positive values reveal surface lowering between 1968 and 2000s. In addition to the positions of 1968 and 2004 glacier outlines the location of five elevation transects are shown.**

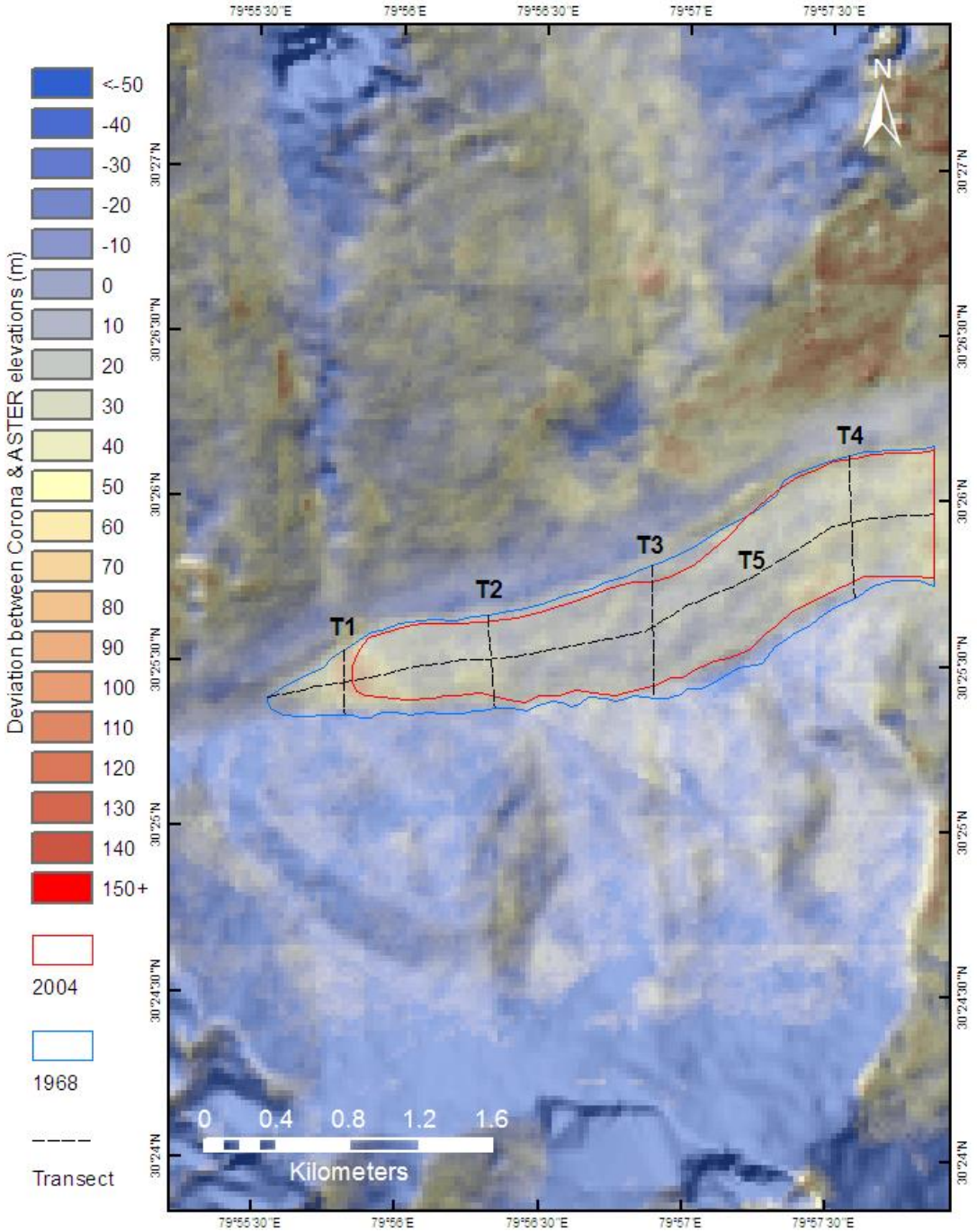


**Figure 6.20: Deviations in the surface of the ND Corona DEM (centred on Uttari Nanda Devi snout), relative to the ASTER GDEM. Positive values reveal surface lowering between 1968 and 2000s. In addition to the positions of 1968 and 2004 glacier outlines the location of five elevation transects are shown.**

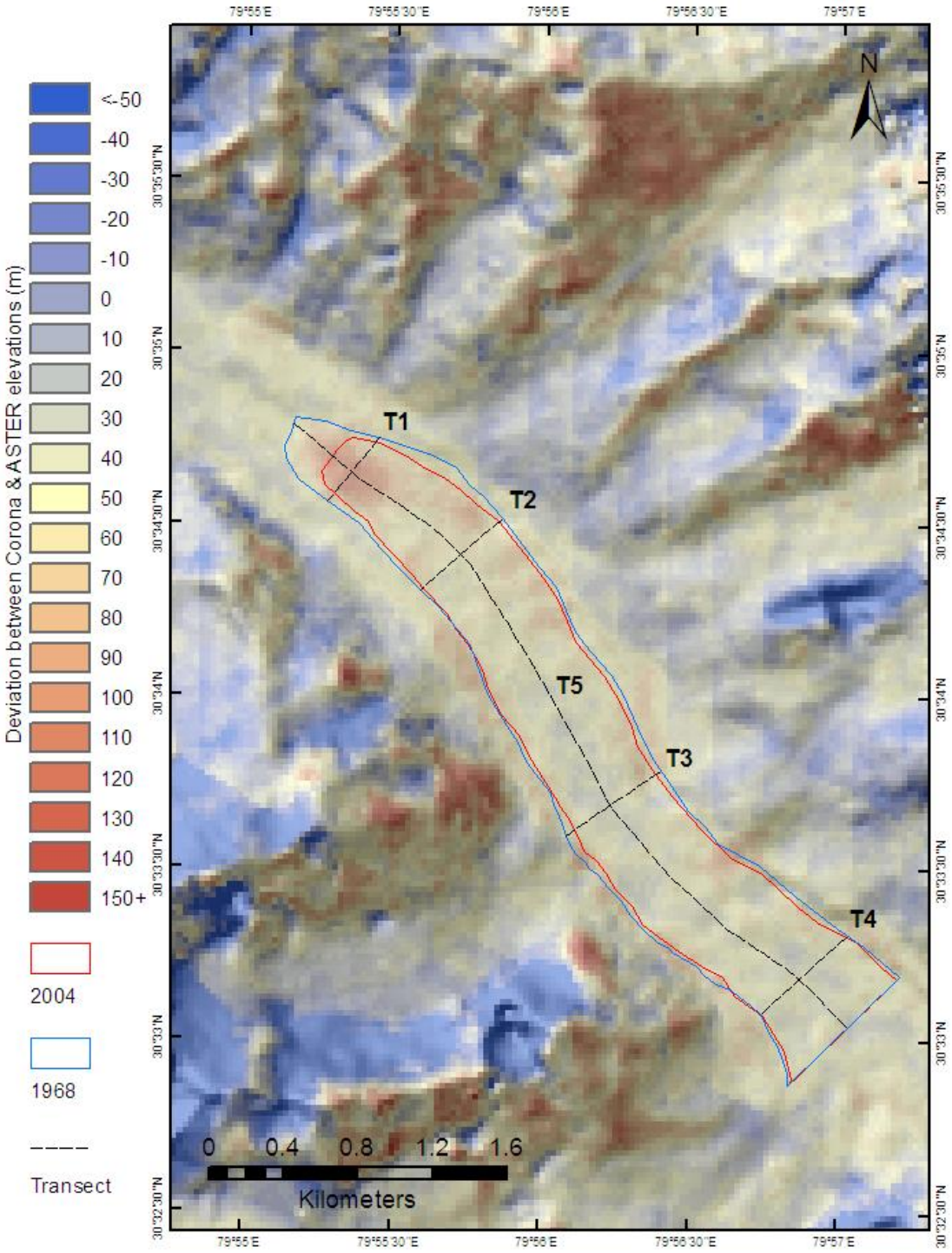


**Figure 6.21: Deviations in the surface of the ND Corona DEM (centred on Nanda Devi 1 snout), relative to the ASTER GDEM. Positive values reveal surface lowering between 1968 and 2000s. In addition to the positions of 1968 and 2004 glacier outlines the location of five elevation transects are shown.**

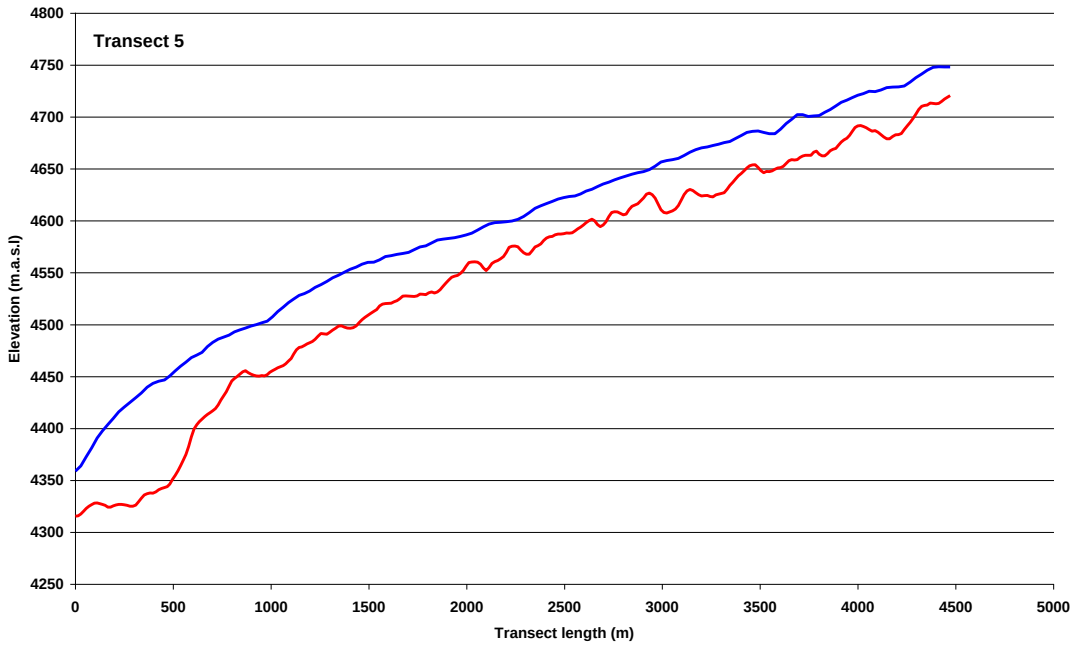


**Figure 6.22: Comparison of Corona DEM (blue) and ASTER GDEM (red) elevations across the length transect (transect 5) on Nanda Devi 1 snout.**

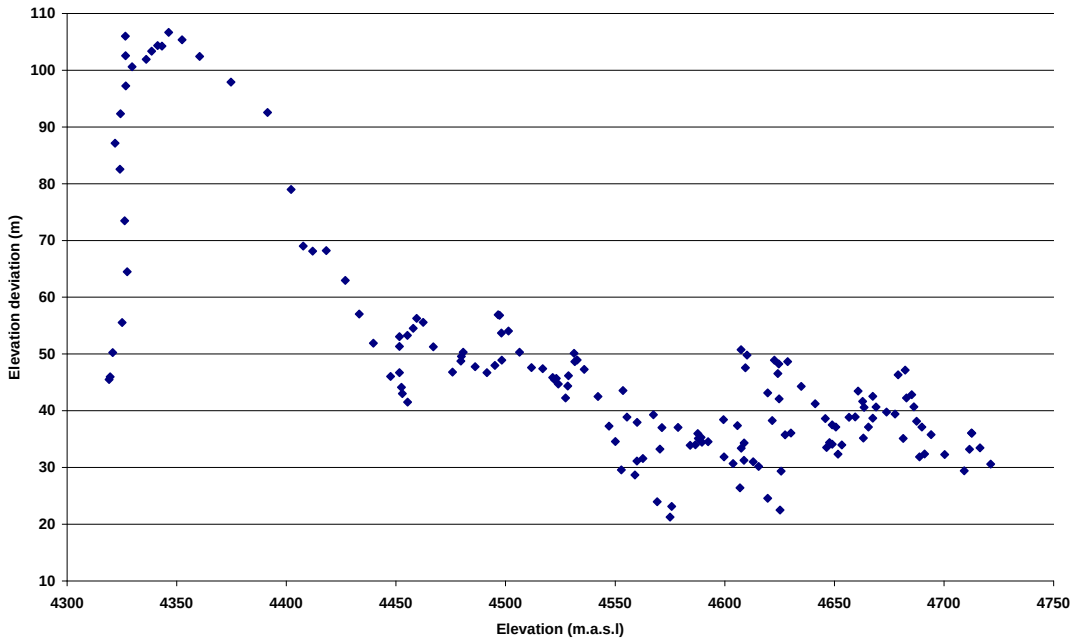


**Figure 6.23: Differences in Corona DEM and ASTER GDEM elevations across transect 5 on Nanda Devi 1 snout.**

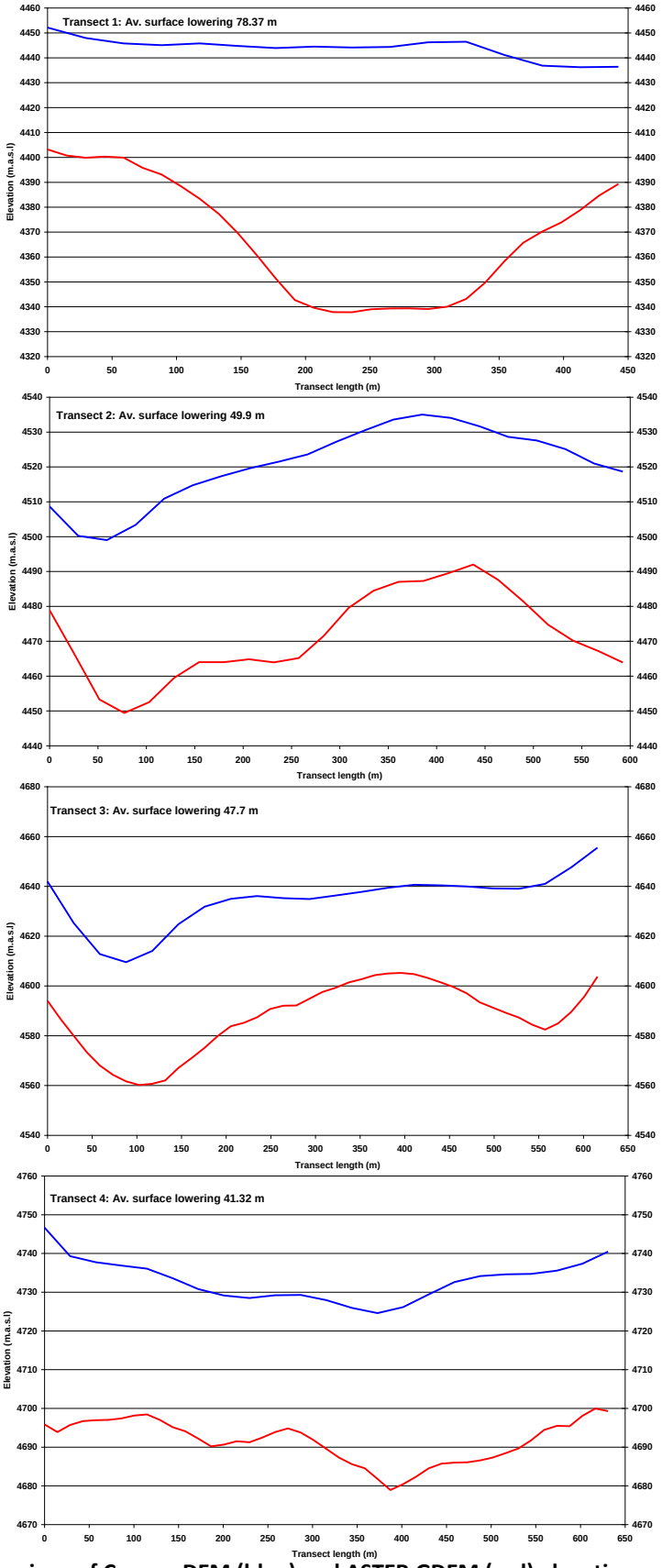


**Figure 6.24: Comparison of Corona DEM (blue) and ASTER GDEM (red) elevation across transects 1-4 on Nanda Devi 1 snout.**

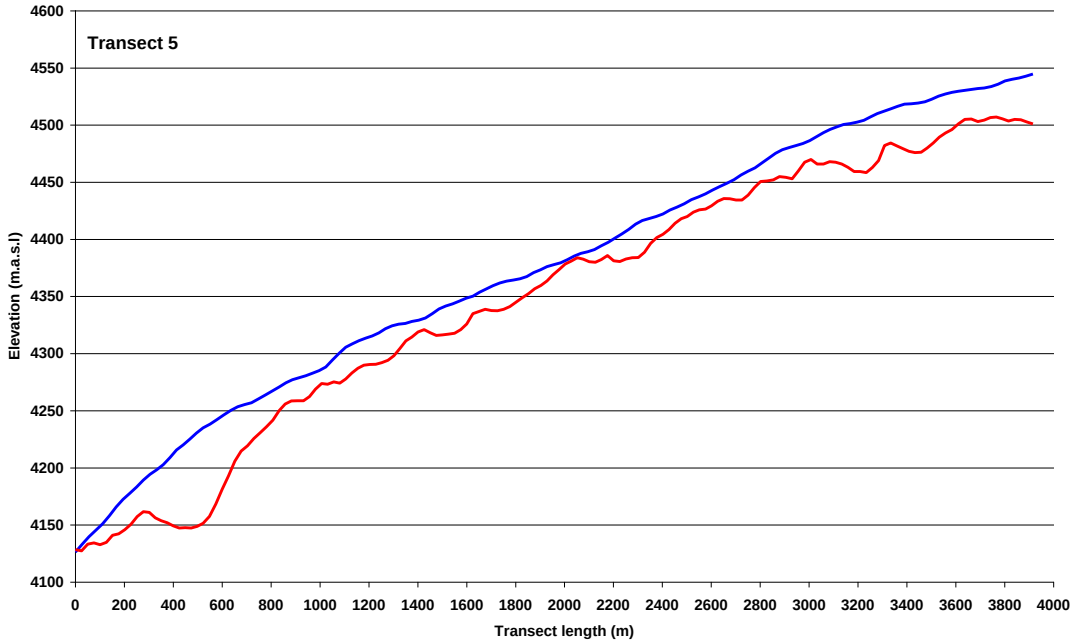


**Figure 6.25: Comparison of Corona DEM (blue) and ASTER GDEM (red) elevations across the length transect (transect 5) on Uttari Nanda Devi snout.**

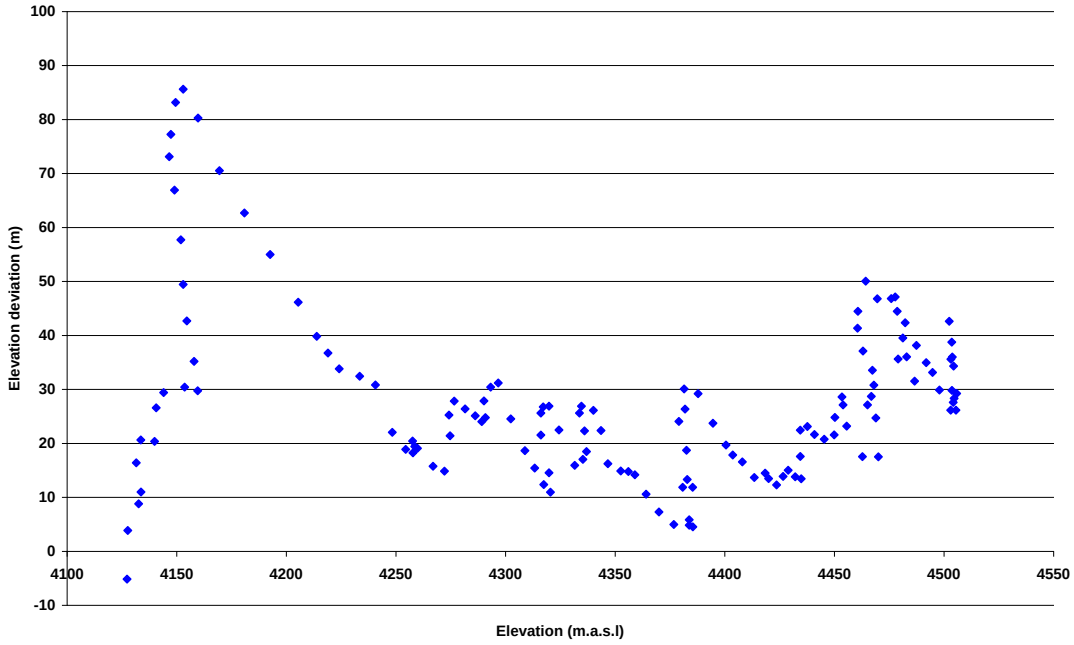


**Figure 6.26: Differences in Corona DEM and ASTER GDEM elevations across transect 5 on Uttari Nanda Devi snout.**


**Figure 6.27: Comparison of Corona DEM (blue) and ASTER GDEM (red) elevation across transects 1-4 on Uttari Nanda Devi snout.**

and were less frequent for more elevated glacier regions. Therefore the influence of DEM extraction errors was often greater as glacier elevation increased.

Alternatively, the surface change characteristics shown for Uttari Nanda Devi may indicate the influence of debris-cover. Visual analysis of Uttari Nanda Devi glacier in the satellite imagery utilised revealed extensive supraglacial debris-cover on the lower glacier trunk. Debris-cover, to varying extents, can influence the geometric responses of glaciers to climate change (Scherler *et al.,* 2011; Benn & Lehmkuhl, 2000). For debris-covered glaciers in the Khumbu Himalaya, for example, surface elevation changes observed by Bolch *et al*. (2008), from 1962 to ~2002, showed similar characteristics as presented for Uttari Nanda Devi glacier. Without a detailed spatial and temporal analysis of debris-cover at Uttari Nanda Devi glacier, this assumption cannot be tested.

## 6.4. Discussion

### 6.4.1. Corona orthorectification using ASTER horizontal and vertical reference data

The advantages of the use of Corona imagery as a glacier mapping tool over other satellite-based image datasets are threefold. Firstly, the Corona archive includes imagery acquired in the 1960s, extending the temporal availability of historic satellite imagery for regions included in the mission coverage, such as the Himalayas. Secondly, the Corona KH-4, KH-4A and KH-4B camera models acquired imagery in stereo, allowing image areas covered to be mapped three-dimensionally through the extraction of DEMs. Thirdly, Corona imagery is available to purchase at a relatively low cost ($30 for an image strip covering ~2630 $km^2$ (KH-4B)). Additionally, with ground resolutions as low as 1.8 m, Corona imagery offers an alternative to aerial photography (Slama *et al.*, 1980). Considering these factors, Corona imagery represents a potentially valuable glacier mapping tool, particularly in regions for which topographic maps and aerial photography are limited, such as the Himalayas (Bhambri & Bolch, 2009).

The advantages of Corona as a mapping tool are countered by the difficulties faced correcting the large geometric distortions present within raw Corona imagery and subsequently transforming image strips into a projected coordinate system (Altmaier & Kany, 2002). These transformation difficulties continue to limit the use of Corona as a source of historic high resolution imagery (Galiatsatos *et al.,* 2008). The central methodological aim of this study was to develop a broadly replicable and low cost method of orthorectifying Corona imagery. This was achieved through the use of: (1) a non-metric camera frame model photogrammetry approach and (2) horizontal and vertical reference data from ortho-ASTER imagery and the freely available ASTER GDEM.

The orthorectification process applied here achieved geometric accuracies of ±7.5 m and ±16.7 m for the Corona imagery used at the GC and ND study sites, respectively. Subsequently, the aim of achieving Corona geometric accuracies within 1 pixel of the horizontal reference source (ortho-ASTER imagery: 15 m) was met (for GC) or closely met (for ND). The geometric accuracies obtained were also shown to match or better those obtained for Corona imagery used for glacier mapping purposes by Bolch *et al.* (2008), Schmidt & Nusser (2012) and Narama *et al.* (2009) ( <±15 m, ~±15 m, <±20 m and <±30 m, respectively). Furthermore, the Corona accuracies achieved compared well with those reported for other geospatial datasets used for Himalayan glacier mapping purposes (e.g. raw ASTER satellite imagery: <±15 m (Bolch *et al*., 2008); ALOS satellite imagery: <±30 m (Narama *et al*., 2009); and topographic maps: <±15 m (Salerno *et al*., 2008).

The methodology applied here to orthorectify Corona imagery differs from that used in previous studies by combining a non-metric camera photogrammetry approach with low cost ASTER reference data in a high mountainous environment. Previously used Corona geometric correction methodologies can be roughly divided into two approaches, (1) image transformation approaches and (2) alternative photogrammetry-based approaches. A summary of the studies that have applied these two approaches to Corona imagery, and the horizontal accuracies achieved, is

provided in chapter 2. By comparing the results of these studies with those achieved here, the following conclusions were made.

(1)For Corona-based glacier mapping studies that only cover small areas and do not require surface elevation information, the transformation approach offers a preferable choice over the comparatively complex non-metric camera frame model approach used in this study. Bhambri *et al.* (2011), for example, showed that the transformation approach can be applied to geometrically correct Corona imagery to an accuracy of <±15 m, using GCPs derived from ASTER imagery. However, the image transformation approach does not provide the photogrammetric framework needed to extract DEMs from Corona stereo pairs and requires a number of image pre-processing steps that hinder its use over large areas (such as creating individual glacier image subsets).

(2) Compared to the empirical photogrammetry approach applied here, rigorous photogrammetric approaches likely represent a better choice for orthorectifying Corona imagery. This conclusion agrees with those made by Casana & Cothren (2008) and Galiatsatos *et al.* (2008), who refer to the accuracy of the rigorous approach when estimating the orientation parameters of the Corona camera. However, as noted in chapter 2, the rigorous approach requires extensive camera model development time and has yet to be tested for Corona imagery acquired in high mountainous environments.

Despite the advantages of image transformation and rigorous photogrammetry approaches, it is the author's belief that, through combining the benefits of photogrammetry (image orthorectification and DEM extraction) with time and cost efficient image processing steps, the methods applied in this study offer a good alternative for studies requiring Corona orthorectification. By using DGPS survey data, other variants of the empirically-based non-metric camera frame model approach have achieved better horizontal accuracies than those presented here (e.g. <±6 m, Altmaier & Kany (2002) and Schmidt *et al*. (2001)) and, where possible, these methodologies would also be recommended. In comparison, however, this study has

shown that Corona imagery acquired over high mountainous terrain can be corrected to a good degree of accuracy without the use of high resolution satellite imagery (such as Galiatsatos *et al.* (2008) and Casana & Cothren (2008)), topographic maps (such as, Namara *et al.* (2009)) or DGPS surveys.

With regards to the glaciological aims of this study, the accuracy of the orthorecitifed Corona imagery produced was such that in most places glaciated features closely matched those visible in ortho-ASTER imagery, allowing planimetric comparisons to be made. Furthermore, the close agreement between the glacier area and length changes observed in this study, for the GC and ND study sites, and those obtained by previous studies (e.g. Bhambri *et al.* (2008) and Dobhal and Mehta (2010)) supports the planimetric accuracy of the orthorecitified Corona images produced. However, despite the general success of the Corona orthorectification procedure, some areas of image distortion were still evident, resulting in spatial inconsistencies when compared to the ortho-ASTER imagery. With the non-metric camera frame model approach applied in this study, the quality of the triangulation process is largely determined by the sample size and distribution of GCPs (Altmaier & Kany, 2002; Galiatsatos, 2004). Here, a number of Corona image strips used lacked sufficient GCPs. Furthermore, GCPs were often located in clusters and transects. These two distribution features have been found to be particularly detrimental to the quality of the triangulation process (Mather, 1999).

GCP sampling in this study was hindered by two main factors. The first factor concerned a range of image quality issues, affecting both the Corona and ASTER datasets, including cloud/snow cover, terrain shadowing, poor image contrast (Corona imagery) and areas of image skewing (ortho-ASTER imagery). Image skewing is a quality issue specific to ortho-ASTER imagery and represents a limitation of the use of this dataset. Hence, freely available Landsat satellite imagery which undergo more rigorous geometric calibrations (Storey *et al*., 2006) could have provided an alternative source of low cost horizontal reference information. However, the higher geometric quality of Landsat imagery, compared to ortho-ASTER imagery, is offset by their higher resolution (30-79 m).

Spatial resolution of the ASTER horizontal and vertical reference sources represented the second GCP sampling constraint. Ideally, when registering one geospatial dataset to another, the spatial resolution of the master dataset should be similar to the slave dataset (Mather, 1999; Kääb, 2005a.; Bhambri & Bolch, 2009). Here, the spatial resolution of the horizontal (ortho-ASTER imagery: 15 m) and vertical (ASTER GDEM data: 30 m) reference sources was relatively coarse compared to the 1.8 m resolution Corona imagery. Due to this, it was sometimes difficult to locate corresponding GCPs. As a result, GCPs were often located in non-vegetated image areas (clustering around glaciers), or along valley bottoms utilising river junction features (forming linear GCP transects), reducing the quality of the geometric GCP network. The use of ASTER reference data, although cost-effective, therefore placed a limitation on the Corona correction process.

As an alternative to the approach used here, Bolch *et al.* (2008) successfully orthorectified Corona imagery (~±15 m), acquired over the Nepalese Himalaya, using the RSG ERDAS Imagine module. Including a photogrammetric model specifically designed for the Corona camera (camera parameter inputs are not specified), RSG was similarly able to utilise ortho-ASTER derived GCPs to correct Corona imagery. However, as an independently developed ERDAS Imagine add-on, the purchasing of the RSG software would represent an additional project expense. Nevertheless, a comparative test between the RSG and non-metric camera frame model approaches for correcting Corona imagery would be an interesting future area of research.

### 6.4.2. Extracting Corona DEMs: Challenges and limitations

In comparison to the orthorectification process, the extraction of DEMs from Corona stereo pairs was less successful. Here, Corona DEMs were extracted with the aim of calculating glacier volume change, through comparison with more recent ASTER GDEM glacier surface elevations. However, due to the magnitude of errors present within the Corona DEMs extracted, the calculation of volume change for glaciers at each of the GC and ND study sites was largely unachievable. Although many glaciated

and non-glaciated terrain features were correctly modelled (in terms of geometry), the vertical accuracy of the two Corona DEMs extracted (GC and ND) was poor. Considering only locations corresponding to GCPs manually derived during the orthorectification process, vertical RMSEs equated to 179 m and 275 m for the GC and ND DEMs, respectively. Assessing the cause of these vertical errors, a number of factors are considered, the first of which is stereo image orientation.

Stereo image orientation is cited as the most critical factor affecting the success of DEM extraction processes (e.g. Nuth & Kääb, 2010; Kääb, 2005a.; Galiatsatos *et al.*, 2008). Errors introduced during stereo pair geometric correction, as a result of poor and/or uneven GCP sampling and GCP positioning errors, are transferred directly to the extracted DEM. Importantly, these errors are then increased by an order of magnitude for overlapping image areas. In this study, issues were encountered with regards to the sampling and distribution of GCPs, resulting in the presence of geometric inconsistencies for some areas of the Corona stereo pairs used. Although not large enough to prevent the delineation of comparable glacier outlines from the orthorecitified Corona imagery, it is clear that GCP sampling had an impact on the DEM extraction process. The number of GCPs sampled within overlapping Corona image areas, for example, was far lower at the ND study site (64 GCPs) compared to the GC study site (169 GCPs) and this is conversely reflected in the respective vertical accuracies reported. Overall, the presence of geometric errors within the orthorectified Corona stereo imagery used is likely to have hindered interest point matching during DEM generation, resulting in the large vertical errors shown.

The Corona DEM errors induced by stereo pair orientation problems are likely to have been superimposed onto other sources of error inherent to all stereo-scopic derived DEMs generated in high mountainous terrain. DEMs generated in high mountainous environments (which are cited as the worst-case scenario for this procedure (Kääb, 2005a.)) often exhibit large topographic distortions. These distortions are a result of slope perspective and topographic shadowing issues related to the geometry of stereo-satellite sensors relative to the surface of the Earth (Nuth & Kääb, 2010; Kääb, 2005a.; Pieczonka *et al.*, 2011). As a consequence, interest point matching on

mountain ridges and slopes is often problematic and large vertical errors are common. Similar to this study, Bolch *et al.* (2008) generated a Corona DEM from a single stereo pair acquired over the Khumbu Himalaya. Compared to an ASTER DEM, they also encountered large Corona vertical errors of up to 300 m for steep slopes, mountain peaks and areas of high elevation. Moreover, when comparing the ASTER DEM used to topographic map data, Bolch *et al.* (2008) found vertical errors on steep slopes of up to 5000 m, which is similar to the error magnitudes shown here.

The results of a vertical Corona DEM accuracy test, performed in the relatively well GCP sampled Gangotri glacier basin, revealed that elevation errors encountered were also influenced by terrain aspect. Overall, vertical errors were shown to be larger on South, South-west, West and North-west facing slopes, with the largest occurring on South-west and West facing slopes. This variance in vertical error according to aspect is again a common attribute of stereo-scopic derived DEMs. In ASTER DEMs, for example, vertical errors tend to be larger on North facing slopes, these areas being obscured from the 27.6° back looking sensor (Kääb, 2005a.). The influence of aspect on Corona DEM errors is discussed by Bolch *et al.* (2008), who found that elevations were generally too low for Southeastern DEM areas and too high for Northwestern areas, in comparison to an ASTER DEM. They conclude that these errors are the possible result of the instability of the Corona camera sensors during image acquisition.

When assessing possible sources of Corona DEM error, it is important to take note of Galiatsatos *et al.* (2008) and McDonald (1995) who state that no two Corona missions were identical and that in some cases even the For and Aft camera systems were different. This suggests that Corona errors (both vertical and horizontal) may be mission specific. Here, the radiometric quality of each of the Corona stereo pairs used, for example, varied considerably. Galiatsatos *et al.* (2008) attributed these radiometric quality issues to differing sun-camera-geometries. Such issues would have again hindered the DEM generation interest point matching process, resulting in error.

Following on from section 6.1, the suitability of the empirically-based non-metric camera frame model approach used here should also be assessed with respect to the extraction of Corona DEMs. As stated by Galiatsatos (2004), the non-metric camera frame model available in ERDAS Imagine LPS is designed mainly for use with aerial photography acquired at relatively low altitudes. In comparison, Corona imagery was acquired from a space orbit (with known flights altitudes only roughly estimated) using a camera platform that was likely to be instable (McDonald, 1995; Mather, 1999). These flight characteristics will likely affect the accurate modelling of unknown Corona camera parameters, which in turn would contribute to errors encountered during DEM extraction. Despite this, Altmaier & Kany (2002) and Galiastatos (2008) have extracted Corona DEMs, to a higher accuracy than achieved here, using stereo pairs corrected via the non-metric camera frame model approach. Altmaier & Kany (2002) for example, reported vertical errors of ~±10 m, whilst Galiastatos (2008) reported errors of ~±12 m. However, these two studies utilised higher resolution geometric correction reference data, highlighting the importance of this variable when extracting Corona DEMs. Additionally, the Corona imagery used by Altmaier & Kany (2002) and Galiastatos (2008) was not acquired over high mountainous terrain.

As with the orthorectification process, when extracting Corona DEMs for high mountainous environments, rigorous photogrammetric geometric correction approaches are again preferable as they better estimate the unknown parameters of the Corona camera. Using a mathematical model specifically designed for the Corona camera and GCPs sampled from a 1:1000 topographic map, Sohn *et al.* (2004), for example, extracted a Corona DEM covering a mixed urban and mountainous terrain with vertical accuracies <6 m. However, the same limitations of this approach apply as discussed in section 6.1 and chapter 2.

Despite the presence of large vertical errors in the two Corona DEMs extracted, glacier downwasting was detected for Gangotri glacier, located in the GC study site, and the Milam, Uttari Nanda Devi and Nanda Devi 1 glaciers, located in the ND study site. Encouragingly, downwasting for the lower portions of three of these glaciers showed a typical pattern, with surface lowering increasing towards the ice terminus.

Furthermore, surface lowering was particularly pronounced within the 1965/68 glacier snout outlines. Vertical accuracy assessment tests, performed for the relatively flat valley bottoms adjacent to each glacier specified, revealed that error within these areas (which have similar slope gradients as the lower glacier snouts) reduced considerably, with vertical RMSEs ranging from ±26.4 m to ±27.7 m. Notably, the terminus regions of each glacier specified well exceeded these error estimates, with maximum ice surface lowering ranging from 86 m and 144 m.

In comparison to the ice surface lowering shown here, for the four glaciers specified, Bolch *et al.* (2008), who compared a 1962 Corona DEM to a 2002 ASTER DEM, revealed maximum ice surface lowering ranging from ~50 m to ~35 m for the Khumbu, Nuptse and Lhotse glaciers in the Khumbu Himalaya, Nepal. Such direct comparisons, however, are difficult to assess as the glaciers selected by Bolch *et al.* (2008) have different characteristics. Aside from differences in size and geographic and climatic setting, the glaciers sampled by Bolch *et al.* (2008) were identified as being heavily debris-covered which is likely to have influenced the magnitude of surface lowering experienced.

The vertical accuracy of the valley bottom test sites selected closely match that reported by Schmidt *et al.* (2001) (±20-25 m), who generated a Corona DEM for mountainous terrain in Morroco, using DGPS reference data and a similar empirical non-metric camera frame model. The accuracy of the valley bottom areas test also matched that reported for Corona DEMs generated by Bolch *et al.* (2008; 2010) (±18-56 m) for the Khumbu Himalayas, using ASTER reference data and the RSG ERDAS Imagine software package. What these selected valley bottom locations and their adjacent glacier termini have in common, aside from low slope gradients, is that each were located in image areas that were particularly well sampled with GCPs. With the non-metric camera frame model utilised here, it is therefore shown that, when the GCP sample is good, Corona terrain surfaces can be modelled with a sufficient accuracy to detect glacier elevation changes over long observation periods. However, as discussed in section 6.1, the use of ASTER data here placed a limit on GCP sampling over entire image strips.

Considering the limitations of the dataset, it is therefore concluded that when using a non-metric camera frame model to extract Corona DEMs, ASTER reference data is unable to provide the geometric image framework needed to produce accurate glacier ice surfaces (in contrast to the planimetric glacier mapping application). Due to the dependence of vertical accuracy on the GCP sample, the use of VHR vertical and horizontal reference data, in combination with the methods applied here, represents an alternative approach. Aside from Cartosat-1 data, SPOT-5 satellite imagery and DEMs, for example, have shown to be a particularly good source of 3D control in high mountainous environments (Berthier *et al.*, 2005; Berthier *et al.*, 2007). Other VHR stereo satellite options include ALOS PRSIM, IKONOS, Quickbird and Geoeye-1.

## 7. Results & discussion: Glacier length & area change

This chapter presents glacier area and length change measurements derived from Corona, ASTER and GLIMS geospatial datasets, between the 1960s/70s and 2000s, for the GC, ND, SB and LT study sites. With reference to the glaciological objectives stated in chapter 3, this chapter also includes accuracy analyses of the manually derived and GLIMS glacier outlines, and an analysis of glacier area change with elevation at each study site. The chapter ends with a detailed discussion of the glacier change measurements presented.

### 7.1. Error Analysis: Manually derived glacier area and length change measurements

Error associated with the glacier area and length change measurements manually derived from the Corona, ASTER and GLIMS geospatial datasets used has been assessed in relation to (1) the precision of the glacier delineation process (or analyst precision) and (2) the spatial resolution and co-registration of the geospatial data used. To assess glacier delineation precision, three test glaciers were selected from the GC study site, ranging in size from 1.5 $km^2$ to 30.2 $km^2$. These glaciers were chosen (1) to represent the size distribution of the glaciers sampled and (2) because large areas of ice are debris-covered. Each test glacier was delineated 9 times from the 2001 ortho-ASTER imagery. The areal extents of these 9 delineations were then compared against a reference glacier delineation, represented by the original glacier outlines derived from the ortho-ASTER source image. The precision test was performed using the ortho-ASTER imagery because (1) the ortho-ASTER imagery was used as the horizontal reference source for the study and (2) at 15 m resolution the ortho-ASTER imagery represents the coarsest glacier delineation reference source.

The glacier delineation precision test results are presented in table 7.1 and figure 7.1. Combining the results for each of the three glaciers, the test reveals a glacier areal extent delineation error of ±0.72%. This delineation error is therefore considered as

**Table 7.1: Glacier delineation precision test results. Differences are calculated in relation to the reference delineations (Reference 1). Glacier 1, 2 and 3 are shown in figure 7.1.**

| Delineation No. | Glacier 1 (km²) | Difference (km²) | Glacier 2 (km²) | Difference (km²) | Glacier 3 (km²) | Difference (km²) |
|---|---|---|---|---|---|---|
| Reference 1 | 30.234 | - | 5.475 | - | 1.560 | - |
| 2 | 30.379 | -0.145 | 5.439 | 0.036 | 1.594 | -0.034 |
| 3 | 30.276 | -0.042 | 5.466 | 0.010 | 1.574 | -0.013 |
| 4 | 30.399 | -0.165 | 5.528 | -0.053 | 1.599 | -0.039 |
| 5 | 30.299 | -0.065 | 5.525 | -0.049 | 1.573 | -0.013 |
| 6 | 30.442 | -0.208 | 5.512 | -0.037 | 1.575 | -0.015 |
| 7 | 30.418 | -0.184 | 5.487 | -0.012 | 1.586 | -0.025 |
| 8 | 30.221 | 0.013 | 5.499 | -0.024 | 1.576 | -0.015 |
| 9 | 30.295 | -0.061 | 5.526 | -0.051 | 1.575 | -0.015 |
| 10 | 30.330 | -0.096 | 5.506 | -0.031 | 1.585 | -0.025 |
| **Average (km²)** | | -0.106 | | -0.024 | | -0.022 |
| **Average % difference** | | 0.350 | | 0.430 | | 1.379 |
| **Combined average % difference** | | ±0.72 | | | | |

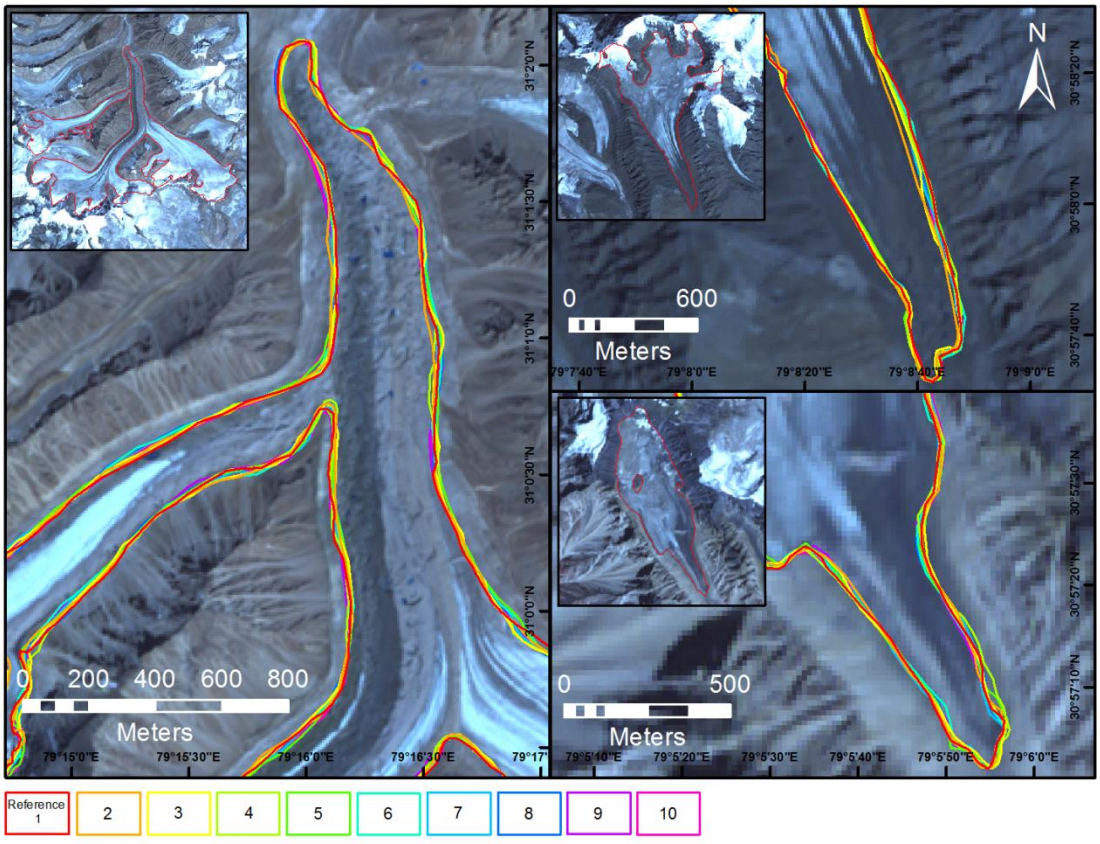


**Figure 7.1: Precision test glacier delineations for glacier 1 (left: 30.2km²), glacier 2 (top right: 5.4km² and glacier 3 (bottom right: 1.5km²).**

the measure of delineation precision for the manually derived glacier outlines presented in this study, excluding the GLIMS outlines. The GLIMS outlines, used at the SB and LT sites, were uploaded into the GLIMS glacier database by a number of analysts and information on their source is limited. The precision of the GLIMS glacier outlines is therefore unknown.

Further analysis of the precision test results reveals that, despite having the smaller areas and perimeters, the largest glacier delineation errors are shown for Glacier 2 and 3. This finding may be indicative of delineation error caused by debris covered ice. In comparison to Glacier 2 and 3, on which debris covers the majority of ice area, glacier 1 is largely free of debris in accumulation zone areas. Glacier ice boundaries in these clean ice areas are therefore easier to identify.

To calculate glacier area and length change error, attributed to the spatial resolution and co-registration of the geospatial data used, the method proposed by Williams *et al*. (1997) and Hall *et al*. (2003) was utilised. First, possible error was calculated in the linear direction (*d*) between each pair of geospatial datasets (GC & ND: Corona & ASTER; SB & LT: GLIMS & ASTER) using the formula:

$$d = \sqrt{r_1^2 + r_2^2} + RMSE \tag{7.1}$$

where $r_1$ represents the spatial resolution (pixel cell width) of the first image, $r_2$ the spatial resolution of the second image and RMSE the co-registration error. For the GC and ND study sites, the $r_1$ and $r_2$ values equated to 1.8 and 15 (spatial resolution of the Corona and ortho-ASTER imagery, respectively). The RMSE value equated to 7.5 m for the GC site and 16.7 m for the ND site (orthorectification RMSE, see section 6.1).

For the SB and LT study sites, the calculation of error in the linear direction is complicated by the use of GLIMS glacier outlines. Information on the delineation source of the GLIMS outlines is limited and therefore an $r_1$ value is not available. In order to estimate a theoretical $r_1$ value, the GLIMS outlines are assumed to be sourced

from historic topographic maps that exist for the Nepalese Himalaya (see Bhambri & Bolch, 2009). Both in the past and at present, topographic maps constructed from aerial photography in the Indian and Nepalese Himalaya have ranged in scale from 1:25,000 to 1:50,000 (Kulkarni, 1991; Bolch *et al*., 2010). Assuming the worst-case scenario (topographic map source at 1:50,000 scale) and applying the map scale to raster spatial resolution conversion formula proposed by Waldo (1987) (raster resolution = *S*/(1000*2), where *S* is the denominator of the map scale (e.g. 50,000)), a $r_1$ of 25 m was assigned to the GLIMS data. The RMSE value between the ortho-ASTER and GLIMS data is also unknown. Other studies that have co-registered topographic maps to satellite imagery have reported RMSE of 2 m to 15 m (e.g. Ye *et al*., 2006). This co-registration error, however, is highly specific to the geospatial data and co-registration method used and therefore in this case a RMSE value was not included when calculating linear error at the SB and LT study sites. As a result, the theoretical linear error calculated for the SB and LT study sites is likely to be under-estimated. The linear errors attributed to the length change measurements presented for the GC, ND, SB and LT study sites are shown in table 7.2.

To convert the linear errors calculated into estimations of glacier area change error (*a*), the following equation was used (Hall *et al*., 2003):

$$a = A \cdot (2d/x) \tag{7.2}$$

Where A = $x^2$, with x = image pixel width, and *d* = error in the linear direction. To estimate the worst-case scenario, the x value was assigned the largest pixel width from each pair of geospatial datasets used. For the GC and ND study sites, x = 15 and for the SB and LT study site the theoretical value of x = 25. The individual glacier area change error estimations are shown in table 7.2. To calculate the error attributed to the total glacier area changes presented, the individual area change errors shown in table 7.2 were multiplied by the number of glaciers sampled at each study site. It is important to add that glacier length and area change errors presented are only estimations. Additional errors may arise from: (1) imagery geometry inconsistencies: Related to bundle block adjustment GCP distribution (Corona imagery) and snow/

**Table 7.2: Error estimates for individual glacier length and area change measurements.**

| Study site | Gl. length change error (±m) | Gl. area change error (±$m^2$) | Gl. area change error (±$km^2$) |
|---|---|---|---|
| LT | 29 | 1458 | 0.00146 |
| SB | 29 | 1458 | 0.00146 |
| ND | 32 | 954 | 0.00095 |
| GC | 23 | 678 | 0.00068 |

cloud cover image quality issues (ortho-ASTER imagery); and (2) debris- and snow-covered ice: Debris- and snow-cover hinder the identification of glacier ice. To minimise the influence of these factors GLIMS glacier delineation guidelines were adhered to.

## 7.2 Historic GLIMS glacier outlines: Qualitative assessment of geometric accuracy

Unlike both the Corona and ASTER derived glacier outlines, whose accuracy could be assessed quantitatively, the accuracy of the 1960/70s GLIMS outlines could only be measured subjectively. In addition to the outline itself, each individual glacier selected from the GLIMS database includes a range of acquisition information. For the GLIMS glaciers used at the SB and LT sites, this included measurement source information, which was given broadly as aerial photography and topographic maps. However, the acquisition information lacked any reference to geometric accuracy. The geometric accuracies of aerial photography and topographic maps can vary considerably according to the methods and techniques used to spatially rectify and project each dataset. As a result, the source accuracy of the GLIMS outlines used could not be inferred from this measurement information alone. Additionally, no information was given in regards to the techniques used to delineate each glacier outline. Due to this lack of information, the accuracy of the GLIMS outlines was assessed qualitatively by visually comparing the positioning of each outline in respect to surface features within corresponding ortho-ASTER imagery.

Overall, the GLIMS outlines matched ortho-ASTER image surface features reasonably well for the lower portions of glaciated areas, with glacier outlines conforming to the boundaries of surrounding LIA lateral and terminal moraines, other local topographical constraints and the general shape of ASTER derived glaciers (e.g. Figure 7.2). The conformity of the GLIMS outlines with these image features would suggest that positional accuracy, relative to ortho-ASTER imagery, is quite good. However, despite still matching topographical features (mountain ridges and peaks), in high elevation locations the comparative difference in the position of GLIMS glacier outlines relative to ASTER-derived glacier outlines was considerable. The extent of these GLIMS-ASTER differences at high elevation, particular at the LT study, site may possibly be indicative of miss-classification errors. In figure 7.3, for example, the position of the GLIMS glacier outline would suggest that glacial area in 1975 extended over a number of high elevation slopes which would be likely too steep to allow for the formation of glacial ice. Possible cause of these possible miss-classification errors is discussed further in section 7.5.5.

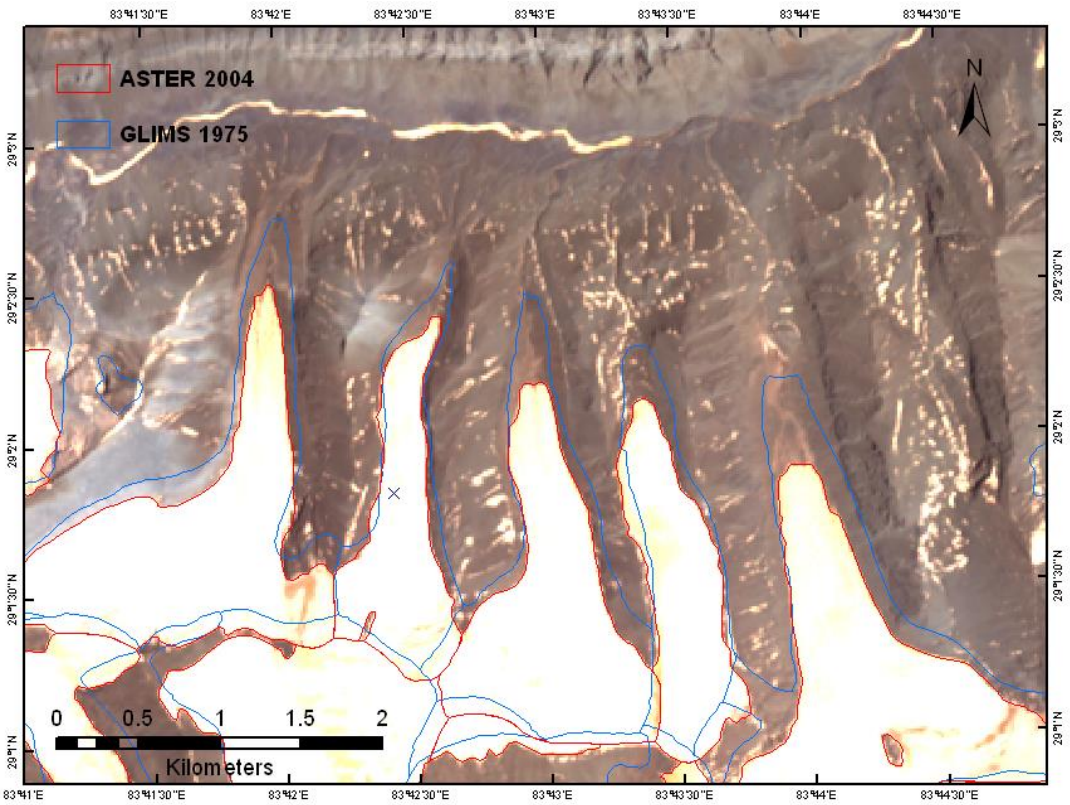


**Figure 7.2: Spatial comparison of GLIMS and ASTER-derived glacier outlines. Despite varying relative to ASTER-derived glacier outlines at high elevation, GLIMS glacier outlines match topographical features of each respective glacier sub-basin well.**

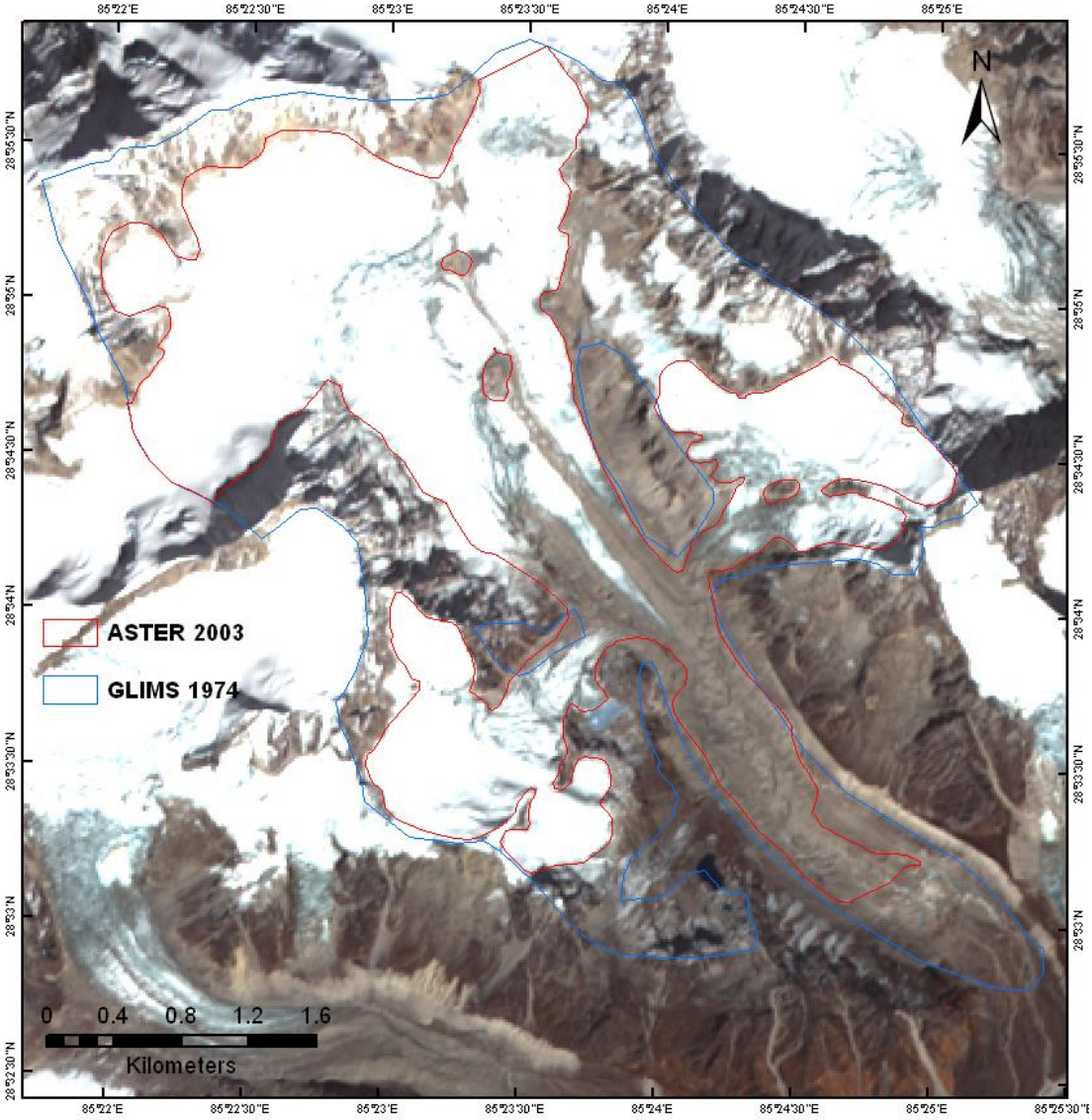


**Figure 7.3: For a number of glaciers, the GLIMS outlines used suggest the existence of additional ice area at high elevation, by comparison to the 2003 ASTER-derived outlines, which extended onto steep mountain slopes. The glacier shown, located in the LT study site, is a typical example of the GLIMS characteristics described.**

## 7.3. Glacier area and length change derived from Corona, ASTER and GLIMS geospatial datasets

The following four sections describe the glacier area and length change measurements made at the GC, ND, SB and LT study sites over each of the given observation periods. To analyse glacier area and length change, measurements are divided according to glacier size, with glaciers being grouped into <0.2, 0.2-1, 1-5 and >5 km$^2$ size classes.

Due to the variability of the earlier glacier observation dates at the SB and LT sites, glaciers sampled were grouped into two separate measurement periods specific to each site. This grouping according to observation date aided comparison of results between study sites. To help characterise differences between each glacier size class used, elevation information is also given, obtained from the ASTER GDEM.

In regards to the glacier area change error estimates calculated in section 7.1, due to their relatively small size, these are only stated in reference to the absolute and relative area changes reported for the entire glacier sample and have not been included within any additional analysis.

### 7.3.1. Gangotri Chaukhamba

Table 7.3 summarises overall glacier area and length change measured for the 141 glaciers sampled at the GC site between 1965 and 2001. These measurements were derived from glacier outlines delineated from orthorectified Corona (1965) and ortho-ASTER (2001) imagery. A snapshot of the glacier area and length changes presented is shown in figure 7.4. Overall, the total glaciated area sampled at the GC site reduced by 32.56±0.096 $km^2$, decreasing from 408.3 $km^2$ in 1965 to 375.79 $km^2$ in 2001, a relative area loss of 7.97±0.29%. Measurements of absolute and relative area loss, as well as length change, for each glacier sampled vary considerably. Absolute area changes, for example, range from <0.01 $km^2$ to >9 $km^2$, whilst relative losses range from <0.5% to 100%. In total, four small glaciers had disappeared by 2001.

**Table 7.3: Glacier area and length change statistics for the GC site.**

| Study area | Gangotri Chaukhamba |
|---|---|
| No. of glaciers | 141 |
| Ice area 1965 ($km^2$) | 408.35 |
| Ice area 2001 ($km^2$) | 375.79 |
| Area change ($km^2$) | 32.56±0.096 |
| Average area loss ($km^2$) | 0.23 |
| Percentage area loss (%) | -7.97±0.29 |
| Average length change (m) | 185±23 |
| Average rate of length change ($m/a^{-1}$) | 5.13 |

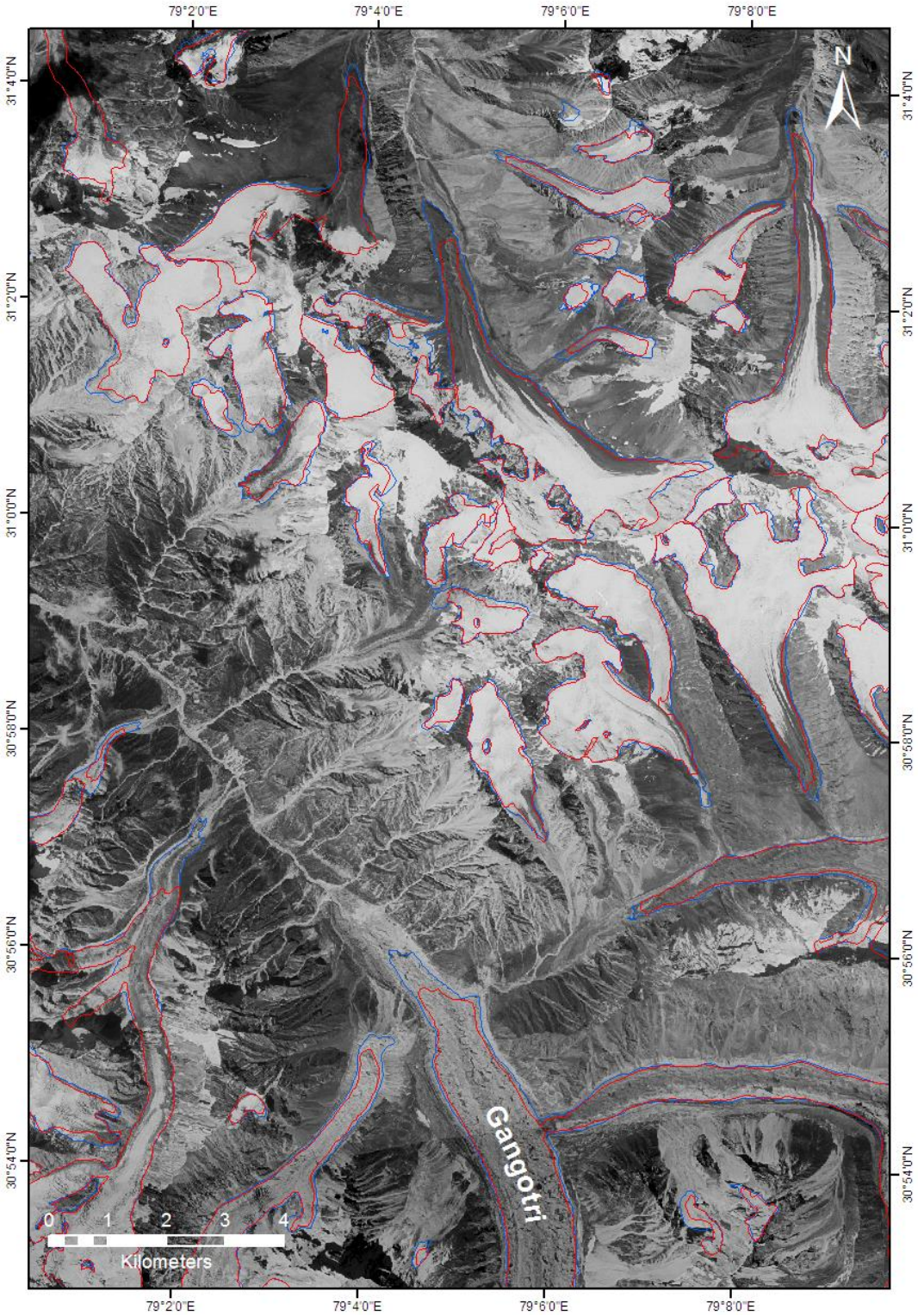


**Figure 7.4: Glacier changes from 1965 (outlined in blue) to 2001 (outlined in red) for an area of the GC site. Glacier outlines have been delineated from orthorectified Corona and ASTER imagery. Background image: Ortho-Corona, 24/09/1965.**

Gangtotri glacier experienced the largest absolute area losses at the GC site, reducing in area from 197.68 $km^2$ to 188.14 $km^2$ between 1965 and 2001. During this observation period five tributary glaciers detached from the main Gangotri trunk. In addition to experiencing lateral shrinkage in lower regions, the terminus of Gangotri glacier has retreated in length by 856±23 m, the second largest length change measured at the GC site (visible in Figure 7.4). The largest length change measured at the GC site equated to 1372±23 m. Although Gangotri glacier experienced the largest individual loss of ice area, this loss represented a relative area reduction of only 4.82±0.01%.

Table 7.4 shows glacier area and length change parameters according to glacier size. Overall, 78.59% of the glaciated area sampled at the GC site is contained within glaciers that are >5 $km^2$ in size. Although only representing 11 out of the 141 glaciers sampled, the >5 $km^2$ size class experienced the largest absolute area loss of 18.16 $km^2$. Larger glaciers are shown to have undergone larger absolute ice area losses, with glaciers <0.2 $km^2$ in size losing an average area of 0.05 $km^2$ compared to 1.65 $km^2$ for glaciers >5 $km^2$ in size. This increase according to glacier size is also shown in relation to length change. For relative ice area loss, the relationship with glacier size is inversed, with glaciers in the <0.2 $km^2$ size class losing 36.91% of their ice area compared to only 5.79% for glaciers in >5 $km^2$ size class (see Figure 7.5). However, relative ice area losses in the two smaller size classes vary in magnitude considerably (0.2% to 100%) compared to the two larger size classes (2.3% to 23%). Topographical analysis of the

**Table 7.4: Glacier area and length changes according to size.**

| Gangotri Chaukhamba | Size Class ($km^2$) | | | |
|---|---|---|---|---|
| | **<0.2** | **0.2-1** | **1-5** | **>5** |
| No. of glaciers | 52 | 51 | 27 | 11 |
| Proportion of total ice area sampled (%) | 1.07 | 6.11 | 14.23 | 78.59 |
| Ice area 1965 ($km^2$) | 6.35 | 28.49 | 60.02 | 313.49 |
| Ice area 2001 ($km^2$) | 4.01 | 22.97 | 53.48 | 295.33 |
| Area change ($km^2$) | 2.34 | 5.52 | 6.54 | 18.16 |
| Average area loss ($km^2$) | 0.05 | 0.11 | 0.24 | 1.65 |
| Percentage area loss (%) | -36.91 | -19.37 | -10.89 | -5.79 |
| Average length change (m) | 132.80 | 138.10 | 205.85 | 582.36 |
| Rate of length change ($m/a^{-1}$) | 3.69 | 3.76 | 5.72 | 16.18 |

glaciers sampled at the GC site, according to size (listed in Table 7.5), reveals that large glaciers tend to originate at higher elevations and extend further down valley compared to smaller glaciers (see Figure 7.6). Consequently, the average median elevations of larger glaciers (1-5 km$^2$ and >5 km$^2$ size classes) are lower than the two smaller glacier size classes.

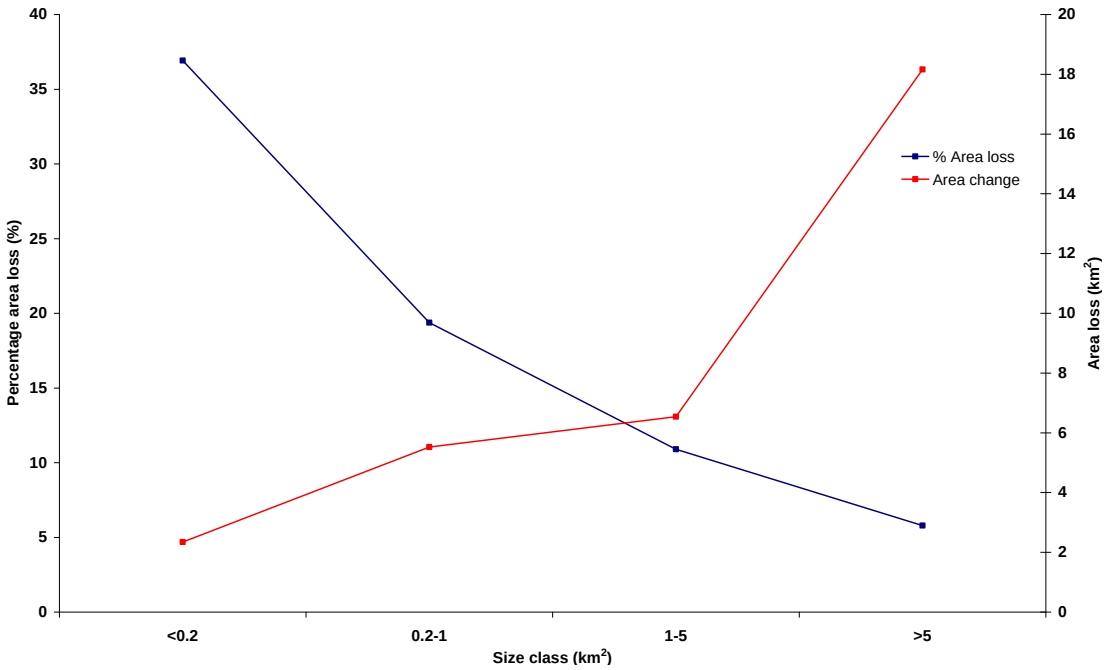


**Figure 7.5: Comparison of absolute area loss and percentage area loss for glaciers within each of the four size classes.**

**Table 7.5: Topographical characteristics of the GC site according to glacier size.**

| Basin topography | Size Class (km$^2$) | | | |
|---|---|---|---|---|
| | **<0.2** | **0.2-1** | **1-5** | **>5** |
| Median Elevation (2001) | 5704 | 5751 | 5628 | 5556 |
| Average terminus elevation (1965) | 5520 | 5403 | 5166 | 4684 |
| Average terminus elevation (2001) | 5580 | 5441 | 5209 | 4776 |

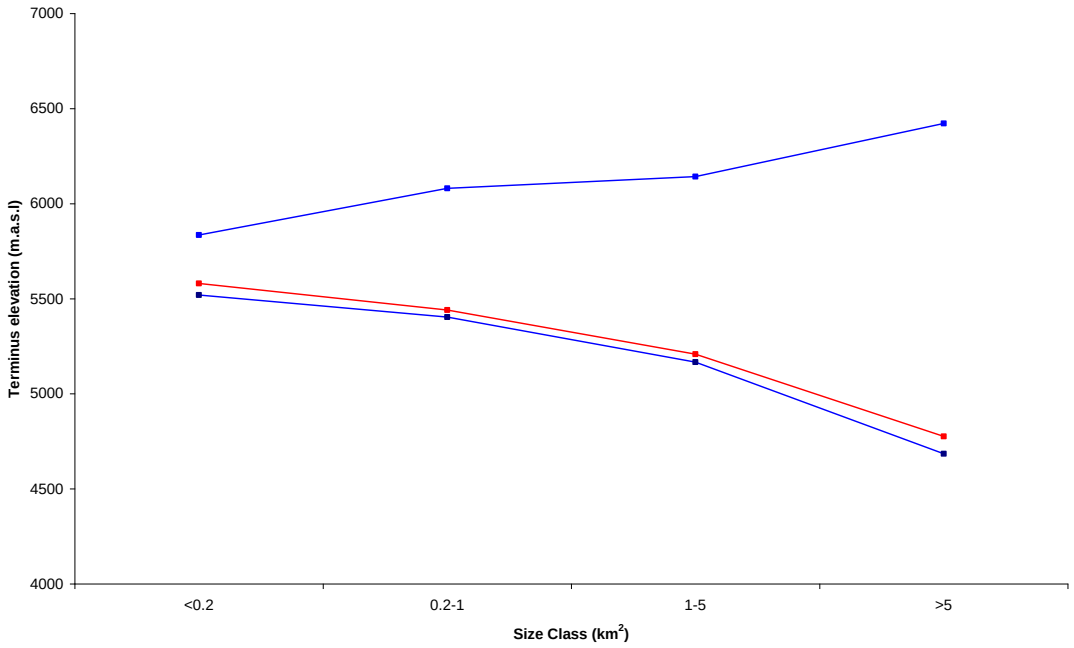


**Figure 7.6: Average maximum and minimum ice elevation in 1965 (blue line) in relation to size and the average minimum elevation of ice in 2001 (pink line).**

### 7.3.2. Nanda Devi

Table 7.6 summarises overall glacier area and length change measured for the 41 glaciers sampled at the ND between 1968 and 2004. These measurements are derived from glacier outlines delineated from orthorectified Corona (1968) and ortho-ASTER (2004) imagery. A snapshot of these glacier area and length changes is presented in figure 7.7, centred on the large Milam glacier. Overall, the total glaciated area sampled at the ND site reduced by 15.03±0.039 $km^2$, decreasing from 199.41 $km^2$ in 1968 to 184.39 $km^2$ in 2004, a relative area loss of 7.54±0.26%.

**Table 7.6: Glacier area and length change statistics for the ND site.**

| Study area | Nanda Devi |
|---|---|
| No. of glaciers | 41 |
| Ice area 1968 ($km^2$) | 199.41 |
| Ice area 2004 ($km^2$) | 184.39 |
| Area change ($km^2$) | 15.03±0.039 |
| Average area loss ($km^2$) | 0.37 |
| Percentage area loss (%) | -7.54±0.26 |
| Average length change (m) | 174.17±32 |
| Average rate of length change ($m/a^{-1}$) | 4.84 |

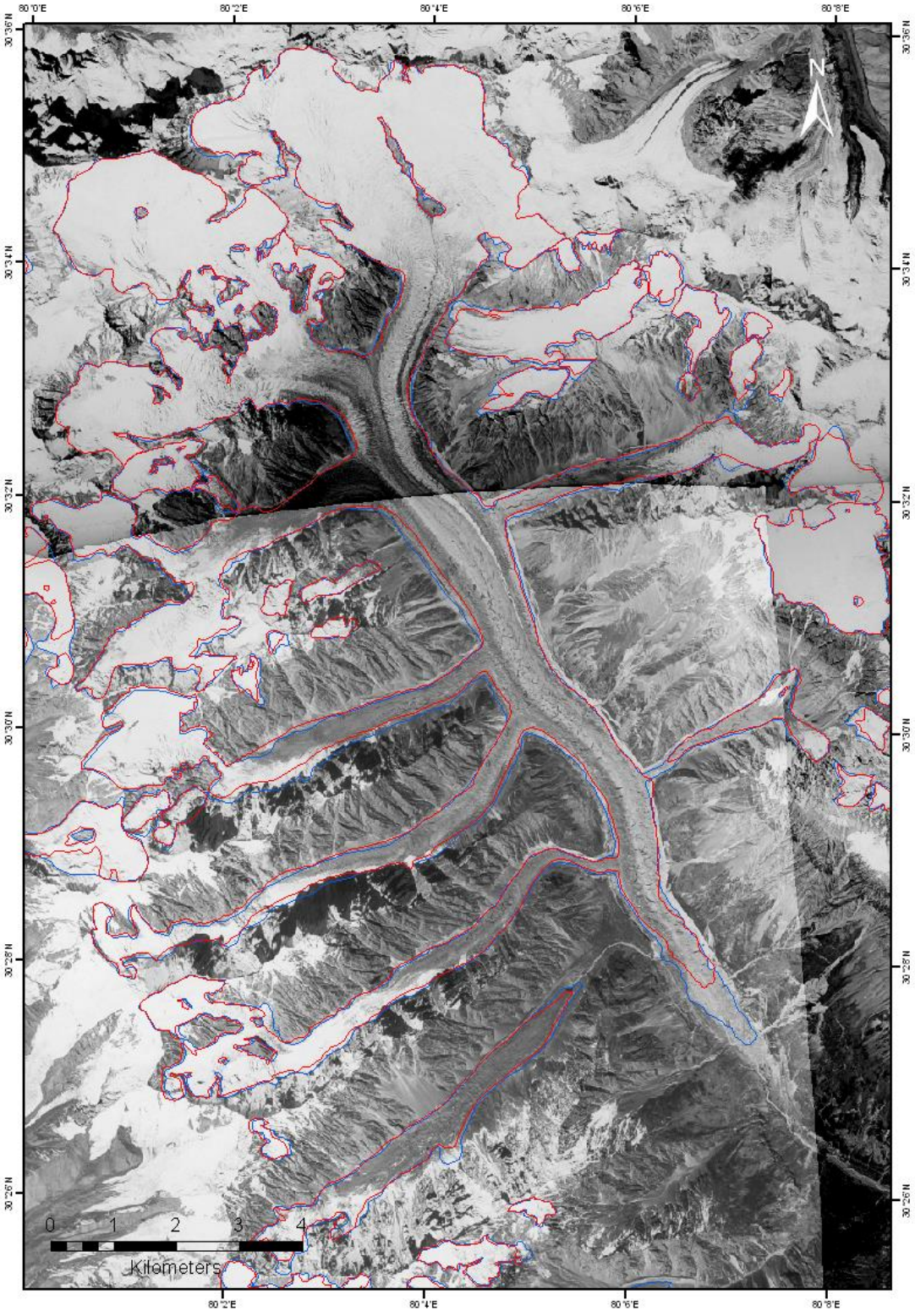


**Figure 7.7: Glacier changes from 1968 (outlined in blue) to 2004 (outlined in red) in a portion of the ND site centred on Milam glacier. Glacier outlines have been delineated from orthorecitified Corona and ASTER imagery. Background image: Ortho Corona, 27/09/1968.**

The largest absolute glacier area loss measured at the ND site was for Uttari Nanda Devi glacier, which reduced in area by 3.87 $km^2$. The Uttari Nanda Devi glacier is the third largest glacier sampled at the ND site and reduced in area from 37.75 $km^2$ in 1968 to 33.87 $km^2$ in 2004, a relative loss of 10.26%. The largest glacier sampled at the ND site, Milam glacier, reduced in area by 2.88 $km^2$ (relative loss of 4.93%) and experienced a snout retreat of 1158±32 m. As a result of the area loss between 1968 and 2004, a large tributary glacier is shown to have detached from the main Milam glacier trunk.

Table 7.7 shows glacier area and length change parameters according to glacier size. Overall, 87.24% of the glaciated area sampled at the ND site is contained within glaciers that are >5 $km^2$ in size. Although representing only 6 out of the 41 glaciers sampled, the >5 $km^2$ size class experienced the largest area loss of 12.67 $km^2$. In comparison, glaciers in the smaller three size classes lost a combined 2.36 $km^2$. Both absolute ice area loss and length change are seen to increase according to glacier size. Glaciers in the <0.2 $km^2$ size class, for example, have on average lost 0.02 $km^2$ in area and 48.88±32 m in length compared to glaciers in the >5 $km^2$ size class which have lost 2.11 $km^2$ and 496.97±32 m, respectively. In relation to relative ice area loss, the relationship shown is inversed with glaciers in the <0.2 $km^2$ size class losing 14.34% of their ice area compared to 7.3% for glaciers in the >5 $km^2$ size class (see Figure 7.8).

Topographical analysis of the glaciers sampled at the ND site, according to size (listed

**Table 7.7: Glacier area and length changes according to size.**

| Nanda Devi | Size Class ($km^2$) | | | |
|---|---|---|---|---|
| | **<0.2** | **0.2-1** | **1-5** | **>5** |
| No. of glaciers | 17 | 13 | 5 | 6 |
| Proportion of total ice area sampled (%) | 1.18 | 3.33 | 8.25 | 87.24 |
| Ice area 1968 ($km^2$) | 2.55 | 6.79 | 16.55 | 173.52 |
| Ice area 2004 ($km^2$) | 2.18 | 6.13 | 15.22 | 160.85 |
| Area change ($km^2$) | 0.37 | 0.65 | 1.34 | 12.67 |
| Average area loss ($km^2$) | 0.02 | 0.05 | 0.27 | 2.11 |
| Percentage area loss (%) | -14.34 | -9.62 | -8.08 | -7.30 |
| Average length change (m) | 48.88 | 84.30 | 340.57 | 585.17 |
| Average rate of length change ($m/a^{-1}$) | 1.36 | 2.34 | 9.46 | 16.25 |

in Table 7.8), reveals that in general larger glaciers originate at higher elevations compared to smaller glaciers (see Figure 7.9). Consequently, the average median elevations of larger glaciers (1-5 km$^2$ and 5 km$^2$) are lower than the two smaller glacier size classes.

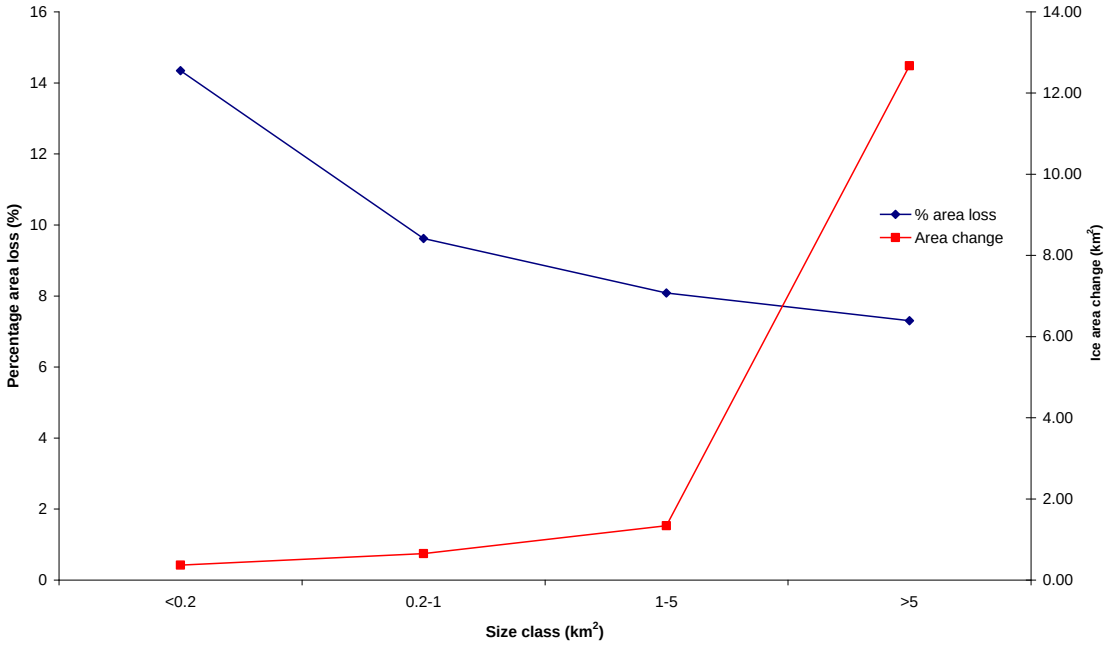


**Figure 7.8: Comparison of absolute area loss and percentage area loss for glaciers within each of the four size classes.**

**Table 7.8: Topographical characteristics of the ND site according to glacier size.**

| Basin topography | Size Class (km$^2$) | | | |
|---|---|---|---|---|
| | **<0.2** | **0.2-1** | **1-5** | **>5** |
| Median Elevation (2001) | 5576 | 5483 | 5006 | 5339 |
| Average terminus elevation (1968) | 5335 | 5037 | 4540 | 4182 |
| Average terminus elevation (2001) | 5371 | 5087 | 4580 | 4231 |

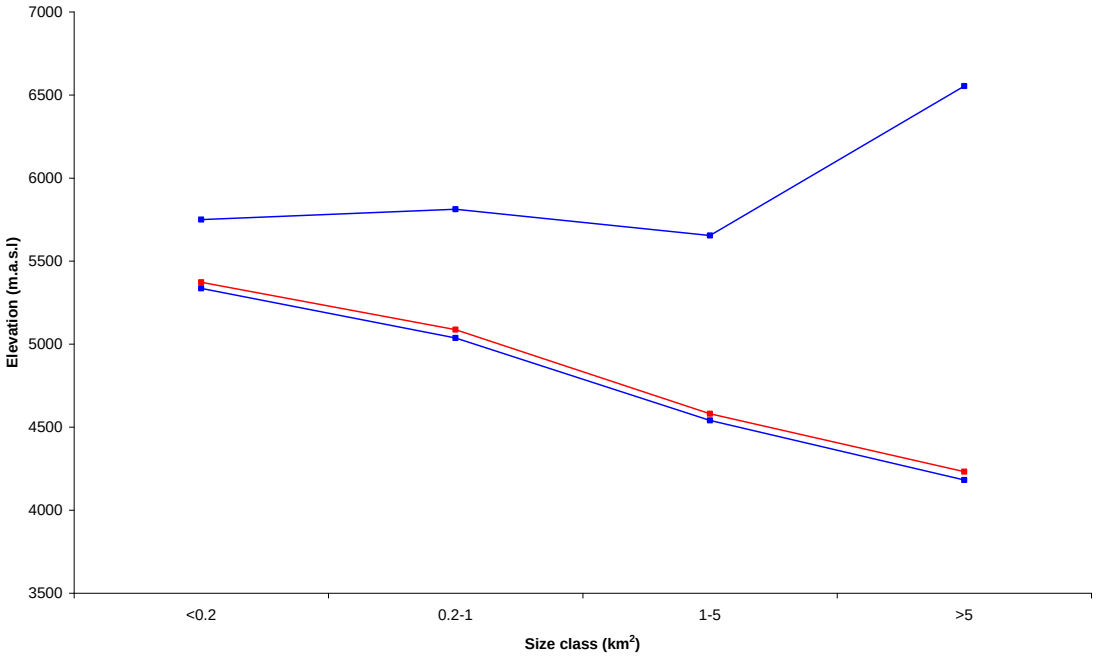


**Figure 7.9: Average maximum and minimum ice elevation in 1968 (blue line) in relation to size and the average minimum elevation of ice in 2001 (red line).**

### 7.3.3. Setibeni

Table 7.9 summarises overall glacier area and length change measured for the 238 glaciers sampled at the SB site between 1959-1975 and 2003-2007. These measurements were made through the analysis of GLIMS glacier outlines (1959-1975) and glacier outlines delineated from ortho-ASTER imagery (2003-2007). A snapshot of glacier area and length changes presented is shown in figure 7.10. Overall, the total glaciated area sampled at the SB site reduced by 170.21±0.347 km$^2$, decreasing from 571.58 km$^2$ in the 1959-1975 period to 401.37 km$^2$ in the 2003-2007 period, a relative

**Table 7.9: Glacier area and length change statistics for the SB site.**

| Study area | Setibeni |
|---|---|
| No. of glaciers | 238 |
| Ice area 1959-1975 (km$^2$) | 571.58 |
| Ice area 2003-2007 (km$^2$) | 401.37 |
| Area change (km$^2$) | 170.21±0.347 |
| Average area loss (km$^2$) | 0.72 |
| Percentage area loss (%) | -29.78±0.2 |
| Average length change (m) | 387.34±29 |
| Average rate of length change (m/a$^{-1}$) | 10.96 |

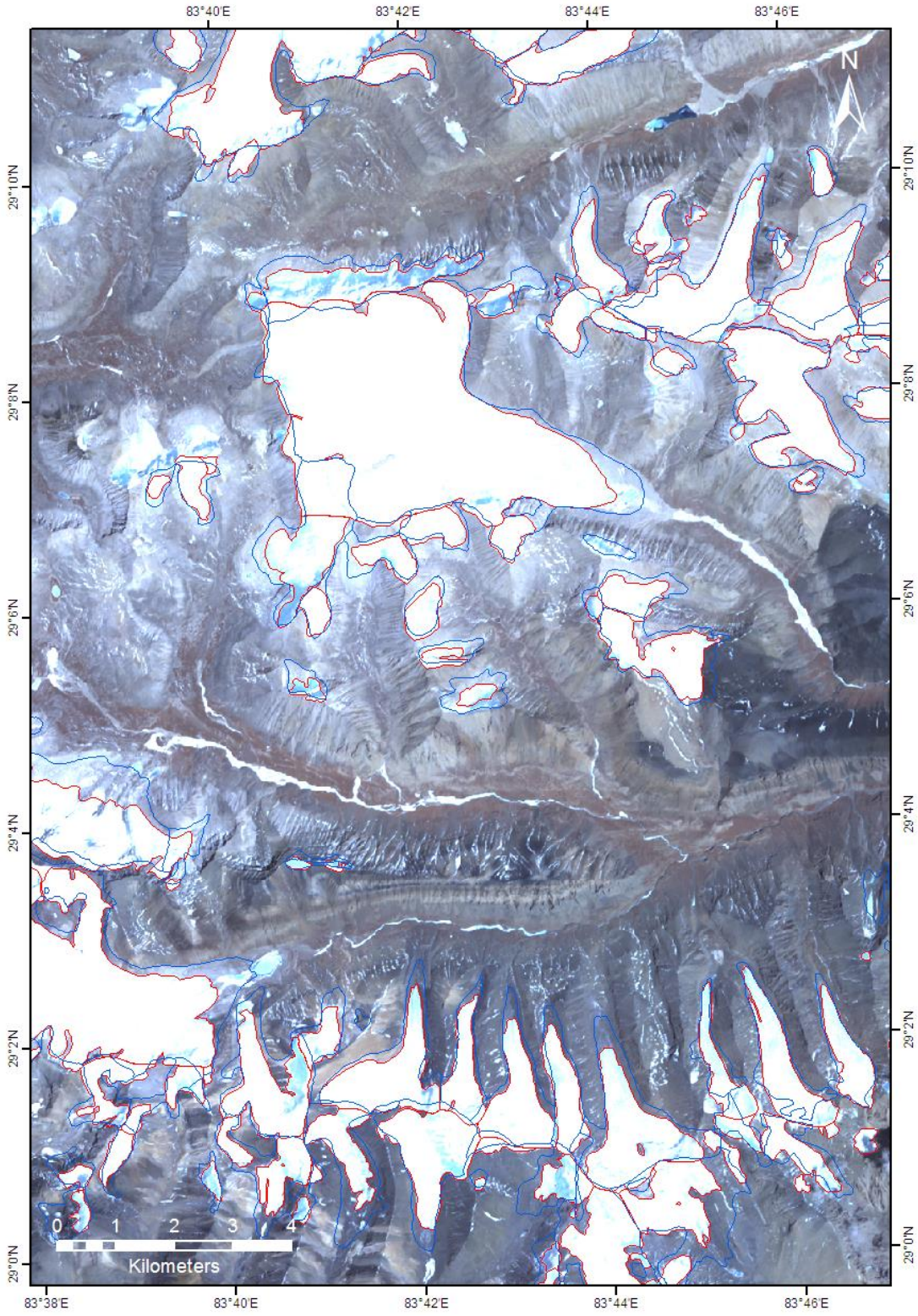


**Figure 7.10: Glacier changes from the period of 1959-1975 (outlined in blue) to 2003-2007 (outlined in red) in a portion of the SB site. Background image: Ortho ASTER, 5/10/2003.**

area loss of 29.78±0.2%. Measurements of absolute and relative area loss, as well as length change, for each glacier sampled at the SB site varied considerably (0.01-24.51 $km^2$, 6.15-96.2%, and 0-3488 m, respectively).

The largest absolute loss of ice area for an individual glacier at the SB site equated to 24.51 $km^2$, reducing in area from 57.51 $km^2$ in 1964 to 32.8 $km^2$ in 2007. The ice area changes for this specific glacier equate to a relative loss of 42.76%. This glacier is notable in that, like other glaciers sampled at the SB site, in addition to losing large amounts of ice area in lower regions the glacier also lost a large portion of its area in the higher regions of its accumulation zone. Table 7.10 shows glacier area and length change parameters according to size and observation interval for the SB study site. For both the 1959-1967 to 2003-2007 and 1970-1975 to 2003-2007 observation periods, the majority of the total ice area sampled is contained within glaciers that are >5 $km^2$ in size.

As with the GC and ND glacier samples, absolute ice area loss is shown to increase according to glacier size for both observation periods. Similar behaviour is also shown for glacier length change. In contrast, relative ice area loss is found to decrease according to glacier size for both observation periods (see Figure 7.11). For the 1970-1975 to 2003-2007 observation period, for example, relative ice area loss for each size class reduces consistently from 56.29%, for glaciers <0.2 $km^2$ in size, to 16.86%, for glaciers in >5 $km^2$ in size. Topographical analysis of the glaciers sampled at the SB site, according to size (listed in Table 7.11), reveals again that in general large glaciers tend to originate at higher elevations and extend further down valley compared to smaller glaciers (see Figure 7.12). Glaciers in 0.2 to 1 $km^2$ size class, however, are the exception, originating from a slightly lower average elevation than glaciers in the <0.2 $km^2$ size class.

**Table 7.10: Glacier area and length change according to size. In addition to glacier size glaciers were also classified into two broad time periods, 1959-1967 to 2003-2007 and 1970-1975 to 2003-2007.**

| Setibeni | Size class ($km^2$) & time period | | | | | | | |
|---|---|---|---|---|---|---|---|---|
| | <0.2 | | 0.2-1 | | 1-5 | | >5 | |
| | 1959-1967 | 1970-1975 | 1959-1967 | 1970-1975 | 1959-1967 | 1970-1975 | 1959-1967 | 1970-1975 |
| No. of glaciers | 24 | 19 | 60 | 59 | 30 | 27 | 11 | 7 |
| Proportion of total ice area sampled (%) | 0.90 | 0.67 | 6.66 | 6.55 | 13.62 | 13.09 | 40.35 | 18.17 |
| Former Ice area ($km^2$) | 10.85 | 6.15 | 44.92 | 38.91 | 79.72 | 67.10 | 236.20 | 87.74 |
| Ice area 2003-2007 ($km^2$) | 3.60 | 2.69 | 26.72 | 26.28 | 54.66 | 52.52 | 161.96 | 72.95 |
| Area change ($km^2$) | 7.25 | 3.46 | 18.20 | 12.64 | 25.06 | 14.57 | 74.24 | 14.79 |
| Average area loss ($km^2$) | 0.30 | 0.18 | 0.30 | 0.21 | 0.84 | 0.54 | 6.75 | 2.11 |
| Percentage area loss (%) | -66.80 | -56.29 | -40.52 | -32.47 | -31.44 | -21.72 | -31.43 | -16.86 |
| Average length change (m) | 161.50 | 280.16 | 283.13 | 268.42 | 724.40 | 338.81 | 1233.73 | 788.57 |
| Average rate of length change ($m/a^{-1}$) | 3.95 | 9.66 | 6.98 | 9.26 | 18.00 | 11.68 | 29.71 | 25.24 |

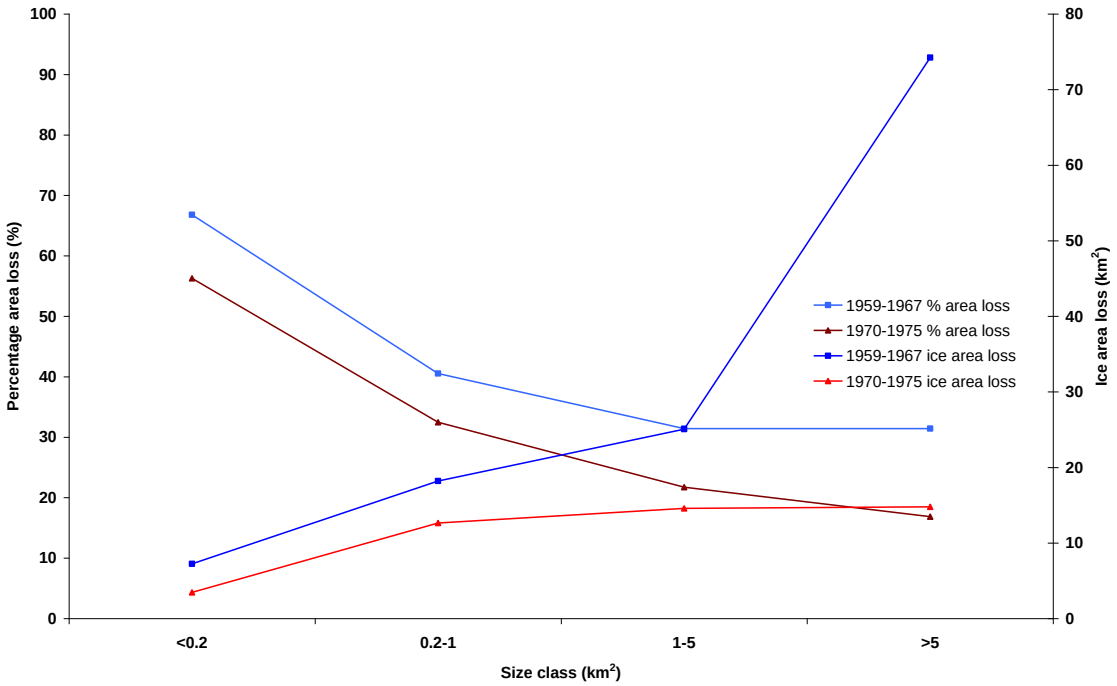


**Figure 7.11: Comparison of absolute area loss and percentage area loss for glaciers within each of the four size classes measured between 1959-1967 to 2003-2007 and 1970-1975 to 2003-2007.**

**Table 7.11: Topographical characteristics of the glaciers sampled at the SB site according to glacier size.**

| Basin topography | Size Class (km²) | | | |
|---|---|---|---|---|
| | **<0.2** | **0.2-1** | **1-5** | **>5** |
| Median Elevation (2001) | 6011.42 | 5893.28 | 5799.49 | 5774.54 |
| Average terminus elevation 1959-1975 | 5718 | 5559 | 5245 | 4687 |
| Average terminus elevation (2001) | 5801 | 5637 | 5349 | 4874 |

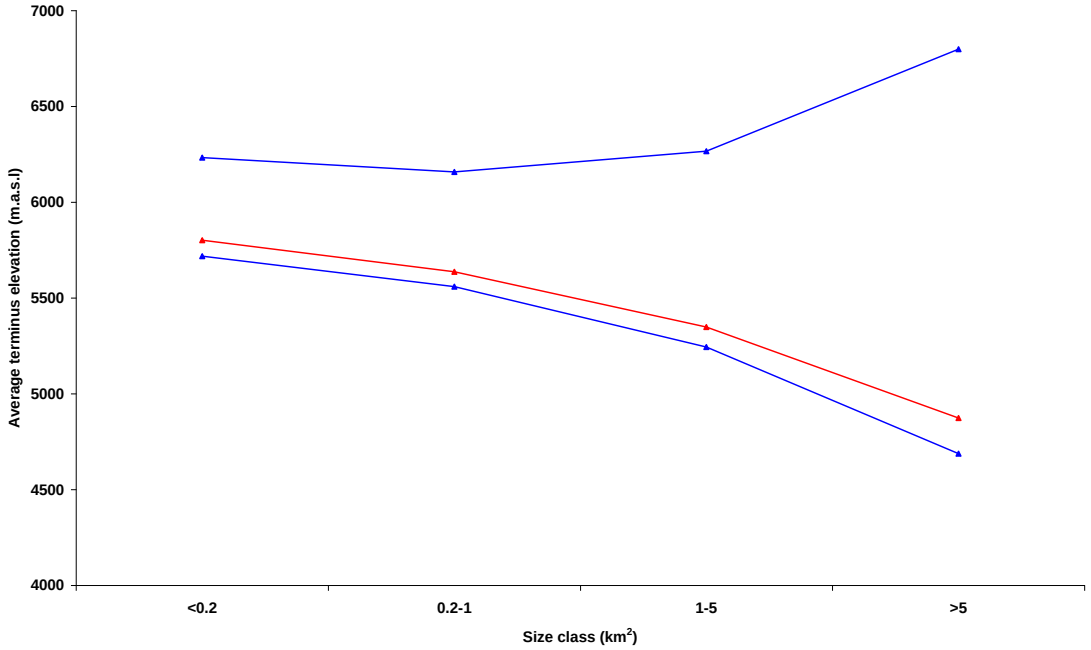


**Figure 7.12: Average maximum and minimum ice elevation in 1959-1975 (blue line) in relation to size, and the average minimum elevation of ice in 2003-2007 (red line).**

### 7.3.4. Langtang

Table 7.12 summarises overall glacier area and length change for the 205 glaciers sampled at the LT study site between 1965-1978 and 2000-2003. These measurements were made through the analysis of GLIMS glacier outlines (1965-1978) and glacier outlines delineated from ortho-ASTER imagery (2000-2003). A snapshot of the glacier area and length changes presented is shown in figure 7.13, centred on the basin of Langtang glacier. Overall, the total glaciated area sampled at the LT site reduced by 376.55±0.299 km$^2$, decreasing from 744.89 km$^2$ in the 1965-1978 period to 368.33 km$^2$ period, a relative loss of 50.55±0.08%. Measurements of absolute and

**Table 7.12: Glacier area and length change statistics for the LT site.**

| Study area | Langtang |
|---|---|
| No. of glaciers | 205 |
| Ice area 1965-1978 (km$^2$) | 744.89 |
| Ice area 2000-2003 (km$^2$) | 368.33 |
| Area change (km$^2$) | 376.55±0.299 |
| Average area loss (km$^2$) | 1.84 |
| Percentage area loss (%) | -50.55±0.08 |
| Average length change (m) | 480.49±29 |
| Rate of length change (m/a$^{-1}$) | 16.32 |

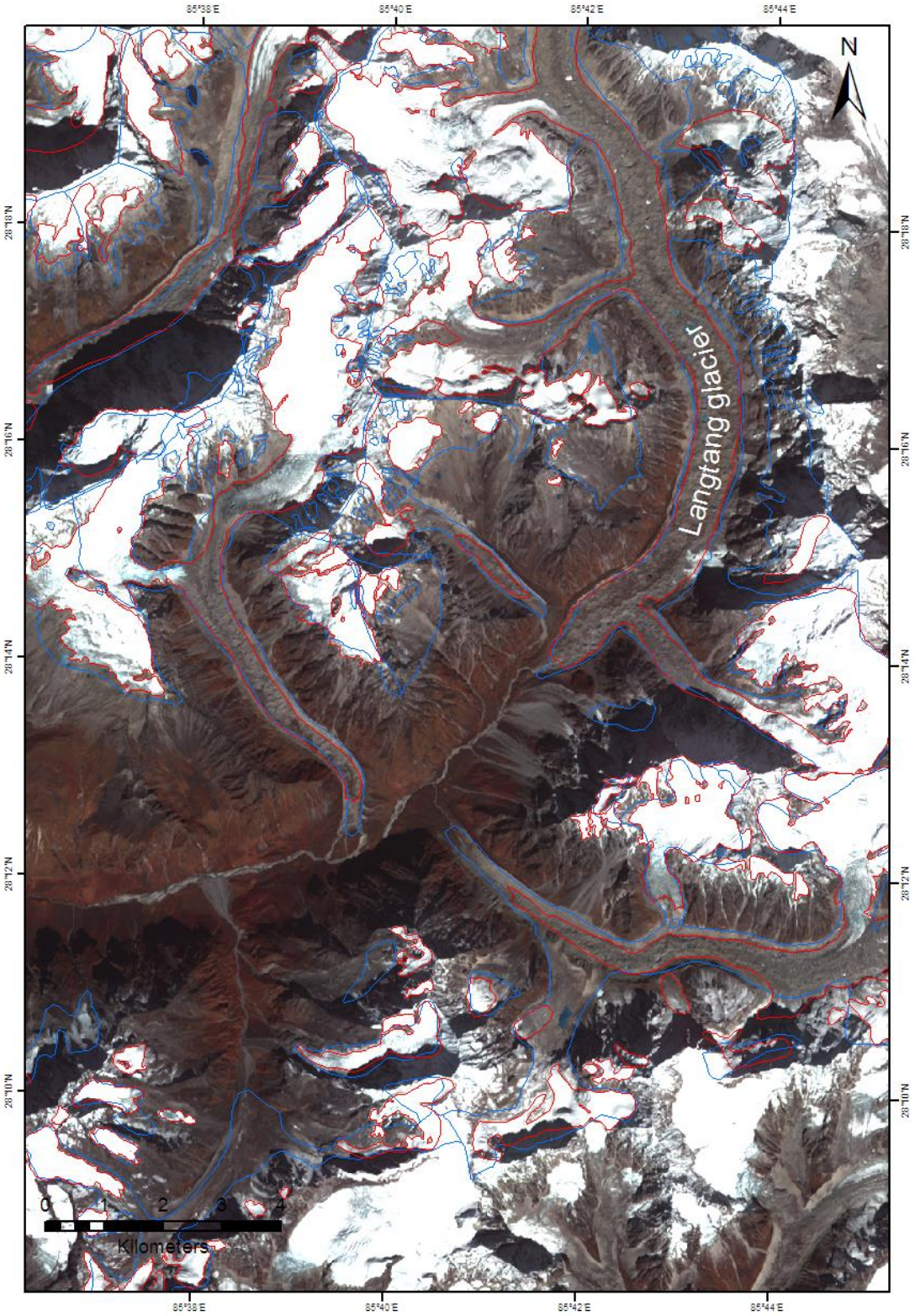


**Figure 7.13: Glacier changes from the period of 1965-1978 (outlined in blue) to 2000-2003 (outlined in red) in a portion of the LT site. Background image: Ortho ASTER, 24/10/2001.**

relative ice area loss, and length reduction, for each glacier sampled at the LT study site varied considerably (<0.01-24.35 km$^2$, 3.85-92.53%, and 0-3065 m, respectively). The largest absolute ice area loss for an individual glacier was measured for Langtang glacier, which reduced in area by 24.35 km$^2$ from 1965 to 2003, a relative reduction of 35.5%. Similar to other glaciers sampled at both the LT and SB study sites, Langtang glacier experienced the largest areal losses in higher regions, where elevated ice sources and steep tributary ice flows reduced considerably (see Figure 7.13). Overall, three tributary glaciers detached from the main Langtang glacier trunk during the observation period.

Table 7.13 shows glacier area and length change parameters according to size and observation interval. For both the 1965-1966 to 2000-2003 and 1974-1978 to 2000-2003 measurement periods the majority of the ice area (as of 2000-2003) is contained within glaciers that are >5 km$^2$ in size. For the 1974-1978 to 2000-2003 observation period, for example, 34.72% of the glaciers sampled are >5 km$^2$ in size. For both observation intervals, glaciers in the two larger size classes experienced significantly larger absolute area losses than glaciers within the two small size classes.

**Table 7.13: Glacier area and length change according to size. In addition to glacier size glaciers were also classified into two broad time periods, 1965-1966 to 2000-2003 and 1974-78 to 2003-2007.**

| Langtang | Size class (km$^2$) & time period | | | | | | | |
|---|---|---|---|---|---|---|---|---|
| | <0.2 | | 0.2-1 | | 1-5 | | >5 | |
| | 1965-1966 | 1974-1978 | 1965-1966 | 1974-1978 | 1965-1966 | 1974-1978 | 1965-1966 | 1974-1978 |
| No. of glaciers | 5 | 27 | 15 | 88 | 11 | 46 | 3 | 10 |
| Proportion of sampled ice area (%) | 0.21 | 1.06 | 1.68 | 11.59 | 6.70 | 27.32 | 16.73 | 34.72 |
| Former Ice area (km$^2$) | 2.63 | 10.85 | 16.25 | 112.62 | 58.24 | 225.31 | 93.90 | 225.10 |
| Ice area 2000-2003 (km$^2$) | 0.77 | 3.90 | 6.17 | 42.68 | 24.68 | 100.62 | 61.62 | 127.90 |
| Area change (km$^2$) | 1.86 | 6.95 | 10.08 | 69.93 | 33.56 | 124.69 | 32.28 | 97.20 |
| Average area loss (km$^2$) | 0.37 | 0.26 | 0.67 | 0.79 | 3.05 | 2.71 | 10.76 | 9.72 |
| Percentage area loss (%) | -70.68 | -64.07 | -62.03 | -62.10 | -57.62 | -55.34 | -34.38 | -43.18 |
| Average length change (m) | 418.40 | 204.44 | 415.27 | 419.39 | 653.00 | 592.15 | 342.33 | 1230.4 |
| Average rate of length change (m/a$^{-1}$) | 11.31 | 7.21 | 11.31 | 14.93 | 17.32 | 21.01 | 9.01 | 42.78 |

However, unlike findings from the other three study sites sampled, absolute area loss does not increase continually according to glacier size (see Figure 7.14).

In terms of absolute area losses, ice area reductions are found to again increase according to size. Glaciers >5 $km^2$ in size measured during the 1965-1966 to 2000-2003 period, for example, lost on average 10.76 $km^2$ of ice area compared to only 3.05 $km^2$ for glaciers 1-5 $km^2$ in size. A similar pattern, in relation to glacier size, is also found for average glacier length change measured during the 1974-1975 to 2000-2003 observation period. However, this pattern is not found for the average glacier length changes measured for 1965-1966 to 2000-2003 observation period. In this case, glaciers <0.2 $km^2$ in size reduced in length by an average of 418.4±29 m, whilst glaciers >5$km^2$ reduced by an average of 343.33±29 m.

For both observation periods, relative ice area loss is found to decrease according to glacier size (see Figure 7.14). For the 1965-66 to 2000-2003 period, for example, percentage ice area loss for each size class reduces consistently from 70.68% for glaciers <0.2 $km^2$ to 34.38% for glaciers >5 $km^2$. Similar to the other three study sites,

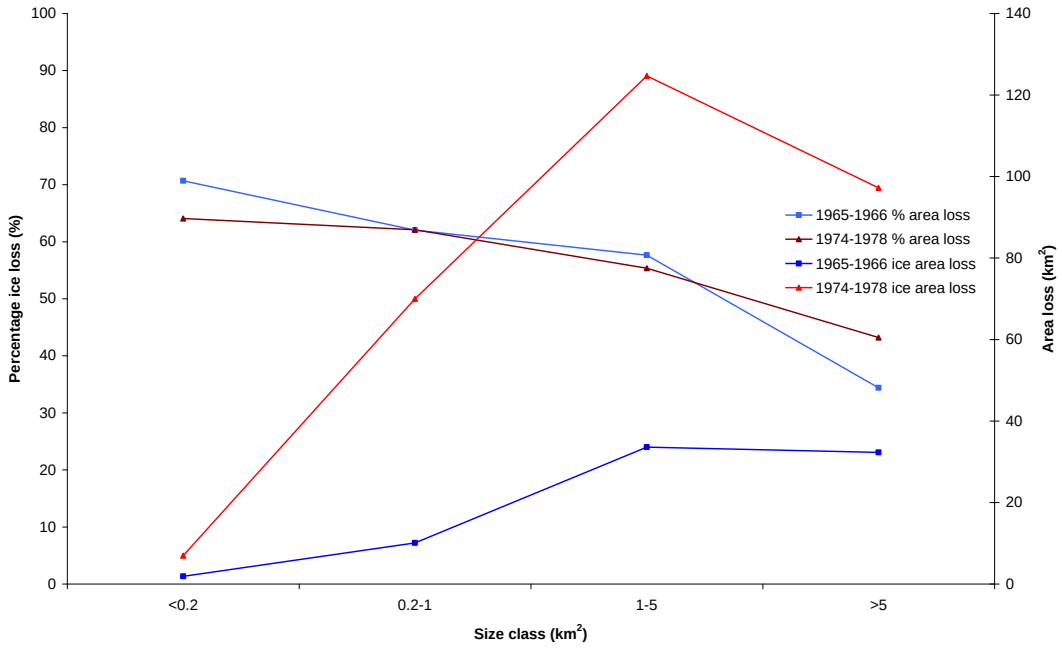


**Figure 7.14: Comparison of absolute area loss and percentage area loss for glaciers within each of the four size classes measured between 1965-1966 to 2000-2003 and 1974-1975 to 2000-2003.**

topographical analysis of the glaciers sampled at the LT site according to size (listed in Table 7.14) revealed that again larger glaciers originate at higher elevations and extend further down valley compared to smaller glaciers (see Figure 7.15).

**Table 7.14: Topographical characteristics of the glaciers sampled at the LT site according to glacier size.**

| Basin topography | Size Class (km$^2$) | | | |
|---|---|---|---|---|
| | <0.2 | 0.2-1 | 1-5 | >5 |
| Median Elevation (2001) | 5519 | 5475 | 5345 | 5384 |
| Average terminus elevation 1974-1978 | 5254 | 5027 | 4666 | 4456 |
| Average terminus elevation (2001) | 5353 | 5180 | 4808 | 4603 |

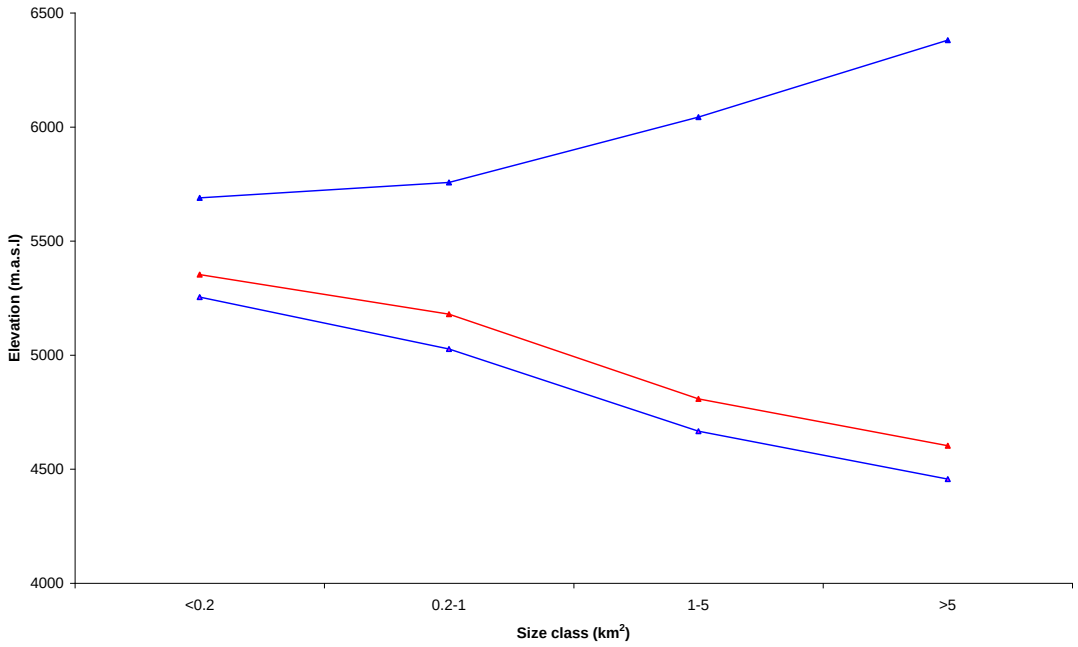


**Figure 7.15: Average maximum and minimum ice elevation in 1965-1975 (in blue) in relation to size, and the average minimum elevation of ice in 2003-2007 (red line).**

## 7.4. Hypsometry of ice area change

Figures 7.16-7.19 present the distribution of ice area losses with elevation for the GC, ND, SB and LT study sites. Before describing these figures it is important to note the following sources of elevation bias which may affect the analysis. Firstly, the elevation distribution of ice area measurements for the later observation period (2000s) was constructed using elevation information from the ASTER GDEM v2. Having been constructed through the merging of ASTER stereo data collected from 2000-2010,

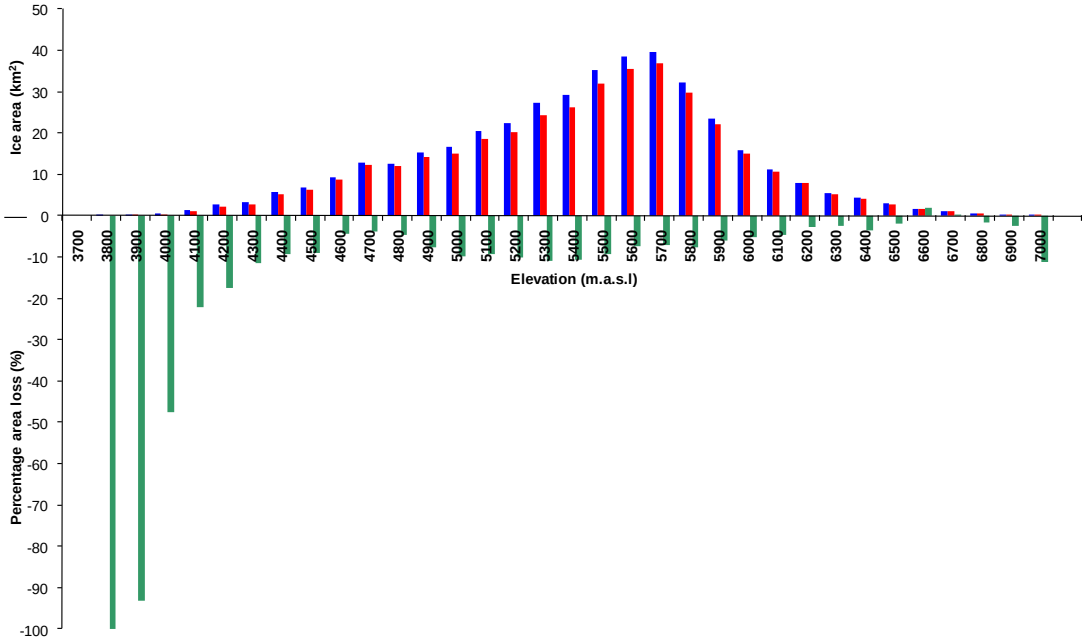


**Figure 7.16: Distribution of absolute ice area (red and blue columns) and percentage ice area losses (green columns) during 1965 and 2001 at the GC site according to 100 m elevation intervals.**

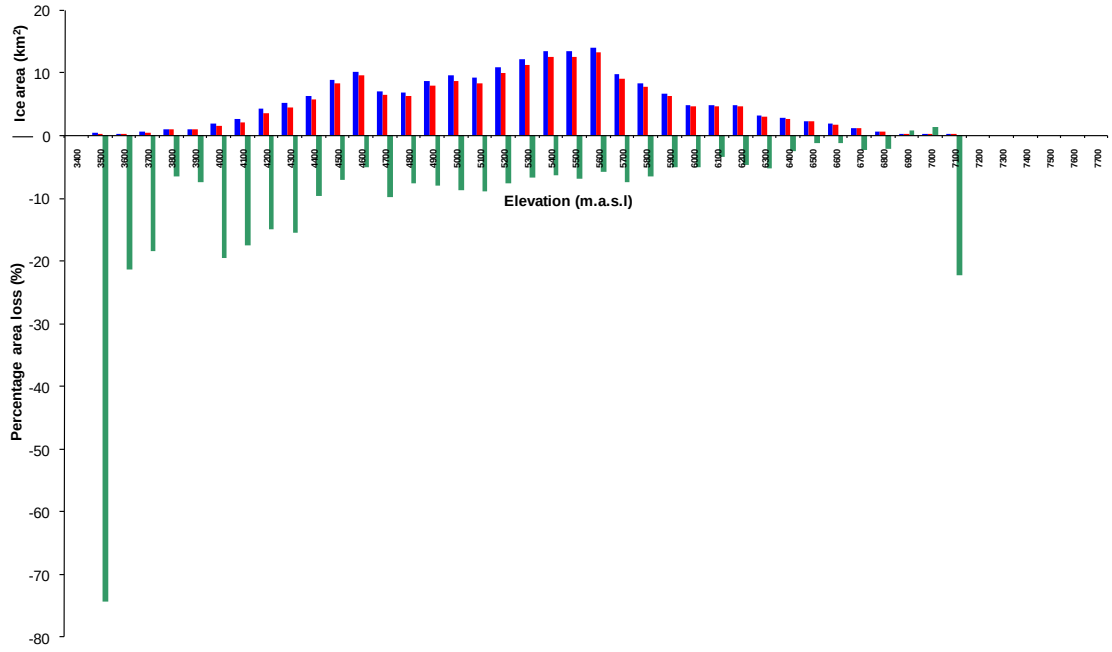


**Figure 7.17: Distribution of absolute ice area (red and blue columns) and percentage ice area losses (green columns) during 1964 and 2004 at the ND site according to 100 m elevation intervals.**

elevation bias may exist due to differential ice surface elevation changes throughout the ASTER GDEM collection period. However, in the case of the 2000s glacier sample, the ASTER GDEM is taken as a reasonable ice surface representation. Secondly, the ASTER GDEM was also used to estimate the elevation distribution of ice area delineated for the earlier observation period (1960s-1970s). In this case the ASTER GDEM is unlikely to represent the true ice surface of the glaciers sampled (due to the ice surface lowering which has likely occurred over the following decades) and the elevation analysis thus only represents a two-dimensional spatial reference highlighting ice area changes.

In the context of the glacier change analysis presented, figures 7.16-7.19 are important because they show a clear distinction in the pattern of ice area loss with elevation between the two westerly (GC, ND) and easterly study sites (SB, LT), both in magnitude and distribution. For the GC and ND glacier sample, although the distribution of ice area with elevation differs, the pattern of ice area loss with elevation is very similar. In both cases the largest relative ice area losses generally occur in the lower elevation bands. At the GC site, relative ice area losses in the two lowest 100 m elevation bands (3800-4000 m.a.s.l) ranged from 93-100%, whilst at the ND site relative ice losses for the two lowest bands (3500-3700 m.a.s.l) ranged from 21-74%. In comparison, relative ice area losses above 4600 m.a.s.l at both sites are greatly reduced (<10%), excluding the 7000-7100 m.a.s.l elevation band at the ND site. Ice area losses estimated for this particular elevation band are likely to be erroneous and possibly result from (1) manual ice classification errors induced by the presence of snow cover and shadowing and/or (2) Corona orthorectification errors (image distortion tended to be worse for highly elevated areas).

Similar to GC and ND, the SB and LT study sites also experience large ice area losses in lower elevations, however, in both cases these are larger in magnitude. The lowest seven 100 m elevation bands at the SB study site, for example, have all experienced deglaciation between the 1959/75 and2003/07 observation intervals. However, in addition to experiencing extensive ice area losses in lower elevations, both the SB and

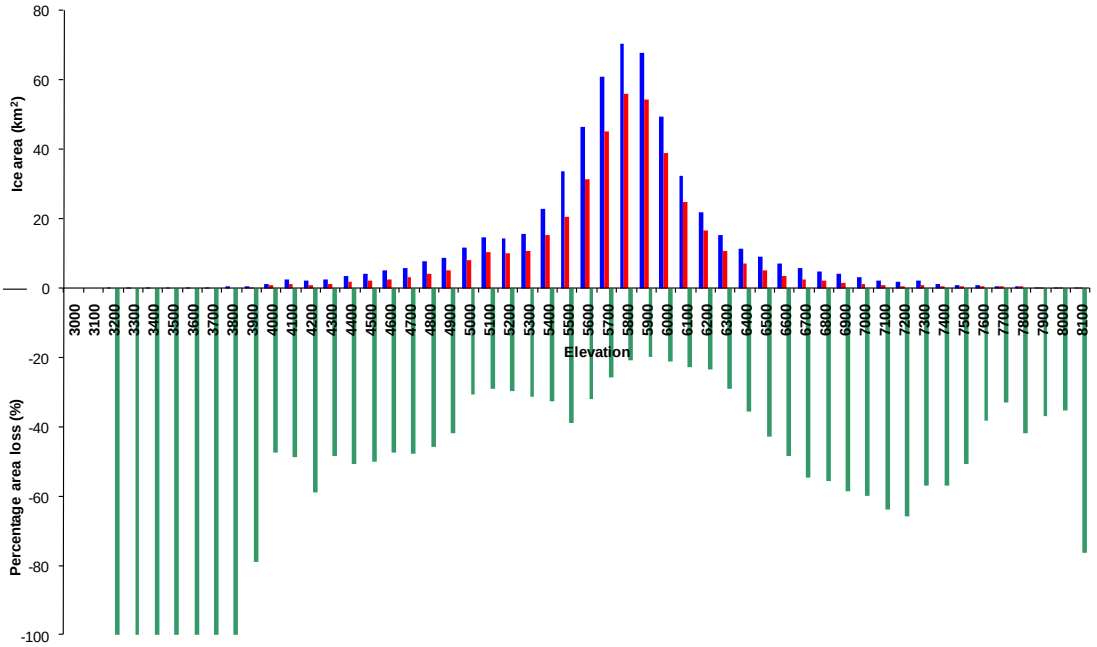


**Figure 7.18: Distribution of absolute ice area (red and blue columns) and percentage ice area losses (green columns) during 1959-1975 and 2003-2007 at the SB site according to 100 m elevation intervals.**

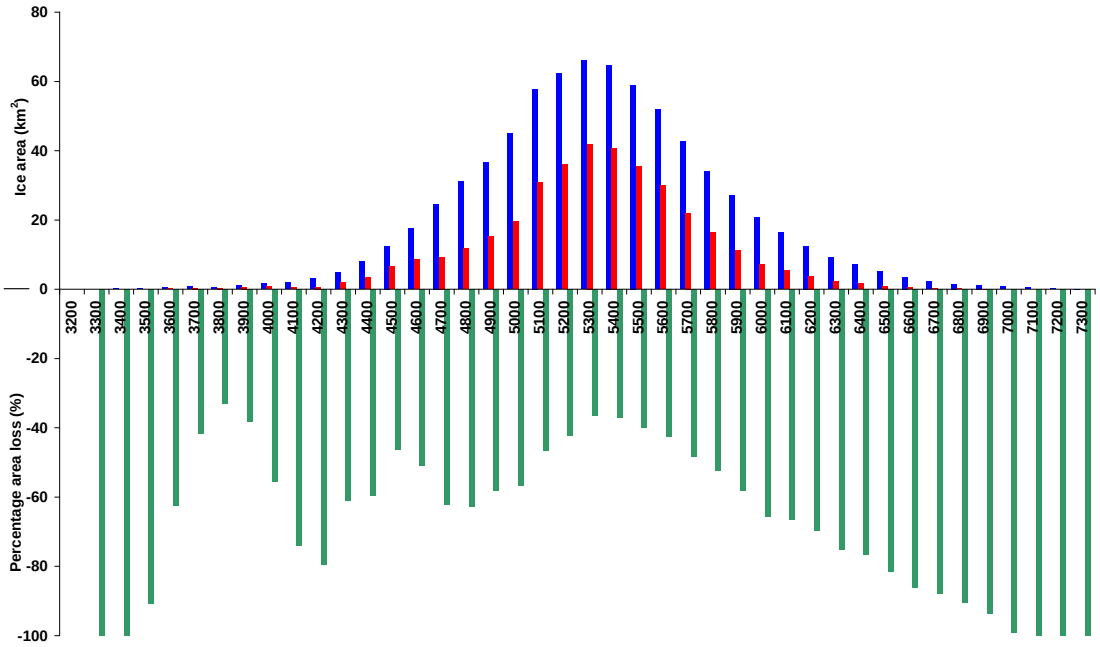


**Figure 7.19: Distribution of absolute ice area (red and blue columns) and percentage ice area losses (green columns) during 1965-1978 and 2000-2003 at the LT site according to 100 m elevation intervals.**

LT study sites have also experienced relatively large ice area losses throughout their entire elevation range. This comparatively heightened ice loss is particularly evident at the LT study site where ice area in every 100 m elevation band is shown to have reduced by at least 33%. Notably, at both the SB and LT sites, relatively large ice area losses are also shown for the highest elevation bands. At the LT site, for example, relative ice area losses above 6000 m.a.s.l increase from 65% to 100%, with the maximum ice area elevation descending from 7300-7400 m.a.s.l in 1965/75 to 7000-7100 m.a.s.l in 2000-2003. Similarly, relative ice area losses above 6000 m.a.s.l at the SB site range between 46% and 88%.

In an attempt to further investigate the possible influence of elevation on the differing rates of ice area and length loss shown in section 7.3, figure 7.20 presents the hypsometry of the ice areas observed during the 2000s for each of the study sites sampled. In comparison to the GC, LT and ND sites, ice area at the SB site is distributed at higher elevations throughout. Overall, 50% of the ice area at the SB site is distributed above 5800 m.a.s.l, compared to 5500, 5400, and 5300 m.a.s.l for the GC, LT and ND sites, respectively. The steep gradient of the ND curve highlights both the uneven distribution of ice area at this site and the large proportion of ice area located

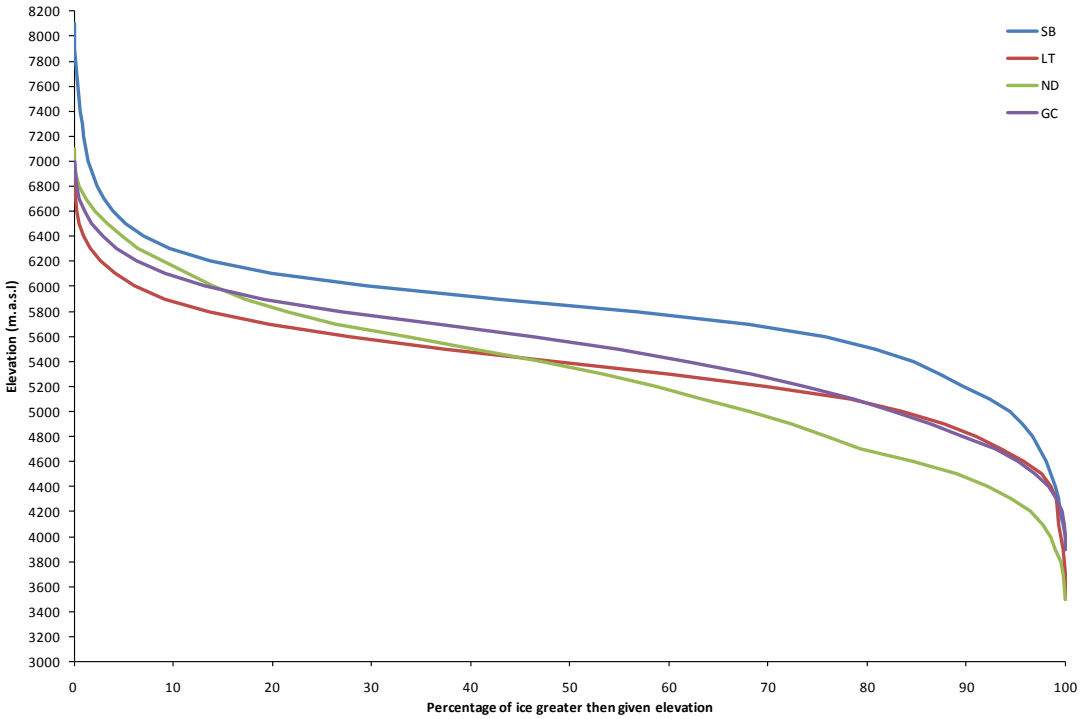


**Figure 7.20: Ice area hypsometry for the GC, ND, SB and LT sites observed during the 2000s.**

in the lower regions of its elevation range. This may be a consequence of the relatively small number of glaciers sampled at the ND site.

## 7.5. Discussion

### 7.5.1. Glacier area and length change, 1960s to 2000s: Contributions to current knowledge

Given the orthorectification of Corona imagery, part of the glaciological aim of this project was to integrate Corona data with other low cost and widely available geospatial datasets (ASTER satellite imagery, GLIMS glacier outlines) in order to map glacier area and length change for regions of the Indian and Nepalese Himalaya. Along with other studies that have been recently published (e.g. Bolch *et al.*, 2008; Bhambri *et al.*, 2011; Schmidt & Nusser, 2012), the use of Corona imagery here further demonstrates the potential of this dataset as a source of historic glacier mapping information in the Himalayas, offering an alternative to aerial photography and topographic maps.

Overall, results reveal that between 1965/68 and 2001/04 glaciers selected at the GC and ND study sites reduced in area by 7.97±0.29% (0.22% $a^{-1}$) and 7.54±0.26% (0.21% $a^{-1}$), and in length by an average of 185±23 m (5.13 m $a^{-1}$) and 174±32 m (4.83 m $a^{-1}$), respectively. In comparison, between the 1960/70s and 2000s, glaciers selected at the SB and LT study sites reduced in area by 29.97±0.2% (~0.78% $a^{-1}$,) and 50.55±0.08% (~1.68% $a^{-1}$), and in length by an average of 387±29 m (~10.18 m $a^{-1}$) and 480±29 m (~16 m $a^{-1}$), respectively. Together with elevation data derived from the ASTER GDEM v2, the glacier area and length change data presented both complements and enhances existing records in the Himalayas.

Glacier measurements across the Himalaya have been mostly derived from satellite imagery or topographic maps. As has been established, glacier mapping from both these sources in the Himalayas is influenced by errors related to factors including spatial resolution, geometric accuracy and the differing processing and glacier

delineation methodologies utilised, amongst others (Bhambri & Bolch, 2009; Kääb, 2005a.). Due to these factors, even when glacier mapping efforts covering similar time periods already exist, it is often valuable to provide repeat measurements derived from different mapping sources and methodologies. Highlighting this point, Bhambri *et al.* (2011) draw attention to the differing areal reduction estimates for Gangotri glacier.

Partly overlapping the GC study area, Bhambri *et al.* (2011) utilised Corona (1968), Cartosat-1 (2006) and IRS-P6 LISS IV (2006) data to estimate glacier area loss in the Garhwal Himalaya. Specifically for Gangotri glacier, Bhambri *et al*. (2011) calculated an area change of -4.4 $km^2$ (0.11 $km^2\ a^{-1}$), which compares with the value of -9.53 $km^2$ (0.26$km^2\ a^{-1}$) shown here. This difference in the two areal loss estimates is attributed to the mapping of glacier area in accumulation zones. Unlike Bhambri *et al.* (2011), in this study all areas of the accumulation zone of Gangotri glacier were considered for the areal loss analysis. Although only small area changes were revealed for the accumulation zones of Gangotri glaciers larger tributaries, area losses observed for many of the smaller high elevation tributaries, for example, were shown to be considerable.

Other studies have also estimated areal changes for Gangotri glacier. Kumar *et al.* (2009), for example, calculated an area loss of 15.4 $km^2$ (0.51 $km^2\ a^{-1}$) between 1976 and 2006, it is presumed from Landsat MSS (1976, 79 m spatial resolution) and Landsat ETM+ (2006, 30 m resolution) data (satellite source is not stated), whilst Ahmad and Hasnain (2004) measured an area loss of 10 $km^2$ (0.62 $km^2\ a^{-1}$) between 1985 and 2001 using a SOI topographic map (1985) and IRS Pan satellite data (2001). In addition to the multi-temporal monitoring, single year observations are also available for Gangotri glacier. Srivastava (2004), for example, estimated the area of Gangotri as 143.58 $km^2$ from a 1966 SOI topographic map. Comparing this measurement with the area calculated for Gangotri by Ahmad & Hasnain (2004) in 2001 (77 $km^2$) suggests an overall ice area loss of 13.53% (0.38% $a^{-1}$) which is considerably larger than the areal losses reported here (4.82%, 0.13% $a^{-1}$).

The glacier area change results presented here for the LT study site can also be compared with the glacier area measurements presented by Shrestha & Joshi (2009). Including a similar glacier sample for the Langtang region, Shrestha & Joshi (2009) revealed a glacier area loss of 27.95% (1.16% $a^{-1}$) between 1976 and 2000. These glacier area reductions are lower than those presented here. Notably, however, the glacier delineations presented by Shrestha & Joshi (2009) were obtained using an automated mapping technique. Automated glacier mapping techniques have often been found to result in large errors, particularly for debris covered glaciers which are numerous in the Langtang region (Raup *et al.*, 2007; Bhambri & Bolch, 2009). Shukla *et al.* (2010), for example, reported mapping errors of up to 26% for debris-covered glaciers delineated automatically from ASTER imagery in the Chenab basin, Indian Himalayas. The errors associated with automated mapping are likely to worsen when used with coarse resolution imagery (Kääb, 2005a.). In the case of Shrestha & Joshi (2009), glaciers were automatically delineated from Landsat MSS and Landsat ETM+ imagery, with a resolution of 79 m and 30 m, respectively. The glacier area change estimates presented here therefore offer an alternative assessment of glacier behaviour in this region over the past ~30 years.

In terms of enhancing existing glacier change records in the Himalaya, the results presented help to reduce current knowledge gaps, brought about by the relative paucity of glacier measurements in the Himalaya, in the following ways. Firstly, this study provides long term glacier area and length change measurements for the ND and SB study sites that, to the author's knowledge, were not available previously. For the Garhwal Himalayas, the ND glacier change measurements concur with those found at the GC study site, both here and by Bhambri *et al*. (2011), suggesting that the glaciers located in this region have responded similarly to local climate changes. For the SB study site, the glacier change measurements possibly add to evidence provided here and by Shrestha & Joshi (2009), that some areas in the Nepalese Himalaya may be more sensitive to localised climate change than others in the Greater Himalayas.

Secondly, this study provides glacier hypsometry information for each of the study sites sampled that was not previously available. The glacier hypsometry presented

represents important additional information about the characteristics of glacier change in each of the study areas selected and the sensitivity of the glacierised area contained to climate change (e.g. Small, 1995; Oerlemans *et al*., 1998; Braithwaite & Raper, 2009). Moreover, this dataset could provide valuable inputs for glacier melt modelling efforts for the areas sampled (e.g. Singh *et al.* (2008)).

### 7.5.2. Glacier area and length change characteristics

In line with the global trends (UNEP & WGMS, 2008), all the glaciers sampled in this study underwent areal reductions between the 1960s and the early 2000s. However, the magnitude of these areal and length glacier reductions differed between the two eastern (SB and LT) and western (GC and ND) study sites. Nonetheless, a number of similar regional glacier change characteristics were identified.

One of the foremost regional similarities observed was that smaller glaciers throughout experienced higher relative ice area losses compared to larger glaciers, confirming the established idea that small glaciers are particularly sensitive to climatic changes (Kulkarni *et al*., 2007; Narama *et al.*, 2009; Ye Baisheng *et al.,* 2003; Lemke *et al.*, 2007). However, it was also shown that there is a larger variability in the relative area changes of small glaciers. For the GC site, for example, glaciers <1 $km^2$, experienced relative area losses ranging from 0.2-100%, whilst glaciers >1 $km^2$ ranged from 2.3-23%. It can therefore be assumed that the sensitivity of the smaller glaciers sampled is more individual than for larger glaciers sampled. The larger variability in the relative reduction of smaller glaciers is explained by the tendency of smaller glaciers to have greater distributions in terms of elevation and aspect (as suggested by Narama *et al.* (2009), Maisch *et al.* (1999) and Paul (2002)).

Although the relative area losses of larger glaciers is shown to be less than for small glaciers, in absolute terms larger glaciers lost considerably larger areas at each of study sites. At the LT study site, for example, glaciers <0.2$km^2$ lost an average of 0.37 $km^2$ during the 1965-66 to 2000-03 period, whilst glaciers >5 $km^2$ lost an average of 10.76 $km^2$. Similar to the pattern of absolute ice area losses, larger glaciers were also

shown to have undergone larger length losses than smaller glaciers. For small and large glaciers, the differences in the length change highlights the limitations of reporting this parameter as a measure of glacier health (such as in Scherler *et al.* (2011) and Zemp *et al.* (2008)) as it often gives a disproportionate representation of the response of an individual glacier to climatic changes. The Gangotri glacier, for example, whose length change has been reported by numerous studies over differing time scales (e.g. Bhambri *et al.*, 2012; WWF, 2009; Tangari *et al.*, 2003), is shown to have reduced in length by 856 m between 1965 and 2001. This value alone would suggest that Gangotri glacier has experienced significant ice area losses over the 36 year investigation period. In fact, Gangotri glacier is shown to have experienced a relative ice area loss of 4.82%, which is small in comparison to the glacier sample as a whole.

Although regional similarities exist in the characteristics of the glacier area and length reductions shown, the relative ice area losses observed for each pair of eastern and western study sites varied considerably. This finding indicates differences in the response of glaciers to climate change in these two regions. However, the glacier change results presented are limited by their spatial coverage, a lack of volume measurements (offering a more comprehensive measure of glacier health), and by possible errors related specifically to the use of GLIMS glacier outlines.

### 7.5.3. Himalayan glacier change trends

The glacier area and length results presented offer further insight into the differing responses of Himalayan glaciers to climate change over the past ~40 years. For the Garhwal Himalaya, the glacier area changes reported at the GC and ND study sites closely correspond in location to those presented by Bhambri *et al.* (2011), who observed areal reductions of 4.6±2.8% (~0.12% $a^{-1}$) between 1968 to 2006. For the Garhwal Himalaya, both the glacier area change results shown here and by Bhambri *et al*. (2011) are lower than those reported for the more western Himachal Himalayas. For the Chenab, Parbati, and Baspa basins, for example, glacier area was reported to have reduced by 21% (0.5% $a^{-1}$), 22% (0.52% $a^{-1}$) and 19% (0.45% $a^{-1}$) between 1962

and 2004, respectively (Kulkarni *et al.*, 2007). Glacier area reductions reported for the Garhwal Himalaya are also less than that reported for the Kang Yatze Massif, Ladakh, (14% (0.34% $a^{-1}$)) between 1969 and 2010 (Scmidt & Nüsser, 2012). Further west along the Himalayan arc, however, glaciers in the central Karakorum began to expand in the 1990s after generally reducing in area since the 1920s (Hewitt, 2005). For glaciers of the Nepalese Himalaya, the relatively large ice area losses reported here for the Setibeni and Langtang regions are supported by observations made by Shrestha & Joshi (2009). However, the glacier area losses shown for these two regions do not correspond with glacier change observations made in the nearby Khumbu Himalaya, Nepal. For the Khumbu Himalaya, Bolch *et al*. (2008), for example, revealed glacier area losses of 5.3% between 1962 and 2005 (~0.12% $a^{-1}$).

Considering glacier length change trends in the Himalayas, Yao *et al.* (2012) compiled an extensive list of length measurements across the Himalayas covering a similar observation period as this study. Overall, 8 glaciers sampled in central Nepal were shown to have reduced in length by an average of 6.3 m $a^{-1}$ from ~1960 to 2005, whilst 20 glaciers sampled in the western Himalayas (from the Uttarakhand to the Himachal Himalayas, India) reduced in length by an average of 16.6 m $a^{-1}$ from ~1966 to 2001. These measurements compare to a combined average glacier length reduction of 13.6 m $a^{-1}$ for the glaciers sampled at the SB and LT sites (located in central Nepal), and 4.98 m $a^{-1}$ for the glaciers at the GC and ND sites (located close to the Himachal Himalayas). These opposing length reduction trends shown here and by Yao *et al.* (2012) are in some ways not surprising. The glaciers sampled by Yao *et al.* (2012), for example, are limited in number, distributed over large areas, and included glaciers of varying sizes. It is therefore difficult to make comparable assessments with the results presented for the GC, ND, SB and LT study sites.

For the GC and ND study sites, in particular, a number of individual glacier length measurements are available which can be compared with the results reported here. Length reduction measurements for Gangotri glacier (GC), for example, range from 1250 m to 1651 m between the 1960s and 2000s, derived from field-based, satellite and SOI topographic map data (Naithani *et al.*, 2001; Tangari *et al*., 2004; Bahuguna,

2007; Bhambri & Chaujar; 2009). In comparison, Bhambri *et al.* (2012) reported a length reduction of 819 m (19.97 m $a^{-1}$) between 1965 and 2006. Here, Gangotri glacier is reported to have reduced in length by 856±23 m (23.77 m $a^{-1}$), corresponding with Bhambri *et al.* (2012) and with field-based measurements made by the GSI from 1971 to 1996, suggesting length reductions of 720 m (28.8 m $a^{-1}$) (Srivastava, 2004). For Milam glacier (located in the ND study site), length reductions shown here (1158±32 m (32.16 m $a^{-1}$)) also correspond closely with field measurements made by the GSI (GSI, 1996-1997), suggesting a length reduction of 939 m (30.2 m $a^{-1}$) between 1966 and 1997. The correspondence of the Gangotri and Milam length reductions observed here with the field measurements made by others, in particular, lends support to the accuracy of the Corona and ASTER data used.

Overall, the glacier area change observations discussed highlight the variability in glacier sensitivity to climate change across the Himalayas. Assessing this variability, however, is difficult because (1) long term mass balance records are limited for the regions specified and (2) long term high elevation climate records are sparse. What is clear is that glacier sensitivity to climate change is largely controlled by variability in the summer monsoon and winter westerlies (Barry, 1992; Hasnain, 1999). The movements of these two climate systems, in respect to the Himalayan arc, has led to the partitioning of glaciers into differing mass balance regimes. According to Thayyen & Gergen (2009), all the glaciers sampled in this study are classed as having 'summer monsoon and winter accumulating regimes'. However, this classification fails to address the relative proportionality of summer and winter snow accumulation received by glaciers at each site.

Glaciers heavily reliant on summer snowfall have been shown to be particularly sensitive to air temperature increases, due to the influence on solid and liquid precipitation portioning (Fujita & Ageta, 2000; Fujita, 2008). In addition to temperature warming (Hasnain, 2000), observations made by Dimri & Mohanty (2007) suggest that winter precipitation in the Himalayas, since the 1970s, may also be reducing (Dimri & Mohanty, 2007). Moreover, other studies have suggested that the summer monsoon has begun to weaken (Bhutiyani *et al.*, 2007, 2009; Alder *et al.*,

2003). Considering the importance of summer monsoon precipitation for glaciers in eastern Himalayans (e.g. Mall *et al*., 2006), glaciers sampled at the SB and LT study sites may have been particularly influenced by the climate changes described, resulting in the relatively large glacier area reductions observed. The comparatively small glacier area changes observed in the Khumbu Himalaya (5.3%, ~0.12% $a^{-1}$) by Bolch *et al*. (2008) between 1962 and 2005, however, do not agree with this assumption.

In comparison to the SB and LT study sites, glaciers sampled in the Garwhal Himalayas may be less reliant on summer monsoon snowfall accumulation, receiving a larger proportion of snowfall during winter (Dobhal *et al.*, 1995; Owen *et al*., 1996; Bhambri *et al*., 2011). This is supported by observations made by Vohra (1981), who suggested that basins near Gangotri glacier receive equal amounts of summer and winter precipitation. The possibility of GC and ND glaciers being able to accumulate significant amounts of mass during two seasons may make them less sensitive to climatic changes which, in turn, may help explain the reduced level of ice area reduction in comparison to SB and LT. However, without analysis of climate data from the areas specified, this assumption remains speculative.

Aside from climatic factors, the variability in the response of Himalayan glaciers to climate change has been shown to be influenced by other factors, including glacier elevation, slope, aspect, glacier size distribution and ice debris-cover, amongst others (Bhambri *et al.*, 2011; Narama *et al.*, 2009; Inoue, 1977; Hewitt, 2005). The influence of ice debris-cover has been found to be particularly important in regards to Himalayan glacier responses to climate change. Analysing glacier length change between 2000 and 2008 for 286 glaciers distributed across the Himalayan arc, Scherler *et al.* (2011), for example, revealed that heavily debris-covered glaciers typically have stable fronts (although may still be downwasting). For the 103 glaciers sampled in the Garwhal Himalayas by Bhambri *et al.* (2011), around 25% of the ice area was covered with debris. In this study, glacier debris-cover was not mapped for the glaciers sampled due to the difficulties involved with delineating debris from satellite imagery

(Bhambri & Bolch, 2009; Raup *et al.*, 2007) and, therefore, the influence of this ice surface characteristic could not be assessed.

### 7.5.4. Regional glacier hypsometry & size distribution

Due to the effect of thermal and precipitation lapse rates on glacier mass balance, it was assumed that ice elevation characteristics at each of the sites studied may have influenced the differing glacier area reduction rates observed. As expected, the glacier change characteristics observed at each study site conformed to the assumption that larger glaciers tend to originate at higher elevations and extend further down valley (e.g. Collins, 2008; Ye Baisheng *et al.*, 2003). Subsequently, higher glaciers are expected to be less sensitive to climate change (e.g. Ye Baisheng *et al*. (2003) and Kulkarni *et al.* (2007)). However, the elevation analysis presented in this study indicates that this simplified relationship between glacier elevation and climate sensitivity does not always hold true when comparing glacier change observations over large regions. Ice area sampled at the SB study site, for example, was found to be distributed at greater elevations compared to the GC and ND study sites sampled, despite having experienced considerably larger total ice area losses (Figure 2.1). Other studies undertaken for large numbers of glaciers, both in the Himalaya and other glaciated mountain regions, have taken this analysis further by statistically testing glacier change and elevation parameters (e.g. Bhambri *et al*., 2001; Andreassen *et al*., 2008). Such testing has revealed poor correlations, suggesting elevation parameters alone cannot be used to gauge glacier sensitivity to climate change.

In terms of glacier size distribution, the assumption that smaller glaciers are more sensitive to climate warming than larger glaciers is well established (IPCC, 2007). Here, results show that a significantly larger proportion of the ice area sampled in the GC and ND study sites is contained within glaciers >5 $km^2$ (78.59% and 87.24% respectively) compared to the SB and LT study sites (58.52% and 51.45% respectively). Therefore, a far greater proportion of ice area within the SB and LT sites is contained in smaller glaciers that are more susceptible to the negative effects of climatic warming (such as the of rising transient snow lines and zero-degree isotherms).

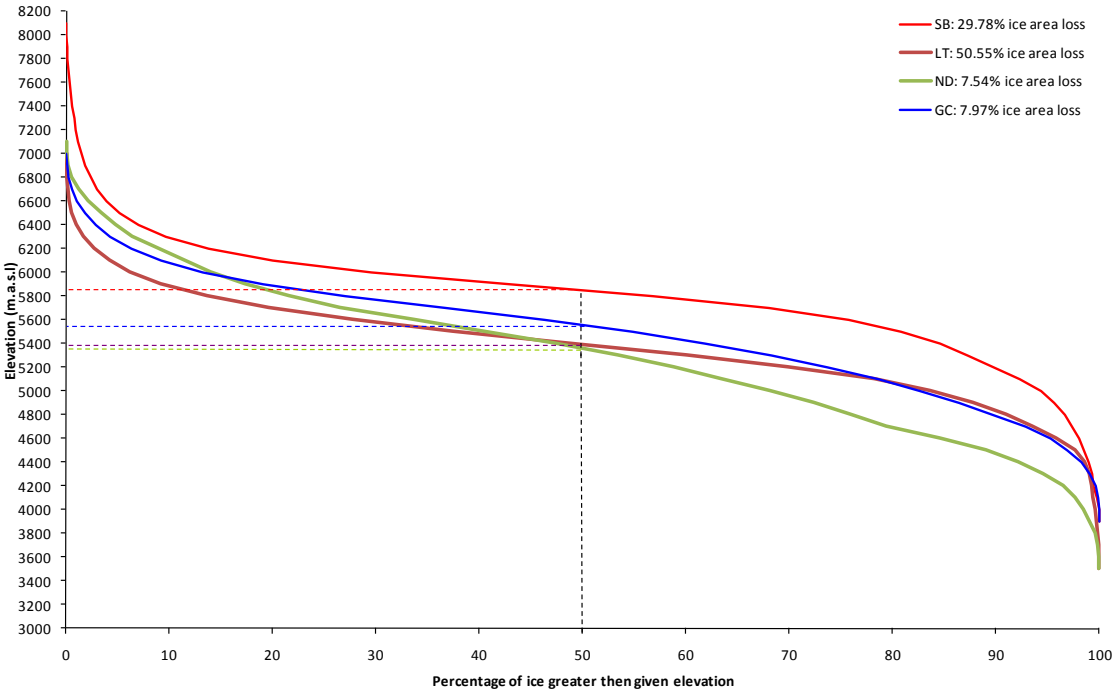


**Figure 7.21: Ice hypsometry of the Gangotri Chaukhamba (GC), Nanda Devi (ND), Setibeni (SB) and Langtang (LT) study sites as of the 2000s with reference to ice area loss from the 1960-70s (in legend). Dashed line indicates the elevation at which 50% of each respective sites ice area is greater.**

The differing distribution of ice area according to glacier size may help to explain the large differences in the glacier area reductions observed for the two eastern and western sites in this study. This idea is limited to an extent by the relatively small glacier samples at the GC and ND sites. Encouragingly, however, the glacier inventory compiled by Bhambri *et al.* (2011) in the Garhwal Himalayas also shows a relatively high distribution of larger glaciers for this region.

### 7.5.5. Accuracy of GLIMS glacier outlines

Due to the paucity of historic glacier measurements across the Himalaya, the availability of pre-1980 outlines within the GLIMS glacier database is potentially valuable. However, as with all spatial measurements, the value and validity of these GLIMS Himalayan glacier outlines is determined by their level of geometric accuracy. Here, the accuracy of the ASTER and Corona satellite imagery utilised, and the glacier outlines derived, could be assessed with reference to accuracy measures quantified by previous studies (ASTER, e.g. Iwasaki (2005) and Fujisada (2005)), through

assessment of the orthorecitifaction process (Corona, see section 6.1) and through assessment of the manual glacier delineation method applied (see section 7.1).

In comparison to the other geospatial datasets used in this study, GLIMS glacier outlines were limited in that the metadata provided included no information on the geometric accuracy of the dataset (despite the availability of positional accuracy fields within the metadata framework (Paul *et al.*, 2010)). Additionally, information referring to the source of each glacier outline was generalised to 'Aerial Photography/Topographic maps', with no reference to scale or spatial resolution. Due to this accuracy ambiguity, and the unavailability of other historic mapping datasets to use as reference, the accuracy of the GLIMS glacier outlines used could only be assessed qualitatively, in relation to the ortho-ASTER imagery, the ortho-ASTER derived glacier outlines, and previously published information.

In terms of the accuracy of the GLIMS glacier outlines used, the first point of concern is the difference in the glacier area losses observed in this study and by Shrestha & Joshi (2009) for the LT study site over a similar time period (glacier change difference of ~0.52% $a^{-1}$). Aside from possible error related to the automated glacier delineation technique used by Shrestha & Joshi (2009), the difference in glacier area change observed at the LT study site may point to errors within the GLIMS data used. Interestingly, glacier area change estimates for the SB study site correspond more closely with those shown by Shrestha & Joshi (2009) (glacier change difference of ~0.38% $a^{-1}$).

When compared to ortho-ASTER imagery, the spatial extent of the GLIMS glacier outlines were shown to correspond well with visible LIA lateral and terminal moraines and other terrain features. This conformity with terrain features would suggest that the positional accuracy of the GLIMS glacier outlines is generally quite good. The GLIMS glacier outlines also matched the general geometric shape of the ASTER derived glacier outlines. However, aside from ablation regions where areal ice loss is expected, large differences between the GLIMS and ASTER-derived glacier outlines were also apparent at high elevations, where ice area losses should be minimal. At the LT study

site, for example, ice hypsometry analysis showed that the maximum ice elevation range reduced by 300 m during the observation period.

The magnitudes of the ice area losses shown at high elevations for the SB and LT study sites would suggest that the delineation of GLIMS glacier outlines in these ice areas may be erroneous. The source of these delineation errors is two-fold. Firstly, errors may be the result of human delineation error. Accurate manual delineation relies on user knowledge and the identification of the boundaries between ice- and snow-cover, which at high elevation can often be difficult. In a GLIMS analysis comparison experiment, where the consistency of data provided by different analysts was studied, Raup *et al.* (2007b.), for example, found that glacier interpretation errors were a significant problem resulting in non-uniform glacier outlines.

Secondly, delineation errors may be the result of poor image and map source quality. Historic topographic maps available for the Himalayas have been identified as containing large errors in glaciated areas related to the interpretation of ice, snow, and debris cover (Vohra, 1980; Agarwal, 2001). Additionally, analysis of historic aerial photography acquired over many Himalayan regions has revealed that the images acquired often contained extensive snow-cover (Bhambri & Bolch, 2009). With the majority of the GLIMS glacier outlines conforming to basin topography at high elevation (mountain peaks and ridges), the presence of snow cover within the mapping data used offers a plausible explanation for the possible delineation errors observed. To summarise, due to the geometric accuracy issues identified, the use of historic GLIMS glacier outlines within Himalayan glacier monitoring studies should be approached with caution. To avoid possible over- or under-estimations of glacier change in regions of the Himalaya, such accuracy issues should either be addressed by the GLIMS project or clearly communicated.

# 8. Conclusion

## 8.1. Corona imagery orthorectification and DEM extraction

Although representing a valuable pre-1980s geospatial data source, Corona imagery is a complex and challenging dataset that exhibits a number of unique characteristics which hinder its application as a historic glacier mapping tool. These challenges, related to the panoramic distortion of Corona imagery, are further complicated here by the application of Corona data in a highly mountainous study area which, for DEM generation in particular, represents a worse-case scenario. The use of Corona imagery for glacier mapping in this study would have represented one of the main points of originality. This originality has been reduced during the progress of the study as other scientists have also begun to demonstrate the potential of Corona imagery as a Himalayan glacier mapping tool (e.g. Bolch *et al*., 2008, Bhambri *et al*., 2011, and Schmidt & Nusser, 2012). These studies, however, cover relatively small areas and utilise methodologies which require expensive spatial reference data and custom-built software packages. Such expense limits the application of Corona data over large swaths of territory. Nonetheless, these Himalayan Corona mapping studies offered an important comparator for the accuracy of the alternative Corona processing approach applied here.

The first methodological aim of this study was to develop a replicable and low cost method of orthorectifying Corona imagery. Despite Corona images exhibiting complex panoramic distortions and lacking important fiducial and principal point parameters, this aim was realised through the use of (1) a non-metric camera frame model photogrammetry approach that had not previously been tested in a high mountainous environment, and (2) horizontal and vertical reference data from ortho-ASTER imagery and the freely available ASTER GDEM. Overall, the geometric accuracy of the Corona imagery orthorecitifed at the GC and ND study sites was estimated to be ±7.5 m and ±16.7 m, respectively. The differences in the geometric

accuracies achieved for the two study sites were attributed to GCP sampling, with the GC study site having a greater number of GCPs in comparison to the ND study site. The Corona geometric accuracies achieved here are similar to those reported by other studies that have orthorectified Corona imagery in high mountainous regions (e.g. Bolch *et al.* (2008), Schmidt & Nusser (2012) and Narama *et al.* (2009)).

The accuracy of the Corona orthorecitification process was sufficient to allow planimetric glacier area to be manually delineated and compared with delineations derived from recent ortho-ASTER imagery. This study demonstrates that Corona imagery can be effectively applied for planimetric glacier mapping purposes over large regions of the Himalayas, further highlighting its potential as a historic alternative to aerial photography and topographic maps that are limited in number and contain errors.

The photogrammetric non-metric camera model used here to orthorectify Corona imagery is available in a commercially standard GIS software package (Erdas Imagine LPS). The use of this software package enabled: (1) geometric distortions present in Corona imagery to be corrected without the use of excessive sampling of GCPs; (2) geometric distortions present in Corona imagery to be corrected without the need for fiducial and principle point flight parameters; and (3) Corona orthorectification to be undertaken without the need for GCPs derived from VHR satellite imagery, topographic maps or DGPS surveying. Considering these three points, the method applied offers an alternative to image transformation and other empirical and rigorous photogrammetric approaches available. However, the non-metric camera frame model is limited in that it was designed mainly for use with aerial photography, acquired at relatively low altitudes. In this respect, rigorous Corona specific photogrammetric methodologies (e.g. Schenk *et al.* (2003) and Sohn *et al.* (2004)), still remain the best choice for orthorectification procedures despite taking time to develop and implement.

The second methodological aim of this study was to extract detailed DEMs from Corona stereo-pairs allowing glacier surfaces from the 1960s to be compared with

those for the 2000s (derived from the ASTER GDEM) so that ice volume could be quantified. In contrast to the Corona orthorectification process, Corona DEM generation faced challenges which resulted in vertical accuracies being insufficient to allow calculation of glacier volume change for a large number of glaciers. The challenges encountered related to (1) geometric inconsistencies in overlapping orthorectified Corona image pairs, resulting from inadequate sampling of GCPs. In contrast to snow-free rock areas, directly surrounding glacier ice and vegetation-free valley bottoms close to glacier snouts, GCP sampling of other image features was limited by the relatively poor resolution of the ASTER reference data and a number of Corona and ASTER image quality issues. These GCP sampling issues were superimposed (2) onto a range of common challenges faced generating DEMs in high-relief terrain (e.g. distortion related to topographic shadowing and slope perspective). Overall, due to the challenges encountered, it is concluded here that, for the purpose of extracting Corona DEMs, the ASTER control data utilised was insufficient. For the extraction of Corona DEMs, horizontal and vertical control data should ideally be sought from a VHR satellite imagery reference source (e.g. IKONOS and Quickbird stereo satellite imagery). The use of such VHR datasets, however, would increase the cost of the undertaking.

Despite the challenges faced, ice surface lowering was detected for the lower portions of four glaciers (Gangotri, Milam, Uttari Nanda, and Nanda Devi 1). Characterised by relatively reduced surface slope gradients (which are more favourable for DEM generation) and located in close proximity to a number of GCPs, surface lowering at the snouts of these four glaciers corresponded well with the Corona-derived glacier outlines, with maximum lowering ranging from 86 m to 146 m. Corona-ASTER elevation comparisons, performed in non-glaciated valley bottoms adjacent to each glacier, suggest that vertical errors in these areas reduced significantly (~±27 m). However, due to the overall magnitude of the vertical errors quantified for the GC and ND Corona DEMS, accuracy of the surface lowering and volume changes revealed for each of the four glaciers was difficult to ascertain.

When comparing glacier change for a large number of glaciers, changes in glacier volumes are particular useful for estimating contributions of ice to river runoff and to sea level change. It was therefore unfortunate that the photogrammetric approach implemented here could not extract sufficiently accurate Corona DEMs. As with the Corona orthorectification process, the accuracy of Corona DEMs extracted using this method would likely improve by using VHR satellite reference data. Such improvements, particularly in vertical accuracy, would enhance the ability to detect glacier elevation changes when compared with more recent DEMs.

**8.2. Himalayan glacier area and length change, from the 1960s to early 2000s**

Despite representing the most highly glaciated region in the world, outside the polar regions, glacier monitoring efforts in the Himalayas fail to compare with the more frequently studied glacierised areas in North America, European Alps and Scandinavia. Here, a glacier mapping study is presented that, by utilising historic (orthorectified Corona imagery and GLIMS glacier outlines) and contemporary geospatial datasets (ASTER satellite data), provides extensive glacier area and length measurements that both complement and enhance current records. The presented glacier changes are distinctive compared to similar Himalayan studies, in their spatial and temporal scale, and give further insight into glacier change variability across the Himalayas since the 1960s. Moreover, for some areas, the data presented offers valuable comparisons to other glacier change observations, some of which may glacier mapping errors.

Overall, glacier area at the GC and ND study sites (Uttarakhand, India) was found to have reduced by 7.97±0.29% and 7.54±0.26% between 1965-2001 and 1968-2004, respectively. By comparison, glacier area reduction at the more easterly located SB and LT study sites (Central Nepal) was higher, declining by 29.78±0.2% and 50.55±0.08% between 1959/75-2003/07 and 1965/78-2003/03, respectively. Similar differences in the magnitude of change were also observed for glacier length. Glacier termini at the GC and ND study sites, for example, reduced on average by 185 m and

174.17 m respectively, whilst at the SB and LT study sites glacier length reduced on average by 387.34 m and 480.49 m respectively.

The large differences in glacier area and length change shown for the two Indian (ND and GC) and Nepalese (SB and LT) study sites represents the most notable glaciological finding of this study. However, aside from these differences, the following cross-regional glacier change characteristics were also revealed: (1) smaller glaciers at each study site experienced higher relative ice area losses compared with larger glaciers; (2) the magnitudes of the relative ice area losses shown for smaller glaciers varied considerably compared with larger glaciers; (3) larger glaciers were identified as having experienced significantly larger absolute ice area and length losses. These findings agree with well known glacier change characteristics observed both in the Himalayas and elsewhere in the world.

The glacier change results presented correspond with other Himalayan studies which when compared also suggest differences in the response of glaciers in the Indian Garhwal Himalaya and Central Nepal to climate change since the 1960s (e.g. Bhambri *et al.* (2011) and Shrestha & Joshi (2009)). Assessing glacier variability across the Himalayas, however, continues to be difficult due to the paucity of long term mass-balance and high elevation climate records. In terms of Himalayan glacier sensitivity to climate change, a number of localised topographical and ice surface characteristics are also influential and information about these factors is potentially valuable. In this study, glacier size distribution and hypsometry analyses revealed the following:

(1) At each study site, large glaciers, which were shown to have undergone smaller relative area change, originated at higher elevations. However, this relationship between glacier size, elevation and areal change was not observed when comparing the characteristics of all the glaciers sampled at each individual study site. The relative glacier area loss at the SB study site, for example, was shown to be over three magnitudes of order larger than that shown for the GC and ND study sites, despite the glaciers sampled being distributed at higher elevations. Such results

indicate a complex relationship between glacier size and elevation when comparing glacier change results over large areas.

(2) A larger proportion of ice area at the GC and ND study sites is contained within large glaciers (>5 $km^2$ in size) compared to the SB and LT study sites. Both in the Himalayas and for other glacierised regions, large glaciers have been found to be less sensitive to climatic warming (e.g. IPCC (2007)). Glacier size distribution therefore must represent an important factor influencing the differing glacier responses shown for the two Indian and Nepalese study sites sampled. However, in addition to the limitations stated previously, this observation may be limited by the relatively small sample of glaciers at the GC and ND study sites.

### 8.3. GLIMS glacier outlines: Reliable source of historic glacier data?

Qualitative analysis of the GLIMS glacier outlines utilised in this study revealed that, in general, their spatial location matched well with local topographical and glacial features visible in ASTER imagery, suggesting their positional accuracy relative to this reference source is good. However, uncertainties were identified regarding the delineation of ice boundaries at high elevation. When compared to contemporary ASTER-derived glacier outlines, for example, large ice area losses were revealed at high elevation which maybe erroneous. It is likely that these high elevation ice area losses result from misclassification of snow covered areas in the reference aerial photographs and topographic maps used. High elevation ice area losses were particularly prevalent at the LT site, which may explain the relatively accelerated rate of ice area reduction shown in this study compared to that reported by Shrestha & Joshi (2009) for the same location. Encouragingly, however, the glacier change observed at the nearby SB study site corresponded more closely with those reported by Shrestha & Joshi (2009).

The historic Himalayan glacier outlines available within the GLIMS database are undoubtedly of value to the scientific community, their ease of access making them ideal for a number of glaciological and hydrological applications. However, the

GLIMS glacier outlines used in this study were limited in that the metadata provided included no information on the geometric accuracy of the dataset and only generalised information on the mapping sources used. To improve the scientific value of future GLIMs glacier outline inputs, mapping accuracy information should therefore be included as an essential prerequisite.

### 8.4. Future research directions

Three research directions are envisioned. (1) As the Corona and ASTER image archives cover a large area of the Himalayas, there is an opportunity to further extend the spatial extent of the glacier change measurements presented in this study, through the application of the methodology developed. In addition to further enhancing historic glacier change records in the Himalaya, additional Corona-derived glacier delineations could represent an interesting comparative dataset for other historic glacier outlines whose geometric accuracy is questionable, such as the GLIMS glacier outlines available Central Nepal and the glacier outlines derived from 1960s topographic maps for the Chenab, Parbati and Baspa basins, India (Kulkarni *et al*. (2007)). Outside the Himalayas, monitoring of other glacierised regions, such as the Andes, is also limited by the lack of detailed aerial surveys and topographic maps and, for historic mapping, is heavily reliant on coarse resolution satellite imagery from the late 1970s and early 1980s (e.g. Landsat MSS: 75 m) (Rivera *et al*., 2002). With the Corona archive covering large areas the Andes, there is an opportunity to perform a similar glacier change study as is presented here.

(2) Following on from the Corona DEM analysis presented in this study, an interesting future development would be to test the use of VHR satellite data as a reference source for extracting a Corona DEM covering a sub-set area of one of the study sites utilised. Here, the Gangotri glacier accuracy test site, for example, would provide an ideal area for which to repeat the Corona image and DEM processing procedure, including VHR reference imagery, allowing for a detailed assessment of ice surface elevations, and vertical and horizontal accuracy to be performed and compared with the results presented in this study. Such analysis would allow further

assessment of the suitability of the non-metric camera frame model used, particularly in respect to extracting Corona DEMs. The use of a smaller study area would also reduce costs incurred by the purchase of VHR satellite imagery.

(3) Without the availability of long term climate records, the assessment of glacier changes shown here, and by other studies across the Himalaya, remains difficult. Through collaboration with Dr. Sebastian Mernild (Senior Researcher at Centro de Estudios Cientìficos, Chile), there is an opportunity to utilise a newly available re-analysis of the NASA's Modern Era Retrospective-Analysis for Research and Applications (MERRA) northern hemisphere product to analyse air temperature and precipitation variability specifically for the Indian Garhwal Himalaya and Central Nepal Himalaya. Modelled using available regional climate records and knowledge of regional climate systems, the MERRA dataset provides air temperature and precipitation estimates, amongst other climate variables, on an hourly time step on a spatially referenced 1 km grid from 1970 to 2010. In lieu of long term field-based climate data, when combined with the glacier change and elevation information presented here, the MERRA dataset may give further insight into the characteristics of climate change and their influence on glacier sensitivity in the two regions specified. To improve the temporal resolution of the glacier change data presented at each study site, in order to better correspond with that of the MERRA dataset, further glacier area and length measurements could be derived from Landsat TM (1980s), Landsat ETM+ (1999 onwards) and ASTER (2000s) satellite data.

## 9.References

Adhikari, S., Marshall, S. J., Huybrechts, P. (2009). A comparison of different methods of evaluating glacier response characteristics: application to glacier AX010, Nepal Himalaya. *The Cryosphere Discussions*, 3, 765-804.

Adler, R. *et al*. (2003). The Version 2 Global Precipitation Climatology Project (GPCP) Monthly Precipitation Analysis (1979-Present). *Journal of Hydrometeorology*, 4, 1147-1167.

Agarwal, N. K. (2001). Remote sensing for glacier mapping and monitoring. *Geological Survey of India Special Publication*, 53, 201-206.

Ageta, Y., Higuchi, K. (1984). Estimation of Mass Balance components of a summer-accumulation type glacier in the Nepal Himalaya. *Geografiska Annaler*, 66A, 249-255.

Ageta, Y., Kadota, T. (1992). Predictions of changes of glacier mass balance in the Nepal Himalaya and Tibetan Plateau: A case study of air temperature increase for three glaciers. *Annals of Glaciology*, 16, 89-94.

Ahmad, S., Rais, S. (1999). *Himalayan glaciers*. New Dehli, APH Publishing Corporation.

Ahmad, S., Hasnain, S. I. (2004). Analysis of satellite imageries for characterization of glacio-morphological features of the Gangotri Glacier, Ganga headwater, Garhwal Himalayas. *Geological Survey of India Specific Publica*tion, 80, 60-67.

Ahmed, N. (1962). Milam glacier Kumaun Himalayas. In Variations of the regime of existing glaciers: Symposium of Obergurgl, Commission of Snow and Ice. *International Association of Scientific Hydrology*, 58, 230-233.

Akhtar, M., Ahmed, N., Booij, M. J. (2008). The impact of climate change on the water resources of Hindukush-Karakorum-Himalayan region under different glacier coverage scenarios. *Journal of Hydrology*, 355, 148-163.

Altmaier, A., Kany, C. (2002). Digital surface model generation from CORONA satellite images. *ISPRS Journal of Photogrammetry and Remote Sensing*, 56, 221-235.

Andreassen, L. M., Paul, F., Kääb, A., Hausberg, J. E. (2008). Landsat-derived glacier inventory for Jotunheimen, Norway, and deduced glacier changes since the 1930s. *The Cryospere*, 2, 131-145.

Archer, D. R., Fowler, H. J. (2004). Spatial and temporal variations in precipitation in

the Upper Indus Basin, global teleconnections and hydrological implications. *Hydrology and Earth System Sciences*, 8, 47-61.

Arendt, A. A., Echelmeyer, K. A., Harrison, W. D., Lingle, C. S., Valentine, V. B. (2002). Rapid wastage of Alaska glaciers and their contribution to rising sea level. *Science*, 297 (5580), 382-386.

Bahadur, J. (1993). The Himalayas: A Third Polar Region. *Snow and Glacier Hydrology* (Proceedings of the Kathmandu Symposium, November 1992). IAHS Publ. No. 218.

Bahuguna, I, M., Kulkarni, A. V., Nayak, S., Rathore, B. P., Negi, H. S., Mathur, P. (2007). Himalayan glacier retreat using IRS 1C PAN stereo data. *International Journal of Remote Sensing*, 28 (2), 437-442.

Bamber, J. L., Rivera, A. (2007). A review of remote sensing methods for glacier mass balance determination. *Global Planetary Change*, 59, 138-148.

Barnett, T. P., Adam, J. C., Lettenmaier, D. P. (2005). Potential impacts of a warming climate on water availability in a snow dominated region. *Nature*, 438 (17), 303-309.

Barry, R. G. (2006). The status of research on glaciers and global glacier recession: a review. *Progress in Physical Geography*, 30 (3), 285-306.

Becker, A., Bugmann, H. (eds.) (1997). *Predicting global change impacts on mountain hydrology and ecology: integrated catchment hydrology/altitudinal gradient studies, Workshop Report 43*. Stockholm: International Geosphere-Biospere Programme (IGBP).

Bayr, J. J., Hall, D. K., Kovalick, W. M. (1994). Observations on glaciers in the eastern Austrian Alps using satellite data. *International Journal of Remote Sensing*, 15 (9), 1733-1742.

Beniston, M., Diaz, H. F. (2004). The 2003 heat wave as an example of summers in a greenhouse climate? Observations and climate model simulations for Basel, Switzerland. *Global and Planetary Change*, 44, 73-81.

Beniston, M., Diaz, H. F., Bradley, R. S. (1997). Climatic change at high elevation sites: an overview. *Climatic Change*, 36, 233-51.

Benn, D. I., Evans, D. J. A. (2010). *Glaciers and Glaciation*. Second edition. Hodder Education, London.

Benn, D. I., Gemmell, A. M. D. (1997). Calculating equilibrium-line altitudes of former glaciers by the balance ration method: a new computer spreadsheet. *Glacial Geology and Geomorphology*, http://ggg.qub.ac.uk/ggg/paper/full1997/tn011997/tn01.htm.

Bergstrom, S., Boggild, C. E., Einarsson, K., Gjessing, Y., Saelthun, N. R., Thomsen, T., Vehvilainen, B., Sand, K. (1992). Snow modelling, water resources, climate change. *Report STF60 A92023, SINTEF NHL.* 12 pages.

Berthier, E., Vadon, H., Baratoux, D., Arnaud, Y., Vincent, C., Feigl, K. L., Remy, F., Legresy, B. (2005). Surface motion of mountain glaciers from satellite optical imagery. *Remote Sensing of Environment*, 95, 14-28.

Berthier, E., Arnaud, Y., Kumar, R., Ahmad, S., Wagnon, P., Chevallier, P. (2007). Remote sensing estimates of glacier mass balances in the Himachal Pradesh (Western Himalaya, India). *Remote Sensing of Environment*, 108, 327-338.

Berthier, E., Arnaud, Y., Vincent, C., Remy, F. (2004). Recent rapid thinning of the 'Mer de Glace' glacier derived from satellite optical images, *Geophysical Research Letters*, 31, L17401, doi:10.1029/2004GL020706.

Berthier, E., Arnaud, Y., Vincent, C., Remy, F. (2006). Biases of SRTM in high-mountain areas. Implications for the monitoring of glacier volume changes. *Geophysical Research Letters,* 33, L08502, doi:10.1029/2006GL025862.

Berthier, E., Schiefer, E., Clarke, G. K. C., Menounos, B., Remy, F. (2010). Contribution of Alaskan glaciers to sea-level rise derived from satellite imagery. *Nature Geoscience*, 3, 92-95.

Bhambri, R., Bolch, T. (2009). Glacier mapping: a review with special reference to the Indian Himalayas. *Progress in Physical Geography*, 33. 672-704

Bhambri, R., Bolch, T., Chaujar, K. R. (2012). Frontal recession of Gangotri Glacier, Garhwal Himalayas, from 1965 to 2006, measured through high-resolution remote sensing data. *Current Science*, 102 (3), 489-494.

Bhambri, R., Bolch, T., Chaujar, K. R., Kulshrestha, S, C. (2011). Glacier changes in the Garhwal Himalaya, India, from 1968 to 2006 based on remote sensing. *Journal of Glaciology*, 57 (203), 543-555.

Bhambri, R., Chaujar, R. K. (2009). *Recession of Gangotri glacier (1962-2006) measured through remote sensing data*. In Proceeding of National Seminar on Management Strategies for the Indian Himalaya: Development and Conservation, HNB Garhwal University, Srinagar, 1, 254-264.

Bhutiyani, M. R., Kale, V. S., Pawar, N. J. (2007). Long-term trends in maximum, minimum and mean annual air temperatures across the Northwestern Himalaya during the twentieth century. *Climate Change*, 85, 159-177.

Bhutiyani, M. R., Kale, V. S., Pawar, N. J. (2009). Climate change and the precipitation variations in the northwestern Himalaya: 1866-2006. *International Journal of Climatology*, 30 (4), 535-548.

Bolch, T., Buchroithner, M., Pieczonka, T., Kunert, A. (2008). Planimetric and volumetric glacier changes in the Khumbu Himal, Nepal, since 1962 using Corona, Landsat TM and ASTER data. *Journal of Glaciology*, 54 (187), 592-600.

Bolch, T., Menounos, B., Wheate, R. (2010b.). Landsat-based inventory of glaciers in western Canda, 1985-2005. *Remote Sensing of Environment*, 114, 127-137.

Bolch, T., Pieczonka, T., Benn, D. I. (2010). Longest time series of glacier mass changes in the Himalaya based on stereo imagery. *The Cryosphere Discuss*, 4, 2593-2613.

Booij, M. J. (2005). Imapact of climate change on river flooding assessed with different spatial model resolutions. *Journal of Hydrology*, 303, 176-198.

Bown, F., Rivera, A., Aguna, C. (2008). Recent glacier variations of the Aconcagua basin, Central Chilean Andes. *Annals of Glaciology*, 48, 43-48.

Braithwaite, R. J. (2009). Review. Raina, V.K & Srivastava, D., *Glacier atlas of India. J. Glaciol.*, 55 (193), 938.

Braithwaite, R. J., Oleson, O. B. (1989). Calculation of glacier ablation from air temperature, West Greenland. In: Oerlemans, J., (Ed.), Glacier fluctuations and climate change, *Glaciology and Quaternary Geology*, Dordrecht, 219-233.

Braithwaite, R. J., Raper, S. C. B. (2009). Estimating equilibrium-line altitude (ELA) from glacier inventory data. *Annals of Glaciology*, 50 (53), 127-132.

Braithwaite, R. J., Raper, S. C. B. (2007). Glaciological conditions in seven contrasting regions estimated with degree-day model. *Annals of Glaciology*, 46, 297-302.

Braithwaite, R. J., Zhang, Y. (1999). Modelling changes in glacier mass balance that may occur as a result of climate changes. *Geografiska Annaler*, 81, 489-496.

Braithwaite, R. J., Zhang, Y. (2000). Sensitivity of mass balance of five Swiss glaciers to temperature changes assessed by tuning a degree-day model. *Journal of Glaciology*, 46, 7-14.

Brocklehurst, S. H., Whipple, K. X. (2004). Hypsometry of glaciated landscapes. *Earth Surface Process and Landforms*, 29, 907-26.

Buchroithner, M, F., Bolch, T. (2007). An automated method to delineate the ice extension of the debris-covered glaciers at Mt. Everest based on ASTER imagery. Proc*. 9th int. Sympos. On High Mountain Remote Sensing Cartography*, 11-22 September 2006 held in Graz, Austria, 8 pages.

Burrough,W. (Ed.), (2003). *Climate into the 21st Century*. Cambridge University Press, Cambridge, U.K., 240 pages.

Casana, J., Cothren, J. (2008). Stereo analysis, DEM extraction and orthorectification of Corona satellite imagery: archaeological applications from the Near East. *Antiquity*, 82, 732-749.

Campbell, G. J., Xin Li., Arora, B. R., Soomro, B. (2005). Inventory of glaciers and glacier lakes and the identification of potential glacial lake outburst floods (GLOFS) affected by global warming in the mountains of India, Pakistan and China/Tibet autonomous region. Final *report for the APN project 2004-03-CMY-Campbell*. 2005 38 pages.

Campbell, J. B. (2006). *Introduction to Remote Sensing (4th edition).*Taylor & Francis, New York.

Challis, K., Priestnall, G., Gardner, A., Henderson, J., O'Hara, S. (2004). Corona Remotely-Sensed Imagery in Dryland Archaeology: The Islamic City of al-Raqqa, Syria. *Journal of Field Archaeology*, 29, 139-153.

Chitranshi, A., Sangewar, C. V., Srivastava, D., Puri, V. M . K., Dutta, S. S. (2004). Recession pattern of Meru Bamak Glacier, Bhagirathi Basin, Uttaranchal. In Srivastava, D., Gupta, K. R., Mukerji, S. (eds.) *Geological Survey of India Special Publication*, 80, 33-38.

Chrysoulakis, N., Abrams, M., Feidas, H., Arai, K. (2010). Comparison of atmospheric methods using ASTER data for the area of Crete, Greece. *International Journal of Remote Sensing*, 31 (24), 6347-6385.

Cogley, J. G., Kargel, J. S., Kaser, G., Van der Veen, C. J. (2010). Tracking the source of glacier misinformation. *Science*, 337, 522.

Collins, D. N. (1988). Influences of climatic fluctuations and changes in glacierised area on runoff from Alpine basins. In: *Proc. Seventh Northern Research Basins Symposium*, 77-86.

Collins, D. N. (1998). Outburst and rainfall-induced peak runoff events in highly glacierized Alpine basin. *Hydrological Processes*, 12, 2369-2381.

Collins, D. N. (2006). Climatic variation and runoff in mountain basins with differing proportions of glacier cover. *Nordic Hydrology*, 37, 315-326.

Collins, D. N. (2007). Changes in quantity and variability of runoff from Alpine basins with climatic fluctuations and glacier decline. *Glacier Mass balance changes and Meltwater Discharge* (selected papers from sessions at the IAHS Assembly in Foz do Iguacu, Brazil, 2005). IAHS Publ. 318.

Collins, D. N., Hasnain, S. I. (1995). Runoff and sediment transport from glacierized basins at the Himalayan scale. *Effects of Scale on Interpretation and Management*

*of Sediment and Water Quality* (Proceedings of a Boulder Symposium, July 1995). IAHS Publ. No. 226.

Conway, W. M. (1893). The crossing of the Hispar Pass. *Geographical Journal*, 1, 23-33.

Cruz, R. V., Harasawa, H., Lal, M., Wu, S., Anokhin, Y., Punsalmaa, B., Honda, Y., Jafari, M., Li, C., Ninh Huu, N. (2007). *Asia. Climate change 2007: Impacts, Adaption and Vulnerability. Contribution of Working Group II to the Forth Assessment Report of the Intergovernmental Panel on Climate Change*, M. L. Parry *et al*., Eds., Cambridge University Press, Cambridge, UK, 469-506.

Daly, C., Neilson, R. P., Phillips, D. L. (1994). A statistical-topographical model for mapping climatological precipitation over mountainous terrain. *Journal of Applied Meteorology*, 33, 140–158.

Dashora, A., Lohani, B., Malik, J. N. (2007). A repository of earth resource information – CORONA satellite programme. *Current Science*, 92 (7), 926-932.

Davore, J. (2009). *Probability and statistics for engineering and the sciences*. Eighth Edition, Brooks/Cole, Boston.

DHM (1997). *Snow and glacier hydrology section, Year book 1995, Supplement V*. Department of Hydrology and Meteorology (DHM), Kathmandu, Nepal, 22 pages.

Dimri, A. P., Mohanty, U, C. (2007). Location specific prediction of maximum and minimum temperature over the Western Himalayas. *Meteorological Applications*, 14, 79-93.

Dobhal, D. P., Gergen, J. T., Thayyen, R. J. (2004). Recession and morphogeometrical changes of Dokriani glacier (1962-1995) Garhwal Himalaya, India. *Current Science*, 86 (5), 692-696.

Dobhal, D. P., Gergen, J. T., Thayyen, R. J. (2008). Mass balance studies of the Dokriani Glacier from 1992 to 2000, Garhwal Himalaya, India. *Bulletin of Glaciological Research*, 25, 9-17.

Dobhal, D. P., Kumar, S., Mundepi, A. K. (1995). Morphology and glacier dynamics studies in Monsoon arid transition zone: An example from Chhota Shigri glacier, Himachal Himalaya. *India Current Science*, 68 (9), 936-944.

Dobhal, D. P., Mehta, M. (2010). Surface morphology elevation changes and terminus retreat Dokriani glacier, Garhwal Himalaya: Implication of climate change. *Himalayan Geology*, 31 (1), 71-78.

Du, M. Y., Kawashima, S., Yonemura, S., Zhang, X. Z., Chen, S. B. (2004). Mutual Influence between Human activities and Climate Change in the Tibetan Plateau during recent years. *Global and Planetary Change*, 41, 241-249.

Du, Y., Guindon, B., Cihlar, J. (2002). Haze detection and removal in high resolution satellite image with wavelet analysis. *IEEE Transactions on Geoscience and Remote Sensing*, 40 (1), 210-217.

Dyurgerov, M. (2002). *Glacier mass balance and regime: data of measurements and analysis*. Occasional Paper 55, Institute of Article and Alpine Research, University of Colorado, Boulder, 268 pages.

Dyurgerov, M. (2003). Mountain and subpolar glaciers show an increase in sensitivity to climate warming and intensification of the water cycle. *Journal of Hydrology*, 282, 164-176.

Dyurgerov, M. B. (2005). Supplement to Occasional Paper 55, updated January 2005 at http://www.nsidc.org

Dyurgerov, M.D., Meier, M.F. (1997). Mass balance of mountain and sub-polar glaciers: A new global assessment for 1961-1990. *Arctic and Alpine Research*, 29 (4), 379-391.

Ebdon, D. (1985). *Statistics in Geography.* Blackwell Publishing, Oxford.

Ehlers, M. (1997). Rectification and registration In: Star, J. L., Estes, J. E., McGwire, K.C., (eds.) *Integration of geographic information systems and remote sensing: Topics in remote sensin*g 5, Cambridge University Press.

EORS. (2007). ALOS user handbook. Available at http://www.eorc.jaxa.jp/ALOS/doc/alos_userhb_en.pdf. [Accessed 20.06.2012]

ERDAS (2010). *ERDAS Field Guide*. ERDAS, Inc, USA.

ERDAS (2009). *LPS Project Manager user's guide*. ERDAS, Inc, USA.

Etzelmüller, B., Bjornsson, H. (2000). Map analysis techniques for glaciological applications. *International Journal of Geographical Information Science*, 14 (6), 567-581.

Etzelmüller, B. (2000). On the quantification of surface changes using grid-based digital elevation models (DEM). *Transactions in GIS*, 4 (2), 129-143.

Evans, I. S. (2006). Local aspect asymmetry of mountain glaciation: a global survey of consistency of favoured directions for glacier numbers and altitudes. *Geomorphology*, 73, 166-184.

Fujii, Y., Higuchi, K. (1977). Statistical analysis of the forms of the glaciers in the Khumbu Himal. *Journal of the Japanese Society of Snow and Ice*, 39 (Special Issue), 9-17.

Fujisada, H., Bailey, G., Kelly, G., Hara, S., Abrams, M. (2005). ASTER DEM performance. *Geoscience Remote Sensing, IEEE Transactions*, 43, 2707-2714.

Fujita, K. (2008). Influence of precipitation seasonality on glacier mass balance and its sensitivity to climate change. *Annals of Glaciology*, 48, 88-92.

Fujita, K., Ageta, Y. (2000). Effect of summer accumulation on glacier mass balance on the Tibetan Plateau revealed by mass-balance model. *Journal of Glaciology*, 46 (153), 244-252.

Furbish, D.J., Andrews, J.T. (1984). The use of hypsometry to indicate long-term stability and response of valley glaciers to changes in mass transfer. *Journal of Glaciology*, 30, 199-211.

Fountain, A. G., Tangborn, W. V. (1985). The effects of glaciers on streamflow variations. *Water Resource Research*, 21, 579-586.

Fushimi, H., In (eds Domoto, A. *et al.*), Tsukiji-Shokan Pub Co Ltd., Japan and The World Conservation Union, Gland, Switzerland, 2000, 42–45.

Galiatsatos, N. (2004). *Assessment of the CORONA series of satellite imagery for landscape archaeology: a case study from the Orontos valley, Syria*. Doctoral thesis, Durham University. Available at Durham E-Theses: http://etheses.dur.ac.uk/281/

Galiatsatos, N., Donoghue, D. N. M., Philip, G. (2008). 'High resolution elevation data derived from stereoscopic CORONA imagery with minimal ground control: an approach using IKONOS and SRTM data. *Photogrammetric Engineering & Remote Sensing*, 74, 1093-1106.

Geological Survey of India. (1999). *Inventory of the Himalayan Glaciers: A Contribution to the International Hydrological Programme,* Special Publication No. 34, edited by M.K. Kaul.

Ghosh, S. K. (2005). *Fundemetals of Computional Photogrammetry.* Concept Publishing Company, New Delhi.

Gjermundsen, E. F., Mathieu, R., Kääb, A., Chinn, T., Fitzharris, B., Hagen, J. O. (2011). Assessment of multispectral glacier mapping methods and derivation of glacier area changes, 1978-2002, in the central Southern Alps, New Zealand, from ASTER satellite data, field survey and existing inventory data. *Journal of Glaciology,* 57 (204), 667-682.

GLIMS (2011). *GLIMS Glacier Database*. Retrieved 26 October 2011, from

http://glims.colorado.edu/glacierdata/

Godwin-Austen, H. H. (1864). On the glaciers of the Mustagh Range. *Journal of Royal Geographical Society*, 34, 19-56.

Guo Liu, J., Mason, P. (2009). *Essential Image Processing and GIS for Remote Sensing*. First Edition. Wiley, London.

Grosse, G., Schirrmeister, L., Kunitsky, V. V., Hubbertem, H. (2005). The use of CORONA Images in Remote Sensing of Periglacial Geomorphology: An Illustration from the NE Siberian Coast. *Permafrost and Periglacial Processes*, 16, 163-172.

Grove, J. M. (1988). *The Little Ice Age*. London: Methuen. 498 pages.

Grove, J. M. (2004). *Little Ice Ages: Ancient and Modern*, (2 volumes). Routledge. London. 718 pages.

GSI (1996-1997). *Annual general report*, Part 8. Volume 131.

Grün, A., Murai, S. (2002). High-resolution 3D modelling and visualization of Mount Everest. *ISPRS Journal of Photogrammetry and Remote Sensing*, 57, 102-113.

Haeberli, W. (2004). Glaciers and ice caps: historical background and strategies of world-wide monitoring. In: Bamber, J.L., Payne, A.J. (Eds.), *Mass Balance of the Cryosphere*. Cambridge University Press, Cambridge, pages 559–578.

Haeberli, W., Epifani, F. (1986). Mapping the distribution of buried ice – an example from Lago delle Loce, Monte Rosa, Italian Alps. *Annals of Glaciology*, 8, 78-81.

Haeberli, W., Hoelzle, M. (2001). The World Glacier Monitoring Service. (http://www.nerc-bas.ac.uk/public/icd/icsi/WGMS.html).

Hagg, W. J., Braun, L. N., Uvarov, V. N., Makarevich, K. G. (2004). A comparison of three methods of mass-balance determination in the Tuyuksu glacier region, Tien Shan, Central Asia. *Journal of Glaciolog*y, 50 (171), 505-510.

Hall, D. K., Bayr, K. J., Schöner, W., Bindschadler, R. A., Chien, J. Y. L. (2003). Consideration of the errors inherent in mapping historical glacier positions in Austria from ground and space (1893-2001). *Remote Sensing of Environment*, 86, 566-577.

Hall, D. K., Chang, A.T.C., Siddalingaiah, H. (1988). Reflectance's of glaciers as calculated using Landsat 5 Thematic Mapper data. *Remote Sensing Environment*, 25 (3), 311-321.

Hall, D. K., Williams, R. S. Jr., Bayr, K. J. (1992). Glacier recession in Iceland and Austria. *EOS, Transactions of the American Geophysical Union* 73, 135-141.

Hanssen, R. F. (2001). *Radar Interferometry – Data Interpretation and Error Analysis*. Kluwer Acedemic Publishers, Dordrecht, 308 pages.

Hartmann, D. L. (1994). *Global Physical Climatology*. Academic Press, San Diego

Hasnain S. I. (1999). Runoff characteristics of a glacierised catchment, Garhwal Himalaya, India. *Hydrological Sciences Journal*, 44, 847-854.

Hasnain S. I. (2000). Status of the Glacier Research in the HKH region.2000, *ICIMOD*, Kathmandu, Nepal.

Hay, L. E., Clark, M. P., Wilby, R. L., Gutowski, W. J., Leavesley, G. H., Pan, Z., Arrit, R. W., Takle, E. S. (2002). Use of regional climate model output for hydrological simulations. *Journal of Hydrometeorology*, 3, 571-590.

Hewitt, K. (1998). Glaciers receive a surge of attention in the Karakoram Himalaya. *EOS Transactions, American Geophysical Union*, 79, 104-105.

Hewitt, K. (2005). The Karakorum Anomaly? Glacier expansion and the 'elevation effect', Karakorum Himalaya. *Mountain Research and Development*, 25, 32-340.

Hewitt, K., Wake, C. P., Young, G. J., David, C. (1989). Hydrological Investigation at Baifo Glacier, Karakorum Himalaya: An Important Source of Water for the Indus River. *Annals of Glaciology*, 13, 103-108.

Hirano, A., Welch, R., Lang, H. (2003). Mapping from ASTER stereo image data: DEM validation and accuracy assessment. *Journal of Photogrammetry & Remote Sensing,* 57, 356-370.

Hock, R. (1999). A distributed temperature-index ice- and snowmelt model including potential direct solar radiation. *Journal of Glaciology*, 45, 149, 101-111.

Hock, R. (2003). Temperature index melt modelling in mountain areas. *Journal of Hydrology*, 282, 104-115.

Hock, R., Jansson, P., Braun, L. (2005). Modelling the response of mountain glacier discharge to climate warming. In Huber, U. M., Bugmann, H. K. M., Reasoner, M. A. (Eds.), 2005. Global Change and Mountain Regions (A state of Knowledge Overview), Springer, Dorrecht. Pages 243-252.

Høgda, K. A., Storvold, R., Laukes, T. R. (2011) SAR imaging of glaciers. In Pellika, P., Rees, W. G. (Eds.) *Remote sensing of glaciers: Techniques for topographic, spatial and thematic mapping of glaciers*, Taylor & Francis, London, UK.

Holland, T. H. (1907). A preliminary survey of certain glaciers in the North-West Himalayas. *Records of the Geological Survey of India*, 35, 47-52.

Houghton, J. T., Ding, Y., Griggs, D. J., Noguer, M., van der Linden, P. J., Dai, X., Maskell, K., Johnson, C. A. (Eds.) (2001). *Climate Change 2001: The scientific Basis: Contribution of Working Group 1 to the Third Assessment Report of the Intergovernmental Panel on Climate Change*, 881 pages, Cambridge University Press, New York.

Huggel, C., Kääb, A., Haeberli, W., Teysseire, P., Paul, F. (2002). Satellite and aerial imagery for analysing high mountain lake hazards. *Canadian Geotechnical Journal*, 39 (2), 316-330.

Immerzeel, W. W., Drooges, P., De Jong, S. M., Bierkens, M. F.P. (2009). Large-scale monitoring of snow cover and runoff simulation in Himalayan river basins using remote sensing. *Remote Sensing of Environment*, 113, 40-49.

Inoue, J. (1977). Mass budget of Khumbu Glacier. *Journal of the Japanese Society of Snow and Ice*, 39 (Special Issue), 15-19.

IPCC (2007). *Climate Change, the IPCC Scientific Assessment*. Cambridge University Press, Cambridge.

Jansson, P., Hock, R., Schneider, T. (2003). The concept of glacier storage: a review. *Journal of Hydrology*, 282, 116-129.

Jones, P. D., Osborn, T. J, Briffa, B. (2001). The evolution of climate over the last millenium, *Science*, 292, 662-667.

Kääb, A. (2005a.) *Remote sensing of mountain glaciers and permafrost creep*. Schriftenreihe Physische Geographie, Department of Geography, Zurich. 48, 266 pages.

Kääb, A. (2005b.). Combination of SRTM3 and repeat ASTER data for deriving alpine glacier flow velocities in the Bhutan Himalaya. *Remote Sensing of Environment*, 94, 463-474.

Kääb, A. (2008). Glacier volume changes using ASTER satellite stereo and ICESat GLAS Laser altimetry: A test study on Edgeya, Eastern Svalbard. *IEEE International Geosciences and Remote Sensing*, 46, 2823-2830.

Kääb, A., Huggel, C., Fischer, L., Guex, S., Paul, F., Roer, I., Salzmann, N., Schlaefli, S., Schmutz, K., Schneider, D., Strozzi, T., Weidmann, Y. (2005). Remote sensing of glacier- and permafrost-related hazards in high mountains: an overview. *Natural Hazards and Earth System Science*, 5, 527-554.

Kääb, A. , Huggel, C., Paul, F., Wessels, R., Raup, B., Kieffer, H., Kargel, J. (2003). Glacier monitoring from ASTER imagery: Accuracy and applications. *EARSel eProceedings*, 2, 43-53.

Kappenberger, G., Steinegger, U., Braun, L, N. Kostka, R. (1993). Recent changes in glacier tongues in the Langtang Khola basin, Nepal, determined by terrestiral photography. *IASH Publication No. 128*, 95-101.

Kargel, J. S., Abrams, M. J., Bishop, M. P., Bush, A., Hamilton, G., Jiskoot, H., Kääb, A., Kieffer, H. H., Lee, E. M., Paul, F., Rau, F., Raup, B., Shroder, J. F., Soltesz, D., Stainforth, D., Stearns, L., Wessels, R. (2005). Multispectral imaging contributions to global land ice measurements from space. *Remote Sensing Environment*, 99, 187-219.

Kargel, J. S., Cogley, G. J., Leonard, G. L., Haritashya, U., Byers, A. (2011). Himalayan glaciers: The big picture is a montage. *PNAS*, 108 (36), 14709-14710.

Karma., Ageta, Y., Naito, N., Iwata, S., Yabuki, H. (2003). Glacier distribution in the Himalayas and glacier shrinkage from 1963 to 1993 in the Bhutan Himalayas. *Japanese Society of Snow and Ice*, 20, 29-40.

Kaser, G., Fountain, A. G., Jansson, P. (2002). A manual for monitoring the mass balance of mountain glaciers. *IHP-V1-Technical documents in hydrology*, 59 pages.

Kasser, P. (1959). Der Einfluss von Gletscherruckgang un Gletschervorstoss auf den Wasserhaushalt. Wasser- und Energiewirtschaft, 6, 155-168.

Kattelmann, R. (1987). Uncertainty in Assessing Himalayan Water Resources. *Mountain Research and Development*, 7 (3), 279-286.

Kayastha, R. B., Harrsion, S. P. (2008). Changes of the equilibrium-line altitude since the Little Ice Age in the Nepalese Himalaya, *Annals of Glaciology*, 48, 93-99.

Kervyn, F. (2001). Modelling topography with SAR interferometry: illustrations of a favourable and less favourable environment. *Computers and Geosciences*, 27, 1039-1050.

Khoshelham, K. (2009). Role of tie points in integrated sensor orientation for photogrammetric map compliation. *Photogrammetric Engineering & Remote Sensing*, 75 (3), 305-311.

Khromova, T. E., Dyurgerov, M. B., Barry, R. G. (2003). Late-twentieth century changes in glacier extent in the Ak-shirak Range, Cnetral Asia, determined from historical and ASTER imagery. *Geophysical Research Letters*, 30 (16), 1863.

Kick, W. (1989). The decline of the last Little Ice Age in High Asia compared with that in the Alps. In: Oerlemans J. editor. *Glacier Fluctuations and Climate Change*. Dordrecht, The Netherlands: Kluwer, pages 129-142.

König, M., Winther, J., Isaksson, E. (2001). Measuring snow and glacier ice properties from satellite. *Reviews of Geophysics*, 39 (1), 1-27.

Kulkarni, A. V. (1991). Glacier inventory of Himachal Pradesh using satellite images. *Journal of Indian Society of Remote Sensing*, 19, 195-203.

Kulkarni, A. V., Alex, S. (2003). Estimation of recent glacial variations in baspa basin using remote sensing technique. *Journal of the Indian Society of Remote Sensing*, 31 (2), 81-90.

Kulkarni, A. V., Bahuguna, I. M., Rathore, B. P., Singh, S. K., Randhawa, S. S., Sood, R. K., Dhar, S. (2007). Glacial retreat in Himalaya using Indian Remote Sensing satellite data. *Current Science*, 92, 69-74.

Kulkanri, A. V., Rathore, B. P., Alex, S. (2004). Monitoring of glacier mass balance in the Baspa basin using accumulation area ration method. *Current Science*, 86 (1), 185-190.

Kumar, R., Areendran, G., Rao, P. (2009). *Witnessing change : glaciers in the Indian Himalaya*. Pilan. WWF-India and Birla Institute of Technology.

Kumar, K., Dumka, R. K., Miral, M.S., Satyal, G.S., Pant, M. (2008). Estimation of retreat of Gangotri glacier using rapid static and kinematic GPS Survery. *Current Science*, 94, 258-262.

Kumar, V., Venkataramana, G., Høgda, K, A. (2011). Glacier surface velocity estimation using SAR interferometry technique applying ascending and descending passes in the Himalayas. *International Journal of Applied Earth Observation and Geoinformation*, 13 (4), 545-551.

Lambrecht, A., Kuhn, M. (2007). Glacier changes in the Austrian Alps during the last three decades, derived from the new Austrian glacier inventory. *Annals of Glaciology*, 46, 177-184.

Larson, C. F., Motyka, R. J., Arendt, A. A., Echelmeyer, K. A., Geissler, P. E. (2007). Glacier changes in southeast Alaska and northwest British Columbia and contribution to sea level rise. *Journal of Geophysical Research- Earth Surface*, 112, F01007, doi:10.1029/2006JF000586.

Leica Geosystems (2006). Leica Photogrammetry Suite Automatic Terrain Extraction. Leica Geosystems Geospatial Imaging, LCC, USA.

Lemke, P., Ren, J., Alley, R. B., Allison, I., Carrasco, J., Flato, G., Fujii, Y., Kaser, G., Mote, P., Thomas, R. H., and Zhang, T.: Observations – Changes in snow, ice and frozen ground, In: *Climate change 2007 – The physical science basis*, Contribution of WG-I to the Fourth Assessment Report of the IPCC, edited by: Soloman, S., Qin, D., Manning, M., Chen, Z., Marquis, M., Averyt, K. B., Tignor, M., and Miller, H. L., Cambridge University press, Cambridge, UK, 2007.

Li, Z., Xing, Q., Liu, S., Zhou, J., Huang, L. (2011). Monitoring thickness and volume changes of the Dongkemadi Ice field on the Qinghai-Tibetan Plateau (1969-2000) using Shuttle Radar Topography Mission and map data. *International Journal of Digital Earth*, DOI: 10.1080/17538947.2011.594099.

Lillesand, T. M., Kieffer, R. W. (2000). *Remote sensing and image interpretation – fourth edition.* Wiley, New York.

Liniger H, Weingartner R, Grosjean M (eds). (1998). *Mountains of the world: water towers for the 21st century*. Mountain Agenda for the Commission on Sustainable Development (CSD), BO12: Berne; 32 pages.

Lin Jijun, Xu Suying (1984). The distribution of glaciers on the Quinghai-Xizang Plateau and its relationship to atmospheric circulations. In: *International Karakoram Project* (ed. By Miller, K .J.), 1, 83-93. Cambridge University Press.

Liu, S. Y.,Ding, Y. J., Li, J., Shangguan, D. H, Zhang, Y. (2006). Glaciers in response to recent climate warming in Western China. *Quarternary Sciences*, 26, 762-771.

Lorenz, H. (2004). Integration of Corona and Landsat Thematic Mapper data for dedrock geological studies in the high Artic*. International Journal of Remote Sensing*, 25, 22, 5143-5162.

MacDonald, R. A. (1995). Corona: Success for Space Reconnaissance, a look into the Cold War, and a revolution for intelligence. *Photogrammetric Engineering and Remote Sensing*, 61, 689-719.

MacDonald, R. A. (1997). *Corona between the sun and the Earth – The first NRO reconnaissance eye in space*. American Society for Photogrammetry and Remote Sensing, Bethesda, Maryland.

Mall, R. K., Gupta, A., Singh, R., Singh, R. S., Rathore, L. S. (2006). Water resources and climate change: An Indian perspective. *Current Science*, 90 (12), 1610-1626.

Mather, P. M. (1995). Map-image registration using least-squares polynomials. *International Journal of Geographical Information Systems*, 9, 543-554.

Mather, P. M. (1999). *Computer Processing of Remotely-Sensed Images: An Introduction (2nd edition).* John Wiley & Sons, Chichester.

Matsuo, K., Heki, K. (2010). Time-variable ice loss in Asian high mountains from satellite gravimetry*. Earth and Planetary Science Letters*, 290, 30-36.

Mattson, L. E., Gardner, J. S., Young, G. J. (1993). Ablation on debris covered glaciers: an example from Rakhiot Glacier, Punjab, Himalaya. IAHS Publ. 218 (Symposium at Kathmandu 1992 – *Snow and Glacier Hydrology*), 289-296.

Mayewski, P. A., Jeshkke, P. A. (1979). Himalayan and Trans-Himalayan glacier fluctuations since AD 1812. *Artic and Alpine Research*. 11, 267-287.

METI/NASA/USGS. (2009). ASTER Global DEM validation summery report. *Technical report*, METI/ERSDAC, NASA/LPDAAC, USGS/EROS.

Mool, P. K., Bajracharrya, S. R., Joshi, S. P. (2007). *Inventory of glaciers, glacier lakes, glacier lake outburst floods: monitoring and early warning systems in the Hindu Kush-Himalayan Region, Nepal*. Kathmandu: ICIMOD, 386 pages.

Müller, F., Caflisch, T., Müller, G. (1976). *Firn und Eis der Schweizer Alpen, Gletscherinventar*. Zürich, Eidgenössische Technische Hochschule. (Geographisches Institut Publ. 57 and 57a.).

Musket, R. R., Lingle, C. S., Sauber, J. M., Post. A.S., Tangborn, W. V., Rabus, B. T., Echelmeyer, K. A. (2009). Airborne and spaceborne DEM- and laser altimetry-derived surface elevation and volume changes of the Bering Glacier system, Alaska, USA, and Yukon, Canada, 1972-2006. *Journal of Glaciology*, 55, 316-326.

Naithani, A. K., Nainwal, H. C., Sati, K. K., Prasad, C. (2001). Geo-morphological evidences of retreat of the Gangotri glacier during 1971-2004. *Current Science*, 95, 9-10.

Nainwal, H. C., Negi, B. D. S., Chaudhary, M., Sajwan, K. S., Gaurav, A. (2008). Temporal changes in the rate of recession: evidence from Satopanth and Bhagirath Kharak glaciers, Uttarakhand, using Total Station Survey. *Current Science*, 94 (5), 653-660.

Narama, C., Kaab, A., Duishonakunov, M., Abdrakhmatov, K. (2009). Spatial variability of recent glacier area changes in the Tien Shan Mountains, Central Asia, using Corona (~ 1970), Landsat (~ 2000), and ALOS (~ 2007) satellite data. *Global and Planetary Change*, 71, 42-54.

Narama, C., Shimamura, Y., Nakayama, D., Abdrakhmatov, K. (2006). Recent changes of glacier coverage in the western Terskey-Alatoo range, Kyrgyz Republic, using Corona and Landsat. *Annals of Glaciology*, 43, 223-229.

NASA/METI (2009). Aster Global DEM Validation: Summary report. https://lpdaac.usgs.gov/lpdaac/media/files/ASTER_GDEM_Validation_Summary_Report.

National Reconnaissance Office (NRO). (1967). *The KH-4B Camera System*, National Photographic Interpretation Centre, September.

Nelson, D., Alleyne, R. (2011). Himalayan glaciers not melting, report finds. *The Telegraph Online*, 27 January. Available at: http://www.telegraph.co.uk/earth/environment/climatechange/8284223/Himalayan-glaciers-not-melting-report-finds.html# [Accessed on 21 February 2011]

Nuimura, T., Fujita, K., Yamaguchi, S., Sharma, R. R. (2012). Elevation changes of glaciers revealed by multitemporal digital elevation models calibrated by GPS Surrey in the Khumbu region, Nepal Himalaya, 1992-2008. *Journal of Glaciology*, 58 (210), 648-656.

Nuth, C., Kääb, A. (2010). What's in an elevation difference? Accuracy and corrections of satellite elevation data sets for quantification of glacier changes. *The Cryophere Discussions*, 4, 2013-2077.

Nuth, C., Moholdt, G., Kohler, J., Hagen, J. O., Kääb, A. (2010). Svalbard glacier elevation changes and contribution to sea level rise. *Journal of Geophysical Research*, 115, F01008, http://dx.doi.org/10.1029/2008JF001223.

Oerlemans, J., Anderson, B., Hubbard, A., Huybrechts, P., Jöhannesson, T., Knap, W. H., Schmeits, M., Stroeven, A. P., Van de Wal, R. S. W., Wallinga, J., Zuo, Z. (1998). Modelling the response of glaciers to climate warming. *Climate Dynamics*, 14, 267-274.

Oerlemans, J. (2001). *Glaciers and Climate Change*. Balkema, Lisse.

Oerlemans, J. (2007). Estimating response times of Vadret da Morteratsch, Vadret da Palue, Briksdalsbreen and Nigardsbreen from their length records. *Journal of Glaciology*, 53, 257-362.

Oerlemans, J., Hoogendoorn, N. C. (1989). Mass-balance gradients and climatic change. *Journal of Glaciology*, 35, 399-405.

Oerlemans, J., Fortuin, J. P. F. (1992). Sensitivity of glaciers and small ice caps to greenhouse warming. *Science*, 258, 115-17.

Ohmura, A. (2001). Physical Basis for the temperature-based Melt-Index Method. *Journal of Applied Meteorology*, 40, 753-760.

Ohmura, A. (2009). Completing the World Glacier Inventory. *Annals of Glaciology*, 50 (53), 144-148.

Ommanney, C. S.L. (1980). The inventory of Canadian glaciers: procedures, techniques, progress and applications. *IASH Publications,* 126, 35-44.

Owen, L. A., Benn, D. I., Derbyshire, E., Evans, D. J. A., Mitchell, W. A., Richardson, S. (1996). Quaternary glacial history of the Lahul Himalaya, Northern India. *Journal of Quaternary Science*, 11 (1), 25-42.

Owen, L. A., Sharma, M .C. (1998). Rates of paraglacial fan formation in the Garhwal Himalaya: implications for landscape evolution. *Geomorphology*, 26, 171-184.

Paterson, W. S. B. (1994). *The Physics of glaciers*. 3rd edition, Pergamon Press, Oxford, 480 pages.

Paul, F. (2002). Changes in glacier area in Tyrol, Austria, between 1969 and 1992 derived from Landsat 5 Thematic Mapper and Austrian Glacier Inventory data. *International Journal of Remote Sensing*, 23 (4), 787-799.

Paul, F., Barry, R. G., Cogley, J. G., Frey, H., Haeberli, W., Ohmura, A., Ommanney, C. S. L., Raup, A., Zemp, M. (2010). Recommendation for the compilation of glacier inventory data from digital sources. *Annals of Glaciology*, 50, 119-126.

Paul, F., Haeberli, W. (2008). Spatial variability of glacier elevation changes in the Swiss Alps obtained from two digital elevation models. *Geophysical Research Letters*, 35, L21502, doi:10.1029/2008GL034718.

Paul, F. A., Kääb, A. (2005). Challenges for glacier inventoring from multispectral satellite data in the Canadian Artic: Cumberland Peninsula, Baffin Island. *Annals of Glaciology*, 42, 59-66.

Paul, F. A., Kääb, A., Maisch, M., Kellenbereger, T., Haeberli, W. (2002). The new remote-sensing-derived Swiss glacier inventory. I. Methods. *Annals of Glaciology*, 34, 355-361.

Paul, F. A., Kääb, A., Rott, H., Sheherd, A., Strozzi, T., Volden, E. (2009). Globglacier: A new ESA project to map the world's glaciers and ice caps from space. *EARSeL eProceedings*, 8 (1), 11-26.

Paul, F., Svoboda, F. (2009). A new glacier inventory on southern Baffin Island, Canada, from ASTER data: II. Data analysis, glacier change and applications. *Annals of Glaciology*, 50 (53), 22-31.

Parry, M. L., Canziani, O. F., Palutikof, J. P., van der Linden, P. J., Hanson, C. E. (2007). *Contribution of Working Group II to the Fourth Assessment Report of the Intergovernmental Panel on Climate Change*. Cambridge University Press, Cambridge, UK, 976 pages.

Peduzzi, P., Herold, C., Silverio, W. (2010). Assessing high altitude glacier thickness, volume and area changes using field, GIS and remote sensing techniques: the case of Navado Coropuna (Peru). *The Cryospshere*, 4, 313-323.

Philip, G., Sah, M. P. (2004). Mapping repeated surges and retread of glaciers using IRS-1C/1D data: a case study of Shaune Garang glacier northwestern Himalaya. *International Jounral of Applied Earth Observation*. 6, 127-141.

Pieczonka, T., Bolch, T., Buchroither, M. (2011). Generation and evaluation of multitemporal digital terrain models of the Mt. Everest area from different optical sensors. *Journal of Photogrammetry and Remote Sensing*, 66, 927-940.

Purdon, W. (1861). On the trigonometrical survey and physical configuration of the Valley of Kashmir. *Journal of the Royal Geographical Society of London*, 31, 14-30.

Qin D.H. (2002). *'Glacier Inventory of China (Maps)*'. Xi'an:Xi'an Cartographic Publishing House.

Qiu, J. (2008). The third pole. *Nature*, 454, 393-396.

Quick, M. C., Pipes, A. (1977). UBC watershed model. *Hydrological Sciences Bullet*in, 22, 161-253.

Racoviteanu, A. E., Paul, F., Raup, B., Khalsa, S. J. S., Armstrong, R. (2009). Challanges and recommendations in mapping of glacier parameters from space: results of the 2008 Global Land Ice Measurements from Space (GLIMS) WORKSHOP, Boulder, Colorado, USA. *Annals of Glaciology*, 50 (53), 53-69.

Racoviteanu, A. E., Williams, M. W., Barry, R. G. (2008). Optical Remote Sensing of Glacier Characteristics: A Review with Focus on the Himalaya. *Sensors*, 8, 3355-3383.

Raina, V. K. (2009). *Himalayan glaciers a state-of-art review of glacial studies, glacial retreat and climate change*. MoEF Discussion Paper. G.B. Pant Institute of Himalayan Environment & Development. 56 pages.

Raina, V. K., Srivastava, D. (2008). *Glacier atlas of India*. Bangalore, Geological Society of India.

Raj, K, B, G. (2011). Recession and reconstruction of Milam glacier, Kumaon Himalaya, observed with satellite imagery. *Current Science*, 100 (9), 1420-1425.

Raper, S. C. B., Braithwaite, R. J. (2005). The potential for sea level rise: new estimates from glacier and ice cap area and volume distribution. *Geophysical Research Letters*, 32: article L05502, DOI: 10.1029/2004GL

Raup, B., Racoviteanu, A., Khalsa, S. J. S., Helm, C., Armstrong, R., Arnaud, Y. (2007). The GLIMS geospatial glacier database: A new tool for studying glacier change. *Global and Planetary Change*, 56, 101-110.

Rees, G. H., Collins, D. N. (2004). *An Assessment of the Impacts of deglaciation on the water resources of the Himalaya*. Wallingford: Centre for Ecology and Hydrology

Rees, G. H., Collins, D. N. (2006). Regional differences in response of flow in glacier-fed Himalayan rivers to climatic warming. *Hydrological Processes*. 20, 2157-2169.

Rees, W. G. (2005). *Remote Sensing of snow and ice*. Taylor & Frances, New York.

Rees, W. G., Pellikka, P. (2010). Principles of remote sensing. In: Pellikka, P., Rees, G. W. (Editors*) Remote Sensing of Glaciers: Techniques for topographic, spatial and thematic mapping of glaciers*, 67-80. Leiden, Netherlands.

Reinwarth, O., Stäblein, G. (1972). Die Kryospäre – das Eis der Erde und seine Untersuchung. *Würzburger Geographische Arbeiten* 36: 71 pages.

Reuters, H. I., Nelson, A., Jarvis, A. (2007). An evaluation of viod-filling interpolation methods for SRTM data. *International Journal of Geographical Information Science*, 21, 983-1008.

Reznichenko, N., Davies, T., Schulmeister, J., McSaveney, M. (2010). Effects of debris on ice-surface melting rates: an experimental study. *Journal of Glaciology*, 56, 384-394.

Richards, J. A., Jia, X. (1999). *Remote Sensing digital image analysis – An introduction*. Springer-Verlang, Berlin Heidelberg.

Rivera, A., Aguna, C., Cassasa, G., Bown, F. (2002). Use of remotely sensed and field data to estimate the contribution of Chilean glaciers to eustatic sea-level rise. *Annals of Glaciology*, 34, 367-372.

Rodriguez, E., Morris, C.S., Belz, J. E. (2006). A global assessment of the SRTM performance. *Photogrammetric Engineering and Remote Sensing*, 72, 249-260.

Roy, B. C. (2001). Geodatic, geophysical and surveying techniques for evaluation of glacier mass balance and dynamics. *Geological Survey of India Special Publication*, 53, 337-45.

Rupa Kumar, K., Sahai, A. K., Krishna Kumar, K., Patwardhan, S. K., Mishra, P. K., Revadkar, J. K., Kamala, K., Pant, G. B. (2006). High resolution climate change scenario for India for the 21$^{st}$ Century. *Current Science*, 90, 334-345.

Salerno, F., Buraschi, E., Bruccoleri, G., Tartari, G., Smiraglia, C. (2008). Glacier surface-area changes in Sagarmatha national park, Nepal, in the second half of the 20$^{th}$ century, by comparison of historical maps. *Journal of Glaciology*, 54 (187), 738-752.

Schenk, T., Csatho, B., Shin, S. W. (2003). *Rigorous panoramic camera model for DISP imagery*. Joint ISPRS/EARSeL workshop 'High resolution mapping from space 2003', October 6-8.

Scherler, D., Bookhagen, B., Strecker, M. R. (2011). Spatialy variable response of Himalayan glaciers to climate change affected by debris cover. *Nature Geoscience*, DOI:10.1038/NGEO1068.

Schmidt, M. (2003). *Development of a fuzzy expert system for detailed land cover mapping in the Dra catchment (Morocco) using high resolution satellite images*. Dissertation for the degree of Doctor of Philosophy, University of Bonn, Germany.

Schmidt, M., Goosens, R., Menz, G., Altmaier, A., Devriendt, D. (2001). The use of Corona satellite images for generating a high resolution digital elevation model. *Geoscience and Remote Sensing Symposium*, 2001. IGGARSS'01. IEEE 2001, 7, 3123-3125.

Schmidt, S., Nüsser, M. (2012). Changes in high altitude glaciers from 1969 to 2010 in the Trans-Himalayan Kang Yatze Massif, Ladakh, Northwest India. *Artic, Antartic and Alpine Research*, 44 (1), 107-121.

Schöner, W., Auer, I., Böhm, R. (2000). Climate variability and glacier reaction in the Austrian eastern Alps. *Annals of Glaciology*, 31, 31-38.

Schowengerdt, R. A. (1997). *Remote Sensing: Models and Methods for image processing*. Academic Press.

Schubert, R., Schellnhuber, H., Buchmann, J. N., Griebhamme, R., Kulessa, M., Messner, D., Rahmstorf, S., Schmid, J. (2008). Climate change as a security risk. London: *German Advisory Council on Global Change and Earthscan*. 248 pages.

Schuler, T., Fischer, U. H., Gudmundsson, G. H. (2004). Diurnal variability of subglacial drainage conditions as revealed by tracer experiments. *Journal of Geophysical Research*, 109.

Sharma, K., Saraf, A. K., Das, J. D., Rawat, V., Shujat, Y. (2010). SRTM and ASTER DEM characterisitcs of two areas from Himalayan region. *International Geoinformatics Research and Development Journal*, 1, 25-31.

Shrestha, A. B., Joshi, S. P. (2009). Snow cover and glacier change study in Nepalese Himalaya using remote sensing and geographic information system. *Journal of Hydrology and Meteorology*, 6 (1), 26-36.

Shrestha, A. B., Wake, C. B., Mayewski, P. A., Dibb, J. E. (1999). Maximum temperature trends in the Himalaya and its vicinity: an analysis based on temperature records from Nepal for the period 1971-94. *Journal of Climate*, 12, 2775-2786.

Shukla, A., Gupta, R. P., Arora, M. K. (2010). Delineation of debris covered glaciar boundaries using optical and thermal remote sensing data. *Remote Sensing Letters*, 1 (1), 11-17.

Singh, P., Arora, M., Goel, N. K. (2006). Effect of climate change on runoff of a glacierized Himalayan basin. *Hydrological Processes*, 20, 1979-1992.

Singh, P., Bengtsson, L. (2004). Hydrological sensitivity of a large Himalayan basin to climate change. *Hydrological Processes*. 18, 2363-2385.

Singh, P., Haritashya, U. K., Kumar, N., Singh, Y. (2005). Hydrological characteristics of the Gangotri Glacier, central Himalayas, India. *Journal of Hydrology*, 327, 55-67.

Singh, P., Jain, S. K. (2003). Modelling of streamflow and its components for a large Himalayan basin with predominant snowmelt yields. *Hydrological Sciences Journal*, 48 (2), 257-276.

Singh, P., Jain, S. K., Kumar, N. (1997). Snow and glacier melt runoff contribution in the Chenab River at Akhnoor. *Mountain Research Development.* 17, 49-56.

Singh, P., Kumar, N. (1997). Impact assessment of climate change on the hydrological response of a snow and glacier melt runoff dominated Himalayan river. *Journal of Hydrology*, 193, 316-350.

Slama, C. C., Theurer, C., Henriksen, S. W., (Eds.) (1980). *Manual of Photogrammetry*, American Society of Photogrammetry.

Smiraglia, C., Mayer, C., Mihalcea, C., Diolaiuti, G., Belo, M., Vassena, G. (2007). Ongoing variations of Himalayan and Karakoram glaciers as witnesses of global changes: Recent studies of selected glaciers. *Developments in Earth Surface Processes*, 10, 25-248.

Sohn, H., Kim, G., Yom, J. (2004). Mathematical Modelling of Historical Reconnaissance Corono KH-4B imagery. *The Photogrammetric Record*, 19, 51-66.

Srivastava, D. (ed.) (2001). *Glaciology of Indian Himalaya*: Geological Survey of India Special Publication No. 63, 213 pages.

Srivastava, D. (2004). Recession of Gangotri glacier. In Srivastava, D., Gupta, K. R., Merkerji, S. (eds.), *Geological Survey of India Special Publication* 80, 21-32.

Steigler, S. E. (1978). *Dictionary of Earth Sciences*. Pan Books, London.

Strozzi, T., Wegmüller, U., Wiesmann, A., Wermer, C. (2003). Validation of the X-SAR SRTM DEM for ERS and JERS SAR geocoding and 2-pass differential interferometry in alpine regions. *Proceedings, IGARSS'03, Toulouse, France*.

Sund, M., Eiken, T., Hagen, J. O., Kääb. A. (2009). Svalbard surge dynmanics derived from geometric changes. *Annals of Glaciology*, 50, 50-60.

Svoboda, F., Paul, F.. (2009). A new glacier inventory on southern Baffin Island, Canada, from ASTER data: I. Applied methods, challenges and solutions. *Annals of Glaciology*, 50 (53), 11-21.

Tachikawa, T., Kaki, M., Iwasaki, A., Gesch, D., Oimoen, M., Zhang, Z., Danielson, J., Krieger, T., Curtis, B., Haase, J., Abrams, M., Crippen, R., Carabajal, C. (2011). ASTER Global Digital Elevation Model Version 2 – Summary of validation results. Land Processes Distributed Active Archive Center and Joint Japan-US ASTER science team (http://www.jspacesystems.or.jp/ersdac/GDEM/ver2Validation/Summary_GDEM2_validation_report_final.pdf).

Tandong, Y., Jianchen, P. and Shiying, L. (2007). Changing Glaciers in High Asia, In *Glacier Science and Environmental Change* (ed P. G. Knight), Blackwell Publishing, Malden, MA, USA.

Tangborn, W., Rana, B. (2000). Mass balance and runoff of the partially debris-covered Langtang glacier, Nepal. *IASH Publication No. 264*, 99-105.

Tangari, A. K., Chandra, R., Yadav, S. K. S. (2003). Temporal monitoring of the snout, equilibrium line and ablation zone of Gangotri glacier through remote sensing and GIS techniques – an attempt at deciphering climatic variabiltiy. *In Proceedings of Workshop on Gangotri Glacier*, Lucknow, 26-28 March 2003 (eds. Srivastava, D., Gupta, K. R., Mukerji, S.), Geological Survey of India Special Publication Number 80, 2004, 144-153.

Tappan, G, G., Hadj, A., Wood, E, C., Lietzow, R. W. (2000). Use of Argon, Corona, and Landsat imagery to assess 30 years of land resource changes in west-central Senegal. Photogrammetric Engineering Remote Sensing, 66 (6), 727-735.

Taschner, S., Ranzi, R. (2002). Comparing the opportunities of Landsat TM and ASTER data for monitoring a debris covered glacier in the Italian Alps within the GLIMS Project. *Proceedings IGARSS 2002*, 4, 1044-1046.

Thayyen, R. J. (2008). Lower recession rate of Gangotri glacier during 1971-2004. *Current Science*, 95 (1), 9-10.

Thayyen, R. J., Gergen, J. T. (2009). Role of glaciers in watershed hydrology: 'Himalayan catchment' perspective. *The Cryosphere Discussions*, 3, 443-476.

Toutin, T. (2004). Review article: Geometric processing of remote sensing images: models, algorithms and methods. *International journal of remote sensing*, 25, 10, 1893-1924.

Toutin, T. (2008). ASTER DEMs for geometric and geoscientific applications: a review, *International Journal of Remote Sensing*, 29, 1855-1875.

Turker, M., Gacemer, A. O. (2004). Geometric correction accuracy of IRS-1D PAN imagery using topographic map versus GPS control points. *International journal of remote sensing*, 25 (6), 1095-1104.

Ueno, K. and 11 others. (2001). Meteorological observations during 1994–2000 at the automatic weather station (GEN AWS) in Khumbu region, Nepal Himalayas. *Bulletin of Glaciological Research,* 18, 23–30.

UNEP (2009). *Recent trends in melting glaciers, tropospheric temperatures over the Himalayas and summer monsoon rainfall over India*. Division of Early Warning and Assessment (DEWA), United Nations Environment Programme (UNEP), Nairobi, Kenya

Vaux, H. J., Balk, D., Cook, E. R., Gleick, P., Lau, W. K. M., Levy, M., Malone, E. L., McDonald, R., Shindell, D., Thompson, L. G., Wescoat, J. L., Williams, M. W. (2012). *Himalayan Glaciers: Climate Change, Water Resources, and Water Security.* The National Academies Press, Washington.

Viviroli, D., Durr, H. H., Messerli, B., Maybeck, M., Weingartner, R. (2007). Mountains of the world, water towers for humanity: Typology, mapping, and global significance. *Water Resources Research*, 43.

Vohra, C. P. (1980). Some problems of glacier inventory in the Himalayas. In Proceedings of the Riederalp Workshop, September 1978, *IAHS-AISH Publication* 126, 67-74.

Vohra, C. P. (1981). Himalayan Glaciers, in: *The Himalaya: Aspects of change*, (eds. Lall, J. S. & Moddie, A. D.), Oxford University press, Delhi, 138-151.

Vohra, C. P. (2010). Glacier of Asia – Glaciers of India. In : Satellite Image Atlas of Glaciers of the world (eds. Williams, R. S., Ferrigno, J .G), *U.S. Geological Survey Professional Paper 1386-F-5.*

Waldo, T. (1987). Measuring spatial resolution. *Proceedings, Land Resources Information Systems Conference*, Beijing, pages 12-16.

Warrick, R. A., le Provost, C., Meier, M. F., Oerlemans, J., Woodworth, P. L. (1996). Changes in sea level. *In* Houghton, J. T., Filho, L. G. M., Callender, B. A., Harris, N, Kattenberg, A., Maskell, K. *Eds. Climate Change 1995: the science of climate change.* Cambridge, etc. Cambridge University Press, 359-405.

Webster, P. J., Magana, V. O., Palmer, T. N., Shukla, J., Tomas, R. A., Yanai, M., Yasunari, T. (1998). Monsoons: Processes, predictability, and prospects for prediction. *Journal of Geophysical Research*, 103, 14451-14510.

WGMS (2008). *Global Glacier Changes: facts and figures*. Zemp, M., Roer, I., Kääb, A., Hoelzle, M., Paul, F. and Haeberli, W. (eds.), UNEP, World Glacier Monitoring Service, Zurich, Switzerland: 88 pages.

WGMS (2011). Database Satistics. Retrieved on 24th October 2011 from http://www.wgms.ch/databasestat.html

Williams Jr. R. S., Hall, D. K., Sigurdsson, O., Chien, J. Y. L. (1997). Comparison of satellite-derived with ground-based measurements of the fluctuations of the margins of Vatnajökull, Iceland. *Annals of Glaciology*, 24, 72-80.

Williams, M. W. (1986). Glacier inventories of Iceland: evaluation and use of sources of data. *Annals of Glaciology*, 8, 184-191.

Wilson, J. P., Gallant, J. C. (2000). *Terrain analysis. Principles and applications*. Wiley, New York, 479pp.

Wolken, G. J. (2006). High-resolution multispectral techniques for mapping former Little Ice Age terrestrial ice cover in the Canadian High Arctic. *Remote Sensing of Environment*, 101, 104-114

WWF. (2005). *An overview of glaciers, glacier retreat, and subsequent impacts on Nepal, India and China*. World Wildlife Fund, Nepal Program.

WWF. (2009). *Witnessing change: Glaciers in the Indian Himalayas*. New Delhi, India: World Wildlife Fund, India Program.

Xing, Q., Li, Z., Zhou, J., Zhang, P. (2011). Comparison of ASTER GDEM and SRTM DEM in deriving the thickness change of small Dongkemadi Glacier on Qinghai-Tibetan Plateau. *Geosciences and Remote Sensing Symposium (IGARSS), 2011 IEEE International*, 3171-3174.

Xu, B., Cao, J., Hansen, J., Yao, T., Joswia, D. R., Wang, N., Wu, G., Wang, M., Zhao, H., Yang, W., Liu, X., He, J. (2009). Black soot and the survival of Tibetan glaciers. *Proceedings of the National Academy of Sciences of the USA*, 106, 22114-22118.

Xu. J., Shrestha, A., Vaidya, R., Errikson, M., Hewitt, K. (2002). *The Melting Himalayas: Regional Challenges and Local Impacts of Climate Change on Mountain Ecosystems and Livelihoods*. International Centre for Integrated Mountain Development

Yao, T., Thompson, L., Yang, W., Yu, W., Gao, Y., Guo, X., Yang, X., Duan, K., Zhao, H., Xu, B., Pu, J., Lu, A., Xiang, Y., Kattel, D. B., Joswiak, D. (2012). Different glacier status with atmospheric circulations in Tibetan Plateau and surroundings. *Nature Climate Change*, 2, 663-667.

Ye Baisheng., Ding Yongjian., Liu Fengjing., Liu Caohai. (2003). Responses of various-sized alpine glaciers and runoff to climatic change. *Journal of Glaciology*, 49, 1-7.

Ye, Q., Kang, S., Chen, F., Wang, J. (2006). Monitoring glacier variations on Geladandong mountain, central Tibetan Plateau, from 1969 to 2002 using remote-sensing and GIS technologies. *Journal of Glaciology*, 52, 537-545.

Zemp, M., Haeberli, W., Hoelzle, M., Paul, F. (2006). Alpine glaciers to disappear within decades. *Geophysical Research Letters*, 33, L13504

Zemp, M., Haeberli, W., Hoelzle, M., Paul, F. (2007). Glacier fluctuations in the European Alps 1850-2000: an overview and spatio-temporal analysis of available data. *In* Orlove, B., Wiegandt, E., Luckman, B. H., *Darkening peaks: glacier retreat, science, and society.* Berkley, CA, University of California Press.

Zemp, M. *et al*. (eds.) (2008). *Global Glacier Changes: Facts and Figures*, UNEP, World Glacier Monitoring Service (WGMS), Zurich, Switzerland, 2008, 88 pages.

Zeng, Q., Cao, M., Feng, X., Liang, F., Chen, X., Sheng, W. (1983). A study of spectral reflection characteristics for snow, ice and water in the north of China. In: Goodison, B (ed.), *Hydrology applications of remote sensing and remote data transmission*, IASH, 145, 451-462.